Fiber Based Coherent Lidars for Remote Wind Sensing

Lindelöw, Per Jonas Petter

Publication date:
2008

Document Version
Publisher's PDF, also known as Version of record

Petter Lindelöw

Fiber Based Coherent Lidars for Remote Wind Sensing

PhD thesis, November 2007

Fiber Based Coherent Lidars for Remote Wind Sensing

Petter Lindelöw

November 7, 2007

Abstract

In this thesis a study of coherent lidars for remote wind sensing is undertaken. Remote wind sensing is important when mast mounted anemometers cannot be used due to economical or practical reasons. One such important field is within the wind energy sector where accurate wind sensing at distances of up to a few hundred meters from the ground is important for site evaluation, turbine power verification and for future applications such as active blade pitch and load control for an optimized output.

Coherent lidars can detect very small frequency variations in collected weak light. A viable solution to remotely sense wind is thus to sense the Doppler shift induced on the received light scattered off aerosols suspended in the atmosphere. Fiber based systems are cost effective and robust, and can operate without safety restrictions; they are thus an ideal choice for non-scientific applications.

The thesis covers a wide field; the state of the art coherent lidar wind sensors is reviewed, the signal model is expanded upon and results of applied research on commercially available lidars, as well as the development and evaluation of a frequency modulated prototype, are presented.

The standard model for coherent lidars sensing dispersed targets was expanded upon by considering the range dependent correlated contribution duration of range gated systems, which significantly affects the narrowband signal to noise description and the weighting of the sample volume. A model of the range dependent collection efficiency obtained by focused fiber based lidars has been developed and verified. These advancements are important for predicting the lidar performance and optimizing the signal processing.

A novel frequency modulation concept, which is promising for the remote sensing of wind, was invented in this study. The technique is based on equidistantly frequency stepped pulse trains and a frequency pursuing local oscillator. It operates at high pulse repetition but will despite this avoid the customary disadvantages; range ambiguity and a limitation of the sensing range. This novel concept could provide more accurate systems while avoiding the use of high peak powers which introduces stimulated Brillouin scattering and non-linear effects as well as putting higher demands on other components in the transmitter.

A frequency sweeper, appropriate for the invented frequency modulation technique, was constructed and evaluated. This sweeper was subsequently used to modify a continuous wave lidar into a frequency modulated prototype and a proof of principle campaign, demonstrated the merits and limitations of the novel technique.

Applied investigations of wind data collected from two different commercial systems revealed that the weighting of the wind distribution spectrum is influenced by single particles with atypically long correlated scatter durations, when sensed by focused continuous wave systems, and by the range dependent collection efficiency, when sensed by focused range gated systems.

Resumé

(Abstract in Danish)

I denne Ph.D.-afhandling er kohærent lidar teknologien for afstandsmåling af vind undersøgt. Afstandsmåling af vind er vigtig i de tilfælde hvor kopanemometre der er monteret i en mast, af praktiske eller økonomiske årsager ikke kan bruges. Præcis vindmåling på afstande op til nogle hundrede meter fra jordens overflade er særligt vigtigt inden for vindenergisektoren for eksempel til vurdering af potentielle møllepladser, turbine verificering og for fremtidige anvendelser, såsom aktiv bladvinkelregulering og belastningskontrol for at opnå et optimeret udbytte.

Kohærente lidars kan detektere meget små frekvensvariationer i et ekstremt svagt lyssignal. Det er derfor muligt at afstandsmåle vindens hastighed ved at måle Doppler-skiftet påført det indsamlede lys reflekteret fra aerosoler der følger luftstrømmen. Fiberbaserede systemer er økonomiske i drift, robuste og kan bruges uden sikkerhedsrestriktioner. De er derfor velegnede til ikke-videnskabelige applikationer.

Denne afhandling vil dække en gennemgang af de nyeste vindmålende kohærente systemer, udviklingen af signalmodellering og resultaterne fra studier af kommercielle systemer såvel som udvikling og evaluering af en frekvens moduleret prototype.

Signalmodellen for kohærente lidars, der måler et distribueret mål, som eksempelvis atmosfæren, er blevet udviklet. Specielt med hensigt på den afstandsafhængige korrelerede periode i refleksionerne der bliver samlet under en målingsperiode. Denne effekt har stor betydning for det smalbåndede signal/støj forhold og for vægtningen af prøvevolumen. En model, der beskriver den afstandsafhængige indsamlingseffektivitet af et fokuseret fiberbaseret lidarsystem, er blevet udviklet og verificeret. Disse fremskridt er vigtige for forudsigelser af en lidars ydeevne og for optimal signalbehandling.

En ny frekvensmoduleringsmetode, som er tilpasset for afstandsmåling af vind, blev udviklet i dette studie. Teknikken er baseret på ækvidistant trinvist frekvensmodulerede pulstog og en frekvens følgende lokal oscillator. Den sender pulser med høj repetition men undgår trods dette de almindelige ulemper såsom afstandsambiguiteter og begrænset målingsafstand. Denne metode kan give mere nøjagtige systemer uden at bruge de høje spidseffekter, der forårsager stimuleret Brillouin spredning, ikke-lineære effekter og gør, at der stilles højere krav om holdbarhed for øvrige komponenter i transmitteren.

En frekvens skanner, der er tilpasset den opfundne frekvensmoduleringsteknik, er blevet konstrueret og undersøgt. Denne frekvens skanner blev herefter brugt til at modificere en kontinuerligt sendende lidar til en frekvensmoduleret prototype. En målingskampagne for at påvise den nye tekniks fordele og begrænsninger blev udført.

Undersøgelser af vinddata indsamlet med to forskellige kommercielle systemer er også blevet lavet. Det er påvist, at enkelte partikler med en utypisk lang korreleret spredningsperiode påvirker vindspektra målt med kontinuerligt transmitterede lidars, og at den afstands-afhængige indsamlingseffektivitet påvirker vindspektra målt med fokuserede pulsede lidars.

“I had always considered that if you thought hard and long enough, you could work out anything. Wind was a hard one though. It had always puzzled me until the day I realized that it evidently was caused by all the trees waving about.”

Terry Pratchett

Acknowledgements

The accomplishment of a thesis requires contributions from several individuals. On this page I would like to sincerely thank them all; for their trust and patience, for the time devoted to reflection and assistance and most of all for support and love.

First, I would like to thank my supervisors Lektor Johan Jacob Mohr at the Ørsted institute, Lektor Christophe Peucheret at DTU•COM, Thomas Feuchter at NKT Research and Professor Erik Lintz Christiansen also at Ørsted. I would also like to thank Christian Vestergaard Poulsen at Koheras who was integral to the instigation of this thesis and provided me with state-of-the-art fiber lasers. I am grateful for all their help and advice throughout this project. Another person who has helped to lift the standard of this thesis as well as my spirits is my office mate Thomas Jensen.

I would like to thank the dynamic lidar-crew at Leosphere, notably Remy Parmentier and Jean-Pierre Cariou. Merci d'écouter mes idées et de m'expliquer vos systèmes impulsés, pendant et après mon séjour chez vous, et de m'offrir de passer ce fabuleux printemps de 2007 à Paris. I would also like to thank their rivals at Qinetiq, notably Mike Harris and David Bryce, two very wise scientists with a fantastic talent for promoting a new technology to a conservative market. Both groups should have great thanks for producing and marketing admirable wind sensors which I have had the pleasure to experiment with.

I am very grateful to my future colleagues at Risø National Laboratory, notably Jacob Mann, Torben Mikkelsen, Ferhat Bingöl, Mike Courtney and Ioannis Antoniou. All great visionaries whom have supplied me with vital inspiration and enthusiasm. Special thanks to Risø for letting me modify their lidar prototype.

Many others have helped me prepare for this thesis. I would like to thank the people I worked with at Optillion and QuMat prior to this thesis, notably Anneli Åström and Jonas Ohlsson. I would also like to mention Urban Eriksson who is a wonderful role model and without whose scientific preparation I would never have made it through this thesis.

Also, I would like to thank the people at KTH in Kista, especially Olivier Douhéret, who taught me everything necessary about how to succeed as a Ph.D.-student.

On a more personal note I would like to thank Charlie for her love and support which means everything to me. I would also; because she has helped me, a lot with the English, like to thank her again.

Jag vill också tacka mina föräldrar, Per och Karin Lindelöw, och min bror, Mårten Lindelöw, för deras stöd och för allt att annat som är viktigt i livet.

And to the ones in Galhampton; at the point I am writing this it looks like I will finish this thesis before it finishes me.

Preface

This study was initiated as a Ph.D. project within NKT Research's Ph.D. school, the Photonics Academy. The project is a combined effort of the Ørsted and COM institutes at the Technical University of Denmark (DTU) and the commercial actors NKT Research and Koheras A/S. The work started on the 1st of November 2004 and was finished on the 31st of October 2007.

The project aimed at combining Ørsted's experience in frequency modulated radar systems, COM's optical system knowledge and facilities and Koheras' ADJUSTIK fiber laser to develop a frequency modulated fiber based wind sensing lidar.

The lidar groups at Qinetiq and Leosphere as well as the wind meteorology group at Risø have been important channels for discussions on applied matters throughout this project.

An external research stay took place at Leosphere AS in Orsay, France from the 16th of April to the 15th of June 2007.

Project overview

Within the lidar community there is an interest to take advantage of the developments of optoelectronic components driven by the high volume market for fiber optic communication to improve the performance of non-scientific lidars[1]. Highly advanced and powerful components in the 1.5 μm wavelength region are affordable, reliable and available off the shelf. Furthermore, the eye is relatively insensitive to the near infra-red wavelengths from 1.5-1.8 μm. Near infra-red atmospheric sensing lidar systems can be designed in order to operate without safety restrictions which is important for non-scientific use. Fiber pigtailed components can easily be integrated as building blocks into a robust system. One such component, which was a key factor for the initiation of this project, is a tunable fiber laser, provided by Koheras, which is extremely coherent since it contains an incorporated Bragg grating.

Radar technology was massively developed during the 20th century and is more mature than lidar technology. Several frequency modulation techniques have been invented to improve the spatial resolution of radars, notably pulse compression. It was foreseen that fiber pigtailed components from the fiber communication industry would be sufficiently advanced to construct a lidar system which mimicked radar modulation techniques. Such experiments had previously been performed in which saw tooth modulation was used for range, velocity and vibration sensing of discrete targets[2].

Qinetiq has developed and commercialized a continuous wave lidar which has received much attention from the wind energy industry. This system achieves range resolution by using a focused telescope. However, erroneous sensing will occur in the presence of strong scatterers displaced from the focused distance, most notably clouds at low altitude, and it quickly loses range resolution with sensing distance.

The initial objective of this thesis was to investigate if linear saw tooth modulation could be used in coherent lidars to improve the performance of wind velocity sensing.

However, it was found early on that saw tooth modulation could not simultaneously resolve range and velocity when used to sense dispersed targets, such as the atmosphere, which ideally scatters homogeneously along the beam path.

As an alternative two new frequency modulation schemes appropriate for velocity sensing of dispersed targets were proposed. One based on random frequency modulation and a delayed local oscillator. A similar method was later found to already have been applied for wind sensing[3]. The other is based on emission of equidistantly frequency stepped pulse trains with a pursuing local oscillator. Both methods allow freedom in the choice of emission rate without introducing range ambiguities or limiting the sensing range. The second concept was chosen as the main track since it gives a better accuracy while the first can use cheaper less coherent lasers. This method caught the attention of NKT Research and in conjunction a patent application was filed in November 2006[4] for a frequency stepped pulse train modulated coherent lidar.

Two frequency stepped pulse train generators were identified and investigated. A frequency sweeper based on a seeded fiber loop is believed to have several advantages and was selected as the main track. Such a loop was constructed and evaluated. This frequency sweeper had several interesting features making it a veritable competitor to the ADJUSTIK tunable fiber laser produced by Koheras AS. The constructed frequency sweeper was used to modify a lidar prototype for a proof of principle study. Velocity measurements of a hard target showed the abilities and limitations of the current set up.

The range dependent collection efficiency of focused fiber based coherent lidars was studied in parallel to the work on frequency modulated systems. An alternative to a commonly used model[5] was established and verified by measuring the energy received by a continuous wave lidar, sequentially focused at different distances, sensing the velocity of an electric fan. This model takes into account small receptor apertures and co-propagation of the local oscillator and the received backscatter in a single mode fiber.

It also became necessary to consider the implications, on the weighting in the sample volume and the narrowband signal, of the range dependent correlation duration of scatter contributing to a range gate.

Two investigations of data collected by commercial lidar systems were performed. The first revealed the influence of the range dependent collection efficiency of a focused range gated system by comparing data collected with a commercial lidar with mast mounted cup anemometers references. The second revealed that the wind distribution spectrum is influenced by single particles with longer scatter durations when sensed by focused continuous wave systems.

A chart providing an overview of the progress of this project is found in Figure 1.

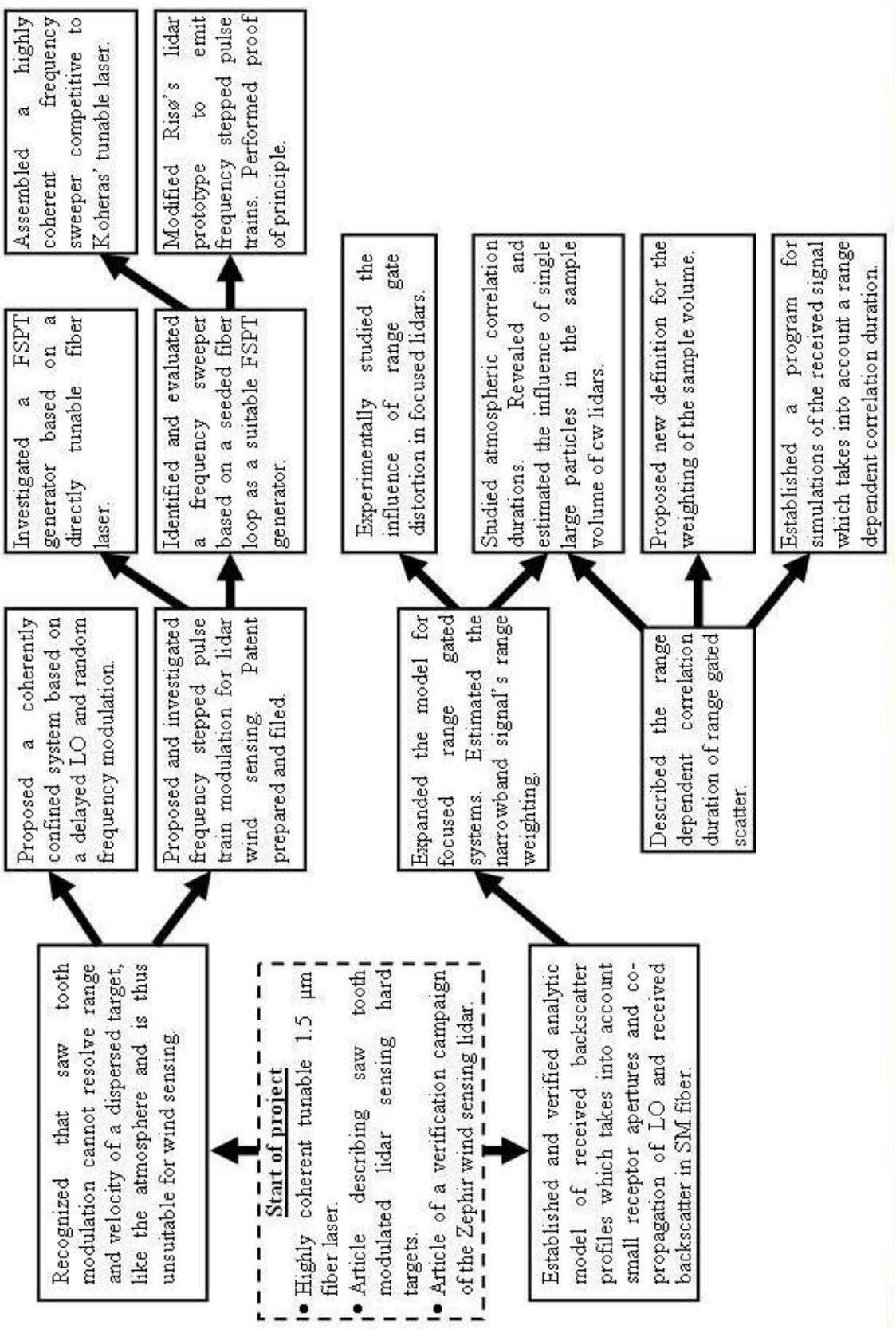

Figure 1 : Overview of project progress.

Chapter Overview

The thesis starts with a general introduction to wind sensing and light detection and ranging. This is followed by a detailed description of coherent lidar technology and particularly of frequency modulated coherent lidars. The focus is on Frequency Stepped Pulse Train modulation, a method which was invented during this thesis. With this frequency modulation technique it is possible to operate at high pulse repetition frequency while avoiding limitations caused by range ambiguities or sensing range.

The experimental part of this study is described in the second part of the thesis. It sets out the construction and evaluation of a fiber loop frequency sweeper, which is an appropriate generator of frequency stepped pulse trains. Furthermore, the modification of a lidar prototype into a frequency stepped system and the results of a proof of principle study are described.

An analysis of the commercial Windcube accuracy dependence on the wind profile brings this thesis to a conclusion.

Two sections are appended to this work; the first discuses the importance of narrow laser linewidths for coherent lidars, the second describes an investigation of the correlated duration of scatter generated by a continuous wave lidar.

A short description of the contents of each chapter follows below.

Chapter 1: Introduction to wind sensing with coherent lidars gives a general introduction to wind sensing, lidars and related terminology. Several concepts which are important for the understanding of wind sensing by coherent lidars are also treated in this chapter. The chapter ends with a discussion on applications and the current state of commercially available wind sensing lidars.

Chapter 2: Coherent lidar gives a detailed description of the coherent lidar technology. The key concept of coherent lidars, heterodyne detection, is explained and quantified. System layouts with several options are described. The temporal and spatial collection of scatter, which is a fundamental concept for proper understanding of coherent lidars, is illustrated. In addition, the lidar equation is introduced and the standard deviation in the wind measurement as a function of pulse energy and PRF is discussed. The optic configuration is described and modeled - something which is vital for a correct estimation of the lidar performance. Finally, the weighting function of the sample volume and the effects of inhomogeneous backscatter coefficient and correlation durations are discussed.

Chapter 3: Frequency modulated coherent lidars reviews previously proposed frequency modulation techniques, namely linear saw-tooth modulation and range gating of scatter generated by pulses containing frequency combs. Subsequently, two similar technologies, which use limited coherence and a delayed local oscillator to generate a coherent signal of the scatter from a distance corresponding to the delay, are briefly described. The core of this chapter is dedicated to the introduction of frequency stepped pulse train modulation which allows freedom in pulse repetition frequency without introducing range ambiguities or limiting the sensing range.

Chapter 4: Frequency stepped pulse train generators is dedicated to describing suitable frequency stepped pulse train generators, notably a frequency sweeper based on a seeded fiber loop containing an erbium doped fiber amplifier and an acousto-optic modulator. The frequency sweeper which was constructed in this project is evaluated, with emphasis on its suitability for coherent wind sensing. The frequency sweeper is also compared to the tunable ADJUSTIK fiber laser as an extremely coherent pseudo-tunable source.

Chapter 5: Frequency stepped pulse train modulated lidar presents the results from a proof of principle campaign with a lidar prototype which was modified to operate in frequency stepped pulse train modulation mode.

Chapter 6: Lidar measurement deviation due to wind shear is an applied section which shows an error analysis of a commercial lidar system. Wind data from a validation campaign of the Windcube in Høvsøre shows a wind shear dependency. This altitude dependent error is likely to arise due to an error in the estimation of the effective sensing altitude of a range gated focused lidar system.

Chapter 7: Conclusions on fiber based coherent lidars for the remote wind sensing bring this thesis to an end.

Appendix A discusses laser coherence.

Appendix B describes a method to estimate the atmospheric correlation duration from measurements using 1.5 μm coherent lidars and studies the influence of large single particles within the sensing beam of a continuous wave lidar

Table of Contents

1. Introduction to wind sensing with coherent lidars

1.1. Wind sensors

Understanding wind, i.e. the flow of air, is important in several sciences, for example meteorology and aerodynamics. Extensive work is carried to predict air flow, from detailed aerodynamic models and forecasting on a global level, to controlled experiments performed in wind tunnels of varying sizes. However, it is not possible to make high resolution predictions of wind velocity around large structure. Furthermore, it is difficult to imitate natural wind flows in wind tunnels and results on miniaturized models cannot always be correctly scaled up with precision. It is also essential to verify and quantify the limitations of these algorithms and models. Accurate measurement of wind flows is therefore important, for example, to sense the incoming wind from an airplane, survey turbulent winds in airports or to supply wind energy information to serve a number of applications within the wind power industry.

Wind is sensed on several scales. Global scale wind sensing over the ocean is done by satellite mounted radar or radiometers. On a smaller scale wind flows are sensed with several technologies which can be divided into local or remote sensors. This chapter gives a brief summary of different wind sensing techniques. A summary of the most common wind sensors can be found in Table 1 and Table 2.

1.1.1. Local wind sensors

Local flow studies can be performed by hot wire anemometers, pitot tubes, particle tracking and particle imaging velocimeters. Dominating local wind sensors are cup and sonic anemometers, see Figure 2.

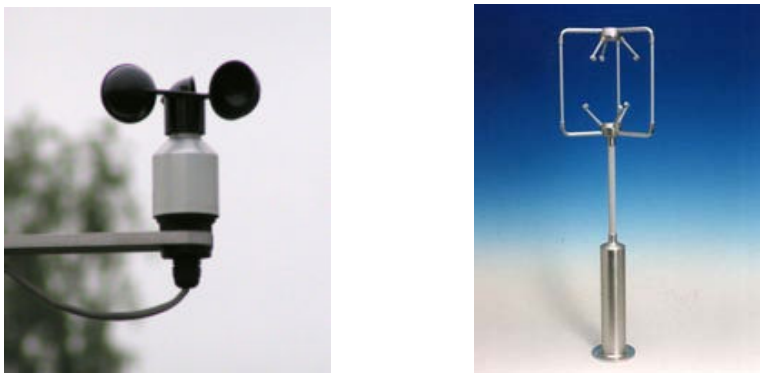

Figure 2 : Cup and Sonic anemometers.

Cup anemometers[6] are cost effective, approximately $ 5000 including a short mast, and robust mechanic wind sensors. They measure the mean horizontal wind speed, typically as ten minute averages due to the inherent inertia. It is advised to only use cup anemometers for high precision wind sensing in the range from 4 to 16 m/s. Mast mounted cup anemometers are currently the choice of preference for the wind energy sector. However, as turbines grow larger the need for wind speed profiles at altitudes above 75 m makes their deployment more problematic, and in the end less cost effective. Properly calibrated and mounted cup anemometers will measure ten minute average horizontal wind velocity with accuracy better than 1 %.

A sonic anemometer[6] measures the time it takes for an ultrasonic pulse (typical carrier frequency 100 kHz) to propagate from the emitter to the receiver, a path length in the order of 10 cm. The pulse propagation duration depends on the wind velocities in the path direction but also on the sound velocity. A priori knowledge of the sound velocity, and thus the air temperature, is needed and sonic anemometers are therefore equipped with precision thermometers.

Sonic anemometers are non-mechanical sensors and thus overcome many of the problems associated with cup anemometers, albeit at a considerably higher price. 3-axis sonic anemometers can provide measurements of the three-dimensional wind vector. Since the sensor is free from inherent inertia it has a high temporal resolution and is appropriate for turbulence studies. However, flow distortions caused by the structure of the instrument can translate into significant errors in the direction and magnitude of the measured wind vector. Sonic anemometers are stated to be able to resolve transit times corresponding to an accuracy of 0.5 cm/s. Nevertheless, in comparisons with cup anemometers they typically yield a standard deviation of several 10 cm/s on ten minute averages.

The primary disadvantages of local systems are that they are expensive, and sometimes it is impossible, to locate them at the site of interest, e.g. above a runway or in front of an airplane. For high altitudes sounding balloons can be used. For altitudes lower than a hundred meters it can be competitive to put up masts. However, masts might need building permits and are difficult and expensive to redeploy. The mast structure will also disturb the air flow.

1.1.2. Remote wind sensors

Remote wind sensing is performed from a large range of distances. Radars and radiometers measure from satellites. A wind sensing lidar is even scheduled to be launched on the Aeolus mission in 2009. Lidars and sodars are in general used to measure within the planetary boundary layer, i.e. up to 1 km. A slightly old but very thorough market survey of remote wind sensing systems was performed by NASA in 2003[7]. A short description of the merits and limitations of the available techniques follows in subsequent chapters.

While local sensors measure the wind velocity with high spatial resolution, essentially at one point, remote sensors concurrently sample a volume of air, which typically is rather narrow and can extend for several tens of meters. Volume sampling is usually a drawback but for many applications the wind distribution in larger volumes contains important information.

1.1.3. Microwave scatterometers, radiometers and radars

Satellite carried radiometers and radars can estimate winds over oceans also during clear air conditions. The emissivity and reflection of the ocean surface depends partly on the sea surface structure. Since capillary waves on the sea surface are correlated to the wind velocity up to ten meters over the surface, it is possible to derive the wind velocity from the captured radiation. This relation is not valid close to shore lines.

Satellite sensors typically average spot sizes of several kilometres with an accuracy of ±2 m/s and ± 20 degrees in direction. The sea surface structure is also influenced by

down winds, rain, wave foam etc., and availability at a site is limited to two measurements per day at fixed times.

Airborne synthetic aperture radars yield standard deviations of about 1 m/s and can measure closer to the shoreline. It is also possible to directly measure Doppler shifts, and thus wind velocity, with microwave radars. However, they operate poorly in clear air conditions and are dependent on clouds or rain.

1.1.4. Sodar

A sodar emits an acoustic pulse, with a 3-6 kHz carrier frequency, and measures the frequency of sound reflected from fluctuations in the refractive index, essentially air layers with different temperatures and pressure which follow the wind. The returned frequency is thus Doppler shifted in relation to the wind velocity in the sound propagation direction. The three dimensional wind vector can be constructed from the returns from at least three different directions. Sodars will typically use three or four transceivers, see Figure 3.

Figure 3 : A transportable sodar system.

Range can be resolved by measuring the propagation time of the scatter. It is thus possible to obtain wind velocity information at several altitudes with one system. However, for precision in altitude the air temperature over the propagation path must be known, since the velocity of sound strongly depends on air temperature. The wind is typically sampled with 20 meters altitude interval.

Sodars rely on temperature shifting in the atmosphere, which leads to a relatively low availability, particularly at high altitude and during the night, typically 70-85 %[8]. The sensitivity is typically low for sodar systems, which leads to long acquisition times. The fact that sodar systems operate in the audible range may be a disadvantage. Sound propagates slowly as compared to electromagnetic radiation. Beam drift is therefore more severe which in turn reduces the SNR. Sodars are also expensive, with an estimated cost of $ 80 000.
Sodars, which are calibrated to a nearby low mast, can nevertheless measure wind with an uncertainty of 2 to 4%[9], but much worse deviations have frequently been reported elsewhere[10]. Commercial sodars sense wind up to a height of 500 m under favorable conditions. Spatial resolution is typically between 5 and 10 meters and with updates every second.

1.1.5. Lidar

Wind sensing lidars operate on similar principles as sodars and retrieve the Line Of Sight (LOS) wind speed from a narrow but extended volume of clear air. 3D wind velocity and turbulence can be constructed from this data. However, instead of emitting acoustic pulses they emit coherent laser light. Light has a much smaller wavelength than sound, hence lidars can have a smaller footprint and the light speed is effectively constant in the atmosphere. More importantly, light will scatter off aerosols and molecules which are well dispersed in the planetary boundary layer, availability is therefore typically close to 100 %. A top and side view of a wind sensing lidar can be seen in Figure 4.

Figure 4 : Top and side view of an early ZephIR prototype.

Commercial lidars sense winds at ranges up to 200 m, with effective sample volume lengths from a few meters up to 30 m. Three dimensional wind vectors are typically constructed from conical scans with an update rate of 1 s. Lidars have shown a standard deviation of 0.2-0.3 m/s during verification campaigns against ten minute averages from mast mounted cup anemometers[11, 12, 13]. A comparative time series of the horizontal wind measured with a lidar and a cup anemometer can be found in Figure 5.

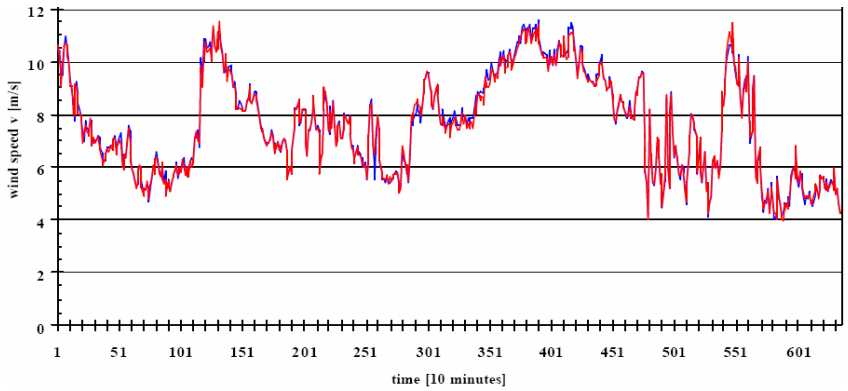

Figure 5 : A comparative time series of the horizontal wind velocity at 65 m measured with a cup anemometer (red) and a cloud corrected ZephIR (blue)[13].

Conically scanned 1.5 µm lidars are thus an excellent option for eye safe remote sensing of 3D winds in the first few hundred meters of the atmosphere over flat terrains. Commercial systems have proved to sense wind averaged over some tens of

meters vertically with a typical accuracy better than 20 cm/s. However, where it is possible to place the instrument at the site of interest, established technologies out-compete lidars. The merits, limitations and principle of wind sensing lidars will be thoroughly discussed in this thesis.

Local sensors	
Technology	**Comment**
Cup anemometer	Still the choice of preference for most commercial applications. Highly accurate horizontal wind velocity but with limited temporal resolution and dynamic range. A calibrated cup anemometer costs about € 700 but raising an equipped mast for wind power site evaluation can cost up to 100 k€.
Sonic anemometer	Measures 3D wind vectors without inbuilt inertia. Suitable for turbulence studies.
PIV, PTV, LDA	Measures flow perpendicular to the system. Typically needs added particles but is, for example, also used for blood flow measurements.
Pitot tube	Measures pressure induced by wind on a thin tube. Typically used to determine airspeed of aircrafts.

Table 1 : List of locally sensing wind sensors.

Remote sensors	
Technology	**Comment**
Lidar	Measures the Doppler shift of scatter generated off aerosols suspended in the wind. Senses wind at distances up to 200 m with spatial resolution from 5-30 m and temporal resolution of 1 s. Comparisons with cup anemometers have shown standard deviations as low as 0.2 m/s on the horizontal wind flow over flat terrain. However many issues are still unresolved. Leosphere and Qinetiq are current suppliers.
Sodar	Similar principle as lidars but sound propagation has several disadvantages and systems typically need to be calibrated with a nearby low mast. Limited availability but senses wind at distances up to 500 m with spatial resolution of 10-20 m and temporal resolution of 1 s. Comparisons with cup anemometers have shown standard deviations of several 10 cm/s. Metek and Scintec are two examples of system suppliers.
Microwave radar	Cannot sense in clear weather, low resolution.
Radio- and scatterometer	Derives wind velocity close to ocean surface from sea surface roughness, does not work over or close to land. Low spatial resolution and accuracy worse than 1 m/s.

Table 2 : List of remote wind sensors.

1.2. Lidar overview

Lidar, ladar and laser radar are different names for range detection systems that operates in the optical frequency region, typically at wavelengths from 0.25 to 10 μm. They are thus the optical equivalent to radars which operates with radiowaves of wavelengths from 0.5 to 500 cm. A lidar will typically emit a pulse and measure the time until scattered reflections return, in some cases they also qualitatively measure some property of the backscattered light, such as the amplitude, polarization or frequency shift.

Although very similar to radars, lidar technology has some fundamental advantages compared to radars due to the considerably shorter carrier wavelength.

Beam divergence
The diffraction limited beamwidth divergence in the far field is proportional to λ/D, where λ is the wavelength and D the diameter of the system aperture. A lidar beam will typically diverge by μrad while radar beams typical diverge by many mrad. Many lidars will in addition operate in the nearfield and are not limited by diffraction. The far-field region is commonly considered to be distances greater than $2D^2/\lambda$, which can be some kilometers for a lidar system. The small beam divergence and the excellent coherence of a lidar thus allow for mapping of physical features with very high spatial resolution. This characteristic is an important feature for traffic surveillance and military applications such as missile guidance.

Backscatter from aerosols
The intensity scattered from an object with a radius smaller than the wavelength scales as λ^{-4}. This scattering mechanism is known as Rayleigh scattering. Mie scattering is more complex and originates from objects with a radius similar to the wavelength, see Figure 6. Optical wavelengths can thus generate significant scatter from microscopic airborne particles and even directly from air molecules. Lidar is therefore used to remotely sense airborne pollution, cloud properties and even wind in clear atmospheres.

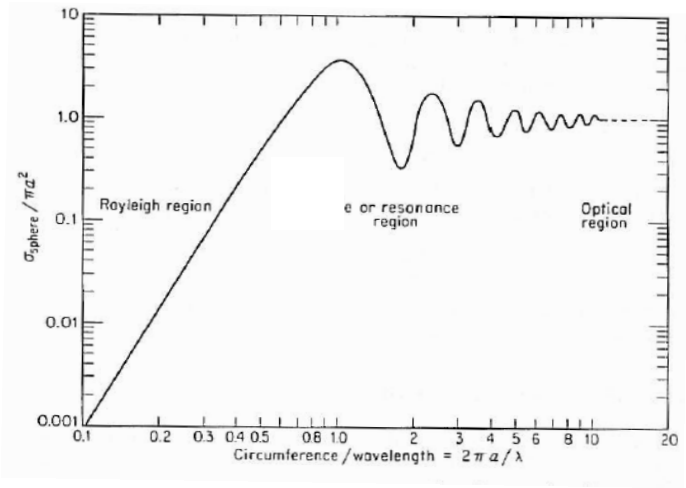

Figure 6 : Cross section of a spherical object, a = radius, λ = wavelength

High energy quanta
Optic photons have an energy rich quanta and can interact with targets in other ways than through elastic scattering. The high photon energy allows it to interact inelastically with atoms and molecules by exciting electrons or interacting with vibrational states of molecules. Either absorption or fluorescence phenomena can be studied.

Lidars are therefore used for remote spectroscopy, for example to quantitatively sense ozone and carbon dioxide. For the same reasons they can be used for measurements of chlorophyll for biomass studies.

In other respects the lidar technology has shortcomings. Since optic radiation has relatively high absorption and scatter probabilities lidars cannot easily penetrate dense materials, e.g. clouds. Approximate attenuation coefficients at sea level for various atmospheric conditions are given in Figure 7. Narrow beams are superior for high resolution measurements but will give lower coverage and scan durations will typically be much longer. Another disadvantage is that the human eye is sensitive to most optical wavelengths, in particular in the visible range of 400-700 nm, so the emitted energy has to be limited.

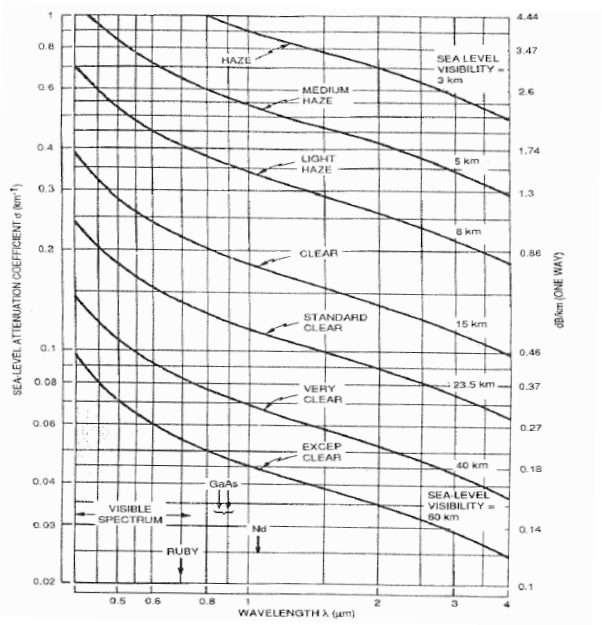

Figure 7 : Attenuation coefficients at sea level for various atmospheric conditions[14].

Lidars are ideally used as a complementary technology for applications where radars are insensitive, e.g. gas or aerosol sensing, or when high directivity is needed, i.e. for target tracking in cluttered environments.

1.2.1. Lidar categories

The term lidar is used for several techniques for remote sensing with lasers. They are generally divided into a few generic types depending on their sensing method. The simplest lidar system is the laser range finder which measures the distance to a solid target by measuring the time of flight of a laser pulse with high precision. When used at high pulse repetition rates it is possible to make line of sight speed and vibration

sensing of hard targets. Fast and highly precise scanning allows for target tracking and extremely detailed 3D imaging. Such systems are often referred to as laser radars.

Another early application was to quantitatively sense backscatter and extinction coefficients; such systems are often referred to as elastic lidars. This data can be extrapolated to give information about aerosols. Size distributions can be determined by using several lasers with different wavelengths. Polarization sensitive receivers show differences of silica particles, ice crystals and pollution[15].

The elastic aerosol lidars were later elaborated to resolve frequency and provide Doppler shifted frequency spectra, thus measuring the wind distribution in clear air atmospheres under the assumption that the return came from aerosols suspended in the atmosphere. Such systems are sometimes referred to as Doppler Wind Lidars (DWL) and are explained in detail in this thesis. A history of the development and utilization of wind lidars can be found in Laser Remote Sensing[16].

Other atmosphere sensing systems are Raman lidar and Differential Absorption Lidar (DIAL) which perform remote spectroscopy. Both these principles are based on inelastic interaction and thus exchange noteworthy amounts of energy with the target[17].

DIAL uses two or more lasers which are close in wavelength so that atmospheric propagation is effectively equivalent. One of the emitted wavelengths is chosen so that it is absorbed by the sensed gas in addition to the scattering losses. By measuring the difference in the received intensity it is possible to derive the total absorption and thus identify and quantitatively measure chemical compounds. Raman lidar looks at the frequency shift induced on the backscatter by excitation of molecular vibrational states.

1.2.2. Lidar terminology

Lidars exist in a manifold of configurations. This section lists important terminology and gives merits and limitations of the different concepts. Coherent detection and focused systems, which are two fundamental concepts in this thesis, are described in detail in chapters 2.1 and 2.4.

Monostatic or bistatic systems

Lidar systems are classified as monostatic or bistatic systems[18]. Monostatic systems share a common transmit and receive path while bistatic systems overlap the field of view of a transmit telescope with the field of view of a receive telescope. A bistatic system will in this way create a very fine spatial confinement since only scatter generated in the overlap volume will be detected. Bistatic systems are less common in practice as it is difficult to achieve a good trade-off between a satisfactory range resolution and a sufficient backscattering volume, while maintaining flexibility in the choice of sensing distance.

Focused or collimated systems

Lidar systems can furthermore be classified as collimated or focused. Collimated systems are common for search and detect applications while focused systems offers benefits for medium range atmospheric sensing. The received backscattered power of

focused continuous wave (cw) systems will depend on distance, as exemplified in Figure 8 and described in chapter 2.4.

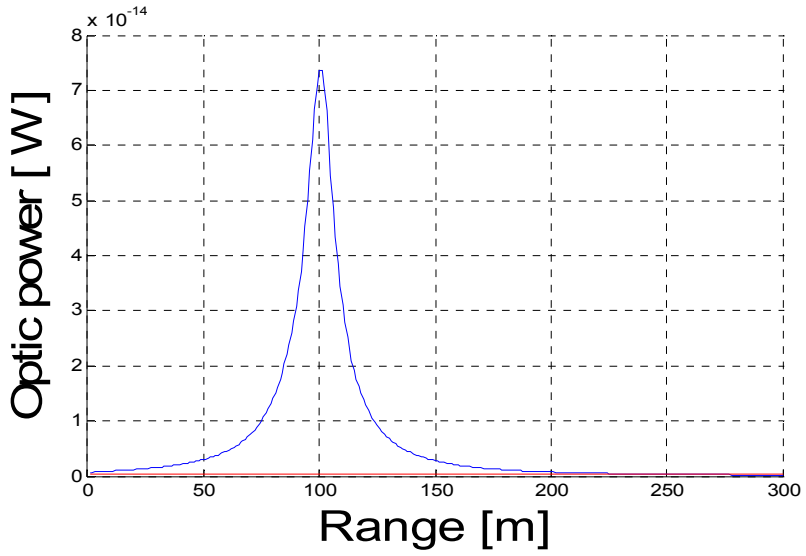

Figure 8 : Received backscatter profile of a focused 1.5 µm monostatic cw system with a 4.4 cm effective lens diameter. The system is focused at 100 m yielding a sample volume with full width half maximum length of 16 m. The red line indicates the received backscatter profile of a collimated system with the same dimensions.

Focused systems can provide effective probe volumes which are better defined than those of realizable monostatic collimated pulsed systems in the first few hundred meters of a homogeneous atmosphere. Focused systems[19] will also collect backscatter more efficiently than collimated systems and can typically use smaller telescopes.

Range gated, cw or frequency modulated systems
Classical lidar systems are range gated, i.e. they measure the duration, T, between the emission of a pulse and the return of the received scatter and deduct the range to target, r, from r = cT/2, where c is the speed of light. For dispersed targets, like the atmosphere, scatter will return continuously after the pulse has left the system. Every sample point will therefore be constructed from the superposition of the scatter generated from a volume of length $cT_{pulse}/2$. Pulsed systems can take advantage of Q-switching technologies which concentrate pump power into a short burst by a sudden increase in the cavity feedback.

In contrast to pulsed systems are the continuous wave (cw) systems which emit continuously. Such systems can only resolve range in bistatic or focused configurations. Continuous wave systems can operate with 100 % duty cycles and are typically used when there is a point in integrating the received signal for relatively long periods. Continuous wave emission is also advantageous in frequency resolved systems since they will return a coherent signal for the target's full correlation time. A constructional advantage is that a cw laser can generate the reference from a reflection of lens surfaces and do not need to be in a Master Oscillator Power Amplifier (MOPA) set up. Since reference and received backscatter will propagate through the same polarizing fiber there is no need to use polarization maintaining fibers.

Frequency modulated systems aim to sustain a high duty cycle while at the same time provide range information and avoid range ambiguities. Frequency modulated coherent lidars are treated in detail in chapter 3.

Direct detection or coherent lidars
Frequency resolving lidars, i.e. systems that measure Doppler shifts, can furthermore be classified on their detection principle as coherent or direct detection systems. Direct detection systems are also referred to as incoherent or non-coherent systems.

Coherent lidars are based on heterodyne detection[20]. They superpose the received scatter and a reference source in a photodiode to mix down the signal to a low frequency band. Coherent lidars are less sensitive to reflections from fixed clutter targets, as their zero Doppler contribution can be filtered out. They have better carrier-to-noise ratio (CNR) for weak scatter as they typically are shot noise limited by the reference source. In addition they are essentially immune to background light as only the spectral components closely surrounding the reference will be unfiltered. A detailed description of coherent lidar follows in chapter 2.

Other methods for detection of short wavelength shifts are classified as direct detection methods, e.g. edge detection[21] using a sharp well-calibrated filter response. The edge technique detects short frequency shifts by transmitting the received light through a high-resolution optical filter, like an etalon or grating. A small shift in frequency results in a large change in detected intensity as illustrated in Figure 9. A fraction of the incoming light is detected on amplitude and works as a reference assuring detection stability during changes in amplitude, as shown in Figure 10. The primary advantage of the edge detection technique is that the demand on long temporal coherence is relaxed compared to using heterodyne detection. There is in principle no need to sample a time series of the scattered wave to register the wavelength shift and the coherence constraint on the laser is thus relaxed.

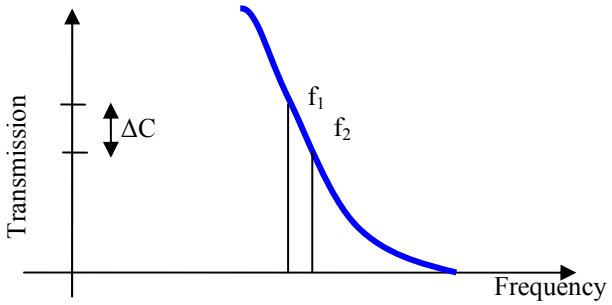

Figure 9 : Spectral response of a high resolution filter in blue. A small shift in frequency results in a large shift in intensity.

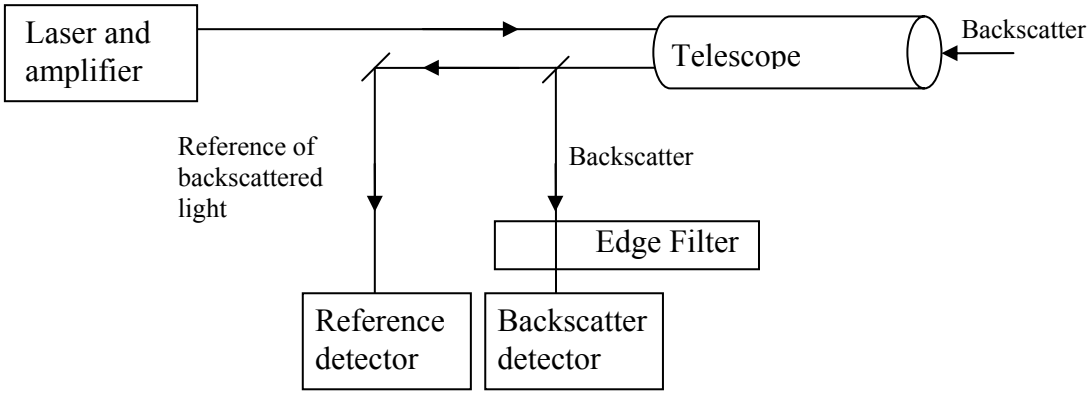

Figure 10 : Basic set up for an edge detection system.

The transmission, $T(f_c)$, of a Gaussian spectrum, h(f), centred around the frequency, f_c, passing a filter with a transmission function, t(f), can be described by

$$T(f_c) = \int_0^\infty h(f)t(f)df \ .$$

The current detected by the Backscatter detector $I_{Backscatter}$ is given by

$$I_{Backscatter}(f_c) = CR_{diode}T(f_c)F_{backscatter} \ .$$

where $F_{received}$ is the received flux, C is the ratio of light going to the backscatter detector and R_{diode} is the responsivity of the detector.

The current detected by the Reference detector $I_{reference}$ is given by

$$I_{reference} = (1-C)R_{diode}F_{backscatter} \ .$$

The transmission for the backscatter signal is then found from

$$T(w_{backscatter}) = \frac{(1-C)}{C}\frac{I_{Backscatter}}{I_{reference}} \ .$$

The transmission T(w) is unambiguously coupled to the Doppler frequency if the laser and the transmission function of the filter have been carefully characterized and assuming that the wind is low turbulent in the sensed volume. Double edge filters and several detector channels can be used for improved sensitivity.

The two principle drawbacks of edge detection are that optical filters are very sensitive to temperature changes or vibrations and the assumption that the wind is uniform in the sample volume.

The demand on uniform wind is due to that direct detection techniques are not truly frequency resolving. Filter transmission functions are calibrated with an assumed width of a Gaussian spectrum. However, the speckled return from a turbulent

atmosphere is typically built up of multiple Gaussian shapes centred on different velocity components.

Scanning configurations

An important characteristic of a lidar system is the scanning configuration. Wind sensing lidars need speed measurements in at least three directions to construct the 3D wind velocity vector. This is typically done by a conical scan with a substantial cone angle, traditionally 30 °. Retrieval can be semi-continuous or the system can sequentially stop and stare in at least three directions. Wind vector construction from conical scanning relies on a uniform wind over the scanning circumference. As the range increases the circumference grows and this assumption becomes less and less probable. Conical scanning also seems to be limited over complex terrains where winds are likely to be non-uniform laterally[22]. Alternative set ups can be three beam paths either by using mirrors or simple by using three lidars. Three beam set ups are expensive but a better option for complex terrains. Conical scanning and three beam configurations are illustrated in Figure 11.

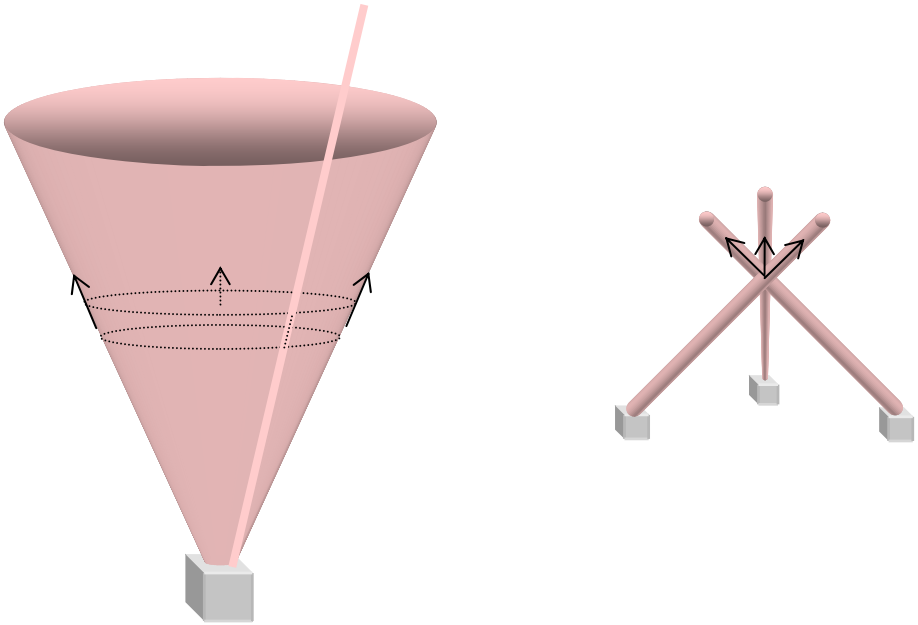

Figure 11 : Scanning configurations for 3D wind vector construction. The volume probed for a 3D wind vector construction is a ring on the side of the surface of the cone; one range gate is marked out with dotted lines.

1.3. Wind sensing lidar applications

Remote wind sensing has commercial applications mainly within the wind power, aerospace and meteorology sectors. Wind sensing lidars have, for the last 5 years been demonstrated on small scale for airports and aircrafts, primarily by CTI, now Lockheed Martin Coherent Technologies, and EADS. Five systems are currently installed in airports and a further is due to be delivered to Charles de Gaulles international airport in 2007.

In the last four years initiatives have been launched to enter the wind power market. The market leader is Qinetiq, who promote their systems via Natural Power Consultants, while the up comers Leosphere presented their Windcube system in 2006. Some 30 systems have been sold for this purpose world wide.

1.3.1. Wind power

Lidars are presently introduced to the wind power sector as a versatile method to assess wind resources prior to wind farm installation. The aim is to reduce development cost and speed up the planning process. In addition, the problems encountered with lower outputs than expected and rotor wobble for turbines constructed in complex sites with turbulent wind flow have highlighted the need for measurements not only in one point at the hub height, particularly for modern size wind turbines with a rotor diameter of up to 60 m.

The wind energy industry and lidar technology seem to be mature enough to start replacing cup anemometers mounted on tall masts. However, it is still important to continue to validate lidar systems and to better understand error sources, for example by investigating cloud influence and the accuracy of conically scanning systems in complex terrain as well as correctly describing the effective sample volumes. Energy output scales as the cube of the wind speed so accuracy is of high importance. There is also room for improvements such as faster scanning, longer range, effective methods to avoid clouds and reduced scan volume for 3D wind construction. Lidars are presently not cost effective for smaller turbines and there is a need for price reduction, the two significant providers take about € 100.000 for their systems.

Initial assessments of the lidar capability for power curve calibration[13] and to study wake and shadow effects in wind farms[23] are ongoing.

Turbine mounted lidars could eventually enhance the wind energy production as they have conceivable use in gust protection and load optimization. Advance warning of wind speed fluctuations could be an initial application which would reduce turbine fatigue damage and thus increase the time of return of investment. Active blade pitch control could be a further option which could directly increase the energy output. A first study of the cost/benefit of turbine mounted lidars has been performed[24].

1.3.2. Aerospace

There is interest in using wind sensing lidars to increase safety at landing and take-off since they can detect and monitor dangerous wind events such as wind shear, microbursts, gust fronts, turbulence and crosswinds and provide advanced warning to pilots during takeoff and landing. They can also detect wake vortexes created by aircrafts so that departing aircraft can be safely cleared for takeoff at a faster rate.

Future implementations are airborne systems for turbulence warning and avoidance. Active flap adjustment can improve safety and increase airplane lifetime, and fuel savings may be achieved by finding optimal cruise conditions.

1.3.3. Meteorology

Tropospheric and stratospheric wind maps are important keys to improve the quality of long term weather forecasts and the understanding of atmospheric and climate dynamics. Today this information is collected from radiosondes and commercial airliners which have limited geographical and temporal availability.

The applications have different needs in range, accuracy and resolution. Wind power engineers are content with ranges exceeding one hundred meters and spatial resolutions of tenths of meters. Airborne flap adjustment systems need high spatial resolution and acquisition rates but at shorter distances, while climate researchers need to sense several kilometers away. Estimations of the requirements for a few applications can be found in Table 3.

Application	**Velocity accuracy [m/s]**	**Spatial resolution [m]**	**Range [m]**
Wind Power	0,1	10-35	0-400
Airport	0,1	10-50	100-2000
Aircraft flap adjustment	< 1	10	150
Meteorology [25]	1-3	0.5-2 k	10 k

Table 3 : Estimations of the requirements of a few DWL applications.

1.4. State of the art of commercial wind sensing lidar

A few system suppliers, lead by Qinetiq and Leosphere, are moving into an early market phase for wind energy applications. The five commercially available systems are listed in this section. Characteristic parameters are gathered in Table 4.

1.4.1. The ZephIR

Qinetiq released their second generation ZephIR wind lidar in 2003 and it is presently marketed by Natural Power Consultants. It is a monostatic cw coherent lidar[11], seen in Figure 12. It can be focused with high precision to 200 m by changing the position of a fiber end. The system can, in this way, make sequential range resolved measurements at different altitudes. 3D wind vectors are constructed from conical scans and the system is eyesafe and does not require permission to be used.

Figure 12 : Second generation ZephIR wind lidar.

The ZephIR emits 1 W continuous power of 1.5 µm laser light with a linewidth of less than 2 kHz. The lidar transmitter is based on an erbium doped distributed feedback fiber laser which is amplified by a high power EDFA amplifier. LOS wind spectra are taken continuously every 10 µs. 256 of these spectra are accumulated to yield one LOS estimation in 2.6 ms. One conical scan gives 25 LOS directions and three revolutions give the 3D wind velocity. The overall acquisition time for one altitude is three seconds. The centroid of the spectrum above a determined threshold value gives the LOS wind estimate. Changing focus to a new altitude takes about one second.

Being a focused system its effective sample volume depends on range. The vertical effective length of the sample volume can be approximated as $\frac{16\lambda h^2 \cos^2(\theta)}{\pi D^2}$ where h is the sensing altitude, D the effective lens diameter and θ the lidar cone angle. The vertical sample length of the standard Zephir configuration, D = 7 cm, λ = 1.5 µm and θ = 30 °, is plotted as a function of altitude, in Figure 13.

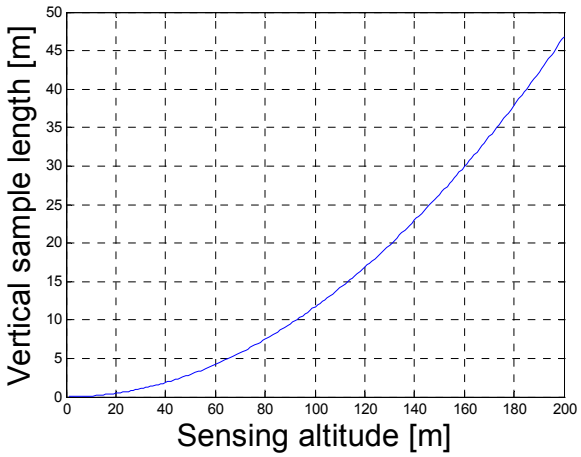

Figure 13 : Vertical effective sample length as a function of sensing altitude for the ZephIR.

Wind speed is stated to be unambiguously retrieved from 2 to 38.4 m/s with stated accuracy of ±0.1 m/s.

A cloud correction method has been explored[26] since cw systems are sensitive to clouds. In the cloud correction configuration the system will periodically sense with a focus at 300 m. The generated spectrum will be dominated by scatter from low clouds since the confinement is low at this focus distance. This cloud spectrum is typically generated once for every set of sensed altitudes, i.e. for five altitudes the cloud correction spectrum is generated every 22 s, which might be an insufficient temporal resolution for corrections. The intended cloud spectrum is then deducted from the spectra retrieved from the sensed altitudes.

1.4.2. The Windcube

France based Leosphere sell the Windcube[12], Figure 14. It is a range gated monostatic coherent lidar which focuses at a fixed distance during operation to increase the CNR. This system is also based on erbium-ytterbium laser technology.

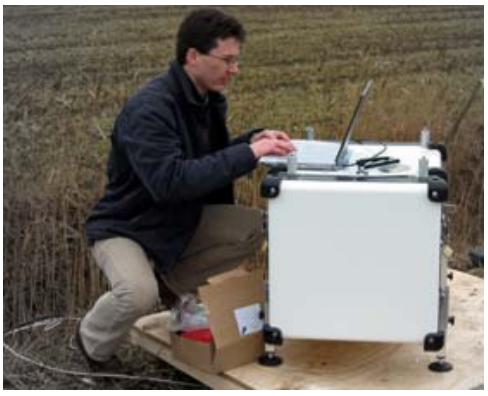

Figure 14 : Windcube during set up.

The Windcube emits 200 ns pulses of 10 µJ energy at 1.54 µm. The PRF is 10 kHz, an acquisition number of 10 000 pulse returns for a LOS speed gives an accumulation duration of 1 s. The range is stated as 45-250 m and the effective probe volume as 30 m. The system senses in four directions, typically in a 30 ° tilt configuration, to

construct the wind velocity. LOS wind velocities of ± 20 m/s can be determined giving unambiguous retrieval of horizontal winds of ± 40 m/s.

The LO is generated from a MOPA setup and is offset by an Acousto-Optic Modulator (AOM). The sign of the wind direction can be retrieved and the influence of Relative Intensity Noise (RIN) is diminished.

Both the Zephir and the Windcube have been verified at the Høvsøre wind energy research site in cooperation with Risø. They have shown excellent linearity with k-values better than 0.95 and standard deviations less than 0.2 m/s[11, 12].

However, the ZephIR is sensitive to clouds and the cloud correction method has been questioned. Consistent verifications of the merits and limitations of the cloud correction method have yet not been published. Furthermore, Qinetiq's system loses confinement with the square of the sensing range. This can, to some degree, be compensated for by using larger optic dimensions. Conical scanning is a limited solution for 3D wind vector construction over complex terrains and for long ranges. The 25 sample directions sensed by the ZephIR make it possible to make fits of the wind velocity and give warnings for algorithm failure due to inhomogeneous winds over the scan circumference. Another issue with the ZephIR lidar is that it has a 180 degree ambiguity in wind direction, i.e. it cannot see the difference of up and down wind. This is due to the fact that the lidar generates the local oscillator from a lens reflection, which therefore cannot be offset. For the same reasons, the Zephir has difficulties in sensing low velocities which appear close to 0 Hz in the wind spectrum. This is due to RIN which typically falls as 1/f.

The Windcube, on the other hand, is not sensitive to clouds and has an offset local oscillator (LO). However, it has issues with range gate distortion due to the combination of range gating and focusing. The acquisition rate is quite slow which implies few directions sensed for the velocity construction. The system with the current acquisition rate is not suitable for imaging of wind velocities, e.g. over a rotor area.

1.4.3. The WindTracer

Lockheed Martin Coherent Technologies are mainly focusing on aerospace applications. They have sold the WindTracer, a collimated range gated monostatic system, since 2001 and they currently have systems in five airports. The highly integrated system in Figure 15 is sold for approximately $1 000 000. The WindTracer operates at 2 µm and is based on a Q-switched Tm:LuAG laser. Lockheed Martin are introducing a second generation of range gated Doppler systems at 1.6 µm[27].

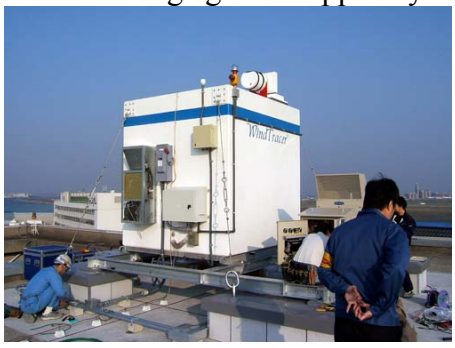

Figure 15 : The Windtracer in Hong Kong Haneda airport.

The WindTracer emits 2 mJ pulses of 400 ns duration at a Pulse Repetition Frequency (PRF) of 500 Hz. It has a telescope lens with 10 cm diameter and performs plane imaging of the LOS component, which can be used to construct the horizontal wind velocity. The WindTracer unambiguously detects ± 20 m/s LOS wind with a stated range of 5 km. When compared to a sonic anemometer at 100 m altitude, the lidar gave a typical accuracy of ± 0.5-1 m/s in the LOS direction[28].

1.4.4. Mitsubishi Electric's wind lidar

Mitsubishi has also developed a wind lidar constructed of fiber communication components operating at 1.5 µm. It is a range gated system with a controllable focus which can be set from 150 m to collimated operation[29]. The transmitter is flexible both in pulse duration and PRF. A typical setting is to emit 600 ns pulses of 6.5 µJ at 1 kHz. It accumulates 1000 spectra for a LOS estimation but the refresh time is 3 s due to data transfer. With an effective aperture diameter of 50 mm it is stated to measure LOS wind of ± 38 m/s up to 1.5 km. This system has yet not been compared to other wind sensors.

1.4.5. Halo Photonics' wind lidar

Halo Photonics was founded in 2007 by Guy Pearson as a spin-off company from Qinetiq's lidar group. They market a range gated monostatic system based at 1.5 µm similar to a previously developed system[30]. The system has an optic diameter of 8 cm and operates at a PRF of 20 KHz with range gates of 20-60 m. Halo states a maximum range of up to 7 km and a LOS speed resolution of a few cm/s with a temporal resolution of 0.1-30 s. The system has so far only been validated with radiosondes.

1.4.6. Other systems

A few other companies, e.g. Hovemere and Swan International offer custom made systems.

Wind sensing lidar development is also pursued at a few universities, notably at the University of Southampton and Ecole Polytechnique. A transmitter providing 50 µJ pulses at 30 kHz, based on an external cavity semiconductor laser amplified by a 20 µm core Erbium Doped Fiber Amplifier (EDFA), has been suggested[31]. A PRF of 50 kHz gives a range ambiguity of 3 km which is approaching the limit for collimated systems. A 290 µJ 4 kHz[32] output from an external cavity semiconductor laser amplified by a 50 µm core EDFA has also been suggested for coherent lidar applications.

System	Range [m]	Accuracy	Acquisition rate	Sample volume, RBP_{FWHM} [m]	Pulse length [µs]	Pulse energy [µJ]	PRF [kHz]	Other
Zephir	5-150	± 0.1 m/s	1 s	$1.2 \cdot 10^{-3} h^2$ (tilt = 30 °)	10	10	100	cw, sensitive to clouds
Windcube	45-250	± 0.1 m/s	4 s + scan duration → 8 altitudes	26 (tilt = 30 °)	0.2	10	10	Only measures in 4 directions
WindTracer	5000	Standard dev about 1 m/s	N.A.	60	0.4	2000	0.5	LOS mapping
Mitsubishi Wind Lidar	1500	N.A.	1 s	90	0.6	6.5	1	

Table 4 : Stated parameters of commercial systems. The RBP_{FWHM} is defined in chapter 2.5.

1.5. Conclusions on wind sensing with coherent lidars

The knowledge of wind flow is important within several fields. For many of them the only viable solution is to sense the wind remotely. Sodars and radars are available remote sensing techniques but lidars are likely to provide the most accurate and reliable sensing. Coherent lidars are fully frequency resolving and are therefore less sensitive to broadband noise and can measure turbulent wind in comparison to incoherent systems. Fiber based lidars are cost effective and robust, and can operate without safety restrictions; they are thus an ideal choice for non-scientific applications.

A few commercial systems are available and have been verified to provide sensing with high availability over flat terrain and in typical atmospheres. Typical standard deviations in the 10 minute average horizontal wind lie in the order of 0.1-0.2 m/s. However, the systems ability to sense accurately over complex terrain, at high temporal resolution and for atmospheres including low clouds remains to be investigated.

2. Coherent lidar

This section gives a detailed description of coherent lidars. Coherent lidars are suitable for high accuracy velocity sensing of dispersed targets since they provide fully spectral resolved sensing and theoretically have quantum limited noise. This technology was initially restricted to using gas lasers, essentially CO_2 lasers[33], but highly coherent and powerful sources and low noise balanced receivers are now available in fiber technology. Due to their high sensitivity coherent lidars can also be used for DIAL applications[34].

Coherent lidars are less sensitive to reflections from fixed clutter targets, as their zero Doppler contribution can be filtered out. They have better CNR when scattering is weak as they generally are shot noise limited by the LO[14]. In addition they are essentially immune to background light as only the spectral component closely surrounding the LO will be unfiltered.

This chapter starts with an introduction to heterodyne detection which is the fundamental technology of coherent lidars. The generation of a heterodyne current, which is the wind signal carrier, is described. This presentation considers the wind as a frequency generator which is an approach that has not been reported previously. It allows descriptions of effects such as inhomogeneous correlation duration within a range gate. In heterodyne detection a laser beam with a frequency f_{trans} generates scatter from a moving target Doppler shifted by $f_{Doppler}$. The received backscatter is mixed with a reference laser of frequency f_{LO}, possibly offset from the transmitted frequency by a known f_{offset}. This produces an intermediate frequency $f_i = f_{received} - f_{LO} = (f_{trans} + f_{Doppler}) - (f_{trans} + f_{offset}) = f_{Doppler} - f_{offset}$, from which the Doppler shift and thereby the target's LOS velocity can be measured.

This chapter also describes the full chain of coherent lidar processing and gives the lidar equation which can be used to predict the performance of a lidar design. Figure of merits for coherent lidars are presented for easy comparisons of different systems and methods.

An alternative model for focused systems is presented which takes into account a small receptor aperture and co-propagation of LO and received scatter in a single mode fiber.

Finally, methods to calculate effective sample volumes, both for focused cw systems and range gated systems, is presented. Effective sample volumes of range gated and cw systems have previously not been compared on the same merits when only the gathered energy has been considered.

2.1. Heterodyne detection

The Doppler shift of the backscatter induced by typical winds gives a very small shift to the carrier wavelength. Wind velocities of 0 - 30 meters induce a Doppler shift of 0 - 40 MHz on a 200 THz carrier frequency when sensed with a 1.5 µm lidar. The wavelength change is thus 0 - 0.3 pm which should be detected with an accuracy of 1 fm. The measurement corresponds to determining how far aerosols travel while the sensing photons travel one wavelength, i.e. 1.5 µm.

It is very difficult, although not impossible, to directly measure a wavelength difference with a precision of 1 fm, i.e. 0.1 m/s wind, with well calibrated and stabilized etalons. However, a typical Optical Spectrum Analyzer (OSA) based on a prism and a detector array has a wavelength resolution limited to roughly 10 pm, which corresponds to a wind resolution of 1000 m/s. Furthermore, the received power is very weak, typically a few pW.

Heterodyne detection[20] is an appropriate technique to measure such wavelength shifts. The method is illustrated in Figure 16 and described in the following section. A detectable beat frequency, corresponding to the frequency difference of the sensed light and a reference with a slightly different wavelength, is generated by mixing the two fields in a square law detector, e.g. a pin diode.

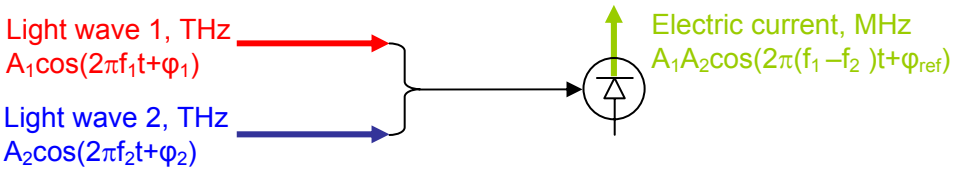

Figure 16 : Heterodyne detection transfers two light waves of THz frequency to an electric current carrying the difference frequency of the two waves, typically less than 100 MHz, when they are combined on a photodiode.

2.1.1. Optical beam mixing in a square law detector

Electromagnetic radiation can be described by the time harmonic

$$E_{field}(t) = A\cos(2\pi ft + \varphi)$$

where A is the amplitude, f the frequency and φ the phase of the electric field E_{field}.

The superposition of this wave with a reference wave gives an electric field E_{mix}.

$$E_{mix}(t) = A\cos(2\pi ft + \varphi) + A_{ref}\cos(2\pi f_{ref}t + \varphi_{ref})$$

where A_{ref} is the amplitude, f_{ref} the frequency and φ_{ref} the phase of the reference field.

The current generated by a square law detector, e.g. a photodiode, is proportional to the irradiance, I, which for the mixed fields is given as

$$I(t) = \frac{E_{mix}{}^2(t)}{c\varepsilon_0} = \frac{\left(A\cos(2\pi ft + \varphi) + A_{ref}\cos\left(2\pi f_{ref}t + \varphi_{ref}\right)\right)^2}{c\varepsilon_0} =$$
$$\frac{A^2\cos^2(2\pi ft + \varphi) + A_{ref}^2\cos^2\left(2\pi f_{ref}t + \varphi_{ref}\right) + 2AA_{ref}\cos(2\pi ft + \varphi)\cos\left(2\pi f_{ref}t + \varphi_{ref}\right)}{c\varepsilon_0}$$

where c is the speed of light and ε_0 is the permittivity in vacuum.

The last frequency component can be expanded to give

$$\cos(2\pi ft + \varphi)\cos\left(2\pi f_{ref}t + \varphi_{ref}\right) = \frac{\cos\left(2\pi\left(f + f_{ref}\right)t + \varphi_{sum}\right) + \cos\left(2\pi\left(f - f_{ref}\right)t + \varphi_{diff}\right)}{2}$$

i.e. it contains the sum and the difference of the two waves frequencies. φ_{sum} and φ_{diff} are the resulting phases.

Photodetectors are not able to respond fast enough to resolve the squared or summed cosine terms, which are in the order of 400 THz in our case, but will filter them to a DC term. The signal current, i(t) can thus be represented as

$$i(t) = C_{rec}\frac{AA_{ref}\cos\left(2\pi\left(f - f_{ref}\right)t + \varphi_{diff}\right)}{c\varepsilon_0} + D_{DC}$$

where C_{rec} is a receiver constant and $D_{DC} = C_{rec}\frac{A^2 + A_{ref}^2}{2c\varepsilon_0}$ is the filtered DC term.

2.1.2. Heterodyne detection in coherent lidar

In the case of heterodyne detection in a coherent lidar the two mixed fields are the received backscatter and a local oscillator. To obtain efficient interference the mixed fields need polarization alignment and spatial overlap. Co-propagating the backscatter and LO in a single mode fiber gives a good spatial overlap on the detector. The polarization by the atmosphere is low since most aerosols are sufficiently spherical to give a negligible polarization, with exceptions e.g. sand dust, but polarization effects in non-polarization maintaining systems are strong. Heterodyne loss due to polarization misalignment are avoided if the LO is generated from a lens reflection so that the LO and backscatter have a common path within the lidar.

The scatter is generated from a long narrow volume of turbulent wind so the received backscatter is the superposition of many reflections with a distribution of frequencies f_i amplitudes A_i and phase φ_i. For a pulsed system this volume is moving with time but for now a fixed contributing volume is considered for simplicity. The implications of a moving volume are considered in chapter 2.5.3. The received field E_{rec} is described by

$$E_{rec}(t) = \sum_V A_i\cos\left(2\pi f_i t + \varphi_i\right)$$

where A_i is the amplitude, f_i the Doppler frequency and φ_i the phase of the field scattered from particle i as it arrives on the detector. The sum is taken over all particles in the volume V.

The irradiance hitting the detector is described as

$$i(t) = \frac{\sum_V A_i^2 \cos^2(2\pi f_i t + \varphi_i) + A_{LO}^2 \cos^2(2\pi f_{LO} t + \varphi_{LO}) + \sum_V 2A_i A_{LO} \cos(2\pi f_i t + \varphi_i)\cos(2\pi f_{LO} t + \varphi_{LO}) + \sum_V 2A_i A_j \cos(2\pi f_i t + \varphi_i)\cos(2\pi f_j t + \varphi_j)}{c\varepsilon_0}$$

and the intrinsically low pass filtered detector current as

$$i(t) = C_{rec} \frac{\sum_V A_i A_{LO} \cos(2\pi(f_i - f_{LO})\cdot t + \varphi_{diff,i}) + \sum_V A_i A_j \cos(2\pi(f_i - f_j)\cdot t + \varphi_{diff,i,j})}{c\varepsilon_0} + D_{DC}\,.$$

The A_i terms are much smaller than the A_{LO} and the sum $\sum_V A_i A_j \cos(2\pi(f_i - f_j)t + \varphi_{diff,i,j})$ can be ignored and the DC term approximated to $D_{DC} = C_{rec} \frac{A_{LO}^2}{2c\varepsilon_0}$.

The local oscillator is typically a diverted fraction of the emitted light and offset in frequency by an AOM. The relation between the scattered light and the local oscillator is thus $f_i = f_{LO} - f_{offset} + f_{Doppler,i}$ where f_{offset} is the offset frequency imposed on the LO and $f_{Doppler,i}$ the Doppler shift induced by particle i.

The heterodyne current can be expressed as

$$i(t) = C_{rec} \frac{\sum_V A_i A_{LO} \cos(2\pi(f_{Doppler,i} - f_{offset})t + \varphi_{diff,i})}{c\varepsilon_0} + D_{DC}$$

The signal current is generally expressed as a function of the optic power of the LO and the received optic power.

$$i(t) = 2R_{diode} \sum_V \sqrt{\eta F_i P_i P_{LO}} \cos(2\pi(f_{Doppler,i} - f_{offset})t + \varphi_{diff,i}) + D_{DC}$$

where R_{diode} is the responsivity of the detector, η is a receiver loss and gain factor, F_i is the collection efficiency of the scatter from particle i as described in chapter 2.4, P_i is the scattered power and $D_{DC} = R_{diode} P_{LO}$.

The wind signal can be deduced since the LO offset is known. The squared absolute of the coefficients obtained from the Discrete Fourier Transform (DFT) of the sampled signal current gives a power spectrum which represents a speckle take of the weighted wind velocity distribution in the sensed volume.

The received power is typically only a few pW. One of the main advantages of coherent lidars is that it is possible to amplify the signal current by increasing the LO power, which is abundant. A lidar system will thus only be influenced by shot noise and noise in the LO, e.g. RIN, while noise sources independent of P_{LO} generally can

be ignored, e.g. detector dark current. Signal amplification is also limited by saturation of the detector. GHz photodiodes are typically saturated at 1 mA corresponding to about 1 mW LO power, which typically is sufficient for LO noise domination in fiber communication receivers.

Noise in the LO, notably RIN, will lead to pink noise, 1/f, in D_{DC}, which can be significant in the signal frequency region, especially in system without a frequency offset between LO and backscatter. This noise will also appear around the offset frequency but only proportional to the square root of the LO power in the power spectrum. It is thus important to use lasers and amplifiers with a very low RIN in the order of -160 dB/Hz[29], e.g. cw fiber laser amplified by EDFAs.

2.1.3. Temporal speckle and spectral broadening of the coherent signal

The signal strength is stochastic since it is a sum of several frequency components with phases from a uniform distribution. The signal will consequently be speckled which necessitates sample accumulation and contain a spectral width which reduces the ideal narrowband CNR.

If the aerosols are randomly distributed and uniformly scattering, i.e. $A_i = A$ for all i, the received amplitude, and thus the signal current, of each frequency component will be speckled and follow a Rayleigh distribution with a mean of $AA_{LO}\sqrt{N\pi/4}$ where N is the number of scatterers. Figure 17 gives the result of a computer simulation of superpositioning 20 waves with random phase and previously reported experimentally obtained results. Nevertheless, the influence of dominant single particles can be significant as shown in appendix B and elsewhere[2].

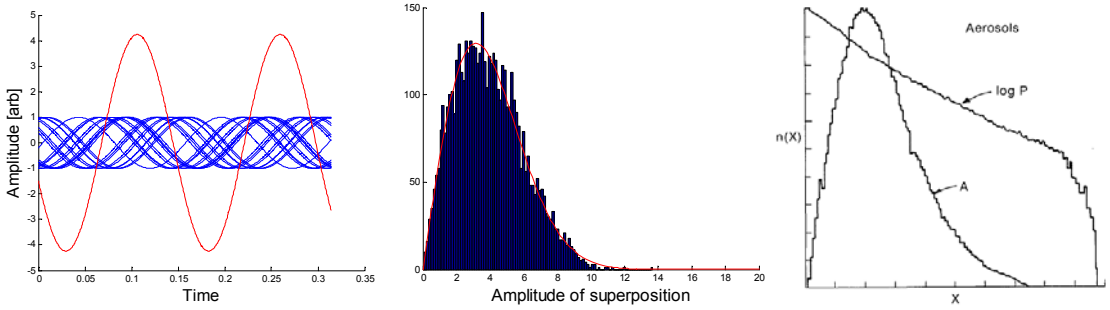

Figure 17 : The superposition (red) of the reflected waves (blue) from 20 uniform particles at random positions and a histogram of the amplitude of the superposition of 5000 uncorrelated speckle takes. The corresponding Rayleigh distribution is outlined in red. A histogram over the current amplitude of experimental data from a CO_2 lidar follows the expected Rayleigh distribution[35].

An uncorrelated speckle take is generated for each wind sample, since the aerosols typically will redistribute relatively to each other between consecutive samples.

In practice the scatter is described by a backscatter coefficient, $\beta(z)$, which is the temporal average of the fraction of the power returned from a meter of scatter per steradian. The averaged received power of a frequency component can then be expressed as

$$\sqrt{P_{rec}(f)} = \int_{\text{sample volume}} \sqrt{PF(z)e^{-2\alpha z}\beta(z,f)}dz$$

where P is the emitted peak power of a rectangular pulse, F(z) is the collection efficiency function described in chapter 2.4, and α describes propagation losses.

The average heterodyne signal current power then becomes

$$\langle i^2(f)\rangle = 2R_{diode}^2 P_{LO} P\eta \int_{\text{sample volume}} F(z)e^{-2\alpha z}\beta(z,f)dz + RIN(f).$$

where RIN(f) is the RIN in the DC term.

The signal spectrum has so far been considered to be built up from discrete frequency components. However, the detected frequency components will be broadened by several factors in a real lidar system. The received energy will thus spread over a wider frequency band, decreasing the narrowband CNR.

The width of the detected wind spectrum depends on:

- the turbulent wind distribution in the sensed volume, which in turn depends on the size of the sensing volume. The full length of the sensed volume is typically 50 m and most lidar systems generally measure upwards with a 30 ° inclination. Wind shear over flat terrains can easily reach 2-3 m/s over 50 m which gives a spectral width of the LOS Doppler spectrum of 2-3.5 MHz.

- the laser coherence[36]. A laser has a certain spectral width due to phenomena, e.g. thermal motion in the lasing media and, typically more significant, cavity vibrations. The detected Doppler spectrum is the convolution of the true wind spectrum with the linewidths of the LO and the emitted light. To achieve wind velocity accuracy of 0.1 m/s with a 1.5 μm system it is necessary to spectrally resolve 130 kHz. However, this does not mean that the laser has to have a linewidth lower then 130 kHz since we are picking the peak, or alternatively the centroid, of the Doppler spectrum. It is non-trivial to achieve 100 kHz linewidths from solid state lasers. Nevertheless, distributed feedback in fiber lasers, externally stabilized laser diodes and YAG lasers can reach sub 100 kHz linewidths with propagation path differences of several km. The laser coherence is thus not a limiting factor in well designed lidar systems. Laser coherence is treated further in appendix A.

- the correlation duration of the scattered signal. The DFT, which generates the power spectrum, broadens the frequency components proportionally to the duration of correlated scatter. The heterodyne spectra will never be narrower than one over the correlated duration. The atmospheric correlation time depends on turbulence, sensed volume and the sensing wavelength. The returned scatter correlation can never be longer than the shortest of the pulse or sample duration. The atmospheric correlation duration has been estimated to be in the order of 1 μs, giving a spectral width of 1 MHz. An experimental estimation of the atmospheric correlation duration has been performed in this project and is treated further in appendix B.

2.2. Fiber based coherent lidar layout

This chapter presents the fiber based coherent lidar system in a boxplot model. The sub-elements of a lidar are described, the development of the lidar signal is traced and relevant noise sources are clarified.

A lidar can be described as consisting of four major units; a transmitter, telescope, heterodyne receiver and signal processing unit as illustrated in Figure 18. Each unit is controlled by input parameters, for example, the electric signal applied to the amplitude modulator which controls the pulse length and thereby the length of the sample volume. Lidar systems typically give a 10 minute average of the 3D wind velocity, but also provide measures of turbulence and backscatter coefficients.

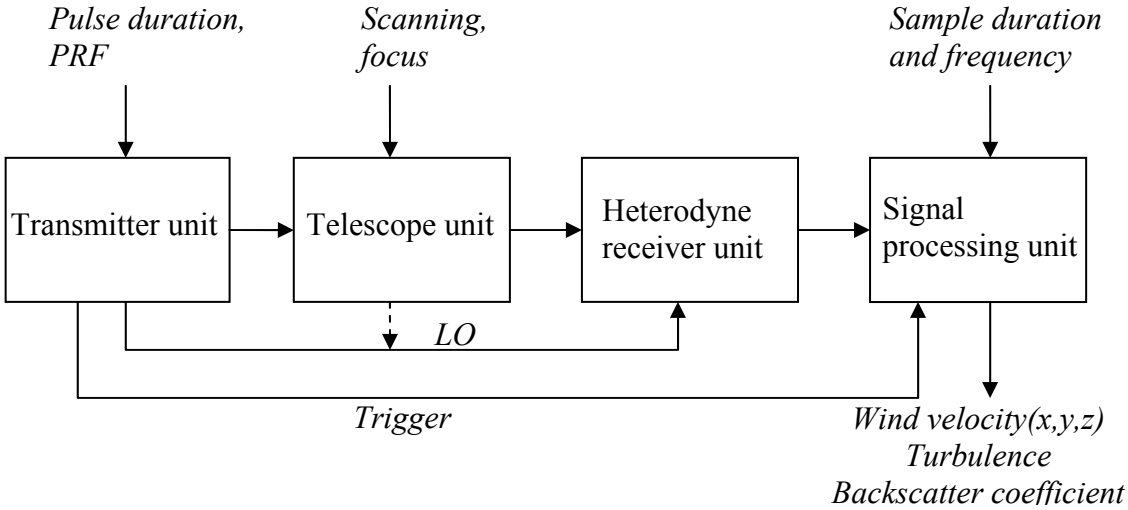

Figure 18 : The four major units of a lidar system, their control parameters and the lidar output.

2.2.1. Transmitter unit

The transmitter unit generates the sensing light and generally the reference LO. A fiber based transmitter contains a seed laser and an amplifier. The transmitter unit may also contain an amplitude modulator, a beam splitter and a frequency modulator as illustrated in Figure 19.

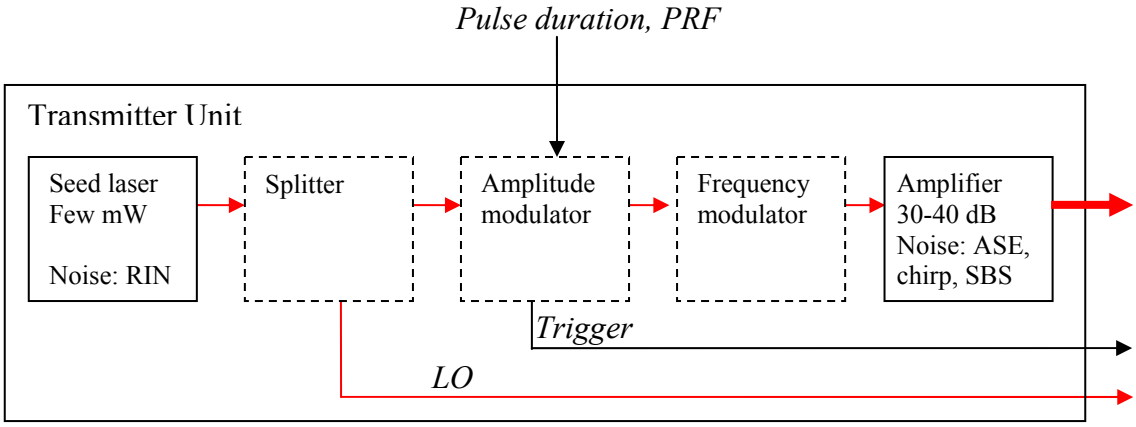

Figure 19 : Layout of the lidar transmitter. Optional components are dashed. Optic signal in red.

The seed laser generates highly coherent continuous laser light. As a lidar will operate with high power in free air it is important to choose the emitted wavelength not only in order to get a high aerosol backscatter and effective collection of light but also such

that the lidar is eye safe for strong intensities according to the American national standard for the safe use of lasers. The eye is extremely sensitive to high power laser light in the 400-1400 nm wavelength region while light in the 1.5-1.8 μm will be absorbed by the tissue in the eyeball and not reach the retina. Nevertheless, exposure of strong intensities at 1.5 μm might still lead to scaring of the cornea.

Furthermore, it is an advantage to use a wavelength which is compatible with the high volume fiber optic communication market. The wavelengths used for single mode long haul fiber communication are bands around 1310 and 1550 nm due to optic fiber transmission properties. The availability of high gain low noise optic amplifiers and the robustness of fiber connected components are especially important.

Highly coherent fiber lasers can be constructed in the 1020-1180, 1525-1585 and 1710-2000 nm wavelength bands. They have excellent stability. The very narrow and long interaction volume between the pump and the stimulated wavelength ensures a low threshold and a high gain which is the basis for the low noise behaviour of fiber lasers. The fiber laser RIN noise is fundamentally limited by Schawlow-Townes phase noise but in reality acoustic noise, pump noise and fast thermal effects set the limit. RIN as low as -160 dB/Hz can be realized[29].

Erbium doped distributed feedback fiber lasers operating at 1.5 μm thus constitute an attractive seed laser. Externally stabilized InGaAs-based laser diodes are another option. For accurate and sensitive wind sensing they should have a linewidth of some 100 kHz and low RIN. Typical fiber lasers emit a few milliwatts.

A fraction of the seed light is typically redirected in a 4-port fiber coupler to form a cw LO. The LO can optionally be generated from a reflection in the telescope module for continuously emitting lidars. Systems with separate LO paths have to be polarization maintaining to avoid losses due to misalignment of the polarization of the received scatter and the LO. LO power is typically in the order of 1 mW.

For pulsed systems the main beam is amplitude modulated. This is typically done by using an AOM. AOMs are relatively slow components with rise/fall times of about 100 ns. If faster pulse forming is needed Mach-Zendher modulators can be used. However, the extinction ratio of these modulators is typically lower than for the AOM.

Another advantage of the AOM is that, simultaneously as it forms the pulse, it also offsets the frequency of the emitted light relative to the LO. The AOM leakage, typically -55 dB, is normally not an issue for pulsed systems with a separate offset LO.

The light is then amplified in a fiber amplifier. It has been proven that a 1 W output and a 3.5 cm aperture would be sufficient for wind sensing up to 150 m during most atmospheric conditions[11]. The amplifier gain should be close to 30 dB for typical seed lasers. Pulsed systems have the advantage of a higher gain factor since the stimulating light is present for a limited duration while it propagates through the doped fiber. The life time of excited states in a doped fiber is very long and the pump energy is essentially stored during the time when there is no stimulating light passing through the fiber. This pump light is released when the stimulating pulse propagates

through the fiber. This Q-switch effect gives rise to the higher gain factor. It has been speculated that the pulse energy might fall with the square root of the PRF[37]. However, a side effect is that the laser will emit a higher Amplified Spontaneous Emission (ASE) during the non stimulated durations. Nevertheless, since coherent lidars are frequency resolving the ASE is typically not a limiting factor. A more severe drawback of amplification of short pulses is the frequency chirp due to Self-Phase Modulation (SPM). High peak powers will in addition generate significant Stimulated Brillouin Scattering (SBS). It has been indicated that a peak power of 10-15 W propagating through even short lengths of single mode fiber would provoke SBS which would limit the lidar performance[29]. A sufficient amplifier gain would then be in the order of 40 dB.

2.2.2. Telescope unit

Apart from the telescope this unit also includes a circulator which redirects the received light towards the receiver unit. If the system has a variable focus setting it is typically done by micropositioning of the fiber end aligned to the telescope. If it is scanning it also contains equipment to control this, e.g. a rotating wedge. The telescope unit is illustrated in Figure 20.

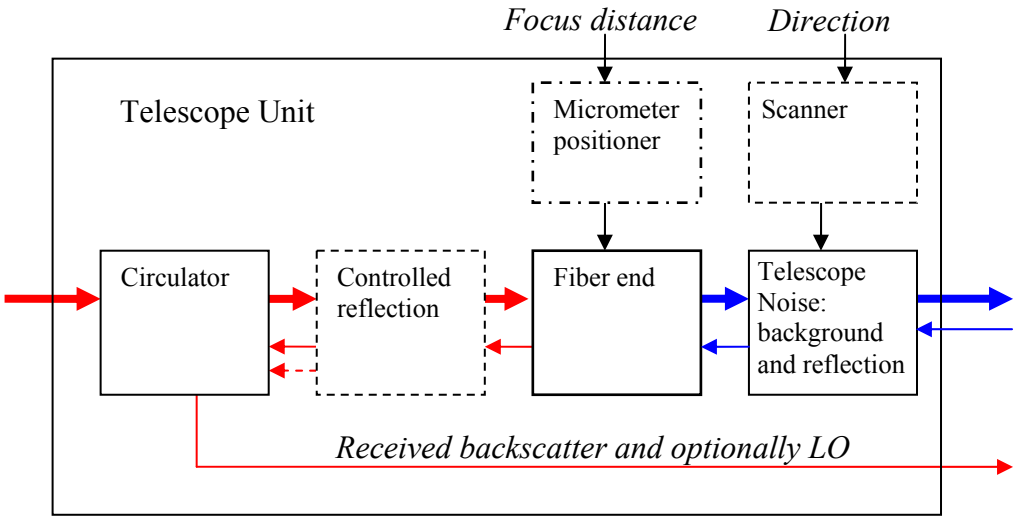

Figure 20 : Telescope unit. Optic signals carried in fiber in red, free optics in blue and optional LO dashed.

For cw systems it is possible to form the LO from a controlled reflection off a surface after the circulator, with the advantage that the emitted light and the LO will pass through the same polarizing path. However, such a LO cannot be offset. Reflected power generated after the circulator in cw systems with a separate LO path will beat with RIN generating noise at the offset frequency, proportional to $\sqrt{P_{LO}P_{reflection}}$, making it difficult to measure low LOS wind speeds. The same applies to pulsed systems with insufficient extinction ratios in the amplitude modulator.

Backscatter of approximately 1 pW average power, received by a well constructed system with low noise, is typically sufficient for wind velocity determination on 100-1000 accumulated speckle takes. The received power depends on the pulse energy and the aperture area. There is thus an economic trade off between amplifier gain and lens radius. Commercial systems currently have diameters of a few cm. A cross section of the telescope unit in the early Zephir model can be seen in Figure 21.

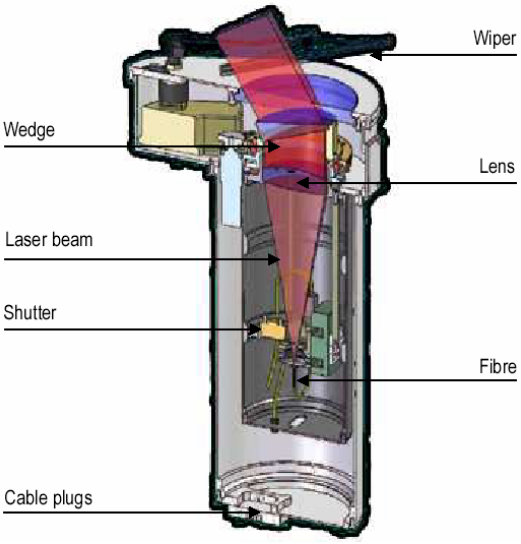

Figure 21 : Cross section of the telescope used in the early model of the Zephir lidar.

2.2.3. Heterodyne receiver unit

The received backscatter and the LO are merged in a fiber coupler and mixed on a square law detector. The generated current is in best practice sent through a bandpass filter to reduce noise from the DC term and noise down sampled from higher frequencies. The filtered current is typically amplified by a Low Noise Amplifier (LNA) in order to make the dynamic range suitable for digitizing. The heterodyne receiver is illustrated in Figure 22.

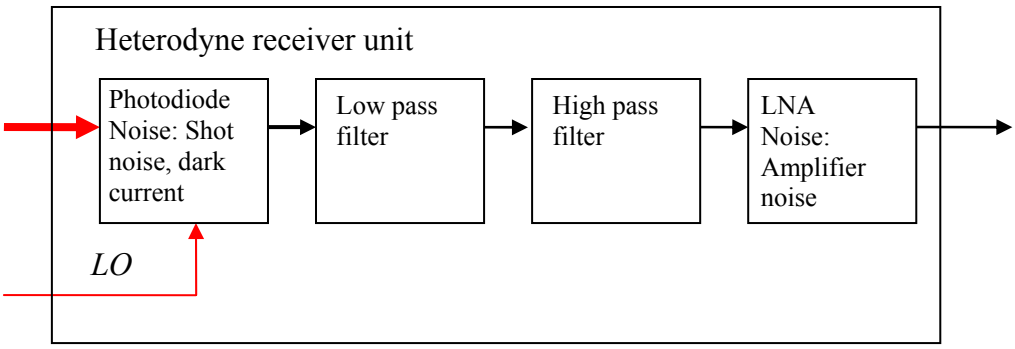

Figure 22 : Box plot illustration of the heterodyne receiver unit.

The square law detector is typically an InGaAs based pin photodiode. The diode should be suited for the signal bandwidth which typically is less than 100 MHz. It is also important that the responsivity is high and that the dark current is low. Fiber communication receivers are available off-the-shelf with quantum efficiencies of more than 80 %, dark currents of few nanoamperes and 3 dB bandwidths well above specifications.

2.2.4. Signal processing unit

The heterodyne current is sampled by a digitizer triggered by the transmitter unit. The sample vector is then fed to a DFT which finds the amplitudes of the sinusoidals in the heterodyne current. A power spectrum is generated by taking the square of the absolute of the Fourier coefficients. A number of power spectra are accumulated into a smoothened wind distribution spectrum from which the LOS wind speed can be

estimated. The LOS wind speeds sensed in at least three directions are finally used to construct the 3D wind velocity. The general layout of this procedure is demonstrated in the illustration of the signal processing unit in Figure 23.

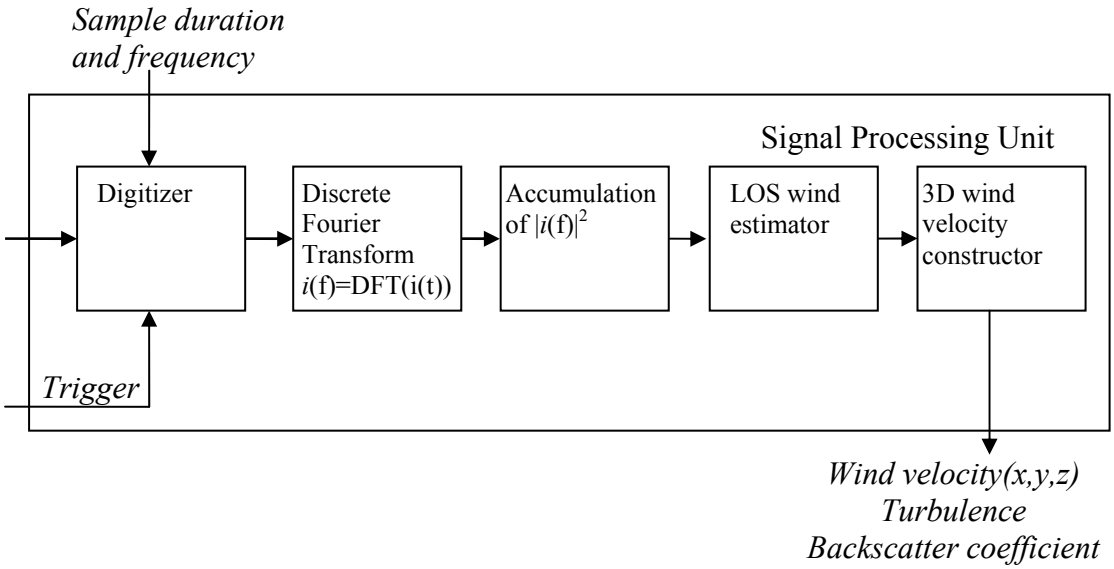

Figure 23 : Signal processing unit.

Digitizing should be done at least at the Nyquist frequency to avoid aliasing, i.e. using a sample frequency, f_s, higher than 2 times the highest frequency in the signal. The sample frequency should therefore be higher than $2f_{offset} + 4v_{max}/\lambda$, where v_{max} is the fastest LOS speed expected. The fastest LOS wind velocities will normally be smaller than 20 m/s for typical applications sensing from the ground with typical scan inclinations. The highest Doppler frequency would then be about 25 MHz for a 1.5 μm system and the frequency offset would have to be about 50 MHz to avoid RIN and ambiguity of up and down wind. A sample frequency of 150 MHz would thus be sufficient to avoid aliasing of wind velocities.

The sample vector digitized during T_{sample} has a length $M = T_{sample} \cdot f_s$, where T_{sample} is the sample duration for one wind speed sample and not the duration between two digitized samples of the heterodyne current. The frequency bin size of the DFT, $f_s/M = 1/T_{sample}$, will be limited if the sampling vector is short.

The length of the sample volume does not depend on the sample duration for cw lidars. However, the signal is typically only coherent for less than 2 μs and longer sampling will not increase the narrowband CNR but could give rise to dominant signals from larger particles in atmospheres with inhomogeneous scatter durations.

The sample duration typically sets the length of the sample volume for pulsed systems. A possibility to increase the frequency resolution without increasing the length of the sample volume is to use zero padding, i.e. expanding the sample vector with zeros. This solution demands an increase in the number of operations for the DFT processor.

The DFT transforms a sampled time series to a spectrum of the included frequency components. The LOS wind speed distribution is given as the λ/2-scaled Doppler

frequency power spectrum i.e. as $\left|DFT(i(t))\right|^2$. Due to speckle and low CNR, some hundred to several thousand speckle takes are accumulated to give a smoothened wind distribution spectrum. The accumulation time for a smoothened wind spectrum depends on the sample duration, the speckle take frequency and the number of accumulations. Continuous wave lidars typically acquire wind spectra continuously and a smoothened LOS wind direction spectrum is generated every T_sN_{accum} e.g. 1 ms for 2 μs sample durations and 500 accumulated spectra. For a pulsed system an altitude is sensed every 1/PRF. The accumulation duration is thus N_{accum}/PRF e.g. 100 ms for 1000 accumulations at 10 kHz. The assumption that the wind is stable over the scan perimeter becomes less accurate as the accumulation duration in one direction increases.

A dominant LOS wind speed is determined for each direction. These values are used for the 3D wind velocity construction. The LOS wind speed can be determined by a simple peak find on the wind distribution spectrum or by finding the centroid of the energy. More elaborated LOS wind maximum likelihood estimators have been established[38, 39, 40].

The LOS wind speed can be expressed as $v = u_{hew}\sin\theta\cos\varphi + u_{hns}\cos\theta\cos\varphi + u_v\sin\varphi$ where u_{hew} and u_{hns} are the horizontal wind components in east-west and north-south directions respectively, u_v is the vertical wind speed, θ is the azimuth angle counted from the north direction and φ is the elevation angle. The 3D wind velocity vector, (u_{hew}, u_{hns}, u_v), can be constructed from at least three LOS wind speed values if the flow is uniform over the scan perimeter. In the easiest form the wind is sensed in the north, θ = 0 °, south, θ = -180 °, and in a third direction, giving the radial components v_n, v_s, and v(θ) respectively. The 3D wind components can be found from

$$u_{hns} = \frac{v_n - v_s}{2\cos\varphi}$$

$$u_v = \frac{v_n + v_s}{2\sin\varphi}$$

$$u_{hew} = \frac{v(\theta) - \frac{v_n - v_s}{2\cos\theta} - \frac{v_n - v_s}{2}}{\sin\theta\cos\varphi} = \frac{v(45) - \frac{v_n - v_s}{\sqrt{2}} - \frac{v_n - v_s}{2}}{\sqrt{2}\cos\varphi} = \frac{v(45) - 1.207(v_n - v_s)}{\sqrt{2}\cos\varphi}$$

A more complicated scheme makes a fit to the “figure-of-eight” formed by the LOS wind velocities plotted in a radial diagram[41].

2.3. Lidar performance

Much work has been dedicated to describe the performance of lidar system by their signal to noise relationships[29, 42]. Since the important signal energy is carried in the heterodyne current of Doppler frequency, and not by the totally received power, it is often referred to as the carrier to noise ratio, CNR. Most authors give the broadband CNR, i.e. the signal power divided by the noise power in the full bandwidth. Since a coherent lidar is fully frequency resolving the narrowband CNR, i.e. the signal power divided by noise in the signal bandwidth, is a better measure. The narrowband CNR definition is more complex since the signal bandwidth has to be defined which is non-trivial, especially for pulsed systems as is described in chapter 2.5.4. The spectral width of the heterodyne current depends on the laser linewidth and the duration of correlated return. The narrowband CNR also depends on the turbulence in the sample volume which in turn depends on the effective sample volume length. The wind distribution is typically wider in a larger sample volume which will lead to larger signal bandwidths and thus lower narrowband CNRs. The signal bandwidth is assumed to be dominated by the atmospheric correlation, pulse or sampling duration in the following description, which is a fair assumption for lidars with typical range resolution sensing moderately turbulent atmospheres.

It is also a common approximation to study ideal lidars in which shot noise is the only significant noise source. However, RIN in the reference source can often be noteworthy, especially when sensing low wind speeds with lidars which do not have a frequency offset on the local oscillator.

2.3.1. Lidar equation

The power received by a lidar is predicted by the lidar equation. An illustration of a lidar set up introducing the scattered fields and the concurrently contributing volume is sketched in Figure 24.

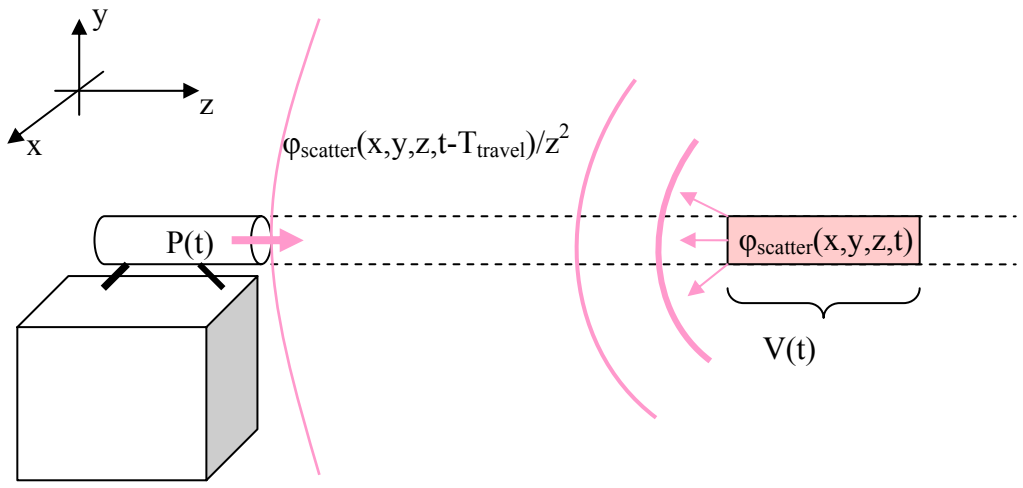

Figure 24 : Sketch of lidar set up. P(t) is the emitted laser power, $\varphi_{scatter}(x,y,z,t)$ is the field scattered at time t and arriving at the lidar at $t+T_{Travel}$. V(t) is the volume from which scatter arrives at the lidar concurrently.

The optic power collected by a coherent lidar, P_{rec}, can be expressed as

$$P_{rec}(t) = \eta_{coll} \int_{V(t)} \varphi_{scatter}(x, y, z, t - T_{travel}(z)) \cdot F_{collect}(x, y, z) \cdot T(x, y, z) dV$$

where η_{coll} describes range independent optical losses during the collection of scattered light, $\varphi_{scatter}$ is the scattered intensity, $T_{travel}(z) = z/c$ is the time it takes for scatter to travel back to the telescope, $F_{collect}(x,y,z)$ is the collection efficiency function which describes the amount of scattered light that is collected by the lidar and T is the one way propagation loss described from Beer's law as $T(z) = \exp\int_0^z -\alpha(z')dz'$ where α is the extinction factor. The integral is taken over the volume, V(t), from which scatter contributes concurrently at time t.

The volume is narrow so the atmosphere can be considered as homogeneous over x and y and the scattered intensity from a plane, i.e. integrated over x and y, is constant. The received power can thus be expressed solely as a function of the distance from the lidar, z.

$$P_{rec}(t) = \eta_{coll} \cdot \int_{z_{start}(t-T_{travel})}^{z_{stop}(t-T_{travel})} \varphi_{scatter}(z, t - T_{travel}) \cdot F_{collect}(z) \cdot T(z) dz$$

where z_{start} and z_{stop} are the borders of the sampled volume at time t. For a cw system the volume will in theory stretch from zero to infinity while for a pulsed system it will stretch over $cT_{pulse}/2$.

The scattered intensity from a disk of thickness dz is given by

$$\varphi_{scatter}(z, t - T_{travel}) = P_{scatter}(z, t - T_{travel}) \cdot \beta(z) \cdot T(z) \cdot dz$$

where $P_{scatter}(z,t)$ is the power profile in space, β is the atmospheric backscatter coefficient in $m^{-1}sr^{-1}$ and η_{trans} describes transmitter optical losses due to truncation and surface reflections.

The power profile in space can be expressed from the emitted temporal pulse profile as $P_{scatter}(z,t) = \eta_{trans} \cdot P(t-z/c)$ as illustrated in Figure 25.

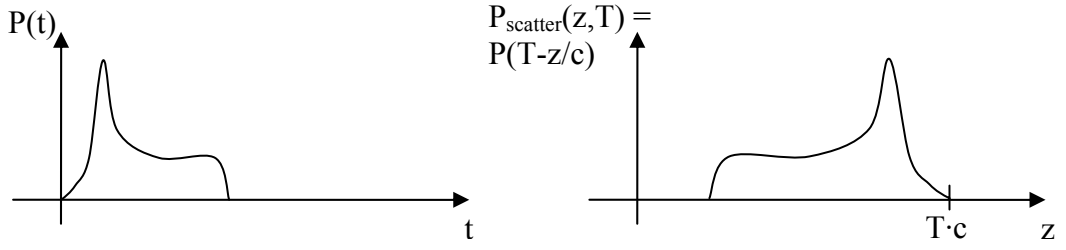

Figure 25 : Temporal pulse profile (left) and power profile in space (right).

The received power can then be expressed from the temporal pulse profile as

$$P_{rec}(t) = \eta_{coll} \cdot \eta_{trans} \cdot \int_{z_{start}(t-T_{travel})}^{z_{stop}(t-T_{travel})} P\left(t - \frac{2z}{c}\right) \cdot \beta(z) \cdot F_{collect}(z) \cdot T^2(z) dz$$

For a cw system the emitted profile is constant, i.e. P(t) = P, and the power received from a homogeneous atmosphere becomes

$$P_{rec} = \eta_{coll} \cdot \eta_{trans} \cdot P \cdot \beta \cdot \int_0^{\infty} F_{collect}(z) \cdot e^{-2\alpha z} dz \,.$$

For focused systems the function $F_{collect}(z)$ can be approximated as a Lorentzian function centered around the focus distance[5]. If propagation losses are disregarded the integral can be solved analytically to give the received power as

$$P_{rec} = \eta_{coll} \cdot \eta_{trans} \cdot P \cdot \beta \cdot \lambda \cdot \left(\frac{\pi}{2} + \arctan\left(\frac{A_{rec}}{\lambda \cdot z_{focus}} \right) \right)$$

where A_{rec} is the receiver aperture and z_{focus} the focus distance.

A model of the collection efficiency function, $F_{collect}(z)$, which gives a similar result but is suited for fiber based lidars can be found in chapter 4.2.1.

For a rectangular pulse in a homogeneous atmosphere the received power becomes

$$P_{rec}(t) = \eta_{coll} \cdot \eta_{trans} \cdot P \cdot \beta \cdot \int_{z_{start}(t-T_{travel})}^{z_{start}(t-T_{travel})+\frac{cT_{pulse}}{2}} F_{collect}(z) \cdot e^{-2\alpha z} dz$$

where T_{pulse} is the pulse duration.

The collection efficiency function $F_{collect}(z) = \eta_{coll} A_{rec}/z^2$ for a collimated system sensing at far range. The pulse length will generally be much shorter than the sensing distance, R, and the integral can be approximated accordingly

$$P_{rec} = \eta_{coll} \cdot \eta_{trans} \cdot \beta \cdot P \int_{z_{start}}^{z_{start}+\frac{cT_{pulse}}{2}} \frac{A_{rec}}{z^2} \cdot e^{-2\alpha z} dz = \eta_{coll} \cdot \eta_{trans} \cdot \beta \cdot P \cdot \frac{A_{rec}}{R^2} \cdot e^{-2\alpha R} \cdot \frac{cT_{pulse}}{2} =$$

$$= \frac{\eta_{coll} \cdot \eta_{trans} \cdot c \cdot \beta \cdot E \cdot A_{rec} \cdot e^{-2\alpha R}}{2R^2}$$

where $E = P \cdot T_{pulse}$ is the pulse energy.

The received energy will spread over a certain bandwidth depending on the atmospheric turbulence and the correlated scatter duration according to Appendix B. The correlated duration is typically limited by the pulse duration for a pulsed system and by the atmospheric correlation duration for a cw system.

The energy collected by a cw system during moderate turbulence can be considered to spread over 0.5-1 MHz due to a limited atmospheric correlation duration of 1-2 μs.

The signal bandwidth of a pulsed system with, $T_{pulse} < 500$ ns, sensing a moderately turbulent atmosphere with a wind distribution spread of less than 1 m/s within the contributing volume, can, to a first approximation, be considered as $1/T_{pulse}$.

2.3.2. Carrier-to-Noise Ratio of the heterodyne current

The narrowband CNR is the ratio of carrier power to noise power within the signal bandwidth and given as

$$CNR(t) = \frac{\left\langle i_c^2(t) \right\rangle}{\left\langle i_n^2(t) \right\rangle}$$

where $\left\langle i_c^2(t) \right\rangle$ is the average of the squared heterodyne current and $\left\langle i_n^2(t) \right\rangle$ is the average of the squared noise current, i.e. the noise variance, within the signal bandwidth.

Heterodyne current power
The heterodyne current strength was derived in chapter 2.1.2 to be

$$i_c(t) = 2R_{diode}\sqrt{\eta_{rec} P_{rec}(t) P_{LO}} \sum_{V(t)} A_i \cos\left(2\pi\left(f_{Doppler,i} - f_{offset}\right)t + \varphi_{diff,i}\right)$$

where R_{diode} is the responsivity of the detector, η_{rec} describes the receiver losses and A_i describes the division of power over the frequency components.

For a pulsed system the heterodyne current can be approximated as

$$i_c(t) = 2R_{diode}\sqrt{\frac{\eta_{rec} \cdot \eta_{coll} \cdot \eta_{trans} \cdot c \cdot \beta \cdot E \cdot A_{rec} \cdot e^{-2\alpha R} \cdot P_{LO}}{2R^2}} \sum_{V(t)} A_i \cos\left(2\pi\left(f_{Doppler,i} - f_{offset}\right)t + \varphi_{diff,i}\right)$$

and the average of the squared heterodyne current thus as

$$\left\langle i_c^2(t) \right\rangle = \frac{R_{diode}^2 \cdot \eta_{rec} \cdot \eta_{coll} \cdot \eta_{trans} \cdot c \cdot \beta \cdot E \cdot A_{rec} \cdot e^{-2\alpha R} \cdot P_{LO}}{R^2}.$$

A cw system will approximately generate a squared heterodyne current with average

$$\left\langle i_c^2(t) \right\rangle = 2R_{diode}^2 \cdot \eta_{rec} \cdot \eta_{coll} \cdot \eta_{trans} \cdot P \cdot \beta \cdot \lambda \left(\frac{\pi}{2} + \arctan\left(\frac{A_{rec}}{\lambda \cdot z_{focus}} \right) \right) \cdot P_{LO}.$$

Noise terms
Shot noise arises from the random generation of electron-hole pairs in the photodiode crystal due to noise in the light field and random absorption events. The shot noise current can be modeled as a Gaussian distribution with a variance of $2eR_{diode}P_{LO}$ where e is the elementary charge, $1.6 \cdot 10^{-19}$ C. Shot noise is spectrally uniform i.e. white noise.
Thermal noise represents the random movement of electrons in a resistance. This noise takes on a Gaussian distribution. The variance of the thermal noise current is given as $4k_bT/R_L$ where k_b is Boltzmann's constant, $1.38 \cdot 10^{-23}$ J/K, R_{load} is the transimpedance of the receiver and T is the temperature on the load. Thermal noise is also evenly distributed spectrally, i.e. white noise. Note that the thermal noise is independent of P_{LO}.

Another important noise factor in heterodyne detection is the relative intensity noise, which describes the instability in the power output of a laser. RIN arises for example from cavity vibrations, fluctuations in the laser gain medium or as transferred intensity noise from the pump source. RIN typically falls off with frequency as pink

noise. At high frequencies it will typically be set to drown in shot noise, but it can be significant at up to several MHz. RIN is usually presented as relative noise power in decibels per hertz at one or several intensities. The variance of a frequency due to RIN is thus calculated from $RIN(f) \cdot P_{LO}^2$. RIN of -150 to -160 dB/Hz above 10 MHz can be achieved by stabilized fiber lasers[29].

Other noise factors are dark current, i.e. the leakage current measured at zero intensity, and the current generated by background light, including backreflected ASE and amplitude modulator leakage as well as circulator leakage. These relatively weak noise sources are independent of P_{LO}. They can therefore generally be ignored for typical local oscillator strengths. Amplification noise in the LNA and digitizing noise are not treated further in this text.

The noise current within the signal bandwidth, B, can thus be modeled as

$$\left\langle i_n^2(t) \right\rangle = \left(2eR_{diode}P_{LO} + \frac{4k_bT}{R_L} + RIN(f) \cdot P_{LO}^2 \right) \cdot B \,.$$

CNR examples
The CNR for a focused cw system can thus be expressed as

$$CNR = \frac{\left\langle i_c^2(t) \right\rangle}{\left\langle i_n^2(t) \right\rangle} = \frac{2R_{diode}^2 \cdot \eta_{rec} \cdot \eta_{coll} \cdot \eta_{trans} \cdot P \cdot \beta \cdot \lambda \left(\frac{\pi}{2} + \arctan\left(\frac{A_{rec}}{\lambda \cdot z_{focus}} \right) \right) \cdot P_{LO}}{\left(2eR_{diode}P_{LO} + \frac{4k_bT}{R_L} + RIN(f) \cdot P_{LO}^2 \right) \cdot B}$$

The received power has a mean of 0.3 pW, corresponding to as little as 2.5 million photons/s, for a typical focused cw lidar sensing a typical clear atmosphere with parameters according to Table 5. The narrowband CNR as a factor of P_{LO} can be seen in Figure 26. For the example system the optimal P_{LO} would be 0.72 mW.

cw lidar parameter	**Symbol**	**Value**
Responsivity	R_{diode}	1 A/W
Loss factors	η_{rec}, η_{coll} and η_{trans}	0.85
cw power	P	1 W
Backscatter coefficient	β	10^{-7} $m^{-1}sr^{-1}$
Lidar wavelength	λ	1.5 μm
Receiver aperture	A_{rec}	28 cm^2, (radius 3 cm)
Focus distance	z_{focus}	100 m
Receiver temperature	T	300 K
Receiver transimpedance	R_L	100 Ω
Relative intensity noise above 5 MHz	RIN(f > 5 MHz)	- 155 dB
Signal bandwidth	B	0.5 MHz

Table 5 : Typical parameters for a focused cw lidar sensing a clear atmosphere.

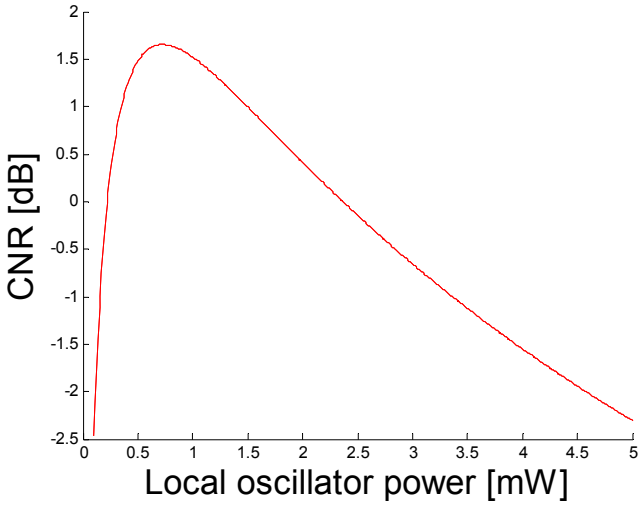

Figure 26 : The CNR as a function of P_{LO} for a cw lidar with parameters according to Table 5.

The CNR of a cw system without a frequency offset on the LO will fall when the LOS wind speed, and thus the Doppler shift, is low since the RIN typically is much higher at low frequencies. It could be of interest to reduce the local oscillator power for this case. However, in practice it is difficult to adapt the P_{LO} to the wind velocity in real time and a compromise value is taken.

The CNR of a pulsed collimated system with parameters according to Table 6 becomes

$$CNR = \frac{\langle i_c^2(t) \rangle}{\langle i_n^2(t) \rangle} = \frac{R_{diode}^2 \cdot \eta_{rec} \cdot \eta_{coll} \cdot \eta_{trans} \cdot c \cdot \beta \cdot E \cdot A_{rec} \cdot e^{-2\alpha R} \cdot P_{LO}}{R^2 \left(2eR_{diode} P_{LO} + \frac{4k_b T}{R_L} + RIN(f) \cdot P_{LO}^2 \right) B}$$

which is plotted as a function of local oscillator power in Figure 27. The received power is in the order of 50 pW for this system.

Pulsed lidar parameter	**Symbol**	**Value**
Responsivity	R_{diode}	1 A/W
Loss factors	η_{rec}, η_{coll} and η_{trans}	0.85
Pulse energy	E	10 µJ
Backscatter coefficient	β	10^{-7} $m^{-1}sr^{-1}$
Extinction coefficient	α	10^{-5} m^{-1}
Receiver aperture	A_{rec}	28 cm^2, (radius 3 cm)
Center of range gate	R	100 m
Receiver temperature	T	300 K
Receiver transimpedance	R_L	100 Ω
Relative intensity noise above 5 MHz	RIN(f > 5 MHz)	- 155 dB
Signal bandwidth	B	5 MHz (T_{sample}=200 ns)

Table 6 : Typical parameters for a pulsed lidar sensing a clear atmosphere.

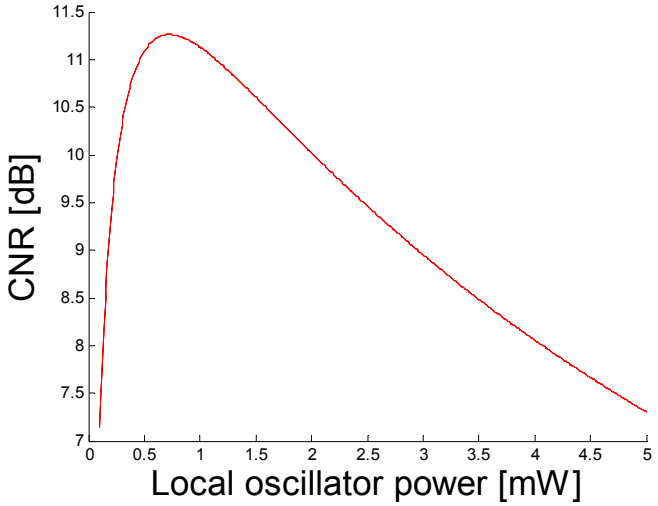

Figure 27 : The CNR as a function of P_{LO} for a cw lidar with parameters according to Table 6.

However, the collection efficiency function is badly described by A_{rec}/z^2 at close range and the CNR can drop with a factor of 50, or -17 dB, when sensing at 100 m distance, as mentioned in chapter 2.5.8. The narrowband CNR will in addition not fully describe the signal clarity in the wind distribution spectrum. The energy scattered from the edges of a range gate will be dispersed over a wider bandwidth since their correlated scatter duration is shorter than T_{pulse}. Different correlation durations within the range gate are further treated in chapter 2.5.6.

It could be of interest to increase the responsivity of the detector in order to be able to use less local oscillator power to reach the maximal CNR. The RIN will be less strong and the CNR higher. Avalanche photodiodes offer a multiplication of the responsivity but saturate faster than pin diodes and introduce an extra noise factor. They are therefore rarely used in practice. A more used practice is to use balanced receivers which reduce the influence of noise which is present in both the received scatter and the local oscillator, e.g. RIN.

2.3.3. The standard deviation in the estimated wind velocity

The accuracy of a wind velocity estimate is not solely dependent on the lidar CNR. The frequency components are speckled and the backscatter coefficient is an average parameter. An important factor is therefore the smoothening effect of the accumulation of normally up to thousands of spectra. The wind is assumed to be effectively uniform in the time period during the accumulation duration. For the 3D wind construction the wind velocity is assumed to be uniform during the scan and over the scan perimeter.

A more interesting measure than the CNR is the standard deviation of the estimated LOS wind velocity, σ_v. The standard deviation decreases with increasing CNR and number of accumulations, N_{acc}. The option to increase the CNR in practice is to increase the peak power. Larger high quality lenses are expensive and longer pulses will reduce the spatial resolution.

Nevertheless, the improvement in σ_v will saturate with increasing CNR or N_{acc}. If the CNR is high there is little point in increasing it further since the signal is already well defined. The available laser power is then better distributed over several pulses to

increase the number of accumulated returns in order to decrease the speckle effects. Another option is to measure in more directions to increase the accuracy of the 3D wind velocity construction. With the same reasoning the energy is better spent in increasing the CNR by concentrating the available power in fewer but stronger pulses, once the speckle is fully developed. However, this is without giving consideration to technological aspects. Peak power is limited by SBS as well as eye safety issues and most fiber optic components are not constructed to sustain high peak power. The accumulation rate of a pulsed lidar is limited by the PRF which controls range ambiguities. Models predicting the σ_v dependence on CNR and N_{acc} are available[38, 43]. Simulations[44] of the standard deviation of the normalized frequency, f/f_s, as a function of the wideband CNR are given in Figure 28.

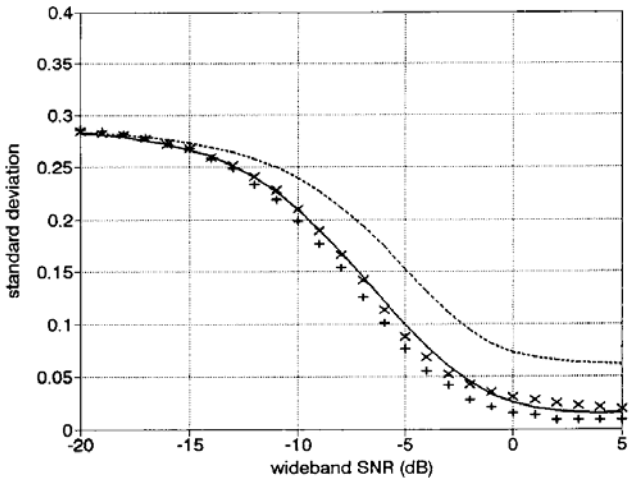

Figure 28 : Standard deviation of the normalized frequency as a function of the wideband CNR. The lines are analytical expressions for a wide (dashed) and a narrow (solid) bandwidth signal while x and + are results from simulations[44].

It is thus possible to find an optimal combination of N_{acc}, i.e. PRF, for a fixed mean power lidar and a fixed accumulation duration, i.e. having a constant PRF*E, e.g. as in Figure 29. The standard deviation has a fairly broad minima centered where the narrowband CNR is about 3 dB.

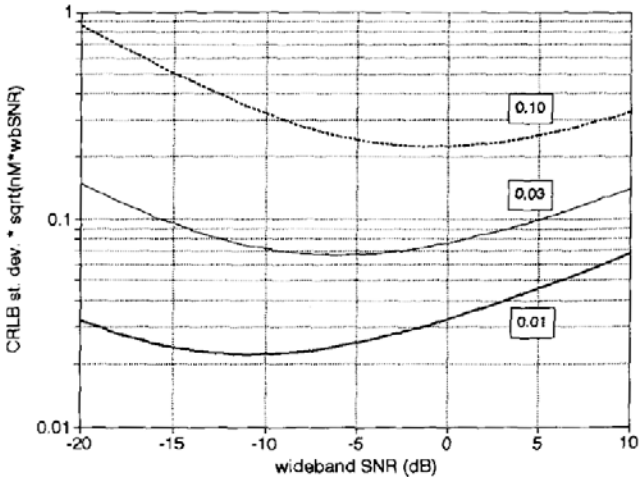

Figure 29 : Cramer-Rao Lower Boundary standard deviation for a fixed mean power lidar and a fixed accumulation duration, where n is the number of accumulations and M the FFT size. The different curves are calculated with different signal bandwidths[44].

In practice it is difficult to optimize the PRF since the narrowband CNR depends on the atmospheric conditions, i.e. the turbulence and backscatter coefficient. Commercial systems generally accumulate a fixed number of several thousand pulse returns for a 3D wind velocity construction. In the region of typical narrowband CNR and numbers of accumulations a standard generalization is that the standard deviation will be proportional to the pulse energy and the square root of the number of accumulations[31, 44], i.e.

$$\sigma_v \propto \frac{1}{E\sqrt{N_{acc}}}.$$

Interesting to note is that most lasers and amplifiers work in a boost mode where they store pump energy during a longer duration to release it concentrated in an amplified pulse. The pulse energy will therefore typically decrease with an increase in PRF and vice versa. It has been indicated that the pulse energy from a fiber amplifier depends approximately inversely upon the square root of the PRF and thus inversely upon the square root of N_{acc} during a fixed observation period. This relation gives a reasonable freedom in trying to find the optimal CNR and PRF combination.

2.4. Range dependent collection efficiency of fiber based coherent lidars

The collection of scatter with a telescope is a fundamental principle for wind sensing lidars. Focused lidars[2, 19] collect backscatter more efficiently than collimated systems and can use smaller telescopes and less peak power to achieve sufficient carrier to noise ratios. Fiber based lidars with fiber end receptors with µm apertures experience range dependent losses as outlined in Figure 30.

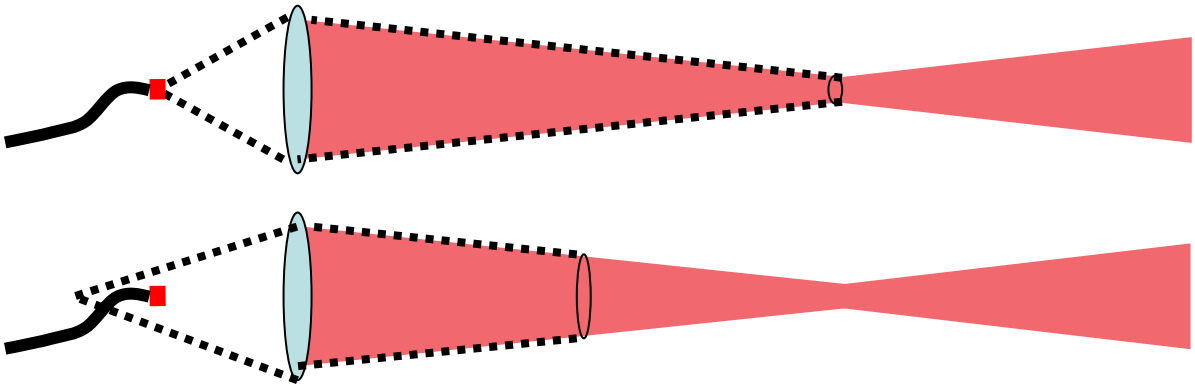

Figure 30 : The backscatter from the focus distance will be imaged on the fiber end (red square) and is ideally collected without loss (top image). Backscatter from other distances will be focused slightly outside the receptor plane and will be collected with loss since the image projection in the receptor plane is larger than the receptor area (bottom image).

The received backscatter is thus dominated by the reflections off aerosols in the volume at which the telescope is focused. Focused lidars are therefore range resolving even if operated in continuous wave mode which simplifies transmission and detection and increases the duty cycle of the system.

However, focused cw systems can only be used for distances up to a few hundred meters as the telescope loses resolving ability with the square of the sensing range. The Zephir which is a focused cw lidar is used for ranges not exceeding 200 meters due to limitations in lens diameter and thus in spatial resolution at long ranges.

A drawback of focused cw lidars, especially when focused at far distances, is that range ambiguities can occur whilst sensing in an atmosphere with a multi component backscatter coefficient[45], e.g. low lying cumulus clouds in an otherwise clear atmosphere.

Functions describing the range dependent collection efficiency are important tools to describe the volume which gives the dominant contribution to the lidar signal as well as for CNR analyses and quantitative estimations of cloud influence. The collection efficiency of focused systems has previously been modeled by Sonnenschein[5]. A revised model, suitable for fiber based lidars, is described in this chapter. The model takes into account small receptor area and copropagation of the LO and the received scatter waves in a single mode fiber. Simulated profiles predict slightly tighter confinement than expected from the previous model.

2.4.1. Collection efficiency function for fiber based coherent lidars

A focused lidar will transmit a narrow beam of light with a waist at distance x_{focus}, typically at 20-200 m. A sketch of a fiber optic based focused monostatic coherent lidar is presented in Figure 31. The lidar has a combined emitter/receptor in the form of a fiber end positioned in front of the focusing lens.

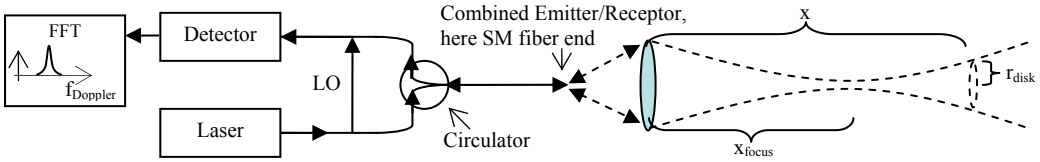

Figure 31 : Sketch of system and principle of a focused monostatic cw coherent lidar based on fiber optic components.

The beam emitted from the single mode fiber defines the volume which reflects light and is well described by Gaussian beam propagation. In the model the volume is divided into disks of aerosols, with a Gaussian beam radius $r_{disk}(x)$, i.e. the beam radius where the center intensity has dropped to 0.135 %.

$$r_{disk}^2 = r_0^2\left(1+\left(\frac{\lambda\left(x-x_{focus}\right)}{\pi r_0^2}\right)^2\right)$$

where x_{focus} is the focus distance, set by controlling the receptor to lens distance x_{fiber}, λ is the wavelength and r_0 the beam waist radius.

The beam waist radius is found from the magnification of the fiber core radius according to Gaussian beam propagation before the ray optics limit, i.e. where x_{fiber}-f is similar to the focus depth $\frac{\pi r_{fiber}^2}{\lambda}$. The lens aperture is assumed to be large enough not to truncate the beam significantly as it is emitted out of the lidar.

$$r_0 = M \cdot r_{fiber} = \frac{\left|\frac{f}{x_{fiber}-f}\right|}{\sqrt{1+\left(\frac{\pi r_{fiber}^2}{\lambda\left(x_{fiber}-f\right)}\right)^2}} \cdot r_{fiber}$$

where M is the magnification factor for Gaussian beam propagation and r_{fiber} the receptor radius, in this case the single mode fiber core radius. The focused beam waist radius, r_0, is typically about 1 cm.

The fiber position can be iterated from $x_{fiber} = f + \frac{x_{foucs}-f}{M^2}$.

The power received from a disk of aerosols at x, $P_{received}(x)$, can be calculated from

$$P_{received}(x) = \int_{receptor} I(x)dA$$

where I(x) is the backscattered intensity from x.

The diffusively backscattered intensity can be considered to be constant over the lens surface and thus over the receptor since the scatter distance is much larger than the lens aperture. The received power from a disk of thickness dx can thus be expressed as

$$P_{received}(x) = \int_{receptor} I(x)dA = \pi r_{fiber}^2 I(x) = \pi r_{fiber}^2 \frac{\pi r_{lens}^2}{\pi r_{projection}^2(x)} I_{lens}(x) = \frac{\pi r_{fiber}^2 \pi r_{lens}^2}{\pi r_{projection}^2(x)} \frac{F_{out}(x)\beta}{x^2} dx$$

where r_{lens} is the effective lens radius, $I_{lens}(x)$ is the intensity in the lens plane of the backscatter from the disk at position x, F_{out} is the emitted flux, β is the backscatter coefficient and $r_{projection}$ is the radius of the projection of the image in the detector plane. Propagation and range independent receptor losses are disregarded in the model.

The effective lens radius is calculated to fit the Gaussian aperture of the fiber end from

$$r_{lens}^2 = r_{fiber}^2 \left(1 + \left(\frac{\lambda x_{fiber}}{\pi r_{fiber}^2}\right)^2\right).$$

The position, x_{image}, and radius, r_{image}, of the image of the disk at x can be found from

$$x_{image}(x) = \frac{f \cdot x}{x - f} \text{ and } r_{image}(x) = \frac{r_{disk} \cdot x_{image}}{x}.$$

The projection of the disk image in the detector plane is illustrated in Figure 32.

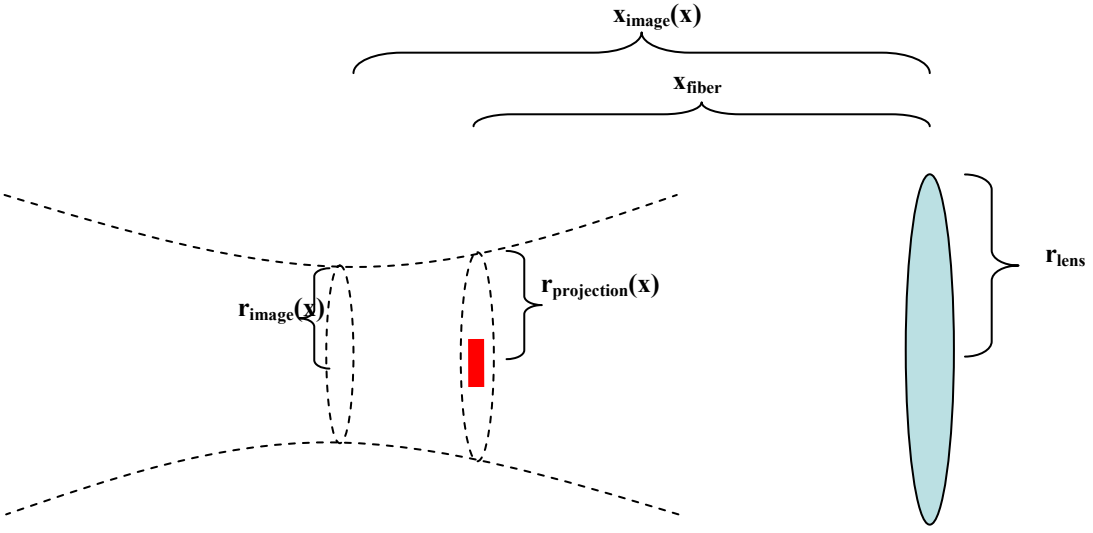

Figure 32 : Description of optic system on detector side.

The radius of the projection, $r_{projection}(x)$, in the detector plane is found by letting Gaussian beam propagation describe diffraction as follows

$$r_{projection}^2(x) = r_{image}^2\left(1+\left(\frac{\lambda(x_{fiber}-x_{image})}{\pi r_{image}^2}\right)^2\right).$$

The collection efficiency function $F_{collect}(x)$ is introduced for future reference.

$$F_{collect}(x) = \frac{A_{fiber}A_{lens}}{x^2 A_{projection}(x)}$$

which describes the relative power collected from a disk of aerosols with unitary thickness at position x.

The received power as a function of distance in a lossless lidar can then be described as

$$P_{rec}(x) = F_{collect}(x)\cdot\beta\cdot F_{out}$$

In the case of far range sensing with a collimated telescope, i.e. $x_{focus} \rightarrow \infty$, $A_{projection}(x)$ equals A_{fiber} and the well known range dependence A_{lens}/x^2 is obtained.

2.4.2. Verification of the range dependent collection efficiency model

It is possible to verify the collection efficiency function by measuring the energy in the heterodyne signal generated from a hard moving target, e.g. a ventilator tilted towards the beam direction, sequentially positioned at different distances. However, in practice it will be difficult to ensure that the target can be aligned so that the lidar hits the target at the same point and the same impact angle for all distances. The Zephir can set the focus distance by micrometer positioning of the fiber end. In this system it is possible to make a more precise verification of the model by keeping hard target at a fixed position and moving the focus.

The results from such an exercise can be seen in Figure 33. A Zephir lidar prototype was aimed at a ventilator positioned at a distance of 105 m. The prototype had a wavelength of 1.545 µm. The ventilator was tilted and covered with cardboard so that light would backscatter with a constant positive Doppler shift of about 7 MHz. The heterodyne current was band pass filtered and sampled at 50 MHz during 5.12 µm.

The peak height above the noise floor directly corresponds to the power received from the target since the system operates in cw mode. The peak heights of about 2750 heterodyne signals were averaged from every lidar focus from 73 – 160 m with 5 or 6 m intervals. Samples uncharacteristic in frequency or power were eliminated by the averaging algorithm. The received power was compared with the modeled collection efficiency from 105 m as a function of focus distance. The standard single mode fiber core diameter was assumed to be 9 µm which corresponds to an effective lens radius of 2.2 cm for the telescope with a 20 cm focal length.

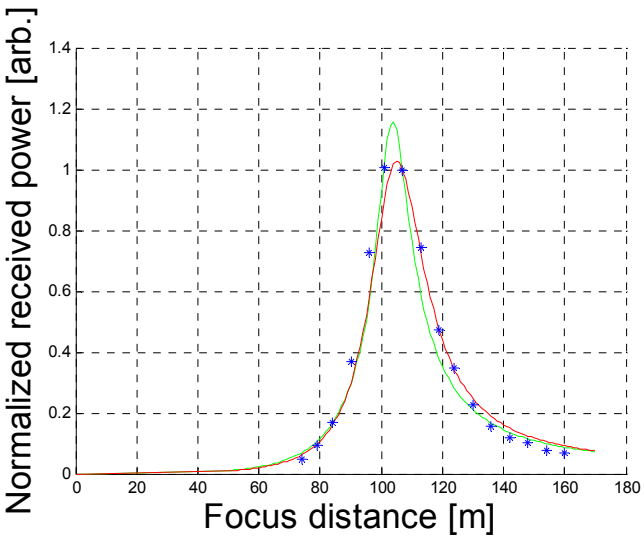

Figure 33 : Verification of the collection efficiency model using a Zephir with a fiber core diameter of 9 µm. Stars are measured values while the two curves show the results of the collection efficiency model for fiber based lidars (green) and Sonnenschein's model (red). Models and measurements were normalized towards the received power obtained when the lidar was focused at 107 m.

Both models seem to describe the collection efficiency fairly well. The model for fiber based lidars seems to predict the returned power well close to the focus, although underestimating the received power from 10 to 20 m on either side of the focus point with as much as 25 %. Sonnenschein's model does not give a fair description for the peak values but gives a better description of the received power from the target at 105 m when the focus is set 10 to 20 m above. This corresponds to a better description of the scatter from the atmosphere 10 to 20 m below the focus point.

2.4.3. Examples of simulated collection efficiency functions

The collection efficiency models thus provide a suitable start for predicting the behavior of focused lidars, e.g. to predict CNRs, the influence of clouds on cw systems or the distortion of the range gate shape in pulsed and focused lidars.

The effect of increasing sensing range can be seen in Figure 34. The simulated collection efficiency functions are based on a system with f = 20 cm, r_{fiber} = 4.5 µm, λ = 1.5 µm and for x_{focus} at 50 m, 100 m, 150 m as well as providing the close range behavior in collimated configuration. Also included are profiles from Sonnenschein's model with the same system parameters.

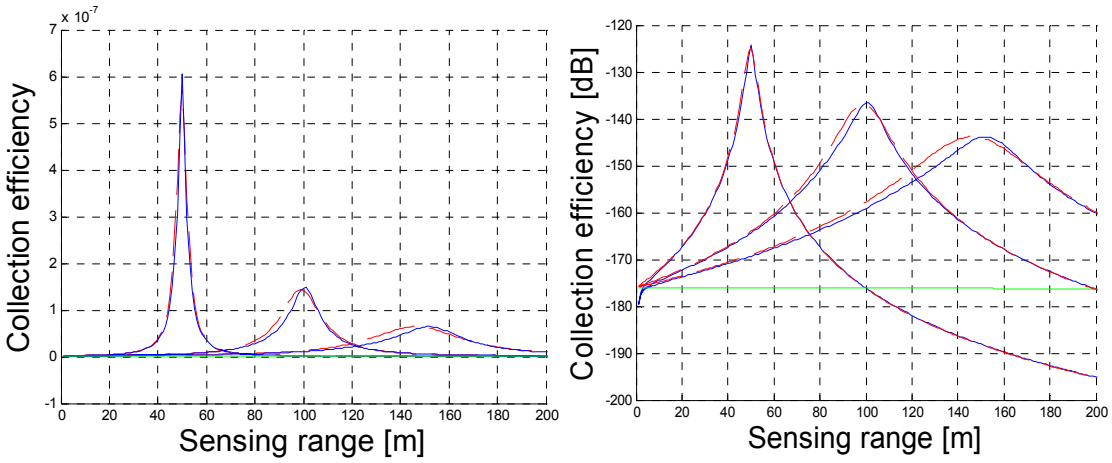

Figure 34 : Collection efficiency functions for a system focused at 50, 100 and 150 meters (blue) and according to Sonnenschein's model (red). The collimated configuration is drawn in green. For a more detailed illustration of the difference with a collimated system the right hand graph gives the collection efficiency function in dBs.

The higher sensitivity at close range of focused systems is evident. The received power from 20 m either side of the focus distance at 100 m will be 50 times stronger than the power from the same 40 m range with the same system collimated.

The model derived in this chapter predicts a maximum slightly closer to the set focus distance than Sonnenschein's model does, which becomes noticeable primarily for distances above 100 m It also predicts a slightly tighter confinement of cw systems with Full Width Half Maximum (FWHM) of the efficiency function about 20 % shorter.

The FWHM of the collection efficiency function can be shown to grow proportionally to x^2_{focus} while the power received from the focus distance, $P_{rec}(x_{focus})$, falls with x^2_{focus}. The power received from the FWHM volume is therefore principally independent of focus distance. The narrowband CNR will nevertheless normally drop with increased sensing distance. This is due to increasing propagation losses as well as a broadening signal bandwidth due to more turbulence in the increasing sample volume.

Focused cw lidars sensing inhomogeneous atmospheres
Focused cw lidars will suffer from range ambiguities when sensing atmospheres with inhomogeneous backscatter coefficients. For example, cumulus clouds can be located from 500 m above ground and be several 100 m thick. The backscatter coefficient can be as high as 10^{-3} $m^{-1}sr^{-1}$ while at the same time it can be in the low 10^{-6} in the atmosphere below.

The power received by a 1 W cw lidar with a standard 30 ° tilt focused at 100 m altitude from an atmosphere containing a cumulus cloud can be seen in Figure 35. The cloud was modeled to start abruptly at 500 m altitude, corresponding to a sensing range of 580 m, with a backscatter coefficient, $\beta_{cloud} = 10^{-3}$ $m^{-1}\cdot sr^{-1}$. The clear air is assumed to have a backscatter coefficient, $\beta_{clear} = 5\cdot10^{-7}/m\cdot sr$. The attenuation in both atmospheres is assumed to be 100 times higher than the backscatter coefficient.

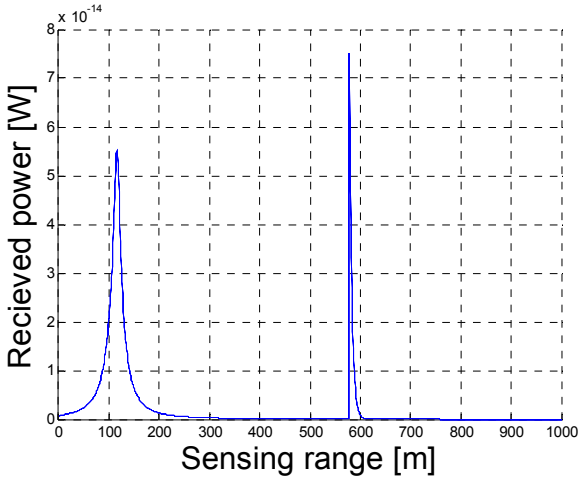

Figure 35: Received optic power from an atmosphere containing a cloud at 500 m altitude, $\beta_{cloud} = 10^{-3}$ and $\beta_{clear} = 5 \cdot 10^{-7}$.

The collection efficiency is about 60 dB better at the focus distance than at 580 m but the received power from the bottom of the cloud is comparable with that from the intended effective sample volume. The obtained wind distribution spectrum will include indistinguishable velocity components from the cloud and from the focused volume.

2.5. Effective sample volumes of coherent lidars

A lidar does not sense the same quantity as a mast mounted anemometer, i.e. the horizontal wind at one altitude. A lidar senses the LOS wind distribution in a weighted sample volume. However, at this stage, wind sensing lidars are typically intended to replace cup anemometers and a knowledge of the wind velocity at a specific altitude is desired.

From the measured weighted wind distribution it is possible to calculate the average wind or estimate the most significant wind signal within the sample volume which generally is assumed to originate from the center of the weighting function describing the signal strength as a function of range. Estimations of the LOS wind speed in at least three directions can then be used to construct the 3D wind velocity.

Verification campaigns comparing lidars with mast mounted anemometers have shown that the accuracy of the estimations of the 10 minute average 3D wind velocity at a point altitude is rather good, with 10-20 cm/s accuracy, in flat terrains and for typical winds[11, 12, 13]. However, results have been less clear in complex terrain[22] or for example in the presence of clouds[45]. It is important to know the true location, size and weighting of the sample volume for accurate interpretation of the wind sensing, for comparisons between different systems and methods as well as for spatial turbulence studies.

Another important characteristic of a lidar, apart from the CNR and the standard deviation of the wind estimate, is therefore the effective sample volume. The sensed volume is a long thin cylinder, typically with a diameter of a few centimeters. The FWHM of the received optic energy as a function of distance has typically been given as the length of the effective sample volume. The received optic energy corresponds directly to the wide band CNR. However, the wide band CNR description does not take into account the range dependent energy spread due to the range dependent correlated scatter duration in a range gate. The wind distribution in the sensed volume and thus the Doppler frequency bandwidth is narrow, normally 1 m/s and 1.3 MHz respectively, compared to the DFT broadening, which is at least 5 MHz for a 200 ns pulse system. The energy scattered from different distances will therefore be considerably mixed in the wind spectrum. Figure 36 illustrates this effect on an idealized wind spectrum built up of two components. Both components scatter the same amount of energy but one has half the correlated scatter duration, i.e. it has a discrete phase shift in the middle of the signal, and spreads the energy content over twice the bandwidth. The fully correlated signal will therefore dominate the wind spectrum.

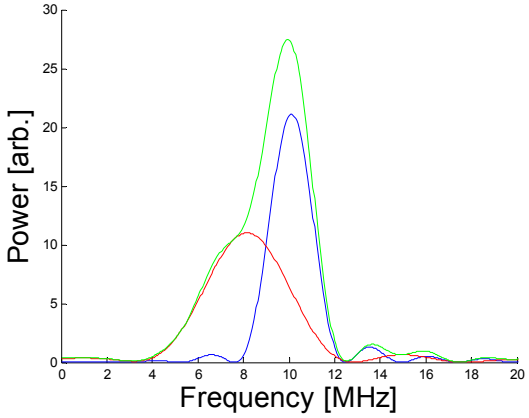

Figure 36 : Idealized wind spectrum (green) built up of two components with the same amplitude and contribution duration; one with a frequency of 8 MHz and a correlated contribution duration of 200 ns (red), the other with a frequency of 10 MHz and a correlated contribution of 400 ns (blue).

The confinement of pulsed systems will be underestimated, unjustifiably favoring cw systems, when using the wideband definition. For modeling of the range gate shape of focused pulsed systems the correlation duration influence is important. The peak height of the Fourier transformed signal is therefore possibly a better indicator in determining the dominant scatter distance and an alternative definition of the effective sample volume length is proposed in this chapter.

2.5.1. Wind Estimation

The LOS wind estimation should preferably be taken from the center of the sample volume when compared to the measurement of a cup anemometer, but in a sensed wind distribution spectrum it can be difficult to estimate which velocity that is scattered from the center. The importance of the estimator of a system with a uniformly weighted sample volume sensing a wind profile which flattens out with height is illustrated in Figure 37.

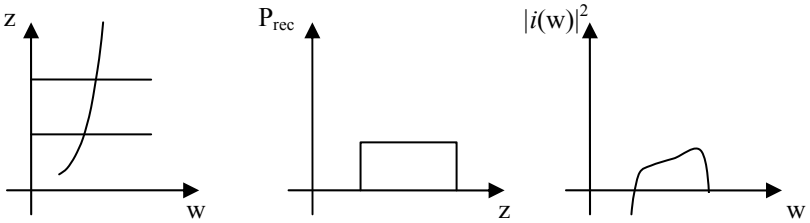

Figure 37 : From left to right; wind profile, received backscatter weighting function and wind spectrum illustrating the difficulty of finding the wind velocity from the center of the sample volume.

The wind estimated from the average or the centroid of this wind spectrum would return a value which is slightly lower than the speed of the wind in the middle of the range gate. However, the wind speed would be overestimated if the most significant wind signal, i.e. the wind distribution peak, is picked, since the scatter from the similar wind velocities in the upper part of the sample volume is overlayered in a smaller bandwidth. It is therefore important that the weighted sample volume function drops off quickly around the centre position.

2.5.2. Received Backscatter Profile and Wind Peak Profile

The Received Backscatter Profile, RBP, is defined as the optic energy received by a lidar during a sample duration as a function of distance. Since the heterodyne current is proportional to the square root of the received optic energy the RBP is linearly related to the wind signal strength in the power spectrum, $i^2(f)$, as a function of distance. The RBP is defined as

$$RBP(z) = \int_{T_{sample}} P_{rec}(z)dt \, .$$

A distance which gives a coherent contribution during τ will spread its energy over a bandwidth $1/\tau$ in the wind distribution spectrum. The wind peak profile, WPP, takes into account the spread of energy in the wind spectrum due to the limited correlated scatter duration and is defined as

$$WPP(z) = \int_{T_{sample}} P_{rec}(z) \cdot \tau(z)dt$$

where $\tau(z)$ is the correlated duration of the received scatter from distance z.

The atmosphere will be assumed to be homogeneous regarding backscatter coefficients and atmospheric correlation duration.

2.5.3. Effective sample volume length of range gated collimated lidars

The length of the contributing volume for a direct detecting lidar, which senses the scattered power from one sample point, is $cT_{pulse}/2$. In contrast, a coherent lidar measures frequencies and needs a non-negligible recording time, normally corresponding to some 50-100 sample points, to retrieve the wind induced Doppler shift. The pulse will propagate during this recording duration, thereby extending the length of the sample volume.

The scatter from the front of a pulse received by the lidar at time t has been generated at a distance $c \cdot t/2$, where $t = 0$ is the time that the pulse front left the system. The scatter generated by the end of the pulse received at time t has been generated at a distance $c \cdot (t-T_{pulse})/2$. Consequently the lidar concurrently receives scatter from a volume of length $cT_{pulse}/2$. Figure 38 shows the scatter generated from a pulse propagating through the atmosphere where the y-axis gives the distance from which the scatter originated.

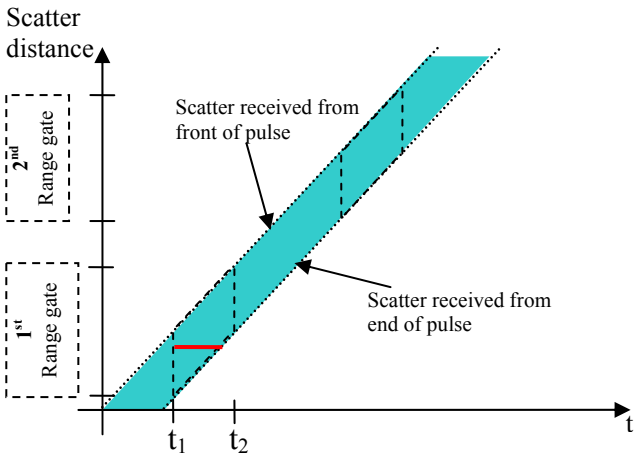

Figure 38 : Distance to the origin of the received scatter as a function of collection time. The spatial extents of two range gates are marked. The contribution duration to the wind spectrum from a distance z is illustrated by the red line.

The range gate length is defined as the length in space from which the detector receives light during one LOS wind observation T_{sample}, from t_1 to t_2. It can be calculated from the scatter received from the front of the pulse at the end of the sample duration minus the scatter received from the end of the pulse at the beginning of the scatter duration:
$ct_2/2 - c(t_1 - T_{pulse})/2 = c(t_2 - t_1 + T_{pulse})/2 = c(T_{sample} + T_{pulse})/2$. However, the ability of a coherent lidar to spatially resolve wind velocity measurements is better than the full range gate length, as any given distance will contribute to the signal with range dependent contribution duration and collection efficiency.

2.5.4. Contribution duration

Scatter distances will not contribute with the same amount of energy to a wind spectrum during the sample duration T_{sample}. Aerosols at the edges of the range gate will only contribute with scatter for the first sample point of the LOS wind observation while aerosols in the centre of the range gate will contribute for the full pulse duration. The contribution duration, $T_{contribution}$, can be illustrated as in Figure 39 if we disregard the digitizing effect due to sampling.

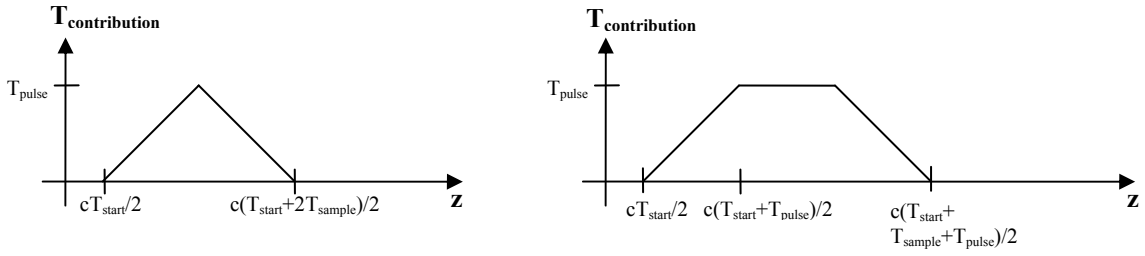

Figure 39 : Contribution duration of scatter to a wind spectrum as a function of distance z. For the typical case when $T_{pulse} = T_{sample}$ (left) and for $T_{sample} > T_{pulse}$ (right).

For a lidar with $T_{pulse} = T_{sample}$, the contribution duration as a function of scatter distance is given by:

$T_{contribute}(z) = T_{pulse} - \frac{2}{c}|z - g_{center}|$ when $z \in$ range gate and where g_{center} is the center of the range gate, $T_{contribute}(z) = 0$ when $z \notin$ range gate.

2.5.5. Received backscatter profile of pulsed lidars

The range dependence of the received power in a collimated system, A_{rec}/z^2, is for now disregarded since pulses typically are short compared to the sensing distance. The telescope effects on range gates are treated later in this chapter. The RBP for a rectangular pulse and gate with $T_{sample} = T_{pulse}$ can then be approximated as

$RBP(z) = \int_{T_{sample}} P_{rec}(z)dt = P_{rec}T_{contribute}(z) = P_{rec}\left(T_{pulse} - \frac{2}{c}|z - g_{center}|\right)$ when $z \in$ range gate and RBP(z) = 0 when $z \notin$ range gate.

The FWHM of the RBP becomes $cT_{pulse}/2$, e.g. 30 m for a system with $T_{pulse} = T_{sample}$ = 200 ns.

The calculation of the weighting function will be more complex if the pulse and gate cannot be represented by rectangular power profiles. The RBP(z) which corresponds to the noise relative energy given to the wind spectrum should be calculated with the normalized gate profile, G(t), included in the integral

$$RBP(z) = \int_{T_{sample}} G(t)P_{rec}(z)dt .$$

The RBP of a pulsed system can be measured by studying the return from a hard target. If the range dependent collection efficiency function can be modeled accurately it is possible to make the RBP measurement with the hard target at one fixed location. The sampled range gated heterodyne current vector captured by the lidar, [i(0),…, i(N)], is Fourier transformed with a translating window according to the following algorithm:

For k = 0 to N = $T_{sample} \cdot f_s$
$RBP(g_{start}+k \cdot c/2f_s) = sum(|DFT(i(N-k), i(N-k+1),…, i(N))|^2)$
$RBP(g_{start}+(N+k) \cdot c/2f_s) = sum(|DFT(i(0), …, i(N-k-1), i(N-k))|^2)$

Where the number of samples $N = T_{sample} \cdot f_s$, and g_{start} is the start of the range gate.

An example of a measured RBP of a pulsed system is given in Figure 89 in chapter 6.1.

2.5.6. Wind Peak Profile of pulsed lidars

The atmospheric correlation duration is generally longer than the pulse duration. The correlated scatter duration from a distance z is therefore equal to the contribution time, i.e. $\tau(z) = T_{contribute}(z)$. The energy scattered from the beginning or the end of the range gate will thus be spread over a wider frequency range than the energy from the centre of the range gate. The wind peak profile of a lidar emitting rectangular pulses

can be approximated accordingly if the range dependent collection efficiency of the collimated telescope is ignored

$$WPP(z) = \int_{T_{sample}} P_{rec}(z) \cdot \tau(z) dt = P_{rec} T^2_{contribution}(z) = P_{rec}\left(T_{pulse} - \frac{2}{c}|z - g_{center}|\right)^2 \text{ when } z \in \text{range gate}$$

$WPP(z) = 0$ when $z \notin$ range gate.

The FWHM of the WPP is found from $WPP_{FWHM} = \left(1 - \frac{1}{\sqrt{2}}\right) \cdot c \cdot T_{pulse} \approx 0.6 \cdot RBP_{FWHM}$.

A lidar emitting a rectangular pulse, with $T_{pulse} = T_{sample} = 200$ ns, has a WPP_{FWHM} of about 18 m.

The WPP indicates that the wind spectrum will be more dominated by the wind velocity in the center of the range gate, than what is expected from the RBP description, as seen in Figure 40. The probability of picking the wind velocity from the center of the range gate is thus bigger than expected from the RBP description.

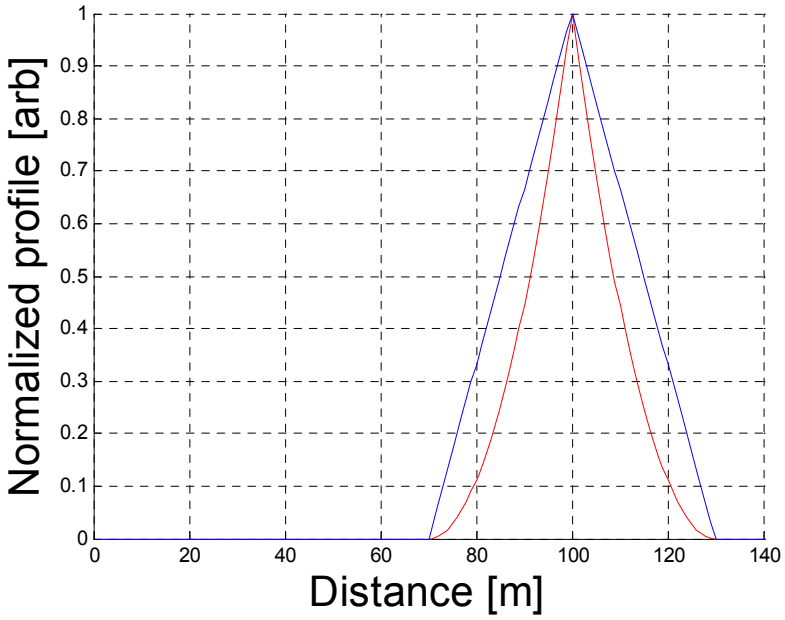

Figure 40 : Normalized RBP (blue) and WPP (red) for a pulsed lidar with $T_{pulse} = T_{sample} = 200$ ns and a range gate centred at 100 m. The range dependent collection efficiency is ignored.

The WPP of a pulsed system can also be measured from a hard target at one fixed location. The WPP is the peak height, instead of the sum, of the velocity spectrum generated from Fourier transforming with a translating window as described earlier for the RBP. A measured WPP of a commercial system is given in Figure 89 in chapter 6.1. As expected it compares well with the measured RBP multiplied with the theoretical correlation duration $\tau(z)$, here the contribution duration, i.e.

$$WPP_{meas}(z) \approx RBP_{meas}(z) \cdot \left(T_{pulse} - \frac{2}{c}|z - g_{center}|\right).$$

2.5.7. Effective sample volume length of focused cw lidars

The contributing volume is theoretically infinitely long for a cw lidar system. The scatter received by a cw lidar during one sample duration has a constant contribution duration, $T_{contribute}(z) = T_{sample}$. The RBP for a focused system is then described by

$$RBP(z) = \int_{T_{sample}} P_{rec}(z)dt = P_{rec}(z)T_{sample}$$

where $P_{rec}(z)$ for focused systems is modeled in chapter 2.4.1.

In a homogeneous atmosphere, i.e. one which does not contain dominating particles, the atmospheric correlation duration, τ_{atmos}, is constant. The correlation duration of the signal is typically limited by τ_{atmos} since cw lidars generally sample for durations which are longer than the correlation duration. The Wind peak profile is thus expressed as

$$WPP(z) = \int_{T_{sample}} P_{rec}(z) \cdot \tau(z)dt = P_{rec}(z) \cdot T_{sample} \cdot \tau_{atmos} = \tau_{atmos} \cdot RBP(z)$$

There is no shape difference between the RBP, the WPP or the collection efficiency function, $F_{collect}(z)$, and any of the descriptions can be used to describe the effective sample length for cw lidars.

The RBP_{FWHM} depends on the focus distance, z_{focus}, and is plotted in Figure 41 for a 1.5 µm lidar with a focal length of 20 cm, a single mode fiber receptor with core radius r_{fiber} = 9 µm and a lens which does not significantly truncate the emitted Gaussian beam.

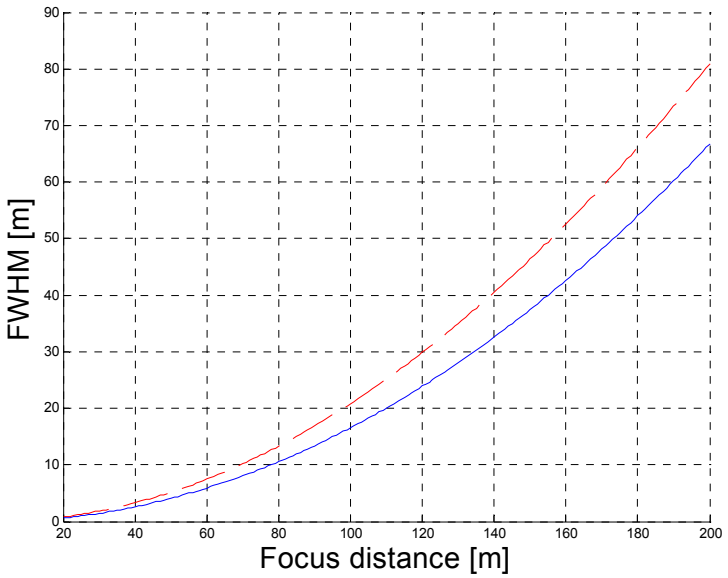

Figure 41 : The RBP_{FWHM} as a function of z_{focus}; blue: model for fiber based lidar, dashed red: Sonnenschein's model[5]. The lidar parameters are f = 20 cm, r_{fiber} = 9 µm, λ = 1.5 µm.

The $RBP_{FWHM}(z_{focus})$ can for many systems be approximated by $\frac{16\lambda z_{focus}^2}{\pi D^2}$, where D is the lens diameter.

2.5.8. Effective sample volume length of range gated focused lidars

Range gated systems can increase the collected energy by focusing the telescope at a distance close to the sensed range gates. If the telescope can reposition the focus it is possible to achieve a tighter confinement at low altitudes by sequentially focusing in the centre of one selected range gate. The RBP of a focused range gated coherent lidar using rectangular pulses to sense a dispersed target can be determined from

$$RBP(z) = \int_{T_{sample}} P_{rec}(z)dt = P_{rec}(z)T_{contribute}(z) = P_{rec}(z)\left(T_{pulse} - \frac{2}{c}|z - g_{center}|\right) \text{ when } z \in \text{range gate}$$

$RBP(z) = 0$ when $z \notin$ range gate

where $P_{rec}(z)$ for focused system is modeled in chapter 2.4.1.

The WPP is given as

$$WPP(z) = \int_{T_{sample}} P_{rec}(z) \cdot \tau(z)dt = P_{rec}(z)T^2_{contribution}(z) = P_{rec}(z)\left(T_{pulse} - \frac{2}{c}|z - g_{center}|\right)^2$$

when $z \in$ range gate and $WPP(z) = 0$ when $z \notin$ range gate.

The ability to increase the received scatter and to tighten the confinement is exemplified by a pulsed lidar focusing on the center of a range gate at 130 m altitude, corresponding to a distance of 150 m for a 30 ° cone angle. The collection efficiency has been modeled according to chapter 2.4.1. The RBP and WPP of this system can be seen in Figure 42 in red and blue respectively. The confinement profile of the corresponding cw system is also included in green dashed. The system and atmospheric parameters can be found in Table 7, the atmospheric correlation duration is assumed to be longer than T_{pulse}.

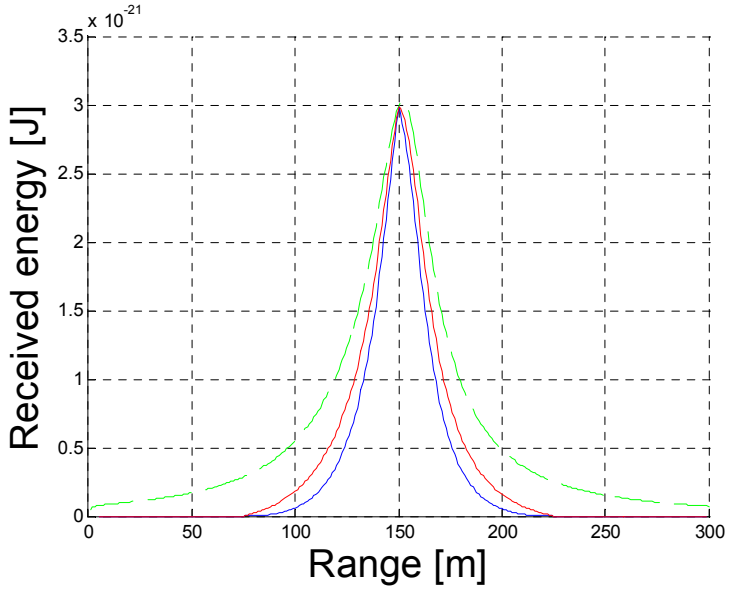

Figure 42 : Confinement profiles for a pulsed and cw lidar. RBP in red and WPP in blue for the pulsed lidar and RBP in green dashed for the corresponding cw lidar. All profiles are normalized to the maximal received energy.

Pulsed lidar parameter	Symbol	Value
Rectangular pulse duration	T_{pulse}	500 ns
Sample duration	T_{sample}	500 ns
Loss factors	η_{rec}, η_{coll} and η_{trans}	1
Emitted power	P	1 W
Backscatter coefficient	β	10^{-7} $m^{-1}sr^{-1}$
Extinction coefficient	α	10^{-5} m^{-1}
Effective receiver aperture	A_{rec}	14 cm^2, (radius 2.12 cm)
Center of range gate	g_{center}	150 m (130 m altitude)
Focus distance	z_{focus}	150 m (130 m altitude)

Table 7 : Parameters for the example lidar system.

The effective sample volume length RBP_{FWHM} = WPP_{FWHM} = 39 m for the cw configuration while RBP_{FWHM} = 29 m and WPP_{FWHM} = 23 m for the pulsed configuration.

In another example three range gates, centered at 80, 100 and 120 m altitude, corresponding to 92, 115 and 139 m distance, are sensed with a fixed focus at z_{focus} = 115 m and with T_{pulse} = T_{sample} = 200 ns. The WPPs for each rang gate are plotted in Figure 43. The lidar has unaltered parameters from the previous example except for the focus and the pulse and sample durations.

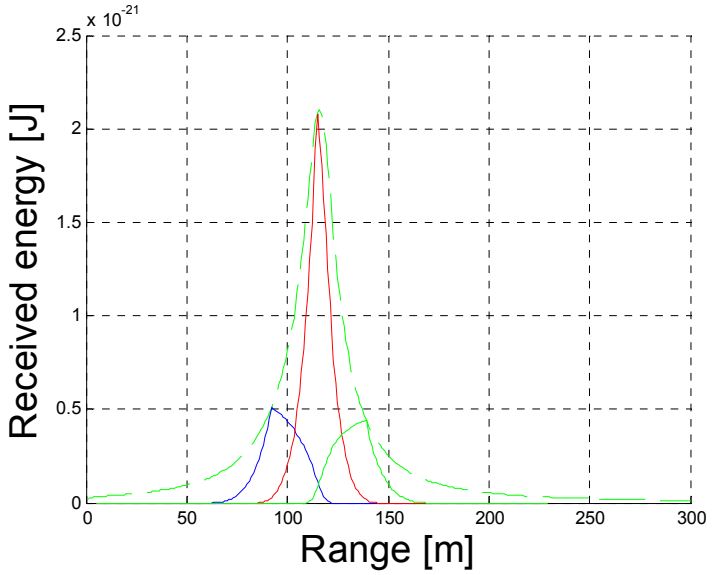

Figure 43 : The WPP for three range gates of a pulsed lidar with range gate centers at 92 (blue), 115 (red) and 139 m (green). The confinement profile of the corresponding cw lidar is outlaid in green dashed.

Note that the two range gate shapes on either side of the focus distance are skewed and that the most significant wind speed in the wind distribution spectrum might not correspond to the wind at the center of these range gates.

The range dependent collection efficiency, A_{rec}/z^2, could be expected to have a strong impact on the range gate shape even for collimated systems when sensing with relatively long pulses at short distances, see Figure 44.

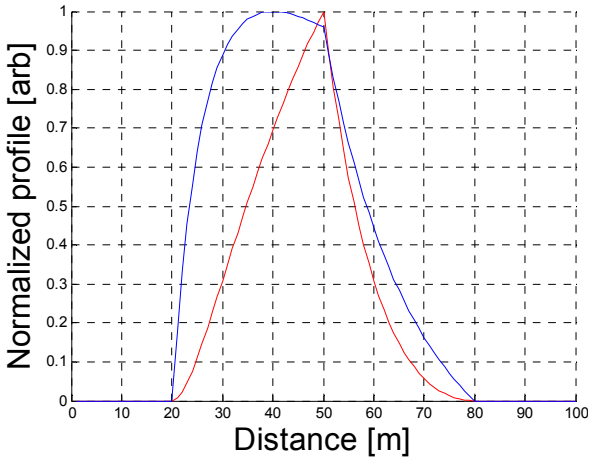

Figure 44 : The normalized RBP (blue) and WPP (red) of a pulsed collimated system with a range gate center at 50 m using 200 ns pulses.

However, as predicted by the model of the collection efficiency function in chapter 2.4, it is likely that the received scatter as a function of range is badly described by A_{rec}/z^2 when the sensing distance is short. In general will the collection efficiency function be relatively flat at close range and the WPP and RBP unskewed.

2.5.9. Confinement of commercial systems.

It is common practice to give the effective sample volume length in the altitude direction since it is postulated, for the 3D wind construction from conic scanning, that the wind is horizontally laminar. The effective sample volume length is then given as the FWHM of the confinement profile multiplied by the cosine of the cone angle. For example, if the lidar senses with a 30 ° cone angle and has a WPP_{FWHM} of 30 m then the effective sample volume length would be given as $\cos(30)*WPP_{FWHM}$ = 26 m.

The effective sample volume lengths of the commercial lidars are compared in Table 8. The range gated Windcube is focused at a fixed distance to increase the received scatter. The RBP_{FWHM} and the WPP_{FWHM} therefore vary with the sensing range.

System	**Pulse length [µs]**	**RBP_{FWHM} [m]**	**WPP_{FWHM} [m]**
Zephir	cw	See Figure 41	See Figure 41
Windcube	0.2	≤ 30 varies with range and focus	≤ 18 varies with range and focus
WindTracer	0.4	60	36
Mitsubishi	0.6	90	54

Table 8 : Comparison of effective sample volume lengths of commercial lidars.

The WPP is likely to give the better description of the sample volume for a fair comparison between cw and pulsed lidars. The break even altitude for the WPP_{FWHM} is around 100, 150 and 180 m for the cw Zephir, modelled according to chapter 2.4.1, compared to the Windcube, WindTracer and Mitsubishi lidar respectively.

2.5.10. Scanned perimeter

In addition to the accumulation of scatter from a sample volume length, a lidar system will construct a three dimensional wind velocity vector from at least 3 LOS measurements typically obtained from a conic scan. This 3D wind construction relies on a uniform wind flow over the scanned perimeter. For successful reconstruction it is stipulated that the wind flow is horizontally laminar in the scanning path. It is therefore important to know the perimeter scanned for the 3D wind construction. For a conically scanned systems this corresponds to a circle with a circumference of $2\pi h \cdot \tan(\theta)$, where h is the altitude of the centre of the sensing volume, and θ is the cone angle.

An error in the cone angle will introduce a proportional error in wind velocity. The cone angle error should not exceed 0.2 ° for a 30 ° configuration or 0.1 ° for a 15 ° configuration to ensure a velocity accuracy of 0.1 m/s for wind velocities of 20 m/s. A cone angle error will also introduce errors on the intended sensing altitude.

2.6. Coherent lidar figure of merit

Coherent lidar systems are complex and exist in many configurations. Figure Of Merits (FOMs), which give simplified descriptions of a lidar's LOS wind speed accuracy, allow for easy comparisons between different systems and methods. The FOM described in this chapter does not consider effective sample volume lengths or ambiguities and should be treated with care for extreme pulse lengths and PRF.

An occasionally quoted FOM[27] for pulsed lidars is given by

$$FOM = D^2 \cdot E \cdot \sqrt{PRF}$$

where E is the pulse energy, PRF the pulse repetition frequency and D the system aperture diameter.

This FOM is approximately inversely proportional to the standard deviation of the LOS wind speed of a well designed pulsed system which senses during a fixed observation period with moderate pulse energies and pulse repetition frequencies so that the CNR is limited and the speckle not fully developed. The FOM is based on the broadband definition of CNR, i.e. it does not take into account the correlation duration dependent spread of the received energy in the Fourier transformation.

A better figure of merit is not only based on the received energy but also takes into account the signal bandwidth. Pulsed systems with typical range resolution will have a signal bandwidth limited by the correlated signal duration and not by the turbulence in the sample volume.

A suggestion for a figure of merit which takes into account the narrowband CNR is

$$FOM = \tau \cdot D^2 \cdot E \cdot \sqrt{PRF}$$

where τ is the longest correlation duration of the frequency components in the heterodyne current.

The correlation duration will typically be limited by the pulse duration, T_{pulse}, for pulsed system while it will be limited by the atmospheric correlation duration, $\tau_{atmos} \approx 1$ μs, for cw systems.

By considering the correlated scatter duration it is also possible to express the FOM of a cw system in similar terms. The PRF is replaced by $1/\tau_{atmos}$ since it describes the number of uncorrelated speckle takes detected during the observation period. A suggestion for a narrowband figure of merit for a cw system could be

$$FOM_{cw} = \tau_{atmos} \cdot D^2 \cdot P \cdot \sqrt{\frac{1}{\tau_{atmos}} \frac{2}{c}} = D^2 \cdot P \cdot \sqrt{\tau_{atmos}}$$

where P is the average power and the 2/c term normalizes the FOM_{cw} with the FOM of pulsed systems.
T_{pusle} is the longest correlated duration in a range gated system but much of the received energy will have significantly shorter correlation duration. The narrowband CNR and the FOM would ideally also take into account this factor but it was chosen to leave such a factor out since it would depend on for example pulse shape.

The FOM taking into account the narrowband CNR gives a better comparison between pulsed and cw systems. Both FOMs have been calculated for the available commercial systems and are listed in Table 9.

System	T_{pulse} [μs]	E [μJ]	D [cm]	PRF [kHz]	Broadband FOM	Narrowband FOM
Zephir	cw	1 W cw	4.4	cw	N.A.	2 μ
Windcube	0.2	10	3	10	1	0.2 μ
WindTracer	0.4	2000	12.7	0.5	720	290 μ
Mitsubishi Wind Lidar	0.6	6.5	5	1	0.5	0.3 μ

Table 9 : Figure of merit for commercial systems the D is taken in m, E in μJ and PRF in Hz.

2.7. Conclusions on coherent lidar

Signal modeling of coherent lidars is important for predictions of the lidar performance and for optimizing the signal processing. In this chapter the construction of the coherent lidar signal was described from the heterodyne current generation and the lidar equation for systems sensing dispersed targets. The temporal and spatial collection of scatter, which is a fundamental concept for proper understanding of lidars, was illustrated. The standard signal model was expanded upon by considering the range dependent correlated contribution duration in a range gate which significantly affects the narrowband signal to noise description and the weighting of the sample volume.

The standard deviation in the wind measurement as a function of pulse energy and PRF has been discussed. Figure of merits for coherent lidars are refined and a definition of the weighting function of the sample volume was proposed.

The range dependent collection efficiency obtained by focused fiber based lidars was modeled by considering the effects of a small aperture size and co-propagation of received scatter and local oscillator. The result of a first verification of the collection efficiency function show that the developed model is appropriate.

3. Frequency modulated coherent lidars

This chapter discusses frequency modulated coherent lidar systems for wind sensing. The chapter includes the motivation for frequency modulation and reviews previously proposed frequency modulated systems. The Frequency Stepped Pulse Train (FSPT) modulation method is described in detail. This method has been developed in this thesis and was submitted for patenting in late 2006[4].

The major concern, considering market growth at this point, is probably price, "plug and play"-ability and to build confidence with users, to which frequency modulation will not offer assistance. However, emerging markets, such as wind sensing in airports, will put higher demands on performance and in a future scenario, with increased competition from pulsed systems, frequency modulation might prove to be a cost attractive alternative to strong amplifiers.

Early lidar systems were based on high peak power lasers, like gas or solid state lasers. Increased use of fiber lasers in the lidar field has been predicted[1] as they are relatively cheap and robust, in comparison to gas or YAG lasers, but still emit a highly coherent radiation at the most eye safe wavelengths.

Most development efforts for fiber based lidars are focused on enhancing the emitted pulse power. Recently several improvements in Q-switched large core fiber lasers have increased the available peak power. A transmitter unit based on an external cavity semiconductor laser amplified by a 20 μm core EDFA suitable for coherent lidar applications has achieved pulse energies of 50 μJ at 30 kHz[31]. Another transmitter proposed for coherent lidar use gave pulse energies of 290 μJ at 4 kHz from an external cavity semiconductor laser amplified by a 50 μm core EDFA[32]. However, the power from fiber lasers is inherently limited due to difficulties to store pump energy in the fiber. The amplifier is already today the single most expensive component in a fiber based coherent lidar. Lidar systems should be cheap, reliable and able to operate without eye-safety restrictions for non-scientific applications.

Stimulated Brillouin Scattering is the dominating limiting pulse energy factor for fiber based systems restraining a systems peak power to 10-15 W in standard single mode fiber[29]. However, SBS can be reduced by using short crystal fibers with large cores. Thus fiber lasers will have difficulties in producing suitable pulses with energies exceeding more than some mJ, although such peak powers can readily be produced with Q-switched YAG or gas lasers.

Other limiting factors are Self-Phase Modulation (SPM), a non-linear effect which induces a chirp on the transmitted pulse, and Stimulated Raman Scattering (SRS), which causes noise in the signal bandwidth when high peak power propagates through optic fiber.

On the other hand, the standard deviation of the wind measurement is also improved by a large number of accumulated samples. However, the observation duration is normally limited since most systems need a high acquisition rate, for example, in order to ensure a uniform wind over the scanning perimeter. High acquisition rates are also important for applications in which the response time is limited. An additional advantage of high PRF lidars is that they can emit higher average powers than high

peak power systems, whilst remaining eye-safe since scanning will distribute the average power over a wider area.

On a technological level it is likely that amplifier dynamics are less severe when the EDFA is stimulated continuously or at high frequency. The pump to emitted average power conversion is more efficient in continuously stimulated systems since the depletion of stored energy by unwanted amplified spontaneous emission is minimized.

Different frequency modulation schemes have, for more than fifty years, been used to increase the effective PRF of radar systems. However, most of them are suited for single hard targets, e.g. vehicles, and not for dispersed targets, such as the atmosphere.

3.1. Previously proposed frequency modulated lidars for wind sensing

3.1.1. Frequency chirped coherent lidar

Methods for increasing the duty cycle of radars sensing single hard targets without introducing range ambiguities have traditionally been based on linear saw tooth modulation in frequency chirping Doppler radars[46].

A Doppler radar emits a linear saw tooth frequency modulation with alternating slopes $\pm\frac{df}{dt}$, as in Figure 45. The frequency of the received backscattered wave will lag behind the frequency of the emitted wave proportionally to the propagation duration. The beat current, generated by mixing the received scatter from a non-moving hard target with a reference copy of the emitted wave, will have a frequency f_b according to

$$f_b = \frac{df}{dt} \cdot \frac{2R}{c}$$

from which the range to target, R, can be deduced.

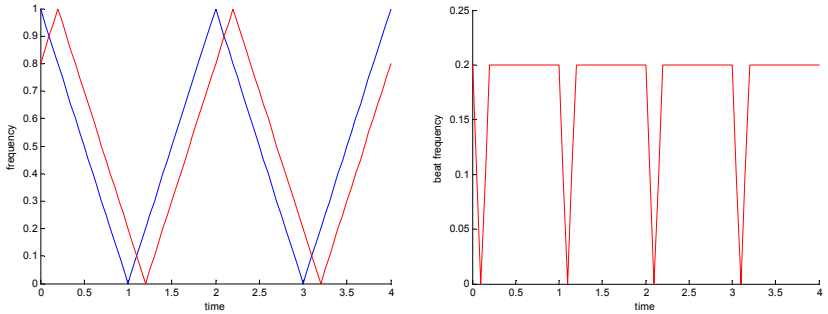

Figure 45 : Emitted (red) and received (blue) frequency as a function of time when the wave is scattered off a single non-moving target (left). The frequency of the beat current as a function of time (right).

If the target is moving the received frequency will also be shifted from the reference frequency by the Doppler shift as can be seen in Figure 46. The linear chirp gives a range-Doppler ambiguity for the moving target, which for a single moving target is resolved by the saw-tooth modulation. The beat frequency will alternate between $f_{b1} = f_r + f_d$ and $f_{b2} = f_r - f_d$, where f_r is the frequency change due to propagation lag and $f_{Doppler}$ is the Doppler shift induced by the moving target. The range and the Doppler shift can be solved accordingly

$$R = \frac{c \cdot f_r}{2\frac{df}{dt}} = \frac{c \cdot f_{b1} + f_{b2}}{4\frac{df}{dt}}$$

$$f_{Doppler} = \frac{f_{b1} - f_{b2}}{2}.$$

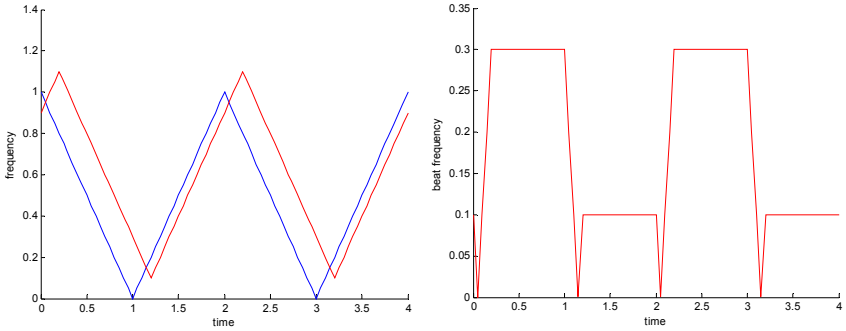

Figure 46 : Emitted (red) and received (blue) frequency as a function of time when the wave is scattered off a single moving target (left). Frequency of the beat current as a function of time (right).

However, a linear saw tooth modulation will give irresolvable range-Doppler ambiguities when sensing wind in the atmosphere where the range resolved frequency shift from a dispersed target is sought. Consider the case where a lidar senses N weakly reflecting moving targets at different ranges. These targets will give rise to 2N frequencies. An example of the generated beat frequencies from the scatter from three weakly reflecting moving targets is given in Figure 47. However, since it is not possible to determine which of the 2N frequencies that are coupled, i.e. the $f_{r,i}$ and $f_{Doppler,i}$, it is not possible to solve the equation system. Saw tooth chirped modulation is therefore unsuitable for range resolved velocity sensing of dispersed moving targets, such as the atmosphere, since it introduces irresolvable range-Doppler ambiguities.

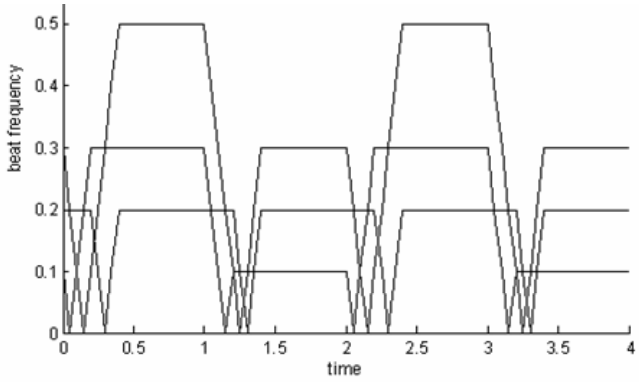

Figure 47 : Beat frequencies generated from the scatter of three weakly reflecting moving targets.

Frequency chirping has been used in lidar for various applications[2]. However, range resolved wind velocity can only be obtained if the beam volume contains a single dominating particle and thus only at that particle's random altitude and not at a specific altitude. Singly dominating particles are not judged to be available frequently enough to give wind measurement with sufficient coverage.

3.1.2. Randomly modulated or low coherent lasers

As an alternative to the method described above it has been proposed to use a limited coherence to confine a contributing range[3, 47]. It is similar in concept to optical coherence tomography and utilizes the inherent fast frequency drift of an unstabilized laser diode, e.g. with a 1.4 MHz FWHM linewidth. Scatter generated by this relatively low coherent cw beam is heterodyned with a delayed part of the transmitted beam, e.g. propagated through a length of optic fiber of optic path L. Scatter generated closely around the delay distance, typically defined as the coherence length, will

constructively contribute to a frequency peak corresponding to the wind from that range. Backscatter from other distances will mix incoherently and can, in a simplified manner, be described as white noise, which constitutes a severe drawback of this method. Other drawbacks are that the system would need one delay line for each sensed altitude and would have to be polarization maintaining since the LO would have a separate path.

A similar approach would be to randomly modulate the frequency of a very coherent source, e.g. by vibrating a fiber laser. The coherence length will be very short at the same time as the instantaneous linewidth will be extremely narrow giving rise to a high narrowband CNR.

To illustrate the method consider a randomly frequency modulated cw system with the LO passing through a delay fiber L. The backscattered frequency, f(x,t), from a distance x at time t can be expressed as

$$f(x,t) = f_{LO}\left(t + \frac{L}{c} - \frac{2x}{c}\right) + f_{Doppler}(x).$$

The generated beat frequency from the scatter originating from $x \neq L$ can, in a simplified manner, be described as randomly distributed around $f_{Doppler}(x)$. The backscatter from x = L/2 will have a synchronized frequency with the LO, i.e.

$$f\left(\frac{L}{2}, t\right) = f_{LO}(t) + f_{Doppler}\left(\frac{L}{2}\right).$$

Integrated over time the Doppler shift grows over a noise of random frequencies, for example as in the simulated signal spectrum in Figure 48 where the frequency modulation was generated by discretely picking frequencies from a uniform distribution.

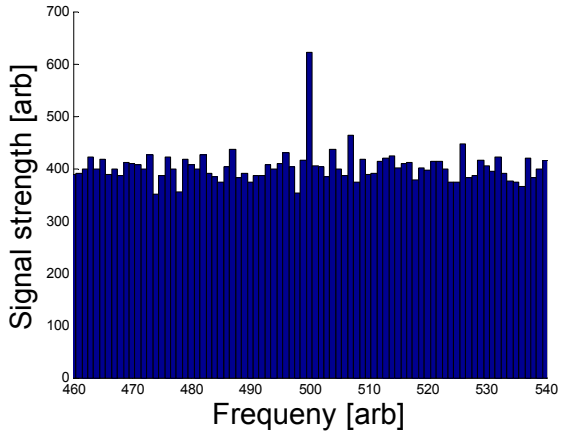

Figure 48 : Simulated signal spectrum generated by a randomly frequency modulated lidar with a Doppler frequency corresponding to 500 at L/2.

The advantage of such systems is that the effective sample volume is independent of both sample duration and range. The temporal correlation of the signal can therefore

ideally be set to the same value as the atmospheric correlation duration. The figure of merit for this system can thus be described as

$$FOM = \tau \cdot D^2 \cdot E \cdot \sqrt{PRF} = \tau^{1.5} \cdot D^2 \cdot P$$

where τ is the correlation duration of the atmosphere and P the average emitted cw power.

3.2. Frequency Stepped Pulse Train Modulated Coherent Lidar

This chapter presents a FM technique, based on equidistantly frequency stepped pulse trains with high PRF and a frequency pursuing LO. This method is appropriate for high duty cycle range resolved coherent lidars sensing of specifically dispersed moving targets. The method has similarities with linear chirp modulation[46], which is commonly used for ranging and velocity sensing of single targets by radar, both in practice and purpose. However, instead of using continuous chirping, the frequency of short pulses is consecutively stepped to discrete levels. The term 'single frequency lidar' used in this chapter is taken to mean a system wherein the transmitted laser light is centered around a single laser frequency, i.e. not stepped in frequency between consecutive pulses.

As will be explained, FSPT modulation provides unique mapping of the Doppler shifted backscatter from a set of self assembled range cells into allocated distinct frequency slots as long as the pulse-to-pulse frequency step is wider than the expected variations of the Doppler shift. The Doppler frequency, or reflected amplitude, from range cells, can thus be sensed with high acquisition rates while the range-Doppler ambiguities, appearing when dispersed moving targets are sensed with linear chirping, will be resolved and range ambiguities, due to the high PRF, are avoided.

The PRF of a single frequency system limits the maximum sensing distance to $z_{\max} = \frac{c}{2 \cdot PRF}$ in dispersed targets since the return from a newly emitted pulse will hide the contribution of scatter from more distant range gates. A single frequency lidar sensing at 3 km is thus limited to a PRF of 50 kHz. This limitation is circumvented by FSPT modulated lidars.

In addition to high duty cycles, the FSPT modulation has the advantage that it can determine the Doppler shift sign and avoid low frequency RIN even when the LO is generated from a fiber end reflection. This is due to the fact that the Doppler shift in higher order frequency slots will appear in a bandwidth significantly displaced from 0 Hertz.

FSPT modulated lidars could potentially reach the resolution and accuracy of low duty cycle systems based on short high peak power pulses at low PRF. However, the range cell positions will be fixed for a specific train configuration in contrast to the range gates of a time of flight system.

FSPT modulation can also be used in differential absorption lidars since the returned power from a range cell can be found by integrating the energy in the corresponding frequency slot. FSPTs can also provide a pseudo tunable alternative to chirping for high duty cycle sensing of single or non-moving targets when fast and stable broadband chirping is difficult to generate.

An appropriate FSPT generator is presented in chapter 4. Results from a FSPT modulated lidar prototype are presented in chapter 5.

3.2.1. Frequency stepped pulse train

A FSPT modulated lidar emits a train of N_{pulse} pulses. The carrier wave frequency is equidistantly stepped between consecutive pulses with an amount Δf.

The FSPT is furthermore described by the duration of fixed frequency, T_{pulse}, and the duration without emission, T_{inter}. In a preferred embodiment the pulses are emitted without intervals, i.e. $T_{inter} = 0$ s. The train is thus emitting continuously and is only pulsed in the sense that the emitted frequency steps every T_{pulse} according to Figure 49.

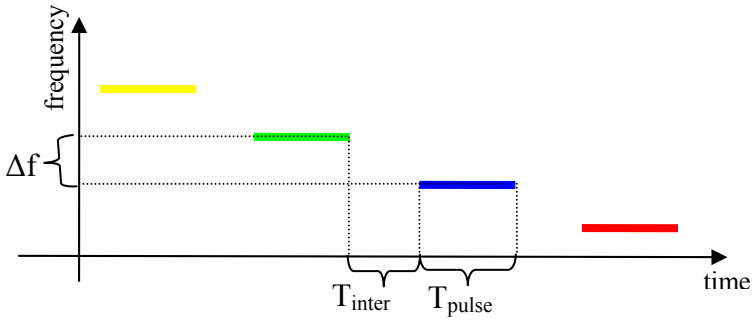

Figure 49 : Representation of a frequency stepped pulse train with a pulse duration, T_{pulse}, an interpulse duration, T_{inter}, and a pulse-to-pulse frequency step, Δf.

The dwell time between two pulse trains has to be large enough not to introduce range ambiguities. However, a new train can start immediately after the first if the system is restarted from a sufficiently offset start frequency or if trains are long enough not to interfere with the previous train. Trains will typically contain more than a hundred frequency stepped pulses in appropriate embodiments and inter-train ambiguities will therefore be unlikely.

Note that the wavelength tuning is sufficiently small to consider standard optic parameters, e.g. reflection factors, coupling fractions and backscatter coefficients, as constant throughout the train. Even tuning over 100 GHz only corresponds to a 0.75 nm shift for a 1.5 µm laser. Nevertheless, frequency stepping ensures that pulse returns will be phase uncorrelated even if the atmosphere can be considered as frozen.

3.2.2. Description of the scatter received from an atmosphere sensed by a FSPT modulated lidar

An FSPT modulated lidar will concurrently receive Doppler shifted and $n \cdot \Delta f$-stepped light scattered from several range sets of the atmosphere. Figure 50 illustrates the scatter distance and frequency of the light received by a FSPT modulated lidar at a time when a pulse of frequency f_α has just left the system.

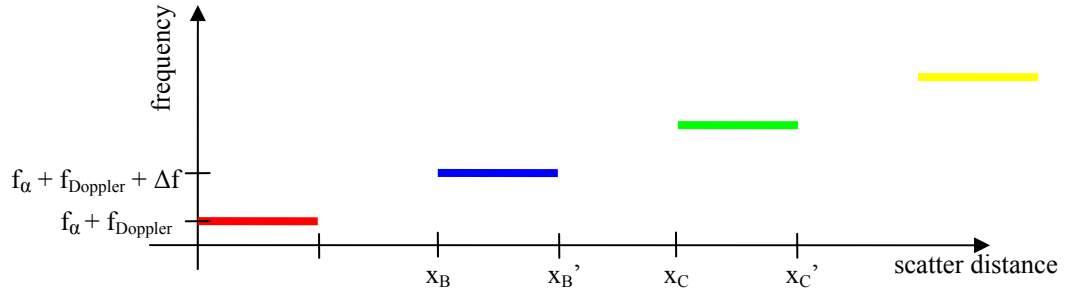

Figure 50 : Diagram showing the frequency, as a function of scattered distance, of light received at t_α by the lidar emitting a train according to Figure 49. Note that $x_A' = (c/2)(T_{pulse})$, $x_B = (c/2)(T_{pulse} + T_{inter})$ and $x_B' = (c/2)(2T_{pulse} + T_{inter})$.

Figure 51 illustrates a time-spatial representation of the scatter received by a FSPT lidar. The colors represent the frequency, $f_x + n\Delta f$, of the generating pulse.

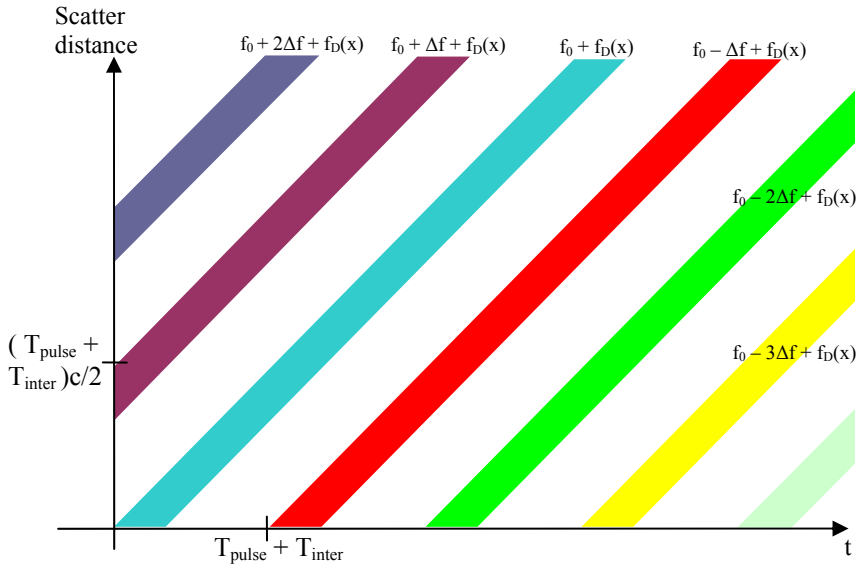

Figure 51 : Time-spatial representation of scatter received by a FSPT modulated lidar. A considerable inter pulse duration is used for clarity.

The range gate signal generated from the return of consecutive frequency stepped pulses is phase uncorrelated since the wavelength has changed from pulse to pulse. The propagation to and back from the target will thus give an effectively random phase to the signal formed from each pulse.

Startup effects will influence the number of contributing pulses. When the n^{th} pulse is emitted there is only backscatter available from the n first range sets since the pulse train only has propagated that far. Trains will typically contain more than a hundred frequency stepped pulses in appropriate embodiments and initial return losses will normally be insignificant.

3.2.3. FSPT lidar set up

This section gives a quick summary, primarily aimed at establishing a system model for a monostatic FSPT modulated lidar. The FSPT in this presentation will be used for generating both backscatter and the pursuing reference LO. In a MOPA set up a separate single frequency cw LO can alternatively be formed and each frequency slot range gated. However, such solutions would have to ensure that the signal stays within the detector bandwidth.

Figure 52 shows a block diagram of a FSPT modulated monostatic coherent lidar in which the LO is generated by splitting out a fraction of the FSPT.

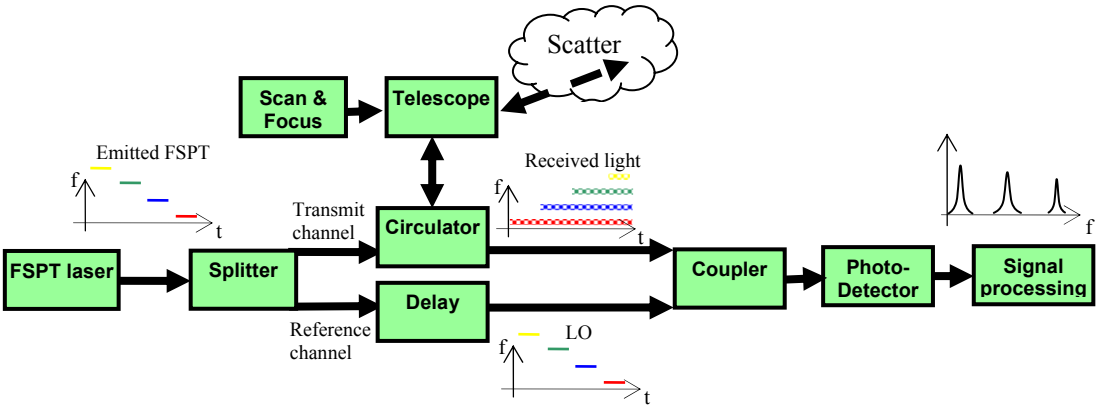

Figure 52 : Diagram of a monostatic FSPT modulated coherent lidar. Inset are, from left to right, the emitted FSPT, the received scatter vs time (top), frequency of LO (bottom), and representation of a set of the wind distribution spectra mapped into the respective frequency slots. Different colors represent Δf-stepped frequencies. The wavy lines represent the Doppler shift spread in the received light.

A laser configuration, e.g. as proposed in chapter 4.2, which emits frequency stepped pulses is coupled to a splitter which splits the beam into a transmit and a reference channel. The LO can optionally be offset in frequency and use a length of fiber with an optical path length delaying the LO with T_{delay}. Undelayed and non-offset systems can advantageously form the LO from a reflection after the circulator instead of using the splitter. The main power passes along the transmit channel through a circulator and enters the atmosphere through a telescope. The Doppler shifted and $n \cdot \Delta f$-stepped backscatter is received by the same telescope and is redirected by the circulator to a coupler where the LO and the received backscatter are mixed on a photodetector, thus generating a beat signal. The generated beat signal is band pass filtered in accordance with the frequency content of interest and amplified by an LNA to give a suitable dynamic range for the digitizer. Triggered sampling during a full LO pulse of duration T_{pulse} gives a sample vector which is Fourier transformed to yield a wind distribution spectrum.

As will be explained, the beat signal will contain a set of well-separated frequency clusters related to the wind in a set of confined ranges. The set of frequency clusters will be uniquely mapped into allocated distinct ranges of frequencies if the frequency step, Δf, is larger than the plausible variations in the Doppler shift. These distinct frequency ranges will be referred to as frequency slots. The spatial range which contributes to a specific frequency slot during a full sampling period will be referred to as a range cell. Each frequency slot will thus contain a spectrum proportional to the

LOS wind speed within the corresponding confined range. It might be useful to split the signal in several channels and filter out each slot separately since noise will be minimized and it will be possible to undersample each channel at a sampling frequency Δf.

A large number of these power spectra are accumulated to yield a smoothened wind distribution spectrum from which the LOS wind speed at a set of altitudes can be estimated. 3D wind velocities at these altitudes can be constructed from at least three LOS estimations obtained either by scanning the lidar[48] or by using multiple transmit-receive paths.

3.2.4. Self-assembled range cells uniquely mapped to allocated frequency slots

This section illustrates and establishes terminology regarding how the backscatter continuously corresponds to the frequency pursuing LO of a FSPT modulated lidar. The self assembled generation of range cells uniquely mapped to allocated frequency slots will be explained.

Start-up effects can be ignored by considering the time, t_α, when several pulses have been emitted and the most recent pulse with frequency f_α has just left the lidar.

Figure 53 illustrates the time-spatial representation of scatter received by a FSPT modulated lidar and how it is related to a frequency pursuing LO delayed with T_{delay}. The frequency of the LO is illustrated by the corresponding color on the lower time axis which is synchronized with the upper axis.

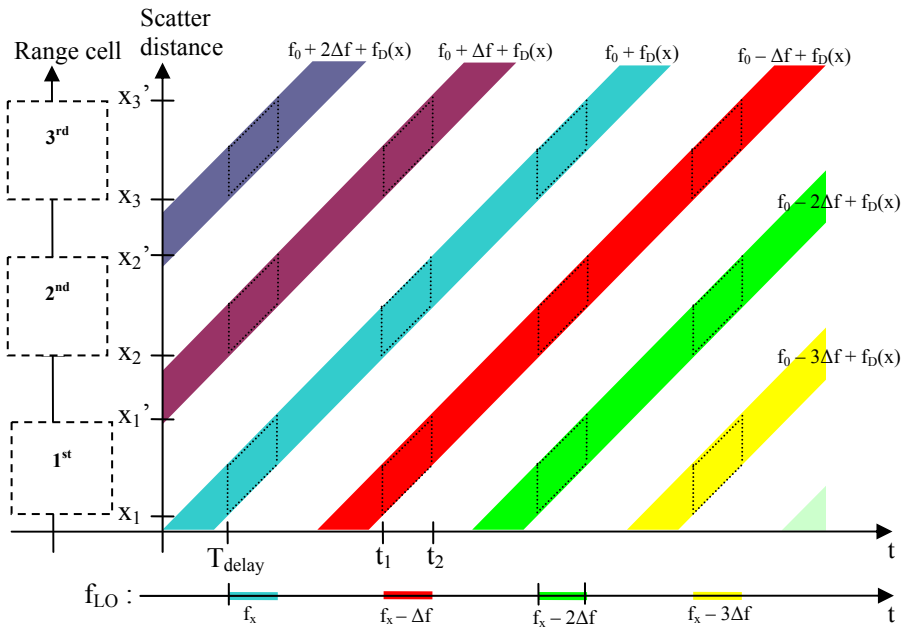

Figure 53 : Time-spatial representation of the relation in frequency between received scatter and a frequency pursuing LO of a FSPT modulated coherent lidar. The LO is delayed by T_{delay} and a considerable inter pulse duration is used for clarity.

Range cells
The LO present during the time t_1 to t_2 will generate a heterodyne spectrum with the scatter originating from position x_1 to x_1', x_2 to x_2' etc. These time-space fields are marked with parallelograms in Figure 53.

The backscatter, originating from aerosols close to the system, in x_1 to x_1', will have a carrier frequency, $f_{scatter}(x_1..x_1')$, which only is shifted from the LO frequency, f_{LO}, with the corresponding Doppler shift $f_{Doppler}(x_1.. x_1')$. When mixed with the LO it will generate a wind velocity related signal in the heterodyne spectrum at

$$f_{scatter}\left(x_1..x_1^{'}\right)-f_{LO}=\left(f_0+n\Delta f+f_{Doppler}\left(x_1..x_1^{'}\right)\right)-\left(f_0+n\Delta f\right)=f_{Doppler}\left(x_1..x_1^{'}\right)$$

where f_0 describes the initial train frequency, n is an integer number describing the LO pulse train position and $f_{Doppler}(x_1..x_1')$ describes the Doppler frequency distribution in x_1 to x_1'.

The scatter received from the same distance during the consecutive pulse, n+1, will keep its relation with the pursuing LO and generate a new speckle take of the wind within x_1 to x_1' at the same position in the spectrum. The scatter originating from x_1 to x_1' can therefore be said to be matched in frequency with the LO and the range will be referred to as the first range cell, differentiated from range gates since they self assemble with centers at specific altitudes for every FSPT parameter set of T_{pulse}, T_{inter} and T_{delay}.

When scatter from particles at x_2 to x_2' reaches the detector, the LO is made up of a pulse which has a Δf-downshifted frequency compared to the pulse that generated that scatter. Scatter from the range x_2 to x_2' will consequently lag behind the LO and be unmatched with Δf. The range x_2 to x_2' will therefore be referred to as the second range cell. This scatter will, during all LO pulses, generate a signal at

$$f_{scatter}\left(x_2..x_2^{'}\right)-f_{LO}=\left(f_0+n\Delta f+f_{Doppler}\left(x_2..x_2^{'}\right)\right)-\left(f_0+(n-1)\Delta f\right)=f_{Doppler}\left(x_2..x_2^{'}\right)+\Delta f$$

where $f_{Doppler}(x_2..x_2')$ describes the Doppler frequency distribution in the second range cell.

Range cell i will extend from x_i to x_i' described from

$$x_i=\left(T_{delay}+(i-2)T_{pulse}+(i-1)T_{inter}\right)\cdot\frac{c}{2}$$

and

$$x_i^{'}=\left(T_{delay}+i\cdot T_{pulse}+(i-1)T_{inter}\right)\cdot\frac{c}{2}=x_i+\frac{cT_{pulse}}{2}$$

Note that the first range cell will be cropped if $T_{delay} < T_{pulse}$ and that neighboring cells will overlap partly if $T_{pulse} > T_{inter}$.

Backscatter from range x_1' to x_2 will arrive when there is no LO present and it will not be sampled. Wind information will not be available from these blank ranges between range cells. However, systems with $T_{inter} < T_{pulse}$, will not have any blank ranges. It is also possible to relocate range cells by changing T_{pulse}, T_{inter} and/or T_{delay}. In this way

it could be possible to get information from partially overlapping range cells simply by changing the pulse durations slightly between consecutive FSPTs. Spectra recorded in milliseconds from partially overlapping range cells can be used to improve the resolution of a measurement or to deduct turbulence in a synthetic aperture scheme.

Distinct frequency windows
The heterodyne signal will thus consist of a set of separated frequency clusters $f_{Doppler}(x_1..x_1')$, $f_{Doppler}(x_2..x_2') + \Delta f$, $f_{Doppler}(x_3..x_3') + 2\Delta f$ ... etc. Assume that the Doppler shift will vary within an anticipated maximum range limited by $\pm f_{Doppler\ max}$. The set of frequencies will then be uniquely mapped into a closed range of frequencies if the frequency step is larger than the plausible variations in Doppler shift, i.e. if the absolute of the frequency step, $|\Delta f|$, is bigger than $2f_{Doppler\ max}$. These closed ranges of frequencies will be referred to as distinct frequency slots. Range cell i will thus generate a wind velocity related signal in frequency slot i extending from f_i to f_i' according to

$$f_i = f_{offset} + \left(i - \frac{3}{2}\right) \cdot \Delta f$$

and

$$f_i' = f_{offset} + \left(i - \frac{1}{2}\right) \cdot \Delta f \cdot$$

Note that the first frequency slot will include velocity ambiguities if $f_{offset} < \Delta f/2$. This ambiguity will reduce to an incapability of telling the sign of the wind velocity in the first range cell when $f_{offset} = 0$.

An example of a set of frequency slots with the response from the first three range cells can be seen in Figure 54.

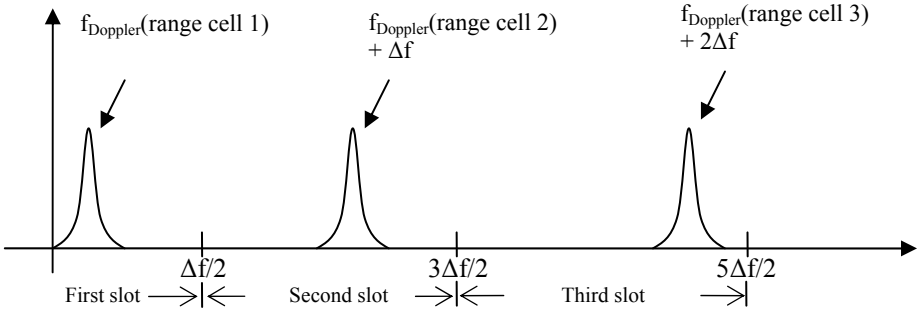

Figure 54 : Illustration of the three first frequency slots with example Doppler spectra responses from the first three range cells.

If the anticipated Doppler shift instead is estimated to vary between $f_{Doppler\ min}$ and $f_{Doppler\ max}$, it is sufficient for Δf to be greater than $f_{Doppler\ max} - f_{Doppler\ min.}$

The wind distribution in each range cell can thus be mapped, continuously and uniquely, into its allocated frequency slot if the frequency step, Δf, is sufficiently long and the train parameters are effectively constant.

The line-of-sight wind speed in range cell i can be found from

$$v_{LOS,i} = \frac{\lambda}{2}\left(f_{center,i} - (i-1)\Delta f\right)$$

where $f_{center,i}$ is the Doppler frequency in frequency slot i estimated to scatter from the center of range cell.

For sensing in the first range cell it is not important that Δf is exact as this scatter will always be compared with a copy of the generated pulse. However, for the other orders it is important that Δf is exact. For a wind speed accuracy of 0.1 m/s Δf has to be more precise than 130 kHz at 1550 nm.

Contribution duration
Scatter distances within a range cell will not contribute with the same amount of energy or correlation duration to the allocated frequency slot, in a similar way as explained in chapter 2.5.6 for range gates. Aerosols in the beginning and the end of a range cell will contribute to the peak for a much shorter time than the aerosols in the middle of the range cell. The duration that aerosols at distance x backscatter a phase coherent signal allocated to frequency slot i, during the LO triggered sample duration T_{pulse}, is denoted $T_{contribute,i}(x)$ and is given from

$$T_{contibute,i}(x) = T_{pulse}\left(1 - \left|\frac{x - c_i}{c_i}\right|\right)\cdot\frac{c}{2} \quad \text{for } x_i < x < x_i'$$

where $c_i = (T_{delay} + (i-1)\cdot T_{pulse} + (i-1)\cdot T_{inter})\cdot c/2$ is the center of range cell i.

Note that aerosols at the edges of a range cell will contribute to two frequency slots for high duty cycle trains with partly overlapping neighboring range cells, i.e. when $T_{pulse} > T_{inter}$.

3.3. Modeling and processing of the FSPT modulated lidar signal

This section treats the sampling and discrete Fourier transformation of the FSPT lidar signal generated from the heterodyne mixing of backscatter from several range cells and the frequency pursuing LO. First, modeling of the lidar signal is described, followed by descriptions of the sampling and Fourier transform procedure. Simulation results of wind distribution spectra from modeled and noise free FSPT lidar signals are included.

3.3.1. The FSPT lidar signal

The FSPT lidar signal current, $i_c(t)$, results from the heterodyne mixing of the current LO with backscatter from several range cells. The received frequencies depend on the scattered distance, due to the frequency step between different range cells, and on the wind distribution within the range cells. This will give rise to a set of broadened Doppler peaks as described in section 3.2.4.

It is reasonable to consider the atmosphere as frozen during T_{pulse} since the correlation duration of the atmosphere is longer than the frequency stepped pulse duration, for normal turbulences and confined volumes.

The first step to a lidar signal model is to describe the backscatter from a single particle during a full LO pulse duration $[t_0,\ t_0+T_{pulse}]$. The received backscattered field, E, from a moving single particle is expressed as

$$E(t) = A\cos\left\{2\pi\left(f_{Doppler} + (i-1)\Delta f + f_0\right)(t-t_0) + \theta_{scatter}\right\} \text{ for } t \in [t_0,\ t_0+T_{pulse}]$$

where
A is the amplitude of the received field, assumed to be constant during $[t_0,\ t_0+T_{pulse}]$
$f_{Doppler}$ is the Doppler frequency of the scatter, assumed to be constant during $[t_0,\ t_0+T_{pulse}]$
f_0 is the base carrier frequency of the transmitter
$\theta_{scatter}$ is the received phase at time t_0
and i is the range cell number in which the particle is confined.

The scatter from this particle is added with the current LO pulse and mixed on a square law detector. The resulting dominating component from the one particle mix can be expressed as

$$i_{one\_particle}(t) = R_{diode} A_{LO} A\cos\left\{2\pi\left(f_{Doppler} + (i-1)\Delta f\right)(t-t_0) + \theta_{mix}\right\}$$

for $t \in [t_0,\ t_0+T_{pulse}]$

where
R_{diode} is the detector responsivity
A_{LO} is the constant amplitude of the LO
and θ_{mix} is the resulting phase of the mixed component at time t_0.

The lidar signal generated from the scatter from range cell *i* is the sum of the individual contributions from particles within the range cell. The frequency components from inter-mixing of scattered fields from different particles can be

ignored since the LO is much stronger than scatter from the particles and the resulting dominating component can be expressed as

$$i_{range\_cell,i}(t) = A_{LO} R_{diode} \sum_{k \in V_i(t)} A_k \cos\left\{2\pi\left(f_{Doppler,k} + (i-1)\Delta f\right)(t - t_0) + \theta_{mix,k}\right\} \quad \text{for} \quad t \in [t_0,$$

$t_0+T_{pulse}]$

where
A_k is the received amplitude of the scattered field from particle k, assumed to be constant during $[t_0, t_0+T_{pulse}]$
$f_{Doppler,k}$ is the Doppler frequency of particle k, spread by turbulence over space but assumed to be constant during $[t_0, t_0+T_{pulse}]$
$\theta_{mix,k}$ is the resulting phase of the mixed component from particle k at time t_0
and the sum is taken for the contributions of all particles within the concurrently contributing volume $V_i(t)$ stretching from $x_{start,i}(t)$ to $x_{stop,i}(t)$ at t where

$$x_{start,i}(t) = \left(T_{delay} + (i-2)T_{pulse} + (i-1)T_{inter} + t - t_0\right) \cdot \frac{c}{2} \text{ and } x_{stop,i}(t) = x_{start,i}(t) + T_{pulse} \cdot \frac{c}{2}.$$

Note that the concurrently contributing volume moves with time.

The total lidar signal can finally be modeled as the sum of the contributing range cells i.

$$i(t) = A_{LO} R_{diode} \sum_i \sum_{k \in V_i(t)} A_k \cos\left\{2\pi\left(f_{Doppler,k} + (i-1)\Delta f\right)(t - t_0) + \theta_{mix,k}\right\}$$

for $t \in [t_0, t_0+T_{pulse}]$

Note that the first range cell is cropped if L_{delay}/c is shorter than T_{pulse}.

In order to perform simulations the range cells are divided into elements according to Figure 55. To represent the random distribution of aerosols and turbulence each element scatters a wave with individual amplitude, Doppler shift and phase from a uniform distribution. The parameters of each element will not change along the time axis as the atmosphere is assumed frozen during $[t_0, t_0+T_{pulse}]$. However, the lidar signal obtained from consecutive returns will be uncorrelated even if the atmosphere can be considered as frozen since it is sensed with a shifted frequency.

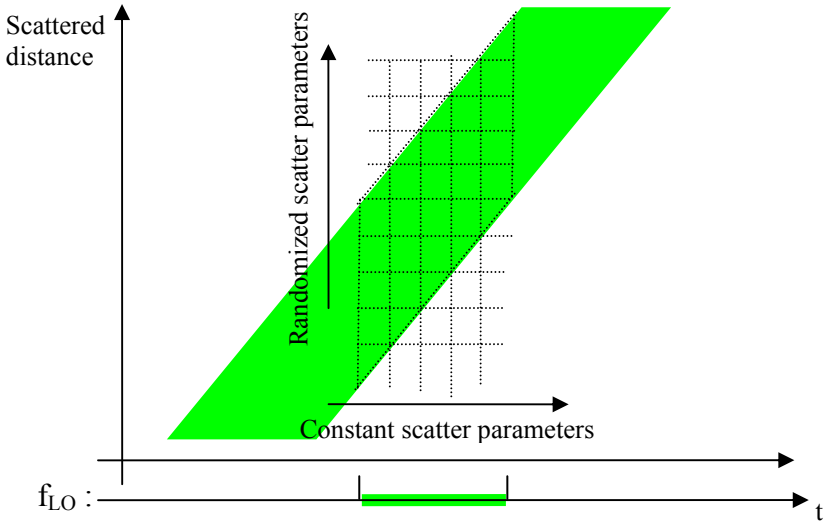

Figure 55 : A time-spatial representation of the range cell parallelogram during T_{pulse}. The range cell is divided into finite elements in order to perform simulations.

For time periods when the LO is not present on the photodetector a weak signal dominated by receiver noise is seen. This signal is not recorded by a FSPT lidar.

Figure 56 shows a simulation of the heterodyne current, $i_c(t)$, resulting from the received backscatter from five range cells during three LO pulses. The correlation-time of the atmosphere was considered to be longer than T_{pulse}. Scatter parameters in an element were thus constant over time. The simulation parameters can be found in Table 10. In the simulation the received power from different range cells was, on average, assumed to be equal.

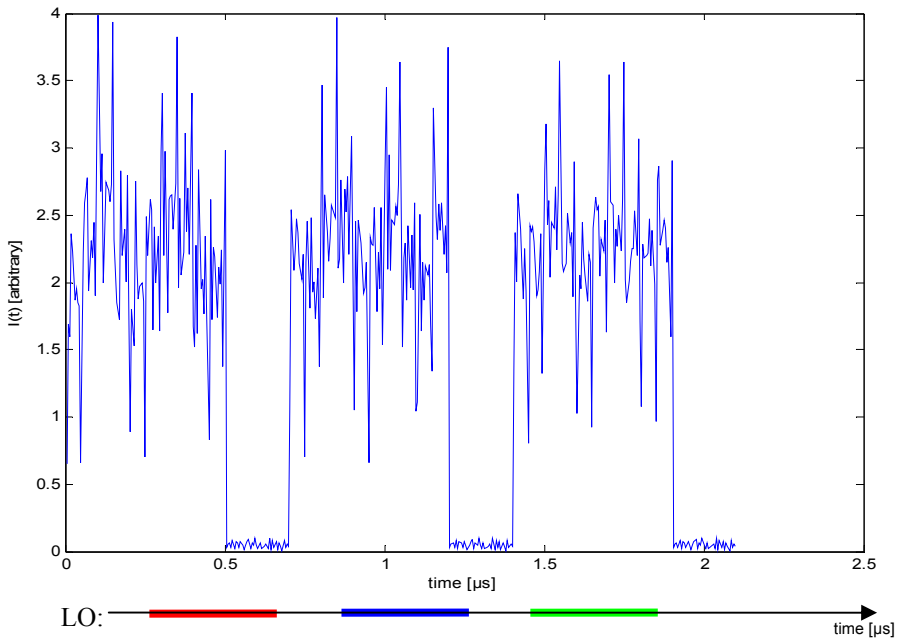

Figure 56 : Example of the heterodyne signal generated from the received scatter from five range cells during three LO pulses. Matching with the frequency pursuing LO is illustrated by the inset LO axis. The simulation parameters are found in Table 10.

Symbol	Parameter	Value
T_{pulse}	Pulse duration	500 ns rectangular shape
T_{inter}	Inter pulse duration	200 ns
Δf	Frequency step between consecutive pulses	20 MHz
$f_{Doppler}$	Average Doppler shift	8 MHz
$\Delta f_{Doppler,k}$	Random Doppler spread to scatter from element k	Uniformly distributed [0,0.5] MHz
A_k	Random amplitude of scatter received from element k	Uniformly distributed [0,1] arb.
θ_{mix}	Random phase of signal from element k	Uniformly distributed [0,2π]
N_{max}	Number of contributing range cells	5
$N_{elements}$	Number of elements in each range cell	200 (20 x 10)
f_s	Sampling frequency	200 MHz

Table 10 : Parameters used for the lidar signal simulation.

The generated wind distribution spectrum during a pulse will have a statistically distributed peak Doppler frequency in each frequency slot due to the randomized distribution of aerosols. Several uncorrelated returns have to be averaged to find the significant Doppler frequency scattered from the center of the range cell. Speckle averaging will be faster with FSPT than for single frequency systems as consecutive pulse returns are uncorrelated and the PRF is high.

3.3.2. Sampling the FSPT lidar signal

Sampling of the lidar signal is easily triggered so that it is exclusively sampled when the LO is present. The sampling frequency, f_s, should, according to the Nyquist theorem, be at least twice the maximum frequency component of the signal, $f_{max,}$ if aliases are to be avoided. The maximum frequency component depends on the number of contributing range cells, N_{max}, limited by range loss, filtering and/or train length, as

$$f_{max} = \frac{\Delta f\left(2N_{max} - 1\right)}{2}$$

The necessary sampling frequency f_s is consequently

$$f_s > \Delta f\left(2N_{max} - 1\right)$$

However, in the case of a system with $f_{offset} = 0$, receiving Doppler frequencies varying from 0 to $f_{Doppler\ max} < \Delta f/2$, the frequency components from range cell *i* are enclosed in frequency slot *i*, stretching from $\Delta f(i\text{-}3/2)$ to $\Delta f(i\text{-}1/2)$. Note that the first frequency slot is an exception and stretches from 0 to $\Delta f/2$. Suitable bandpass filters of width Δf can thus single out the contribution from each range cell. To reduce the demands on the digitizer and data storage it is then possible to undersample the filtered frequency slot. It is sufficient to sample at $f_s = \Delta f$ to retrieve the Doppler frequency. The signal frequency from range cell *i*, $\Delta f(i\text{-}1) + f_{Doppler}$, will instead be represented by its alias at $f_{Doppler}$. The signal information has thus moved from the high bandwidth $[\Delta f(2(i\text{-}1)\text{-}1)/2, \Delta f(2i\text{-}1)/2]$ to the low bandwidth $[0, f_{Doppler}]$ without loss of information of the Doppler frequency.

3.3.3. Fourier transforming the FSPT lidar signal

The sampled vector of the heterodyne current from pulse j, $I_j(n)$, is discrete Fourier transformed to give a speckle take of the wind distributions in the range cells in the corresponding frequency slots. The magnitude of each Fourier element is summed over all accumulated pulses to yield the smoothened power spectrum

$$\hat{I}^2(k) = \sum_j | \mathrm{DFT}[I_j(n)] |^2.$$

A simulated power spectrum accumulated from 100 pulses of a heterodyne signal, such as that in Figure 56, generated from the finite element model with parameters according to Table 10, can be seen in Figure 57. The signal is noise free except for the randomization in time and space of the target parameters. In order to show all Doppler peaks in the same graph only the DC component was filtered and sampling was done at f_s = 200 MHz.

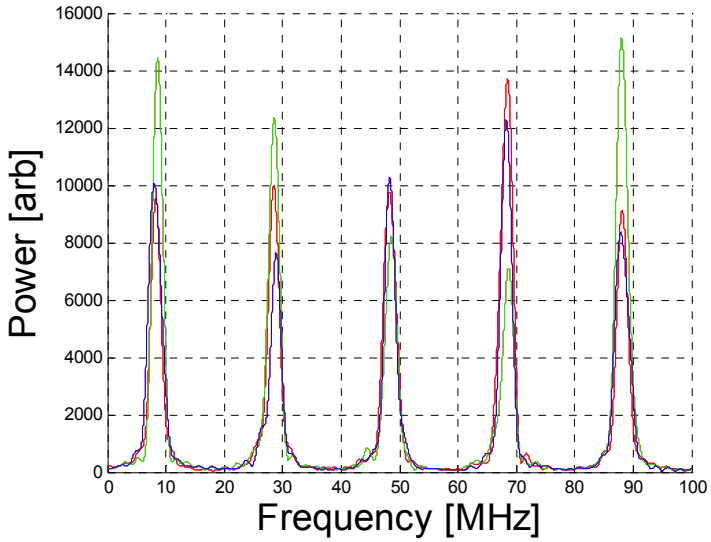

Figure 57 : Plot of three simulated noise free power spectra with signal parameters according to Table 10. The spectra are accumulated during 100 pulses each. The importance of the accumulation of the spectra obtained from a large number of pulses can, for example, be seen in the third frequency slot where the Doppler peak is expected at 48.25 MHz but the three simulations give it at 48.3, 48.2 and 48.6 MHz.

It is possible in coherent detection to make a Fourier transform over zero padded pulses to get improved resolution in the wind spectrum. For a FSPT modulated lidar it is natural to concatenate several sample vectors and in this way improve the frequency resolution whilst keeping the number of operations minimal.

This simulation tool can be used to study the imaging of wind distributions and the accuracy of estimators e.g. during different wind profiles and WPPs.

3.4. Performance considerations of FSPT modulated lidars

This section gives guidelines regarding the selection of the pulse train parameters and their implications on system performance. Figures of merit for the FSPT modulation concept are compared to those of corresponding pulsed and cw systems.

3.4.1. Specifications of the FSPT parameters

The demands on T_{pulse}, T_{inter}, average laser power, Δf, etc depend on the actual application and lidar configuration. However, some general guidelines are given in this section.

The pulse duration, T_{pulse}, should preferably be short, e.g. < 1 μs, for any pulsed remote sensing systems in order to obtain a WPP which falls off quickly around the range cell center so that the wind in the center of the range gate can be estimated with high accuracy. However, the width of the Doppler peak in the DFT spectrum is inversely proportional to the pulse duration. The DFT spectra will be significantly smeared and limit the accuracy in velocity if T_{pulse} is too short, e.g. < 100 ns. However, T_{pulse} can be set just higher than the average atmospheric correlation duration when the confinement is dominated by focusing, e.g. up to 3 μs. This ensures isolation from cloud reflections at a minimum altitude of about 500 m for a system which is delayed so that the first range cell center is at 150 m and has a 30° tilt.

A FSPT modulated system avoids range ambiguities regardless of the inter pulse duration. T_{inter} can thus be short in order to limit, or even avoid, blank ranges and to increase the duty cycle so that low peak power can be emitted. A FSPT lidar would preferably emit continuously. The PRF would then be in the order of 0.3 - 5 MHz, yet, it will not cause range ambiguities or limit the sensing range.

Any lidar system designed to measure frequency with high accuracy has to use highly coherent lasers. The velocity is obtained from the Doppler shift, using $v_{LOS} = \frac{\lambda \cdot f_{Doppler}}{2}$. The laser linewidth should not drift more than 130 kHz during the propagation time difference between the LO and the back and forth propagation of the pulse, if the velocity accuracy of a 1.5 μm system should be better than ± 0.1 m/s.

The FSPT method puts a further demand on frequency accuracy when sensing the velocity in several range cells. The pulse-to-pulse frequency step, Δf, has to be accurate, as the velocity in range cell i is taken from $(i\text{-}1)\cdot\Delta f + f_{Doppler}$. The frequency difference, $i\cdot\Delta f$, between the frequency pursuing LO and the pulses which generate scatter from range cell i must be accurate to ± 130 kHz on average if the velocity accuracy for a 1.5 μm system should be better than 0.1 m/s. Note that the spectrum in the first frequency slot is obtained by mixing the backscattered signal from the first range cell with the LO, both originating from the same pulse. Thus it is not crucial that the frequency step is accurate when sensing is exclusively done in the first range cell. The FSPT coherence requirements are relaxed for coherent DIAL measurements where the backscattered energy within a range cell, and not the Doppler frequencies, is measured with high accuracy.

The pulse-to-pulse frequency step, Δf, has to be sufficiently large to avoid ambiguities from Doppler shifts intruding into neighboring frequency windows. Low atmospheric

winds will rarely exceed 30 m/s horizontally. Plausible Doppler shifts, $f_{Doppler} = \pm\frac{2v_{LOS}}{\lambda}$, will then be limited to ± 20 MHz for a 30° cone angle and Δf should be in the order of 40 MHz for a 1.5 μm laser.

3.4.2. Figure of merit of FSPT modulated lidars

Compared to single frequency range gated lidars

FSPT modulation effectively disperses the available energy over time. The peak power will fall but the number of uncorrelated wind distribution spectra accumulated during an observation period will increase. Key factors deciding the efficiency of FSPT modulation are the peak power to PRF relation and the standard deviation dependence on PRF and narrowband CNR. These have been discussed in chapter 2.3.3, but need further investigation.

It can be expected that the pump power conversion will be more effective when a fiber amplifier is stimulated continuously than when it is stimulated by a pulse, partly due to decreased ASE. It has been suggested that the energy in amplified pulses will fall as $\frac{1}{\sqrt{PRF}}$ and not as $\frac{1}{PRF}$. The narrowband CNR will thus also fall with $\frac{1}{\sqrt{PRF}}$. However, the number of speckle takes would increase. The standard deviation of the wind estimate would be effectively constant, regardless of PRF, for fiber amplified lidars sensing at low narrowband CNR during an observation period yielding several thousand speckle takes. The narrowband FOM of such a system can be given as

$$FOM = \tau \cdot D^2 \cdot E \cdot \sqrt{PRF} = T_{pulse} \cdot D^2 \cdot C$$

where C is a fiber amplifier constant.

FSPT-modulated lidars could therefore be expected to achieve the same accuracy as the corresponding single frequency range gated lidars with the same amplifier power and optic dimensions. The advantage of FSPT modulation is that the optimal trade off between PRF and pulse energy can be found so that high peak powers, provoking non linear effects, can be avoided and cheaper EDFA solutions can be used. For this optimization, range ambiguities or limitations in sensing range by the high PRF will not have to be considered.

Compared to focused cw systems

The energy scattered towards a FSPT modulated lidar will be shared between frequency slots and some will even be lost during the LO's inter-pulse durations. At short ranges, where the collection efficiency dominates the weighting of the sample volume, the RBP from the targeted range cell will effectively be the same as that for a cw lidar. At these distances it will be advantageous to use a pulse length which is comparable to the average atmospheric correlation duration. The narrowband FOM would thus be similar for the two concepts

$$FOM = D^2 \cdot P \cdot \sqrt{\tau_{atmos}} \ .$$

At longer distances, where both the collection efficiency function and the contribution duration is of similar importance for the confinement, some of the energy which would have been received by a cw system during the same sample duration would be lost since the scatter is generated by pulses. However, at these distances the spectrally well defined wind distribution, with a resolution in the order of 1 MHz, sensed by a cw lidar would normally be significantly spread by the turbulence in the long sensing volume. The missing energy would therefore not contribute significantly to the narrowband CNR. The signal strength generated by a FSPT modulated lidar would normally decrease but the wind distribution spectra would be narrower, increasing the possibility to estimate the wind velocity from the range gate center.

Finally, at long ranges, where the collection efficiency function falls off slowly around the focus distance, it is difficult to find the significant wind velocity without making assumptions about the wind profile. FSPT modulation using short pulses will still give narrow wind peak profiles and will make estimations of the wind velocity at the center of the range cell easier. However, the narrowband CNR, which is proportional to the correlated duration of the signal, would significantly decrease compared to that obtained at close distance.

The main advantages of using FSPT-modulated focused lidars instead of cw emitting focused lidars is that the WPP will fall off faster around the focus distance for the former, particularly for a focus at long range. This will give a higher possibility to pick the wind velocity from the center of the range gate. FSPT modulated systems will also be insensitive to cloud reflections and less influenced by single particles scattering with atypically long correlation durations which are outside the range cell center altitude since their contribution duration to the allocated frequency slot will be short.

A focused cw system, based on a fiber laser and a high power EDFA with an average output power of 1 W and a lens diameter of 7 cm, has proven to give reliable wind measurements up to 116 m also in very clear atmospheres[11]. A similar performance can be expected of an FSPT modulated lidar emitting a similar average power and having the same optic dimensions. The FSPT modulated system can, in addition, reach distances not available to focused systems but with a lower signal strength than at short ranges.

It is also plausible that the emitted power from an amplifier stimulated by a continuous FSPT could be stronger than that from of a cw stimulated amplifier since several energy level transitions are included during the lifetime duration of the excited states, approximately 10 μs, in a fiber amplifier.

3.5. FSPT modulated coherent lidar examples

FSPT modulation can be used in either focused or collimated system configurations. Three system examples are given in this section. Rectangular power profiles and continuously emitting FSPTs are assumed throughout this discussion and the collection efficiency function has been modeled according to the description in chapter 2.4.1.

Collimated FSPT modulated lidar
The normalized WPPs for the first three range cells of a collimated FSPT modulated lidar, continuously emitting rectangular pulses with T_{pulse} = 200 ns and T_{delay} = 0 s, are drawn in Figure 58.

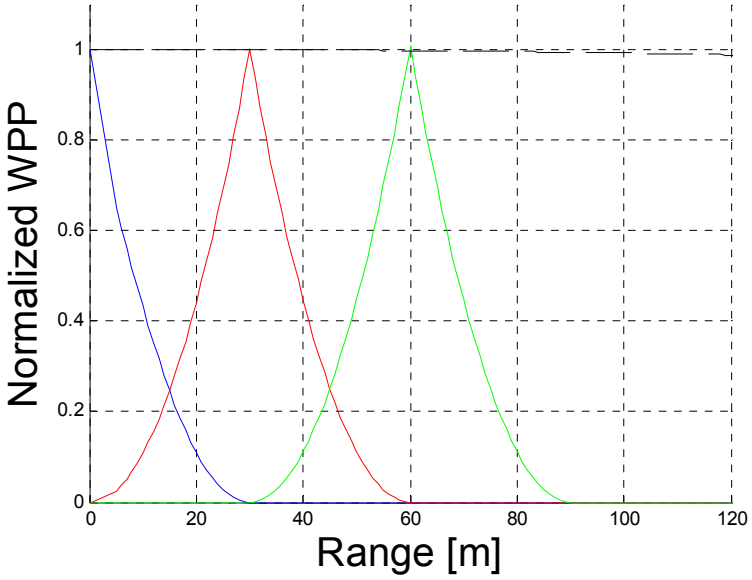

Figure 58 : Normalized wind peak profiles of the first three range cells of an undelayed collimated FSPT modulated lidar. Range cell one in blue, two in red and three in green. The dashed black line outlines the normalized collection efficiency function of the collimated system.

The full width half maximum of the wind peak profile of the range cells are equivalent to the FWHM of one range gate of a single frequency system, the

$$WPP_{FWHM} = \left(1 - \frac{1}{\sqrt{2}}\right) \cdot c \cdot T_{pulse} \approx 18 \text{ m}.$$

Focused FSPT modulated lidar
When the wind distributions in several range cells of a focused system are sensed simultaneously it is important to calculate the shape of the WPP in order to predict which distance contributes with the most significant wind signal.

The WPP of a cw system and the range cells of an undelayed FSPT-modulated lidar, continuously emitting rectangular pulses with T_{pulse} = 500 ns, are compared in Figure 59. The monostatic system has a receptor radius of 4.5 µm. The focus is set so that the collection efficiency function is maximized at the center of the third range cell at 150 m.

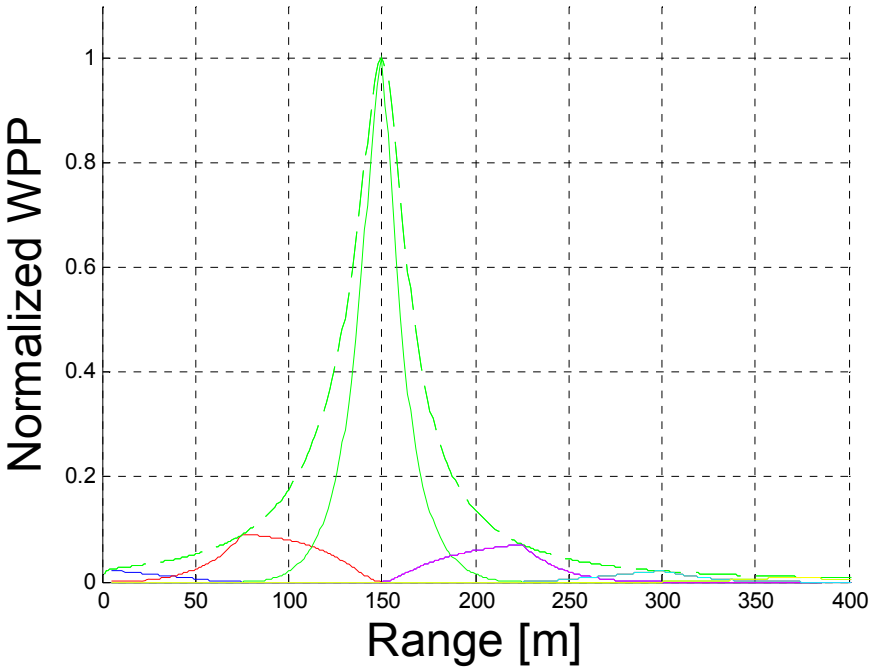

Figure 59 : Comparison of the profiles of a cw system (black dashed) and a FSPT modulated lidar continuously emitting rectangular pulses with duration T_{pulse} = 500 ns. Range cell one is drawn in blue, two in red, three in green, four in magenta and five in cyan.

The WPP_{FWHM} of the third range cell of the FSPT modulated lidar is 23 m, which can be compared to the WPP_{FWHM} of 37 m for the single frequency cw system.

Note that the WPPs of the other range cells are skewed. Correctly estimating the wind in the range cell center can therefore be difficult. If refocusing is fast the best praxis is to sense one altitude at a time and focus in the center of each range cell.

FSPT modulated lidar with transferable focus position
Several sets of the train parameters, T_{pulse} + T_{inter} and T_{delay}, would have to be used in order to cover close lying altitudes. For example, the wind velocity at altitudes from 100 to 250 m with 30 m intervals should be sensed with an undelayed FSPT modulated lidar. Assume that the maximum acceptable effective sample volume length is 35 m along the sensing direction, i.e. 30 m in altitude, and that the lidar has a 30 ° cone angle. Note that the FSPT generator described in chapter 4.2 has the peculiarity that T_{pulse} + T_{inter} has to be constant. In this example T_{inter} was assumed not to be able to be shorter than 100 ns. Parameters of five suitable FSPTs, the WPP_{FWHM} for the range cells when the system is focused at the range cell center and the WPP_{FWHM} for the corresponding cw system can be found in Table 11.

Altitude [m]	Range cell center [m]	Range cell number	T_{pulse} [μs]	T_{inter} [μs]	FSPT WPP_{FWHM} [m]	cw WPP_{FWHM} [m]
100	115	2nd	0.66	0.1	17	22
130	150	2nd	0.9	0.1	27	38
160	185	2nd	0.84	0.4	36	58
190	219	3rd	0.55	0.18	35	83
220	254	4th	0.46	0.1	35	113
250	289	5th	0.42	0.1	34	146

Table 11 : List of train parameters suitable for an undelayed FSPT modulated lidar sensing wind at altitudes from 100 to 250 m with 30 m intervals. The effective sample volume length of the FSPT modulated system is compared to the effective sample volume of the corresponding cw system.

The effective sample volume length of the FSPT modulated system can be given as the FWHM of the wind peak profile. This value can be compared to the FWHM of the collection efficiency function, corresponding to the equivalent effective sample volume of a cw system. FSPT modulation will give narrow sample volumes with a rapidly dropping weighting function. The possibility to pick the wind velocity in the center of the range gate increases and influence of significant scatter outside the effective sample length is effectively suppressed.

Sensing at low altitudes, e.g. < 75 m, could be done in cw mode since the collection efficiency is very narrow around the focus distance, thus eliminating most cloud reflections, and giving a short sample volume length. Alternatively, the wind velocity could be found in lower order frequency slots formed by the trains used for sensing at long range. A drawback of this is that the pulse duration, and thus the correlated backscatter duration, is unnecessary short. Another option is to sense in the first range gate using rather long pulses, e.g. 3 μs.

3.6. Range gated lidar emitting frequency comb pulses

A multi-frequency carrier wave system has previously been proposed and patented[49] by CTI, now Lockheed Martin Coherent Technologies. However, the method is mainly aimed at improving the acquisition rate of hard target sensing. The technique is based on range gating of pulses containing several frequencies simultaneously. The frequency content is thus concentrated in time as compared to the frequency stepped pulse train modulation, described in chapter 3.2.

Such a lidar would time gate a pulse comprising a known set of narrowly spaced frequency components, as illustrated in Figure 60.

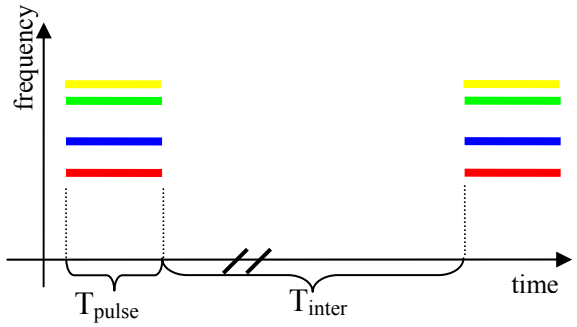

Figure 60 : Frequency content of the emitted pulses in the frequency comb modulated coherent lidar concept.

The generated scatter is a Doppler shifted copy of the emitted pulse. The received scatter would be mixed with a single frequency cw LO thus constructing a spectrum which contains a comb of Doppler peaks, all related to the target velocity in the range gate. This frequency comb would be autocorrelated with a known reference comb spectrum generated by mixing the cw LO with an unshifted pulse return, as illustrated in Figure 61.

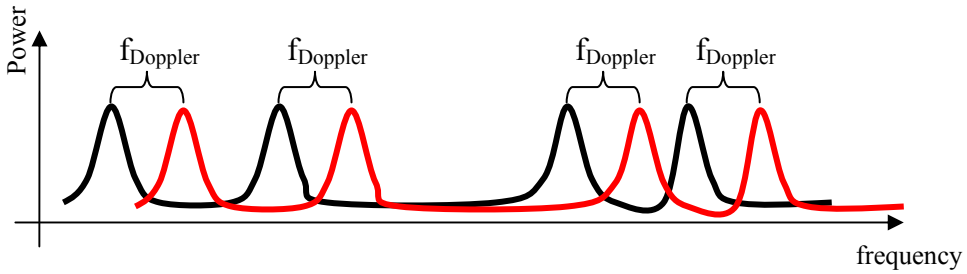

Figure 61 : Known reference (black) and observed (red) spectra from a coherent LIDAR emitting pulses simultaneously containing multiple frequencies, according to the CTI concept. The Doppler shift can be found by studying the autocorrelation between the two spectra.

The immediate advantage is an increase in the number of uncorrelated speckle takes $T_{obs} \cdot PRF \cdot N_f$, where N_f is the number of frequencies in the pulse and T_{obs} the observation period. Note that the PRF has to be limited to avoid range ambiguities and not limit the sensing range in a dispersed target

However, the available pump power is divided over the N_f frequencies. It is possible that the emitted multi-frequency energy would be slightly higher than what would be the case if the amplifier was stimulated by a single frequency since multiple transitions between different, although close lying, long life time energy levels are active simultaneously. The energy in one frequency component would nevertheless be expected to fall approximately as $1/N_f$.

The narrowband defined lidar FOM of a frequency comb modulated system is thus typically

$$FOM = T_{pulse} \cdot D^2 \cdot \frac{E}{N_f} \cdot \sqrt{PRF \cdot N_f}$$

i.e. a factor $\frac{1}{\sqrt{N_f}}$ lower than the corresponding low CNR single frequency system.

Frequency combed lidars are therefore mainly suitable if the CNR is high so that the signal is well defined, e.g. when sensing hard targets.

The proposed frequency comb generator resembles the FSPT generator presented in chapter 4.2. However, the loop is fed continuously during several revolutions, thus adding a frequency to the pulse for each round and building up the known set of simultaneously existing frequencies, before a pulse is switched out of the transmitter.

3.7. Conclusions on frequency modulated coherent lidars

The standard deviation of a wind measurement is improved by accumulating a large number of speckle takes. However, the observation duration is normally limited since most systems need a high acquisition rate. Frequency modulation offers to divide the energy used for generating scatter over time thus allowing the use of transmitters which emit less peak power and high accumulation rates.

A few frequency modulated coherent lidars have previously been proposed. Linear saw-tooth modulation and range gating of scatter generated by pulses containing frequency combs are suitable for hard target sensing.

Frequency stepped pulse train modulation is conversely a novel method appropriate for range resolved coherent lidar sensing at high duty cycles of primarily dispersed moving targets, e.g. for wind sensing. The technique is based on equidistantly frequency stepped pulse trains and a frequency pursuing local oscillator. FSPT modulation provides unique mapping of the Doppler shifted backscatter from a set of self assembled range cells into allocated distinct frequency slots as long as the pulse-to-pulse frequency step is wider than the expected variations of the Doppler shift. It operates at high pulse repetition but will despite this avoid the customary disadvantages; range ambiguity and a limitation of the sensing range.

This novel concept could provide more accurate systems while avoiding the use of high peak powers which introduces stimulated Brillouin scattering and non-linear effects as well as putting higher demands on other components in the transmitter. It is likely that amplifier dynamics are less severe and pump power conversion more efficient when an EDFA is stimulated continuously or at high frequency.

4. Frequency Stepped Pulse Train generators

Tunable laser are attractive for many applications, e.g. Optical Coherence Tomography (OCT) or fine detailed spectroscopy[50]. A specific kind of tunable laser is the frequency sweeper which produces a pseudo-tuned output by stepping via discrete narrow lying wavelengths. Such sources have been developed since comparable linear wavelength tuning can be difficult to achieve. Equidistantly stepped frequency sweepers have a specifically conceivable use as FSPT generators for FSPT modulated coherent lidars.

Described in this chapter are two different methods for generating equidistantly frequency stepped pulse trains appropriate for wind sensing; one based on a fiber laser which is tuned by piezoelectrically straining the incorporated fiber grating and the other on a seeded fiber loop containing an Acousto-Optic Modulator (AOM) and an Erbium Doped Fiber Amplifier (EDFA). Such a fiber loop sweeper was constructed in this project. The results from an evaluation of this device's suitability as a source in FSPT modulated coherent lidar wind sensing are presented.

The constructed frequency sweeper has properties which make it competitive when compared to a commercial tunable fiber laser. The advantages and limitations of this source are discussed in the end of this chapter.

4.1. Frequency sweeper based on piezoelectrically tuned fiber laser

Fiber lasers can be tuned by applying a voltage over a piezoelectric crystal affixed to the fiber. Expansions and contractions in the piezoelectric crystal are translated to a strain in the Fiber Bragg Grating (FBG). The amplified lasing mode is changed, and the emitted wavelength thus tuned, in relation to the change in Bragg reflector distance.

A commercial fiber laser from Koheras A/S[51] responds with an increase of 0.15 pm in wavelength per volt applied to the actuator, i.e.

$$\lambda(V) = \lambda_1 + k_\lambda V$$

where λ_1 is the starting frequency, in our case about 1574 nm at room temperature, V is the applied voltage and k_λ is a wavelength tuning constant of 0.15 pm/V.

Translated into frequency this gives

$$f(V) = \frac{c}{\lambda(V)} = \frac{c}{\lambda_1 + 0.15 \cdot 10^{-12} \cdot V} \approx 190 \cdot 10^{12} - k_f V$$

where k_f is a frequency tuning constant of 18 MHz/V.

The output during tuning, which would introduce Doppler-range ambiguities in the wind spectrum generated by a frequency modulated coherent lidar, has to be blocked as the fiber laser emits continuously. This can be done with an Electro-Optic Modulator (EOM) or an AOM as illustrated in Figure 62.

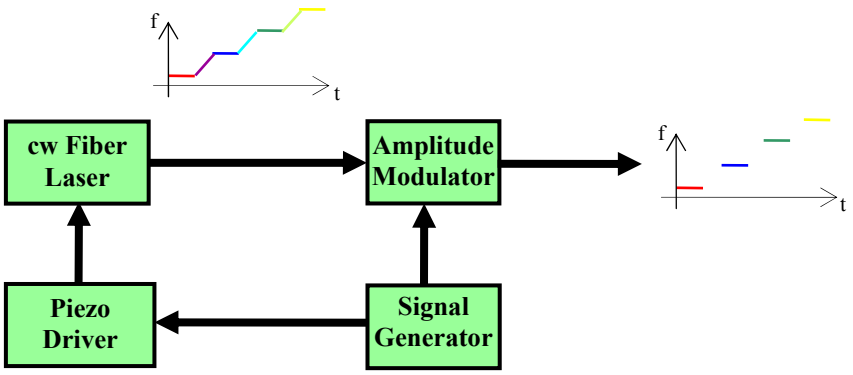

Figure 62 : FSPT generator based on a piezoelectrically tuned fiber laser. The train evolution is illustrated by the inset frequency vs. time graphs.

The piezo driver and the amplitude modulator are synchronized by a common clock. The modulator thus blocks transmission during tuning and the final output is the desired equidistantly frequency stepped pulse train.

EDFA amplification can be done before or after amplitude modulation. Amplification before amplitude modulation means that the modulator must support high peak powers and that pump power which could be used to increase the peak power in the pulses will be lost. Amplification after amplitude modulation is thus probably a better option but might cause generation of more ASE.

When calculating the response of a piezo-electric actuator the element is modeled as a capacitor and the voltage response follows

$$\frac{dV}{dt} = \frac{I_{peak}}{C}$$

where I_{peak} is the peak current available from the piezo driver and C is the capacitance of the element, in this case 32 nF.

With this piezo element and a suitable driver, e.g. from Dynamic structures[52], it should be possible to tune a frequency step of 50 MHz in 1 µs. A 50 MHz step corresponds to a range-Doppler ambiguity isolation of LOS wind velocities slower than approximately 20 m/s corresponding to horizontal winds of 40 m/s sensed with a 30 ° cone angle.

The piezo element can be strained with maximum 200 V, which corresponds to 3600 MHz or 72 steps of 50 MHz, before it needs resetting. A 500 kHz PRF system with $T_{pulse} = T_{inter} = 1$ µs thus has to be reset after 144 µs. If the system can be reset in 5 µs this corresponds to an ambiguity range of 22 km and a sensing duty cycle of 48 % in the first range gate.

The exact wavelength stability of the stepped fiber laser is unknown. Drift due to temperature instabilities should not be limiting on time scales of less than milliseconds. Increased noise due to tuning, noise from the voltage supply, and frequency ringing after the tuning stop would have to be investigated.

This generator might not reach the criteria for an FSPT lidar system, which depends on pulsing for confinement and senses in higher order range cells, as T_{inter} probably will be long and the pulse-to-pulse frequency step is likely to vary outside specifications. Nonetheless, a configuration where $T_{inter} = 1$ μs and the frequency step slightly varies could be sufficient, e.g. for isolation of cloud signals or for focused high duty cycle lidars which uniquely measure the wind within the first range cell.

4.2. Lightwave Synthesized Frequency Sweeper

A frequency sweeper sometimes referred to as a Lightwave Synthesized Frequency Sweeper (LSFS) had previously been suggested to produce pseudo linear chirping for Frequency Domain Optical Coherence Tomography[53] (FD-OCT) and reflectometry[54].

This frequency sweeper produces a train of equidistantly stepped pulses. The emission could theoretically be continuous. The frequency step is produced by consecutive passes through an AOM which induces an extremely stable Doppler shift on the passing light. This solution is thus a promising generator for FSPT modulated coherent lidar wind sensing.

4.2.1. System description

A suitable embodiment of an FSPT generator for coherent lidars is the LSFS[55, 56], illustrated in Figure 63.

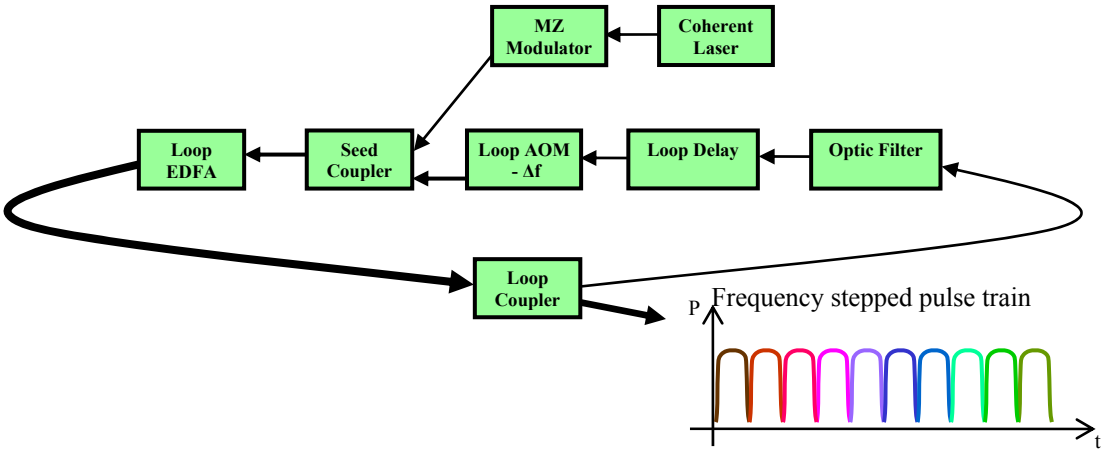

Figure 63 : A LSFS set up for generating FSPTs. Inset is a graph giving the emitted power over time with the frequency illustrated by color. The power of the light in the loop is indicated by the width of the arrows.

The LSFS is a loop including an AOM and an amplifier. A filter in the loop suppresses the build up of ASE noise and a fiber optic loop delay ensures a separation between consecutive pulses.

A triggering seed pulse with carrier frequency f_0, pulse duration T_{pulse} and peak power P_{seed} is fed into the loop via a seed coupler. The seed pulse, can for example, be generated from an amplitude modulated coherent laser, e.g. a highly coherent fiber laser with incorporated fiber grating[57] modulated by an AOM or a Mach-Zehnder (MZ) modulator. The amplitude modulator should have a strong extinction ratio to avoid additional light entering the loop.

The seed pulse is amplified by an EDFA before most of the power is coupled out of the loop. A fraction continues in the loop and is delayed so that the front of the returning seed pulse will meet the end of the same seed pulse once it reaches the seed coupler for the second time. Before it reaches the end of the seed pulse, the carrier frequency will be Δf-stepped in frequency by the loop AOM, and broadband noise, notably light spontaneously emitted from the EDFA, will be filtered. The new

frequency stepped pulse is then amplified by the loop EDFA before a large part of it is emitted, thus becoming the second pulse in the FSPT, also of duration T_{pulse}. A fraction of this new pulse stays in the loop and becomes a seed pulse for the consecutive 2Δf-stepped pulse. Loop revolution continues until the build-up of noise becomes too strong at which time the LSFS is purged by closing the loop AOM. The LSFS will subsequently be restarted by a new seed pulse.

4.2.2. Specifications of the Lightwave Synthesized Frequency Sweeper's parameters

This configuration is especially appropriate for generating equidistantly stepped FSPTs with high PRF for coherent lidars. The pulse duration is set by the feed pulse length. Commercial MZ[58] modulators can form practically rectangular pulses with T_{pulse} smaller than 1 ns. However, the extinction ratio is generally specified to 25 dB. Commercial AOMs[59] achieve much higher extinction ratios, typically specified to 55 dB, however, with rise and fall times typically of 120 ns.

The pulse separation can easily be minimized in the LSFS set up. It is controlled by matching of the loop delay and the pulse duration so that

$T_{inter} = T_{loop\ delay} - T_{pulse}$.
Where $T_{loop\ delay}$ is the time it takes for a pulse to propagate through the loop.

A set of loop delays are necessary if the LSFS should emit FSPT with different $T_{pulse} + T_{inter}$ in order to self assemble range cells with centers at close lying distances. The LSFS could theoretically emit continuously if the loop length was adjusted to fit with the seed pulse duration, i.e. $T_{loop\ delay} = T_{pulse}$. The duty cycle of the lidar is then maximized and the range cells will overlap optimally. However, the seed pulse will in practice have a certain rise and fall time and safety margins should be applied.

Long interpulse durations will not only produce blank ranges but Amplified Spontaneous Emission (ASE) will grow more when the amplifier is unstimulated, forcing restarts of the pulse train earlier.

The amplifier and the loop losses can be balanced in order to make the LSFS emit pulses with a constant peak power. Commercial EDFAs[60] give strong amplification and can give highly coherent polarized light with average powers up to 100 W from a mW input signal without introducing significant noise. In practice it is preferable to post amplify the signal leaving the FSPT generator by an external high power EDFA with the intention to keep the power level low in the loop in order to spare sensitive components. The emitted power will oscillate due to dynamics in the EDFA and the loop. However, these oscillations are on time scales which are much longer than the pulse length and the pulses are effectively rectangular, also after amplification. Pulse-to-pulse power variations are insignificant for velocity measurements as the backscattered power level is not quantified from these measurements.

The loop AOM gives the frequency step between consecutive pulses. The frequency step is induced by light reflecting off a traveling refractive index change generated by an acoustic wave which propagates through a crystal, e.g. a $LiNbO_3$ rod. The acoustic wave frequency, and thus the refractive index propagation velocity, can be controlled

with high accuracy, yielding accurate and stable frequency shifts between consecutive pulses.

Long trains are important for coherent lidar sensing in order to avoid range ambiguities and to maintain a high duty cycle in distant range cells. The sweep length of an LSFS is in practice currently limited by the build up of ASE. ASE will induce white noise in the coherently detected wind spectrum. It will also decrease the power of the intended frequency component since it drains pump power, both in the loop and the post amplification. ASE build up can be reduced by including optic and/or polarization filters in the loop. The sweeping length would ideally be limited by the filter bandwidth since the loop losses will exceed the loop gain once sweeping reaches the filter edge. Frequency pursuing filters have been used to increase the maximum train length[61]. However, simple optic filters are typically sufficient for wind sensing applications. The LSFS can easily be restarted in less than a few microseconds by closing the inner AOM.

All opto-electronic components are commercially available in the 1.5 μm wavelength range. They are typically fiber pigtailed and can thus be easily assembled to a robust LSFS.

4.2.3. Noise factors in Lightwave Synthesized Frequency Sweepers

There are four relevant sources of noise in the LSFS.

ASE noise is broad bandwidth white noise and will essentially be filtered out from the heterodyne current. However, ASE will drain power from the loop and post amplifiers and should therefore be minimized.

It is possible that the EDFA response to a stimulating pulse will create more RIN than a continuously stimulated EDFA. However, it is likely that the LSFS, which has a loop amplifier which is stimulated at high PRF, will produce less RIN than the corresponding single frequency range gated system.

A third issue with the LSFS is that the loop will introduce a polarisation shift for each revolution. This will lead to polarisation losses, especially for range cells at far distances, when the pulse that generates the relevant scatter and the present LO pulse have a large difference in the number of times they have revolved around the loop. Polarisation losses are avoided in a polarisation maintaining loop which either use polarisation maintaining fiber or includes a polarisation filter.

A slightly more serious problem could arise if the extinction ratio of the loop modulator is insufficient. A frequency component, lagging behind the intentional frequency with Δf, will be added to the second pulse. This frequency component will pursue the intentional component and successively grow stronger. It will also in turn leak and generate further $n \cdot \Delta f$-lagging components, as can be seen in Table 12.

LO	Scatter from 2nd range cell	Beat signal
f_0 : -30 dB	NA	NA
f_0-Δf : -30 dB f_0 : -30-r_e dB	$f_0 + f_{Doppler}$: -120 dB	**Δf + $f_{Doppler}$:** -30-120 dB $f_{Doppler}$: -30-120-r_e dB **Δf :** -30-30-r_e dB
f_0-2Δf : -30 dB f_0-Δf : 3-30-r_e dB f_0 : -30-2r_e dB	f_0-Δf +$f_{Doppler}$: -120 dB $f_0 + f_{Doppler}$: -120-r_e dB	**Δf + $f_{Doppler}$:** -30-120 dB $f_{Doppler}$: 3-30-120-r_e dB 2Δf + $f_{Doppler}$: -30-120-r_e dB **Δf :** 3-30-30-r_e dB **2Δf :** -30-30-2r_e dB
f_0-3Δf : -30 dB f_0-2Δf : 4.8-30-r_e dB f_0-Δf : 4.8-30-2r_e dB f_0 : -30-3r_e dB	f_0-2Δf + $f_{Doppler}$: -120 dB f_0-Δf + $f_{Doppler}$: 3-120-r_e dB $f_0 + f_{Doppler}$: -120-2r_e dB	**Δf + $f_{Doppler}$:** -30-120 dB $f_{Doppler}$: 4.8-30-120-r_e dB 2Δf + $f_{Doppler}$: 3-30-120-r_e dB 3Δf + $f_{Doppler}$: -30-120-2r_e dB **Δf :** 4.8-30-30-r_e dB **2Δf :** 4.8-30-30-2r_e dB **3Δf :** -30-30-3r_e dB
…	…	…

Table 12 : The development of the heterodyned signal obtained from a FSPT modulated lidar with a balanced LSFS and a loop modulator with extinction ratio r_e. Only mixing with scatter from the 2nd range cell is considered. The LO is generated from a reflection off a lens surface and is assumed to be 30 dB weaker than the emitted pulse power. The received scatter from the 2nd range cell is assumed to have lost 120 dB of the emitted power.

For typical trains this lagging frequency component will be sufficiently suppressed so that it will not generate any significant beat signal with the returned scatter. The scatter generated with lagging frequency components can clearly also be disregarded. However, the multiple frequencies in the relatively strong LO will homodyne and generate avalanching frequency components in the frequency slot centers, nΔf. This noise will possibly disturb the signal from low LOS wind velocities if appropriate post correction cannot be applied.

Similarly to lop leakage, a Δf-lagging frequency component will be added to the emitted pulse for every revolution if the seed modulator leaks. These components will form weak $T_{pulse}+T_{inter}$ delayed trains which will generate signals in the frequency slot centers when they beat against each other.

Light experiencing reflections on both sides of the loop delay would give a similar contribution of n·Δf-lagging frequencies. This contribution can easily be avoided by introducing an isolator before the loop delay.

4.3. Evaluation of a Frequency Sweeper Lightwave Synthesized

The LSFS concept was evaluated, with emphasis on its viable use as a FSPT generator for coherent lidar applications. Pulse profiles, train lengths, step accuracy, coherency and noise were measured.

4.3.1. Pulse profile

A LSFS was constructed and connected to an experimental set up, illustrated in a boxplot in Figure 64, for the evaluation tests.

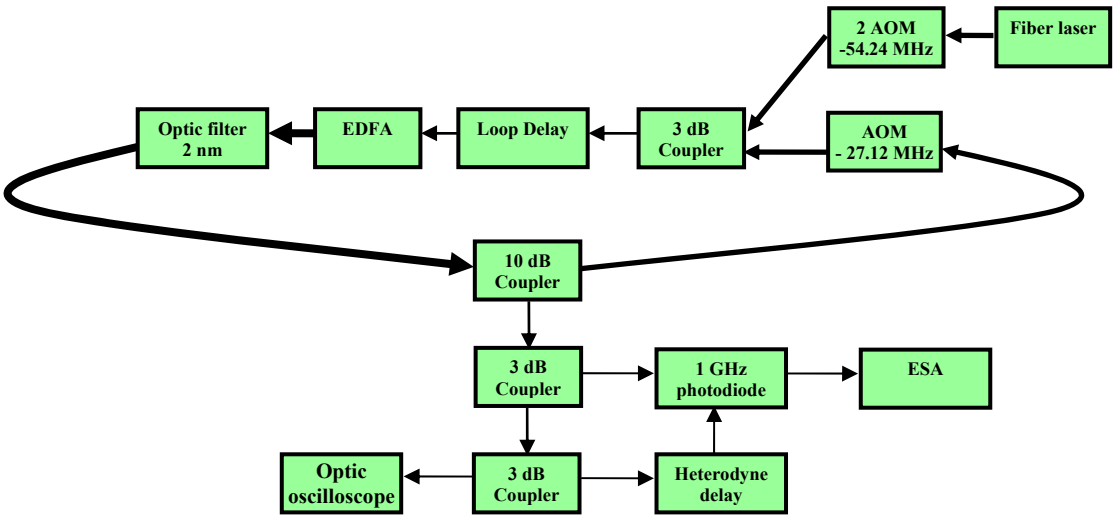

Figure 64 : Boxplot of the constructed LSFS and the experimental set up from evaluation of its viable use as a FSPT generator for coherent lidar applications.

The ADJUSTIK fiber laser from Koheras was set to emit the maximum average power, 5 mW, of 1574 nm light continuously. The laser has a FWHM linewidth of 1.6 kHz and 70 kHz when measured in a homodyne setup with propagation differences corresponding to 200 m and 39 km respectively in free space, see appendix A. The seed pulse was formed of the fiber laser cw emission by two AOMs, in order to decrease seed leakage. The AOMs are produced by NEOS and each one has a loss of 2.5 dB and a specified extinction ratio of 40 dB. Together they induce a -54.24 MHz frequency shift on the fiber laser emission. The seed pulse was fed to the loop via a 3 dB coupler. The seed pulse thus had a peak power of approximately 0.8 mW after a total of 8 dB seeding losses.

The seed pulse passed through the delay loop before it was amplified by a HW0T EDFA from Highwave. This amplifier gives low gain at 1574 nm. However, it is sufficient to balance the loop losses since they are limited to approximately 6 dB, originating mainly from the 10 dB coupler, the loop AOM and the 3 dB coupler. The pulse then passed through a 2 nm optical bandpass filter which was centered around the fiber laser wavelength. A tenth of the pulse was guided out of the loop and transmitted to the measurement equipment by the 10 dB loop coupler. Before the front of the pulse reentered the delay loop, at a suitable time after the seed pulse end, it was frequency shifted with -27.12 MHz by the loop AOM. The loop was purged, after a train with desired length had been produced, by closing the loop AOM. A new seed pulse restarted the LSFS after an additional few pulse durations.

The LSFS output was coupled to a Tektronix optic oscilloscope and the amplifier pump power was tuned until the amplifier gain balanced the loop losses and a train with a relatively stable peak power was obtained. The pulses emitted from a balanced LSFS are expected to have a peak power of

$$P_{LSFS} = P_{seed} \cdot G \cdot r_c \approx 0.8 \text{ mW} \cdot 4 \cdot 0.1 = 320 \text{ } \mu\text{W}$$

where P_{LSFS} is the peak power of the frequency stepped pulses, P_{seed} is the peak power of the seed pulse, G is the amplifier gain which equals the loop losses of approximately 6 dB in the balanced mode and r_c is the coupling fraction of the loop coupler.

The peak power measured on the oscilloscope is about 70 μW, in agreement with the expected values once corrections have been applied for the two 3 dB couplers before the measurement equipment. Several different loop delay lengths were used in order to produce FSPT with different PRF. The inter pulse duration was kept short in order to produce high duty cycle trains.

The pulse repetition frequency, $PRF_{LSFS} = \frac{1}{T_{pulse} + T_{\text{int}er}}$, depends on the loop delay as

$$PRF_{LSFS} = \frac{c}{\left(L_{delay} + L_c\right) \cdot n_{ref}}$$

where L_{delay} is the length of fiber in the loop delay, L_c is the inherent delay in the loop excluding the intentional loop delay, notably due to the erbium doped fiber length, and n_{ref} is the refractive index of the optic fiber, approximately 1.5 for 1.5 μm light.

The set of delay lines used and the measured PRFs and pulse durations, given as the duration of the pulse with flat peak power, are listed in Table 13. Examples of the obtained pulse profiles can be seen in Figure 65.

Loop delay [m]	**Measured PRF [MHz]**	**T_{seed} [ns]**	**Measured T_{pulse} [ns]**
230	0.74	1290	1060
130	1.15	820	620
90	1.43	670	480
50	1.85	520	300
30	2.56	400	190
0	4.26	230	0

Table 13: PRF and measured T_{pulse}, given as the duration of the pulse at peak power, for different delay lines and different seed signals applied to the seed modulator, T_{seed}.

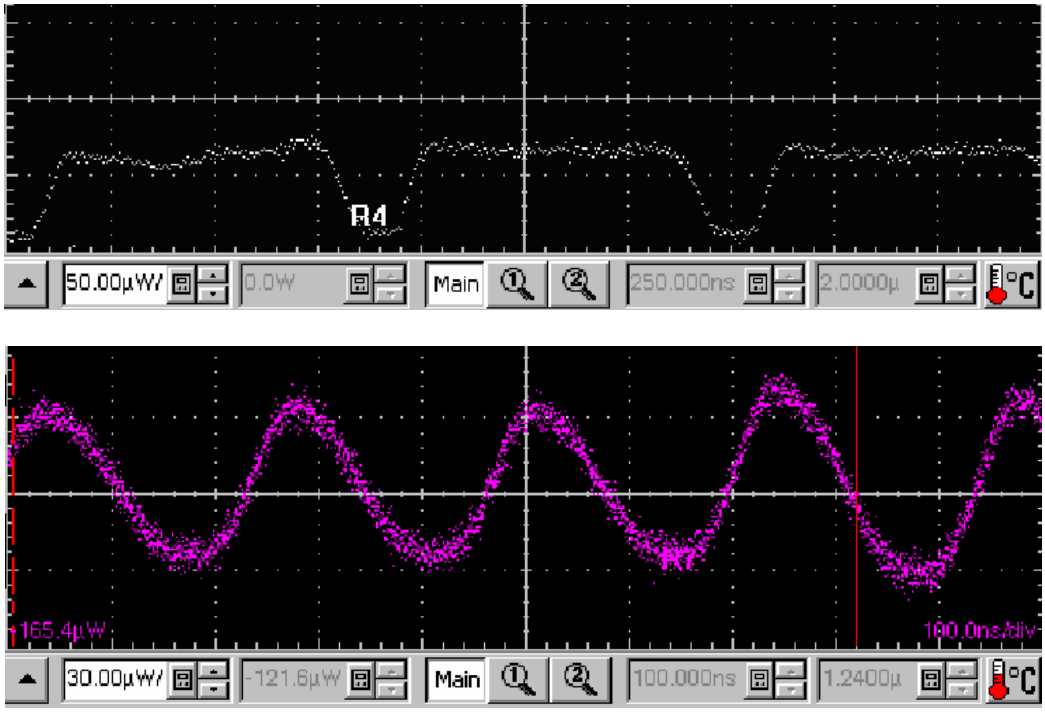

Figure 65: Pulse profiles from the LSFS. Top image: Delay line 130 m, seed signal T_{seed} = 820 ns. Bottom image: Delay line 0 m, seed signal T_{seed} = 230 ns.

The AOM is a relatively slow amplitude modulator. The rise and fall times were measured to approximately 110 ns. Nevertheless, pulses with relatively rectangular pulse shapes were formed since the high PRF will eliminate the typical boost of the power in the pulse front. However, the rise and fall time of the amplitude modulation on the seed pulse dominates the shape of short pulses.

The inherent delay in the loop, disregarding from the intentional delay in the loop delay, can be estimated to about 45-60 m from the measured PRF.

4.3.2. Train length

The train length is, as mentioned, limited by the growth of noise. The ASE noise growth can be estimated by studying the power growth in the valleys, i.e. during the inter pulse durations. The temporal resolution of the optic oscilloscope is coarse when studying long trains. Nevertheless, a base line will form in the power vs time plot. This base line outlines the power during the inter pulse durations and the approximate duration until sudden growth of ASE is quite clear.

For this experiment the time before purging, T_{purge}, of the loop was sequentially increased and the train development was surveyed. The out power has a peculiar but repeatable dynamic, e.g. as seen in Figure 66. The dynamic depends both on T_{seed} and T_{purge}. The power in the valleys, the time at which noticeable ASE growth starts and the start of the consecutive pulse train are indicated in the graph.

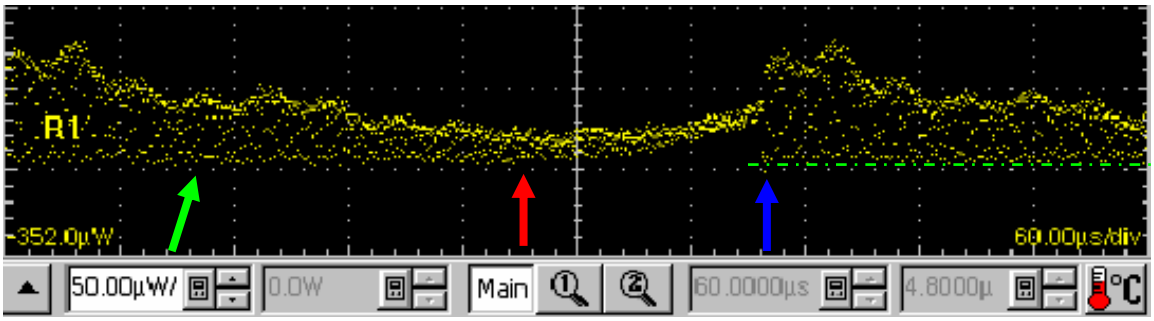

Figure 66 : FSPT generated by the LSFS set up in Figure 64. The power during the inter pulse durations are indicated by the green arrow, the time at which significant ASE growth is noticeable is indicated by the red arrow and the start of the consecutive pulse train by the blue arrow. The green dashed line aids the eye to see the period without noticeable ASE growth.

Note that the dynamic behavior is relatively slow and the peak power in a pulse can be considered as constant, as seen when a short section is studied, e.g. in Figure 65.

The decreasing power trend before ASE growth is probably due to that the wavelength is swept towards the filter edge. The decrease of stimulating power will most likely lead to faster ASE growth, which in its turn decreases the pump energy available for amplification of the pulse and thus starts a cycle of increasing ASE growth.

The train length before ASE growth was typically about 500 pulses long. It did not, to a large degree, depend on the pulse duration, i.e. trains with slower PRF experienced ASE growth after a longer time than trains with a faster PRF.

4.3.3. Step accuracy

The step accuracy of the loop AOM was studied by mixing the LSFS output with a cw LO branched from the seeding fiber laser, as illustrated in Figure 67.

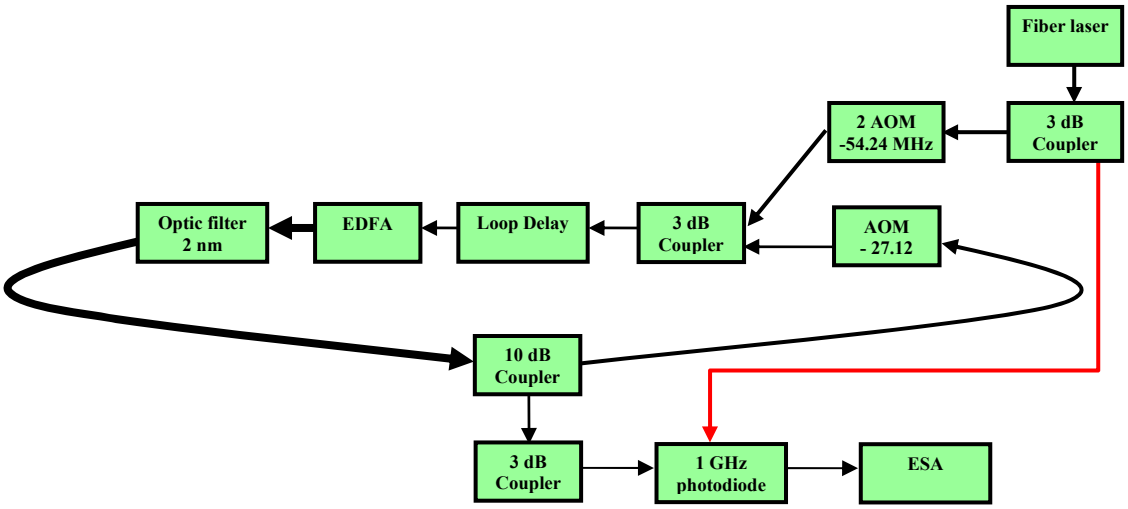

Figure 67 : Set up for studying the step accuracy of the loop AOM.

The studied train had a PRF of 1.15 MHz and was 97 µs long. It thus included 111 pulses and the carrier frequency was tuned over 3.03 GHz before being reset. The heterodyne signal from the photo detector, with a specified 3 dB bandwidth of 1 GHz,

was studied in an E4407B Electrical Spectrum Analyzer (ESA) from Agilent with a 26.5 GHz bandwidth. The obtained averaged spectrum can be seen in Figure 68.

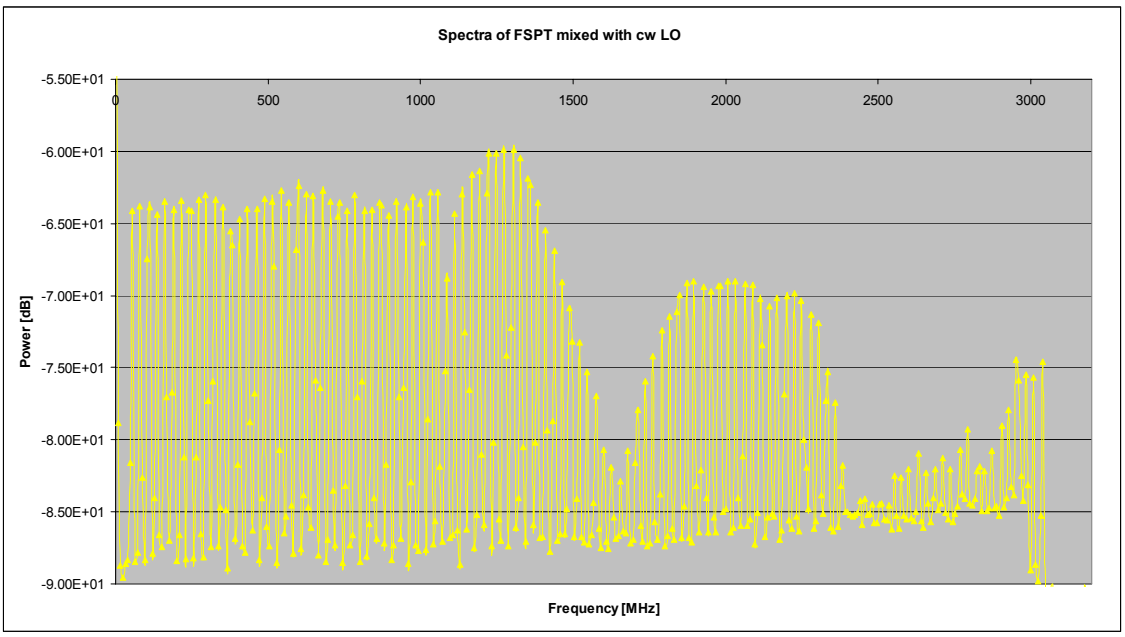

Figure 68 : The heterodyne spectrum obtained from mixing trains, containing 111 pulses, from the LSFS with a cw LO. It is possible to identify the frequency components at multiples of 27.12 MHz all the way up to 3 GHz.

It was possible to identify frequency components at multiples of 27.12 MHz all the way up to 3 GHz, i.e. for the full train. The rapid drops in response at about 1.1 GHz and after 1.4 GHz are due to the limited bandwidth of the detector. Note that the first frequency component observed is at 54.24 MHz since the seed modulators induces an initial $2\Delta f$ shift to the light.

Figure 69 depicts overlaid zooms of the first three frequency peaks obtained from mixing a cw LO and a train with a PRF of 1.85 MHZ which is restarted every 5 µs. These frequency components are generated from the pulses that have made 0 - 2 revolutions in the loop and thus passed 2 to 4 times through an AOM. Note that the peaks have been shifted with an appropriate multiple of 27.12 MHz so that their overlap can be studied.

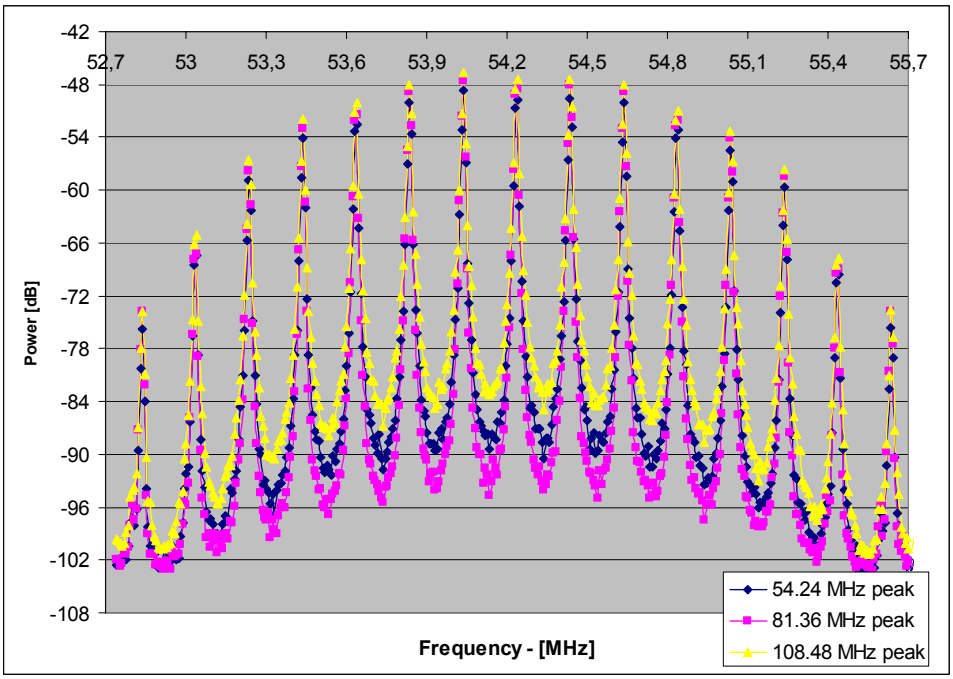

Figure 69 : Overlaid spectra of the first three frequency peaks generated from mixing a cw LO with a train with a PRF of 1.85 MHZ from an LSFS which is restarted every 5 µs.

The spectra are split up in lines since each peak is generated in the ESA from a Fourier transformation taken over several pulses. The envelope spread over 3 MHz fits with the pulse duration of about 300 ns at full power. The same frequency component is detected every 5 µs which should give a spacing of the split lines of 200 ns, which is also observed in the measured spectrum.

The observed accuracy in the frequency shift can, as expected, be described as excellent. The AOM thus has the qualities to generate the equidistant frequency steps appropriate for FSPT modulated lidars sensing wind.

4.3.4. Noise

It has thus been shown that the constructed frequency sweeper can generate trains with suitable T_{pulse}, T_{inter} and Δf. It now remains to ensure that there has not been a degradation of the coherency and that no significant noise sources have been introduced.

To verify the spectral purity in the pulses, the LSFS output was split into two paths by a 3 dB coupler. One path was delayed with $2\cdot(T_{pulse} + T_{inter})$ in a length of single mode fiber. The overlap of the trains was studied in the optic oscilloscope and the image is reproduced in Figure 70.

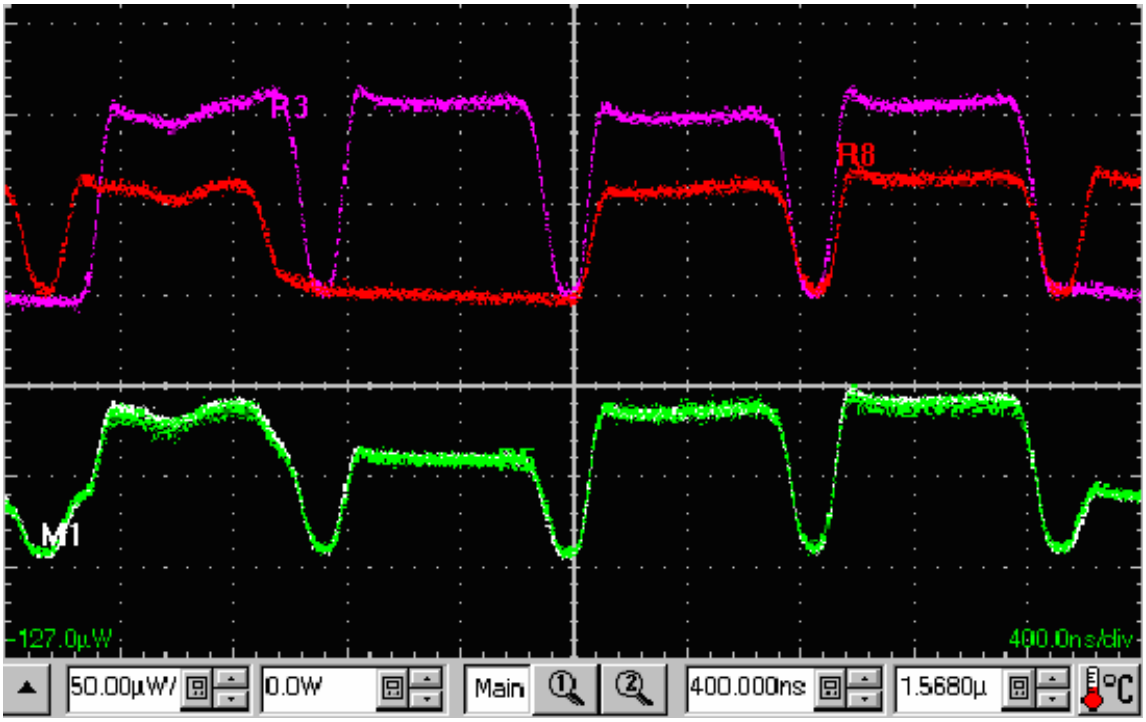

Figure 70 : Shape of the frequency stepped pulse trains used for the study of noise and coherency. The undelayed train is drawn in magenta and the train delayed with $2\cdot(T_{pulse} + T_{inter})$ in red. The profile of the combined trains after a 3 dB splitter is drawn in green. The overlap with the calculated profile (red + magenta) of the combined trains in white is excellent and therefore difficult to see. The strange profile of the first pulses from the left is due to an imperfection in the oscilloscope.

The pulse overlap is extremely tight, possibly with a slightly longer delay, which could be estimated to less than 10 ns corresponding to 2 m of fiber. Note that the delayed train has about half the power of the undelayed train since it went through an additional 3 dB coupler, as can be seen in Figure 64.

The profile of the combined trains was also studied with the oscilloscope and compared to the calculated spectrum obtained by adding the profiles measured on the individual trains and dividing by two for the extra 3 dB coupler. The overlap is excellent and therefore difficult to see in Figure 70. This is an indication that polarization effects in the loop are small and typically can be disregarded from when closely separated pulses are the origin to the wind signal, as in the early range cells.

The two trains were mixed on the 1 GHz photodetector and the resulting heterodyne current was observed by the ESA which gave the spectrum in Figure 71 and Figure 72. The FSPT was 36 µs long had a PRF of 1.15 MHz and thus included 41 pulses.

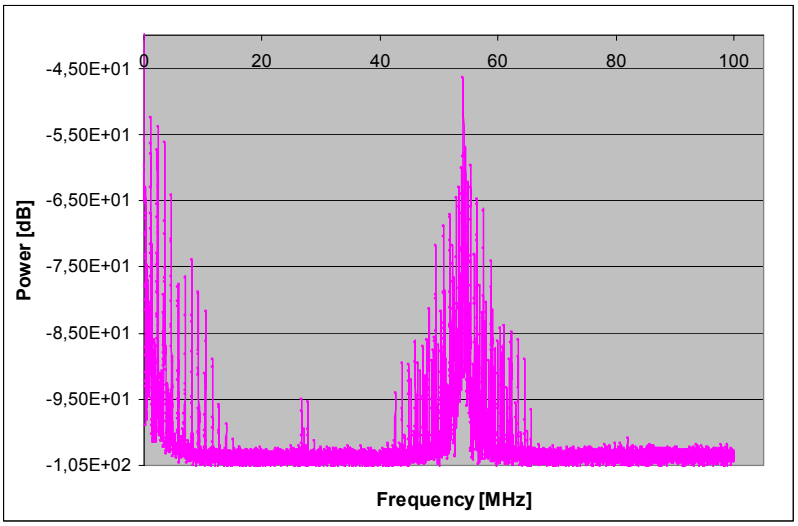

Figure 71 : The heterodyne spectrum obtained from mixing a FSPT with a PRF of 1.15 MHz with a two pulse delayed copy of itself.

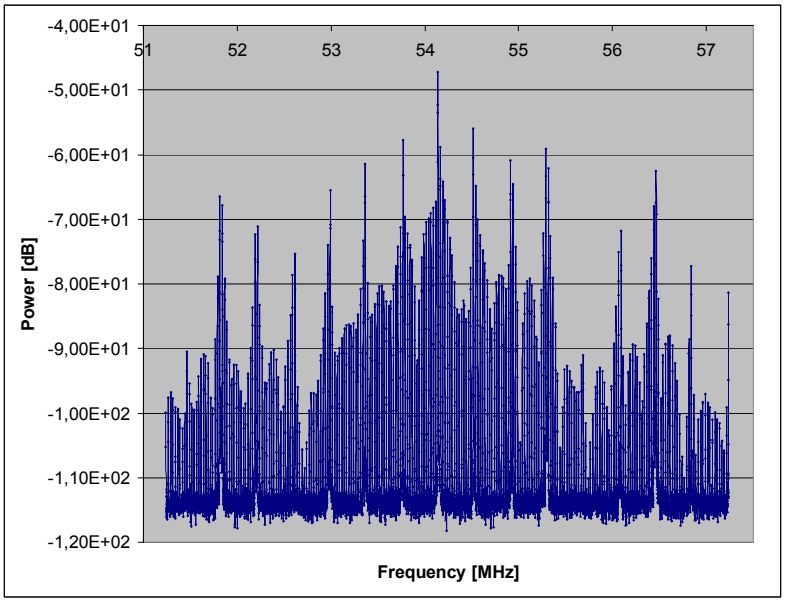

Figure 72 : Narrow bandwidth study of the peak pulse in Figure 71.

A weak impurity, of about -50 dB, can be seen at Δf = 27.12 MHz. This impurity could originate from seed or loop modulator leakage, or from a double reflection from both sides of the loop delay as explained in chapter 4.2.3. However, the broad spectral width of the impurity, as compared to that of the main signal, indicates that it has been mainly generated from a slightly unsynchronized pulse overlap, i.e. that the delay length before the heterodyne mixing is slightly shorter than two pulse durations. Short parts of the weak tails from consecutive pulses would then beat against each other and form a wide signal similar to the one observed in the measured spectrum at 27.12 MHz.

There is also an indication of noise at $3\Delta f$ = 81.36 MHz. This impurity cannot be explained by a pulse overlap, which only generates a frequency component at $(k-1)\Delta f$, where k is the intended delay, counted in number of pulses, imposed on one path. In

our case (2-1)Δf = 27.12 MHz. It is likely that this noise originates from loop or seed modulator leakage. A similar noise level would exist at 27.12 MHz, but it could be hidden by the previously mentioned pulse overlap in this configuration.

It is possible that these side modes might increase, relatively to the main mode, when post amplified by a strong EDFA since they could experience less gain saturation. Studies of the side mode strength, generated by trains of differing length, could reveal the modulator leakage quantitatively.

The broad noise, at frequencies up to 15 MHz, is due to the fact that the ESA is untriggered and thus samples over several pulses and thus measures the large amplitude modulation which contains several low frequency components. The unexpected width of the signal at -54.12 MHz also has its origin in the untriggered sampling. The sample will include the return of partial pulses which will have a very short correlation duration and thus generate a low wide spectrum. This noise will not occur in a triggered setup which Fourier transforms the signals individually.

The narrow bandwidth study also reveals a more disturbed spectrum than, for example, the spectrum in Figure 69, originating from a mix of a cw LO with a train with slightly slower PRF. This is again due to the fact that the ESA makes Fourier transforms over several trains and also partial pulses. The more chaotic spectra is due to the fact that the heterodyne current generated from a pulse pair is phase uncorrelated to the heterodyne current generated from the next pulse pair. A correlated phase comes back once per train i.e. approximately every 37 µs, 1 µs purge time included. The spectrum is therefore split up in lines separated by 27 kHz, which relates well to the 25 kHz observed. The spectrum envelope is broader than the expected 1.6 MHz, however the pulses are not truly rectangular. The origin of the 330 kHz separated lines is not known. A more relevant investigation, with possibility for triggered sampling and thus Fourier transformation of individual pulses, was performed on the FSPT modulated lidar and is described in chapter 5.

4.4. The light wave frequency sweeper for other applications

The constructed LSFS has potential not only as a generator of FSPT for coherent remote sensing. The demand on frequency purity and low noise is high for wind sensing applications but for other applications, e.g. OCT or THz generation, is extended tunability more important. It is a simple technology which can be assembled from available fiber communications components. The coherency is primarily dependent on the quality of the seed laser.

The maximum train length was significantly increased by introducing a polarization filter in the loop, since it will filter half the unpolarized ASE in each revolution. The longest train produced was 760 μs long and had a PRF of 1.15 MHZ, i.e. corresponding to 874 pulses with a + 27.12 MHz between consecutive steps, giving a total frequency sweep of 23.7 GHz. ASE growth was not observed in this setup. The limitation in train length was instead the increasing loop looses as the pulse frequency swept towards the filter edge and thus slowly decreased the peak power of the pulses.

The power loss, due to the frequency being swept towards the filter edge, could be compensated for by successively increasing the amplifier gain or by optimizing the filter center wavelength so that the starting frequency is slightly offset and the train sweeps through the filter center. Another possibility for increasing the train length is to use rapidly tuneable filters which follow the swept wavelength.

The sweep length is decided by the number of pulses in a train and the size of the frequency step between consecutive pulses. If it is the number of loops, i.e. noise build up, and not the filter edge which limits the train length it is possible to use a longer frequency step. Drivers which induce a 1.3 GHz shift in the AOM are commercially available for the 1550 nm wavelength range.

Although the LSFS sweeps the frequency pseudo-linearly, and does not tune the wavelength continuously, it will effectively be linear also in wavelength for relevant sweeping ranges of NIR light, as can be seen in Figure 73. The longest train achieved in this project swept over 23.7 GHz which corresponds to a pseudo tuning of about 196 pm from the original 1574 nm.

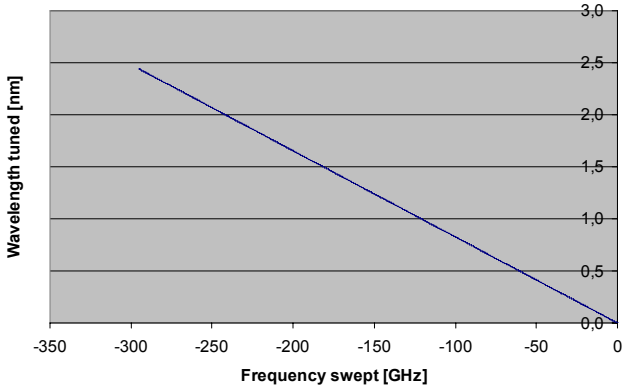

Figure 73 : The wavelength pseudo tuning is effectively a linear function of swept frequency in the NIR region. In this graph the initial wavelength was 1574 nm.

The tuning of the constructed LSFS is sufficiently long to be observed with a simple wavelength meter. The measured spectrum of the train, observed with a Hewlett Packard 7004A Optical Spectrum Analyzer, is given in Figure 74. The wavelength meter effectively measures the train linewidth, i.e. all the wavelengths in the train at once, since it has a low temporal resolution. The wavelength meter also has a relatively low spectral resolution and the linewidth obtained from the first pulse was measured from a train which only contained the first pulse. This one pulse train was generated by having the loop AOM closed and seeding the loop with the same intervals as before.

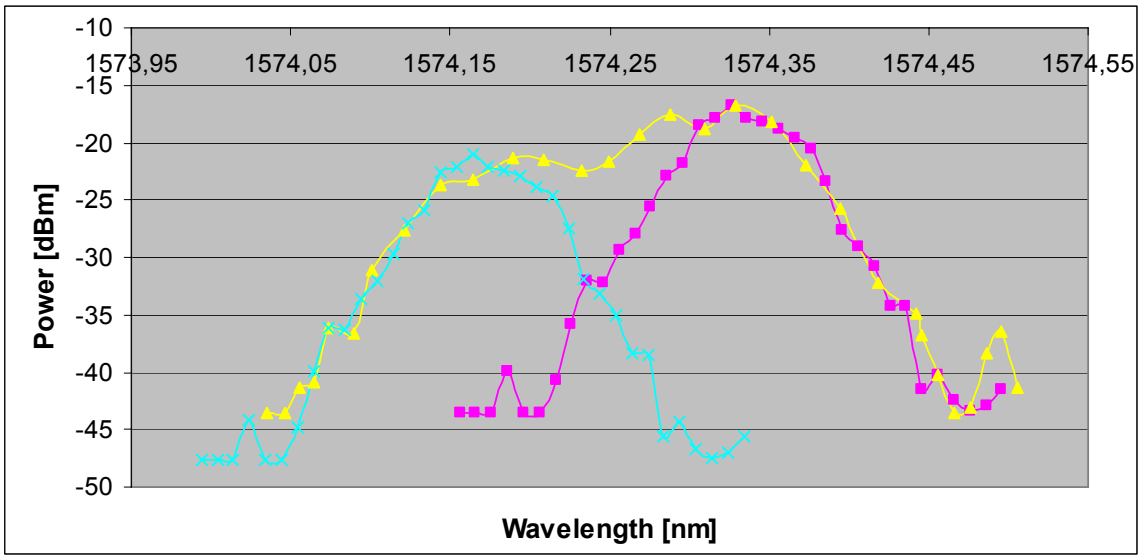

Figure 74 : Spectrum obtained from an LSFS emitting a 874 pulses long FSPT with a frequency step of + 27.12 MHz between consecutive pulses (▲), the linewidth measured with the loop AOM closed (■) and the estimated linewidth produced by the last pulse (×).

The center wavelength of the first pulse was measured as 1574.33 nm. The wavelength of the last pulse was roughly estimated to be 1574.16 nm by fitting the linewidth measurement from the one pulse measurement with the end flank of the measured spectrum of the train. The total tune length can thus roughly be estimated with the wavelength meter to 170 pm by taking the difference of the first and final pulse's wavelength center. This value corresponds reasonably well with the predicted 196 pm.

The constructed LSFS, which did not have an optimised filter center position, can generate extremely coherent laser light which continuously makes rapid sweeps pseudo linearly over approximately 190 pm. Compared to the commercially available Adjustik tuneable fiber laser it has a longer sweep range, 190 pm instead of 60 pm, which most likely can be extended, it will not suffer from hysteresis, like the piezo tuned fiber laser, and tuning will be much faster. The examined train with a PRF of 1.15 MHz and a 27.12 MHz frequency step will tune 1 GHz in 32 µs. The Adjustik can achieve such tuning at a similar rate, however the speed of the LSFS can easily be upgraded by increasing the frequency step between consecutive pulses. The LSFS output will also have a narrower instantaneous linewidth since the piezo element introduces vibrations on the fiber. However, the LSFS can suffer from Δf-lagging

components but for most applications the measured 50 dB suppression of these side modes will be sufficient.

Note that the LSFS is pseudo-tuneable, i.e. it cannot perform continuous tuning and therefore it is not possible to stop at a specific wavelength, e.g. for spectroscopy. However, since the train is well defined in time it is possible to trigger on the signal so measurements are made exclusively at the specific wavelength. The frequency step of tens of MHz corresponds to approximately 0.2 pm stepping so very few wavelengths will be missed.

One possible application of a LSFS optimized for wavelength tuning can be as a highly coherent tuneable THz generator based on heterodyne mixing of the output from only one laser. The advantage being that the two mixed beams would be automatically frequency locked. A train of 2000 pulses with a frequency step of 1 GHz split in two paths, of which one is delayed in a fiber length corresponding to approximately 1000 pulses, would recombine on a square law detector to generate a highly coherent beat signal with a carrier frequency of 1 THz. Tuning could be done by changing the delay or the pulse duration.

Pseudo frequency sweepers in other wavelengths could also be envisioned either by using other laser sources or by using frequency doubling/tripling. A possible target could be a low power tunable highly coherent UV source.

4.5. Conclusions on Frequency Stepped Pulse Train Generators

A lightwave synthesized frequency sweeper, appropriate for FSPT modulation, has been constructed and evaluated. This FSPT generator is based on a seeded fiber loop containing an erbium doped fiber amplifier and an acousto-optic modulator.

The frequency sweeper can provide trains with pulse durations in the interesting range for lidars of 200 nanoseconds to a few microseconds. Train lengths approximately 500 pulses long can be reached before growth of amplified spontaneous emission and the lidar can restart within a few microseconds. The frequency is equidistantly stepped between consecutive pulses with extreme accuracy and insignificant amounts of broadband noise are introduced. However, side modes, likely to originate from seed or loop leakage, will grow for every revolution and will limit the train length and could even deteriorate the accuracy in sensing of low LOS velocities.

The frequency sweeper has an exclusive exact broad bandwidth pseudo-tunability combined with an extreme coherence making it an appropriate source also for other applications, e.g. OCT or THz-generation.

5. FSPT modulated lidar

In this chapter the FSPT modulation is experimentally demonstrated. The modification of a focused cw lidar prototype into a frequency stepped pulse train emitting lidar is explained and proof of principle results from velocity measurements of a hard target positioned in the second range cell are described.

5.1. FSPT proof of principle campaign

5.1.1. Modification of lidar prototype

The metrology group at Risø National Laboratory owns an early prototype of the Zephir lidar. This lidar was borrowed for a period of three weeks and modified into FSPT modulation mode for a proof of principle study. The focused 1 W cw lidar is illustrated in a box plot in Figure 75. An undelayed, non-offset local oscillator is generated from a controlled reflection inside the telescope. The telescope has a 7 cm lens diameter. The receptor is a standard single mode fiber with a 4.5 µm core radius and the effective Gaussian lens radius is estimated to be 2.2 cm.

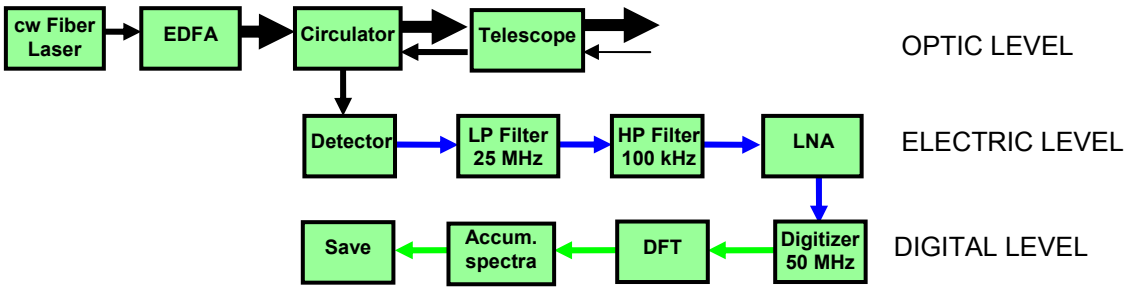

Figure 75 : Layout of the focused cw lidar prototype. Optical signals are shown in black, electric currents in blue and transferred data in green.

The most evident component that needs to be replaced in the modification of the cw prototype into a FSPT modulated lidar is the cw laser. The source was replaced with the FSPT generator described in chapter 4.3. However, the original 1554 nm fiber laser used in the cw lidar prototype replaced the 1574 nm laser in the LSFS used during the evaluation. This new laser has a slightly better coherence, and anti-reflection coatings as well as the controlled reflection which generates the LO are adapted for the 1554 nm wavelength in the cw lidar prototype.

Furthermore, the optic filter in the LSFS had to be adjusted so that it was centered at 1554 nm instead of at 1574 nm. The amplifier pump current was reduced to give a stable peak power level of the emitted pulses in the train since the gain of the amplifier is higher for the 1554 nm wavelength.

The original 1554 nm fiber laser emits a maximum of 3 mW and is thus slightly weaker than the 1574 nm fiber laser used in the LSFS evaluation. The stable peak power level of the balanced train can thus be estimated to be about 190 µW, which fits well with the measured peak power of 60 µW in Figure 77 after corrections for the two 3 dB couplers.
The modified frequency sweeper includes a loop delay of 90 m and thus emits trains with a PRF of 1.43 MHz. The LSFS is set to emit 17 pulses before the loop is purged and fed by a new seed pulse.

Scatter will mainly be collected from the hard target positioned in the second range cell as will be explained. The signal will therefore appear in the second frequency slot, extending from $\Delta f/2 = 13.56$ MHz to $3\Delta f/2 = 40.68$ MHz. The 25 MHz Low Pass (LP) electric filter therefore had to be removed. The High Pass (HP) filter and the amplifier were also removed since they oscillated due to the high dynamics in the unfiltered current from the photodiode. In addition, the sampling frequency had to be adjusted to avoid aliases. A sufficient sampling rate for sensing up to the second frequency slot would have been 81.36 MHz. Nonetheless, digitizing was performed at 200 MHz to reveal other possible components of higher frequency, e.g. signals from the third range cell.

Triggering of the digitizer was introduced so that the sampled spectrum could be synchronized with the start of the seeding with a new pulse. Finally, the raw data from the sampled heterodyne current was saved for signal processing

The final layout of the FSPT modulated lidar prototype can be seen in the box plot in Figure 76.

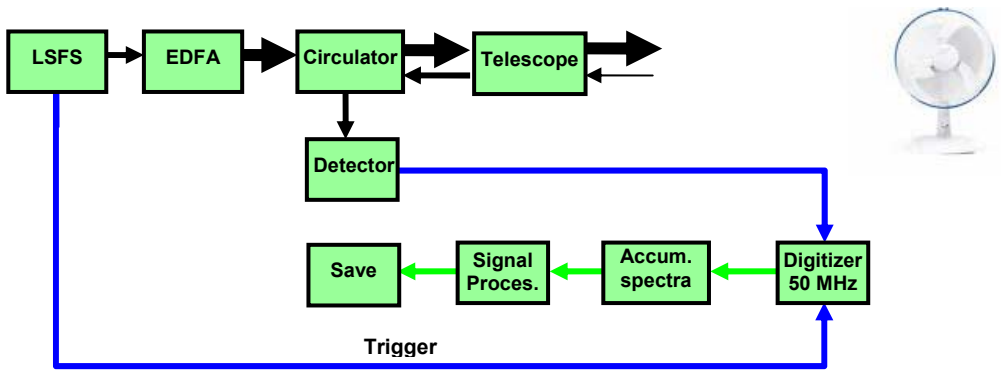

Principal parameters of the FSPT modulated lidar prototype:

FSPT:	Power: 190 µW λ: 1554 nm Δf = 27.12 MHz PRF = 1.43 MHz N_{pulse} = 17
EDFA:	Gain: 38 dB Peak power: 1.1 W
Telescope:	$R_{receptor}$ = 4.5 µm R_{lens}= 3.5 cm
Digitizer:	f_s = 200 MHz
DFT:	$N_{samples}$ = 80 or 2048 (originally 2048)
Accumulated spectra:	A = 256

Figure 76 : The layout and main parameters of the FSPT modulated lidar prototype.

The final configuration can easily be switched in this fiberpigtailed configuration. The FSPT modulated mode is altered to cw mode simply by bypassing the loop so that the seed laser directly and continuously feeds the EDFA amplifier. The lidar in cw mode is still without filtering and sampling is as in the FSPT mode. The lidar will therefore not correspond in spectral resolution and CNR to the original prototype. Returning back to FSPT modulated mode is equally easy. Reliable velocity reference measurements could thus be taken in cw mode for evaluation of the FSPT modulation accuracy.

5.1.2. Emitted Frequency Stepped Pulse Trains

The pulse profiles from the modified LSFS can be seen in Figure 77. The pulses have a stable peak power level during approximately 480 ns and a PRF of 1.43 MHz. The peak power is about 60 µW.

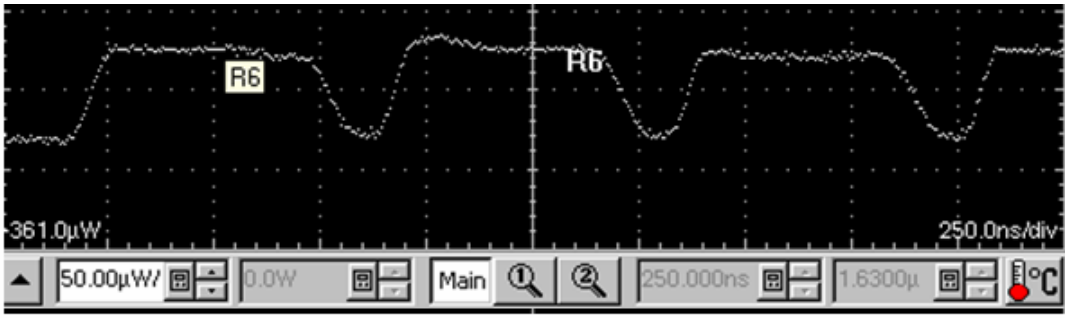

Figure 77 : Profile of emitted train before amplification. Peak power estimated to be 60 µW

The pulse train was also measured in the oscilloscope after post amplification. The output was sent through a 27 dB attenuator before measurement in order not to destroy the detector. The pulse shapes were effectively copied after amplification as can be seen in Figure 78. The emitted peak power can be estimated to 1.1 W from the measured 550 µW after corrections for 33 dB loss from the attenuator and the couplers. The gain of the EDFA can thus be deduced as approximately 38 dB. Note that the peak power is higher than the emitted power of 0.7 W, obtained with the lidar in cw mode, even though the amplifier was stimulated with less power than when stimulated directly by the cw fiber laser.

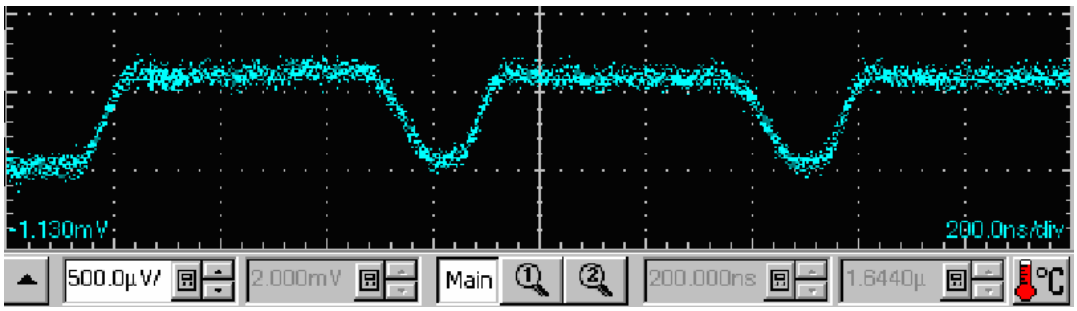

Figure 78 : Profile of emitted train after amplification and 33 dB attenuation.

The balanced pulse train after amplification can be seen in Figure 79. The train has a duty cycle of about 72 % and the average power can thus be estimated to be approximately 0.72·1.1 W = 0.8 W.

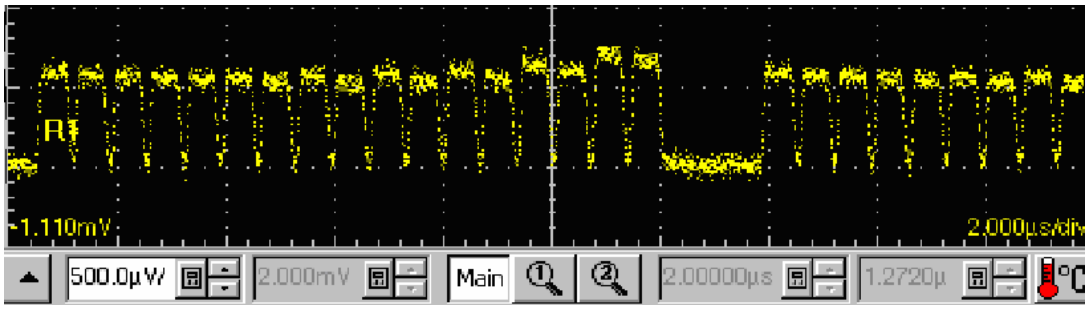

Figure 79 : Pulse train after amplification and 33 dB attenuation.

5.1.3. Signal processing in FSPT modulated lidar prototype

The sampled heterodyne current is dominated by the frequency pursuing LO, as can be seen in Figure 80. However, the sampled signal does not replicate the signal observed in the oscilloscope. This is likely due to a limitation in the photodetector bandwidth so that the detector cannot follow the stale pulse flanks without a small overshoot. The marked 265 ns long sections with stable power durations are selected for DFT processing. A software HP filtering is applied to remove low frequencies arising due to zero padding of the highly dynamic signal.

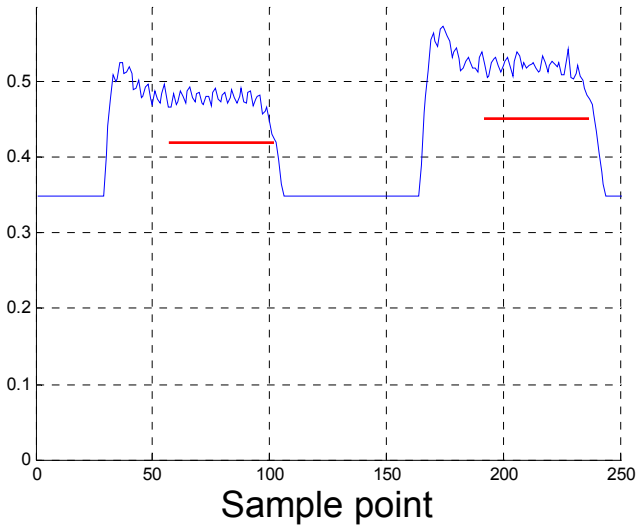

Figure 80 : Sampled signal from the lidar in FSPT mode. Note that the peak power duration is shorter than the duration that was observed with the oscilloscope. Also note the overshoot of the pulse fronts. The selected sample duration is shown in red.

Each section includes 53 sample points. Two approaches are taken for the Fourier transformations. At first each sample vector is zero padded and transformed in a 512 point DFT. This allows surveillance of the spectral content of the signal from each pulse.

Secondly, the sample vectors from several pulses are concatenated and jointly transformed into the frequency domain by a 512 point DFT. This approach gives an averaged spectrum at the highest spectral resolution per number of operations.

5.1.4. The campaign target

An electric ventilator was placed 105 m away from the lidar in a 200 m long underground corridor. The ventilator was tilted against the beam direction so that it would induce a Doppler shift on the reflected frequency. A piece of cardboard was affixed to the fan blades so that the fan would have a constant LOS velocity at the beam spot.

The refractive index turbulence is expected to be low in the tunnel since the temperature is stable and the draft is low. This was confirmed by a beam spot which hardly fluttered when studied on IR sensitive paper.

The FSPT-modulated prototype was focused on the fan at 105 m. The system's effective sample volume was modeled according to the collection efficiency model for fiber based systems in chapter 2.4.1 with the simplification of considering rectangular

pulses with T_{pulse} = 480 ns and T_{inter} = 220 ns. The resulting WPP can be seen in Figure 81.

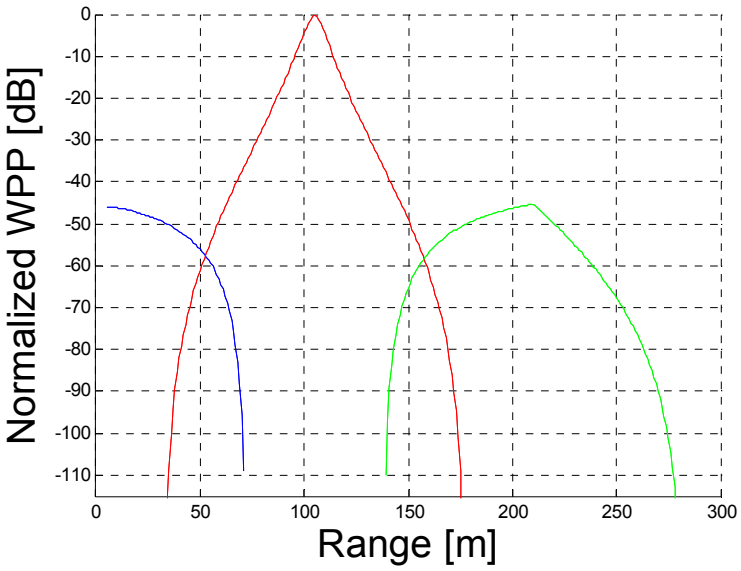

Figure 81 : Modeled WPP for the FSPT modulated lidar prototype setup described by rectangular pulses with T_{pulse} = 480 ns and T_{inter} = 220 ns.

In this set up the only significant scatter will arrive from the ventilator. Nevertheless, the WPP is still important since it indicates the spectral definition and division of the collected scatter over the frequency slots. The ventilator at 105 m is placed in the center of the second range cell. The signal should thus be maximized and a spectrally well defined signal will appear exclusively in the second frequency slot, i.e. the ventilator should not give any contribution to the first and third frequency slots.

The true Doppler shift of the ventilator was estimated by using the lidar in cw mode. Five speckle takes, with the corresponding 265 ns and 200 MHz sampling, from the lidar in cw mode are shown in Figure 82.

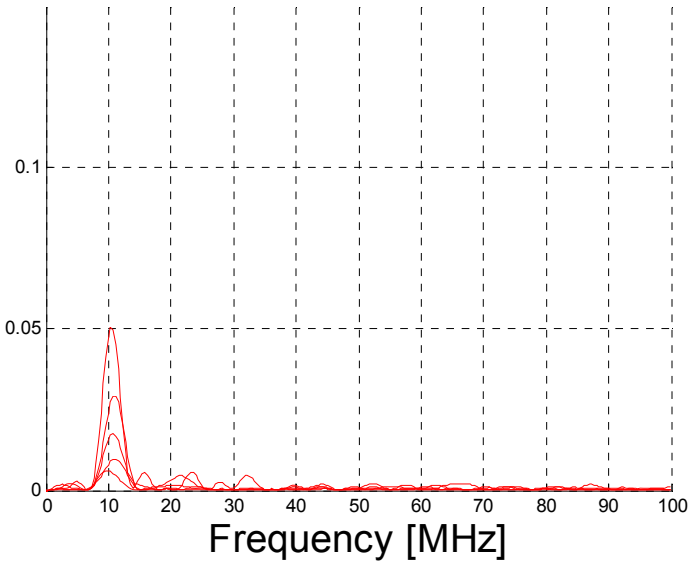

Figure 82 : Five Doppler spectra obtained from the fan sensed by the lidar prototype in cw mode.

The average signal strength in the power spectra obtained by the prototype in cw mode, estimated from 56 pulses, is 25 mW. The average Doppler shift from the fan was estimated to be 10.8 MHz. Translated into velocity this amounts to 8.4 m/s. Note that the rotational direction of the fan cannot be deduced since the non-offset lidar cannot find the sign of the Doppler shift.

5.2. Velocity spectra sensed with FSPT modulated lidar

5.2.1. Individual Fourier transformation of sample vectors

The spectra obtained by the prototype in FSPT mode during the first six LO pulses are plotted in Figure 83. The same axes scales are used enabling easy comparison with the plots of the signal from the lidar in cw mode, Figure 82.

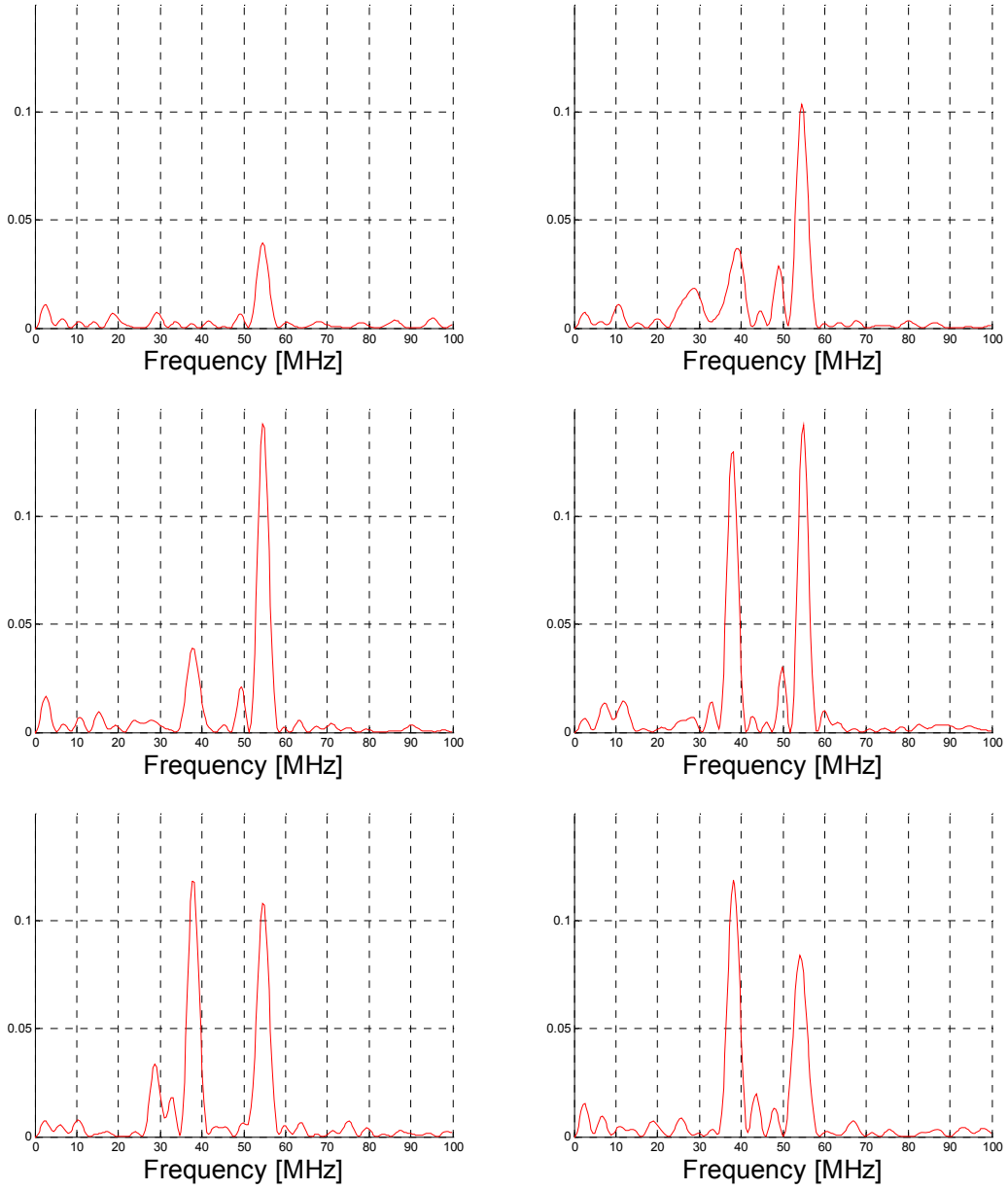

Figure 83 : The consecutive spectra obtained during the first six LO pulses with the lidar in FSPT modulated mode (from top left). Note the fan signal at approximately 38 MHz and the noise at 54 MHz.

The signal strength variation in the spectra is expected since every pulse gives a speckle take of the ventilator velocity. An unexpected signal is clearly apparent at $2\Delta f$ = 54.24 MHz. Indications of noise at 27.12 MHz can also be seen in some spectra, notably in the second and fifth LO pulse. These side modes will be treated further in chapter 5.3.

The first spectrum does not contain a ventilator signal. This is expected since the scatter from the ventilator has not yet traveled back to the lidar when sampling of the first pulse takes place.

In the following spectra a signal in the second frequency slot is clearly noticeable. The signal from the fan is estimated to be centered at 38.15 MHz, and thus in the second frequency slot, from ten smoothened spectra accumulated from LO pulses two to seven, i.e. over 60 pulses.

The deduction of the LOS velocity of the fan in range cell 2, v_{LOS}, is described in chapter 3.2.4 and will in this case be given as

$$v_{LOS} = \frac{\lambda}{2}\left(f_{center,i} - (i-1)\Delta f\right) = \frac{1.554\mu m}{2}\left(38.15MHz - (2-1)\cdot 27.12MHz\right) = +8.6m/s \cdot$$

The spin direction of the fan can be determined when sensing with the lidar in the FSPT modulated set up - something that was not possible in the cw mode which cannot reveal the sign of the Doppler shift. The positive velocity deducted from the second range cell indicates that the ventilator is turning against the lidar in the hit spot.

The velocity measured in FSPT modulated mode is in good accordance with the estimation from the cw mode of 8.4 m/s. The accuracy of the measurement is likely to be limited by a slight wobble of the cardboard covered fan blades and thus a slightly different hit angle for the measurements taken with the prototype in the two different modes.

The signal strength is slightly higher for the FSPT mode than for the cw mode. The signal strength is measured as 42 mW when averaged over 60 pulses. The increased narrowband CNR is expected since the peak power was stronger in the FSPT mode while all other parameters are constant, i.e. we do not use the long correlated scatter duration of the target which would otherwise be possible to sense in cw mode. The signal strength is expected to be about $P_{FSPT}/P_{cw} = 1.1/0.7 = 1.6$ times larger in FSPT mode, which is reasonably coherent with the measured value of 42/25 = 1.7 times.

It is also reassuring to note that the measured signal width of approximately 4 MHz fits well with the expected 1/265 ns = 3.8 MHz.

5.2.2. Fourier transformation of concatenated sample vectors

It is possible to study phase coherent contributions in the heterodyne current by studying spectra generated from Fourier transforms of the concatenated sample vectors from consecutive pulses. The spectrum generated from concatenated sample vectors should grow narrower and stronger if there is a phase correlation in the signal generated over consecutive pulses.

The spectrum generated when the sample vectors from the second to the seventh pulse in the previously studied FSPT were concatenated is shown in Figure 84.

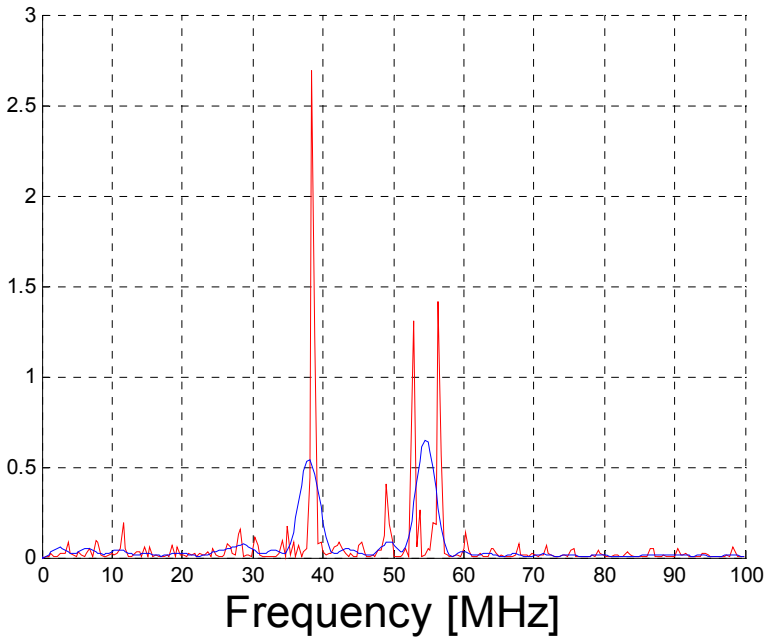

Figure 84 : The spectrum generated when the second to the seventh pulses returns were concatenated (red) is compared to the accumulated spectra generated individually by the same six pulses.

It is rather surprising that the signal from the ventilator becomes narrower when the pulse returns are concatenated since consecutive pulse return are expected to be phase uncorrelated. The collected scatter and LO have experienced different propagation paths and the pulse returns should thus also have a random phase compared to the LO phase. Thus they should, in a first approach, neither form a phase correlated beat signal. Further investigation of this phenomenon is necessary as it could be an unexpected advantage of FSPT modulated lidars.

Other trains include more noise at 54.24 MHz and even significant noise at 27.12 MHz, as can be seen in Figure 85, which shows the accumulated power spectrum from ten pulse trains. This noise would make it difficult to accurately sense the velocity of an object in the third and second range cell with a low LOS velocity. The narrowing effect of concatenating the sample vectors is evident for all trains.

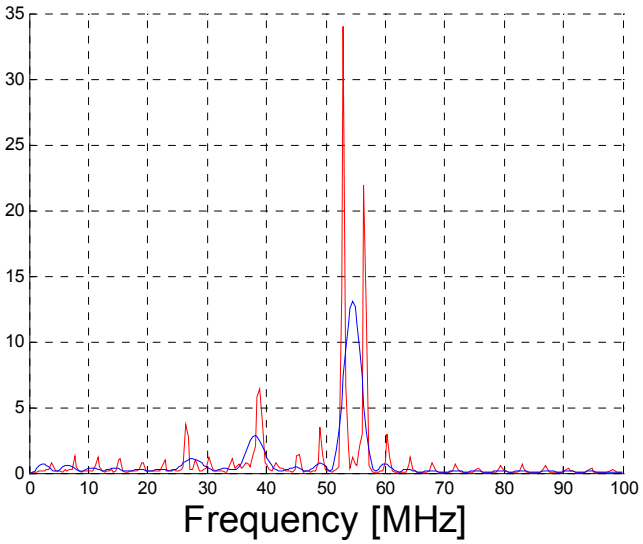

Figure 85 : The spectrum generated from the concatenated sample vectors from pulse 2 to 7 accumulated over 10 trains (red) is compared to the accumulated spectrum generated individually by the same sixty pulses.

However, the phase coherency in the FSPT mode does not seem to be as strong as the completely phase correlated signal obtained in the cw mode, as can be seen in Figure 86.

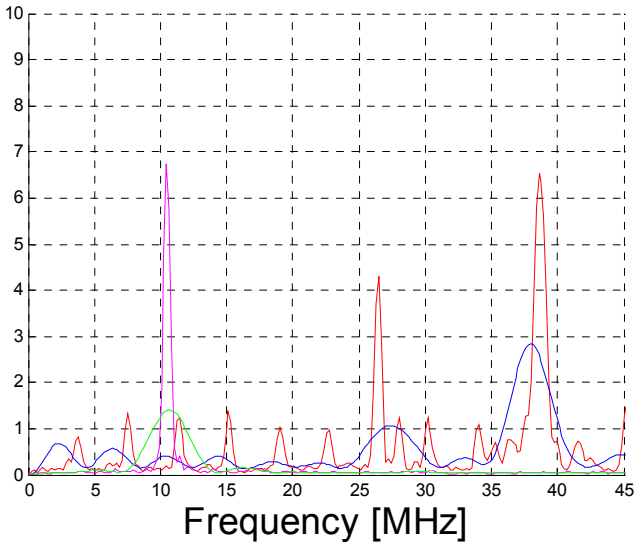

Figure 86 : Doppler spectra from the fan sensed in; cw mode with concatenated sample vectors (magenta), cw mode with Fourier transform of individual pulse returns (green), FSPT mode with concatenated sample vectors (red) and FSPT mode with Fourier transform of individual pulse returns (blue).

However, the cw generated signal peak increases by a factor of 4.8 times; it is expected to increase by a factor of 6 since the correlated duration increases from 1 pulse duration to 6 pulse durations. On the other hand, the FSPT generated signal peak only doubles.

5.3. Noise in the frequency slot center

Strong frequency components are evident in the second and third frequency slot centers, as seen in Figure 85. However, note the unexpected lack of noise in the fourth frequency component at 81.36 MHz. Without proper post processing, e.g. by subtracting the noise measured on a tap on the LO line, this noise will make measurements of low LOS velocities and low CNR signals such as those reflected from aerosols unfeasible.

As expected, the spectra obtained during the first LO pulse does not contain a signal, but unexpectedly it contains noise at 54.24 MHz. Noise in the first pulse could be expected if the seed modulator leaks. The seed pulse is amplitude modulated by two AOMs and leakage through both seed modulators could form a component which lags behind with $2\Delta f$. However, leakage through only one of the modulators would generate a signal at Δf which is expected to be approximately a power two stronger. Noise at 27.12 MHz is evident in the first pulse in some trains, however, always much weaker than noise at 54.24 MHz, as can be seen in Figure 87.

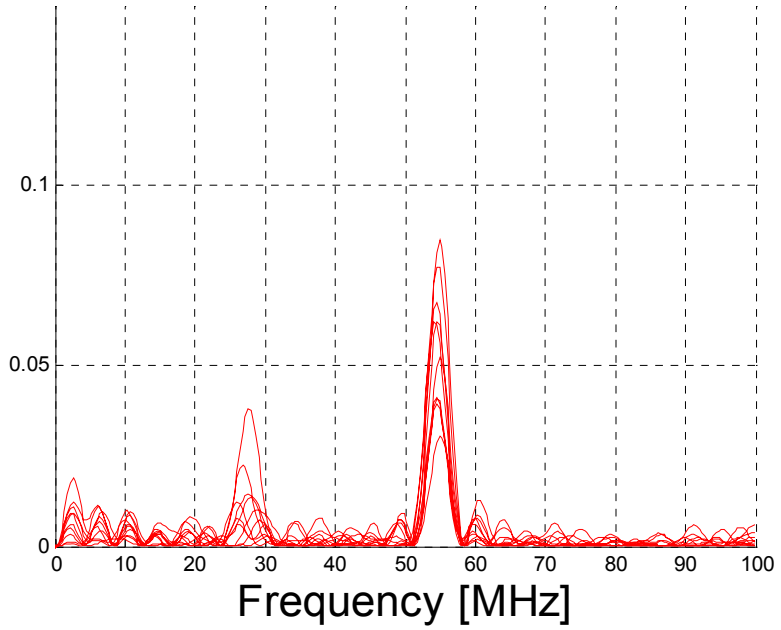

Figure 87 : Spectra from the first LO pulse in ten trains. Note that noise at 54.12 MHz is dominating over the noise component at 27.12 MHz.

The noise observed in the spectrum from the first pulse repeats chaotically in the consecutive spectra. However, when the average peak signal from ten pulses is taken, as in Figure 88, it is possible to see that the noise at 54.12 MHz will grow almost linearly, as predicted for loop leakage in chapter 4.2.3.

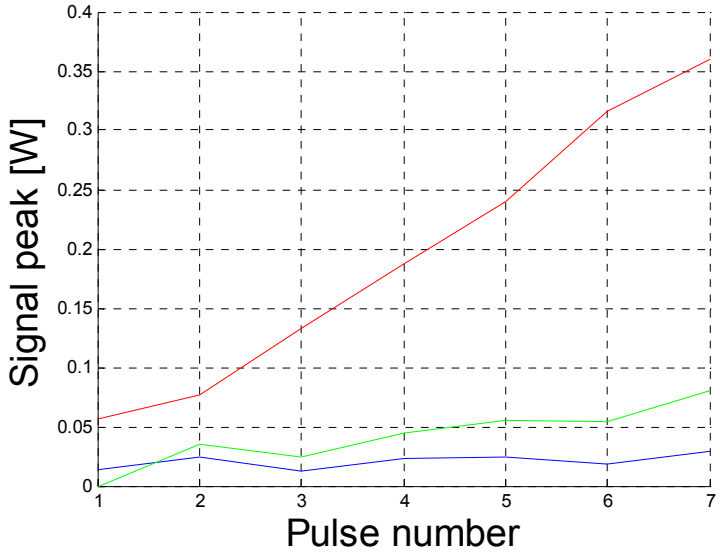

Figure 88 : The average peak value of the signal and noise terms as a function of the LO pulse number.

Note also that the recorded noise in the second frequency slot center at 27.12 MHz appears to be stable over the pulse number, as expected for seed modulator leakage. However, for seed leakage we would expect similar noise at 81.36 MHz. The fact that the frequency slot center noise originates from other phenomena cannot be excluded.

Furthermore, it should be noted that the fan signal also grows with pulse number for the recorded spectra. This is not due to an increase in emitted pulse power which is monitored. However, the growth of noise at 54.24 MHz flattens out if it is calibrated with the signal power obtained for the same pulse.

The noise terms could be expected to be phase correlated since they propagate along identical paths. Note that the noise component at 54.24 MHz has split up into two distinct lines separated with 3.5 MHz.

5.4. Conclusions on FSPT modulated lidar

The LSFS constructed in chapter 4 was successfully used to modify a continuous wave lidar into a FSPT modulated prototype. The signals observed with the prototype showed several interesting features. The measured velocity was well replicated when compared to the corresponding measurement using the lidar in cw mode. Almost the double signal strength was obtained in FSPT mode which is promising when regarding the pump power conversion efficiency of FSPT stimulated amplifiers.

However, significant amounts of noise were observed in the centers of the second and third frequency slots. This noise could occur from the seed and loop modulators but does not completely follow the expected behavior.

Several unexpected phenomena, which need further investigation, were observed, e.g. the sporadic appearance of signals in the frequency slot centers and the indication of phase correlation in the beat signal generated by the FSPT modulated lidar.

The foundation for further experimental studies of FSPT modulated lidars and optimization of the frequency sweeper has been laid. Methods to mitigate or correct for the frequency slot center noise will be necessary before wind measurements can be performed. Funds for a PhD project which will study noise characteristics of the LSFS have been secured.

6. Lidar measurement deviation proportional to wind shear

This chapter presents an investigation of wind data from a verification campaign of the Windcube commercialized by Leosphere. The investigation focuses on the wind velocity deviation of the lidar measurements compared to cup anemometer measurements as a function of wind shear.

6.1. The Windcube system in the Høvsøre verification campaign

The lidar is a pulsed coherent lidar which senses wind velocity in the first two hundred meters. Three dimensional wind velocity vectors are constructed from LOS measurements from four points in a conical scan with a 30 or 15 º cone angle.

The lidar is focused to increase the collected backscattered power from the first few hundred meters. The focus is manually set, normally at an altitude between 100 - 150 m. During the campaign the focus distance is expected to lie somewhere in the 50 - 200 m range. The system has an effective beam radius of 1.5 cm.

The Windcube system emits pulses with constant profiles and uses a truncated Gaussian shaped gate of 200 ns. The pulse shape is slightly asymmetric with more energy in the beginning of the pulse. The more distant half of the range gate will therefore contribute with slightly more energy. The averaged normalized RBP and WPP, not including range dependent collection efficiency, of the range gate in Figure 89 was measured from a hard target as explained in chapter 2.5.5 and 2.5.6. The average centroid value is at 31.6 m and has a RBP_{FWHM} = 28.5 m. The asymmetry is less important in the WPP. The centroid value is at 31.4 m and WPP_{FWHM} = 20.3 m. The RBP multiplied with τ(z), here the contribution duration, should theoretically give the WPP. The measured RBP multiplied with the theoretical correlation duration, $\tau(z) = \left(T_{pulse} - \frac{2}{c}\left| z - g_{center} \right| \right)$, is compared with the measured WPP in Figure 89. They compare very well, as expected.

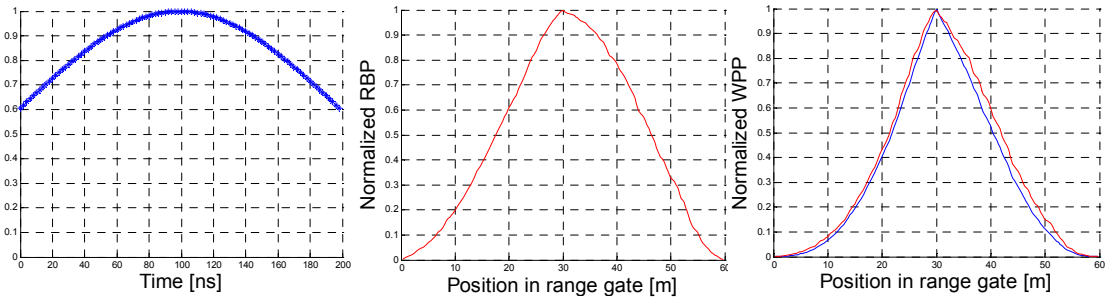

Figure 89 : From left to right; the Gaussian shaped gate, the measured RBP of the range gate, not including the collection efficiency, and finally the measured WPP, disregarding focus effects, in red and the RBP·τ(z) in blue.

Both profiles should be multiplied with the collection efficiency function, $f(z, f_{focus})$, to give the range gate shape at a distance for a specific focus distance.

6.2. The data set

The Windcube verification campaign took place from the 20th of February to the 14th of May 2007 at Risø's wind energy test site in Høvsøre[12]. The wind data is given as ten minute averages of the wind velocity measured by well calibrated cup anemometers and by the lidar. The wind is sensed at 60, 80, 100 and 116 m altitude. The wind data is filtered on wind direction, rainfall and wind velocity so that only measurements in dry weather with horizontal wind speeds faster than 4 m/s coming from a sector where the cup anemometers are unperturbed by the met mast and the surrounding turbines are considered. The horizontal wind data measured by the lidar has been post-corrected with 2.2 % and 2.1 % due to an overestimation of the intended cone angle with 0.7 º and 0.3 º for the intended 30 º and 15 º configurations respectively. This error also induces an underestimation of the actual range gate center altitude with 0.4, 0.5, 0.7 and 0.8 m for the respective range gate in the 30 º configuration and approximately 0.1 m for the 15 º configuration for all altitudes.

The data is taken during three periods. The first period from the 20th of February to the 16th of March is taken with a 30 º cone angle. The range gates were supposedly centered at 60, 80, 100 and 115 m altitude during this period. The 115 m range gate was moved to 116 m as to better correspond with the cup anemometer altitude from the 16 of March to the 16 of April. For the last period between the 17th of April and the 14th of May the lidar was configured to use a 15 º cone angle and the focus was supposedly moved further away. No other intentional changes were performed on the system during the measurement period.

From this data we calculate the lidar error at an altitude, $\Delta w(h)$, which is defined as the lidar horizontal velocity measurement minus the cup measurement, i.e. $\Delta w(h) = w_{lidar}(h)-w_{cup}(h)$. We also define the wind profile gradient, $w_{grad}(h)$, as the horizontal wind velocity increase between two cups, i.e.

$$w_{grad}(h_i) = \frac{w_{cup}(h_{i+1}) - w_{cup}(h_i)}{h_{i+1} - h_{i+1}}.$$

The wind gradient at 116 m is an exception and is defined as, $w_{grad}(116) = (w_{cup}(116)-w_{cup}(100))/16$, since there are no cup anemometers above 116 m.

The wind gradient has an irregular horizontal wind velocity dependence in this data set, an example of which can be seen in Figure 90. Parameters for the linear fit of the wind gradient vs velocity for the different periods and altitudes can be found in Table 14.

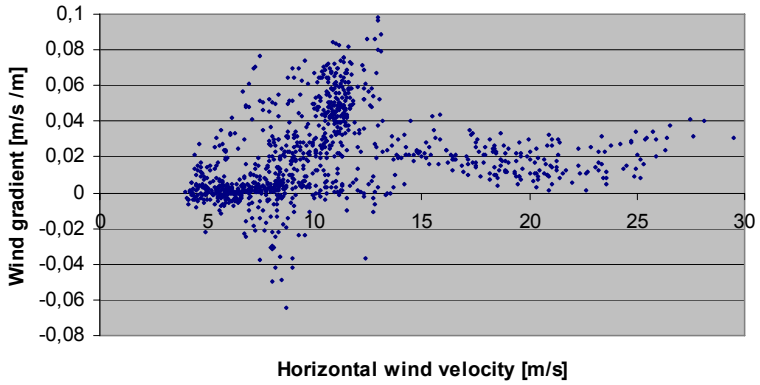

Figure 90 : Wind gradient dependence on horizontal wind velocity at 100 m for the 30 º configuration during period 2.

Altitude / Period	60	80	100	116
1	$0.0038w_{cup}$ + 0.014 $R^2 = 0.25$	$0.0028w_{cup}$ - 0.001 $R^2 = 0.17$	$0.0047w_{cup}$ - 0.024 $R^2 = 0.36$	$0.0049w_{cup}$ - 0.028 $R^2 = 0.45$
2	$0.0018w_{cup}$ + 0.012 $R^2 = 0.12$	$0.0004w_{cup}$ + 0.023 $R^2 = 0.01$	$0.0011w_{cup}$ + 0.008 $R^2 = 0.06$	$0.0014w_{cup}$ + 0.004 $R^2 = 0.09$
3	$0.0025w_{cup}$ - 0.007 $R^2 = 0.39$	$0.0013w_{cup}$ - 0.005 $R^2 = 0.23$	$0.0019w_{cup}$ - 0.009 $R^2 = 0.34$	$0.0019w_{cup}$ - 0.001 $R^2 = 0.38$

Table 14 : Linear fit parameters of the wind gradient's dependence on velocity.

The lidar values were plotted against the cup values and least square fits were made to estimate the lidar accuracy, see Figure 91. The parameters of this comparison are listed in Table 15. The obtained standard deviation and average error will depend on the wind conditions during the evaluation, which are most uniform during period 1.

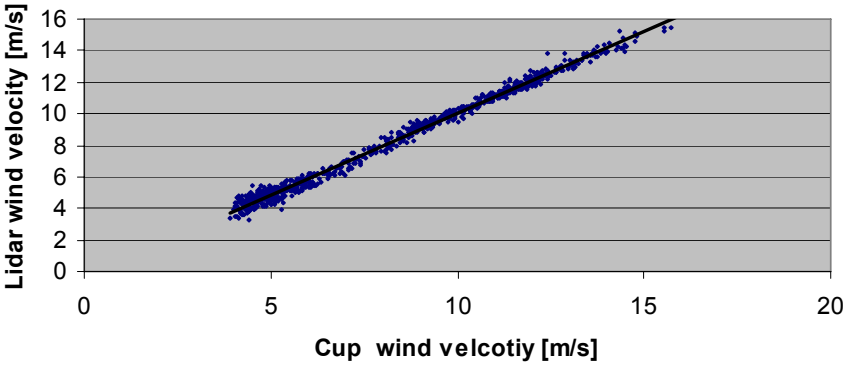

Figure 91 : Horizontal wind velocity measured by lidar and cup at 100 m in the 15 º configuration.

Period 1	k	m	R^2	Average Error	Standard deviation
Range gate center 60 m	1.041	-0.095	0.992	0.26	0.19
80 m	1.000	0.041	0.995	0.04	0.14
100 m	1.001	0.027	0.997	0.04	0.13
116 m	0.987	0.057	0.997	-0.08	0.13

Period 2	k	m	R^2	Average Error	Standard deviation
Range gate center 60 m	1.004	0.039	0.996	0.07	0.31
80 m	0.989	0.126	0.997	0.01	0.27
100 m	0.996	0.035	0.997	-0.02	0.27
116 m	0.992	0.076	0.997	-0.02	0.28
Period 3	**k**	**m**	**R^2**	**Average Error**	**Standard deviation**
Range gate center 60 m	1.030	-0.153	0.990	0.10	0.35
80 m	1.018	-0.171	0.993	-0.02	0.30
100 m	1.038	-0.337	0.994	0.00	0.33
116 m	1.043	-0.042	0.993	-0.03	0.36

Table 15 : Parameters of the least square fit of the lidar and cup comparison.

The lidar has a standard deviation of 0.2-0.3 m/s and an average error within 0.1 m/s. It seems convincingly linear with wind velocity when compared to the cup anemometer. The configuration with 15 º cone angle seems to give a slightly worse R^2 value and a higher standard deviation. The lidar seems to be slightly overestimating for most wind speeds. It appears to be an advantage to use a wider cone angle in this study of flat terrains and sensing altitudes restricted to 116 m.

However, a time series of the lidar and cup values, e.g. Figure 92, shows that the lidar deviates differently over time.

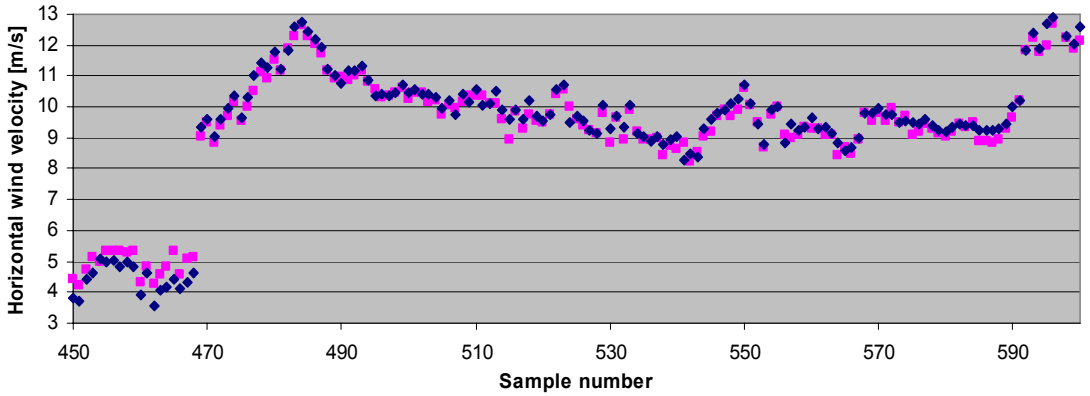

Figure 92 : A time series over the horizontal wind velocity measured by the Windcube (♦) and a cup anemometer (■) at 100 m altitude.

There are no fundamental aspects that imply that there should be a wind velocity dependent error when sensing wind with coherent lidars, except for the increased RIN at low frequencies of non-offset systems. However, in practice it can be difficult to ensure less than a 0.5 º deviation from the intended cone angle. On the other hand, it is non-trivial to estimate the wind in the center of the sample volume from the wind distribution spectrum obtained with any lidar configuration. It is also a technological challenge to set the actual center at the intended altitude, especially so for focused range gated systems. Such altitude errors would reveal themselves as a velocity error dependent on the wind profile.

6.3. Relation between the lidar error and the wind gradient

The time series of lidar and cup wind speeds at 100 m in Figure 93 shows a sudden shift in the sign of the lidar error from sample 4 to sample 5. The shift coincides with a shift in wind shear profile from a normal positive gradient, i.e. velocity increases with height, to an unusual negative gradient, i.e. velocity decreases with height. The gradient shift occurs at the fourth value. At the same point the lidar changes from being overestimating to being underestimating. This behavior would be typical for a lidar which underestimates the actual sensing altitude, i.e. for a lidar which is measuring at a higher point than the verifying cup anemometer.

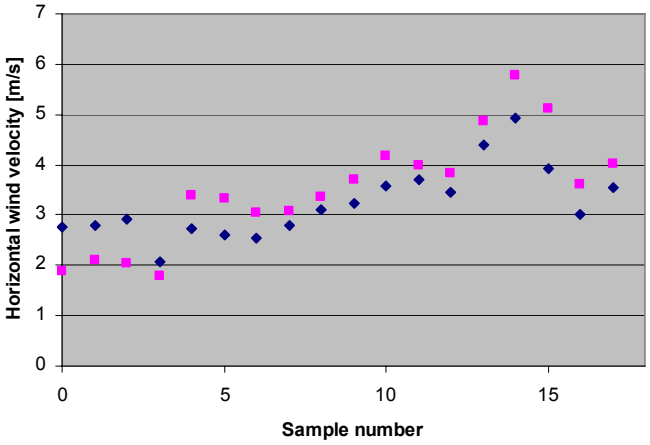

Figure 93 : Horizontal wind velocity measurements by the Windcube (♦) and a cup anemometer (■) at 60 m altitude. Between the fourth and fifth sample the wind gradient changed from positive to negative. At the same time the lidar changes from being overestimating to being underestimating.

The lidar error dependence on wind gradient can be seen in the linear regression plots in Figure 94. The regression parameters for the different periods and altitudes are listed in Table 16. The lidar error can be uniquely connected to the wind gradient if the lidar error can be expected to be independent of the wind velocity or if the wind gradient is uncorrelated to the wind velocity in the data set. The regression coefficient will thus give the altitude error assuming that the wind profile is linear between the cup and the actual sample volume center. These assumptions are fairly well, although not strictly, fulfilled for these data sets and the regression coefficient gives a plausible estimation of the altitude error. In the ideal case the m value will give an indication of a possible average bias since the lidar ought to measure the correct value independently of altitude error when the wind gradient = 0 m/s per meter in altitude.

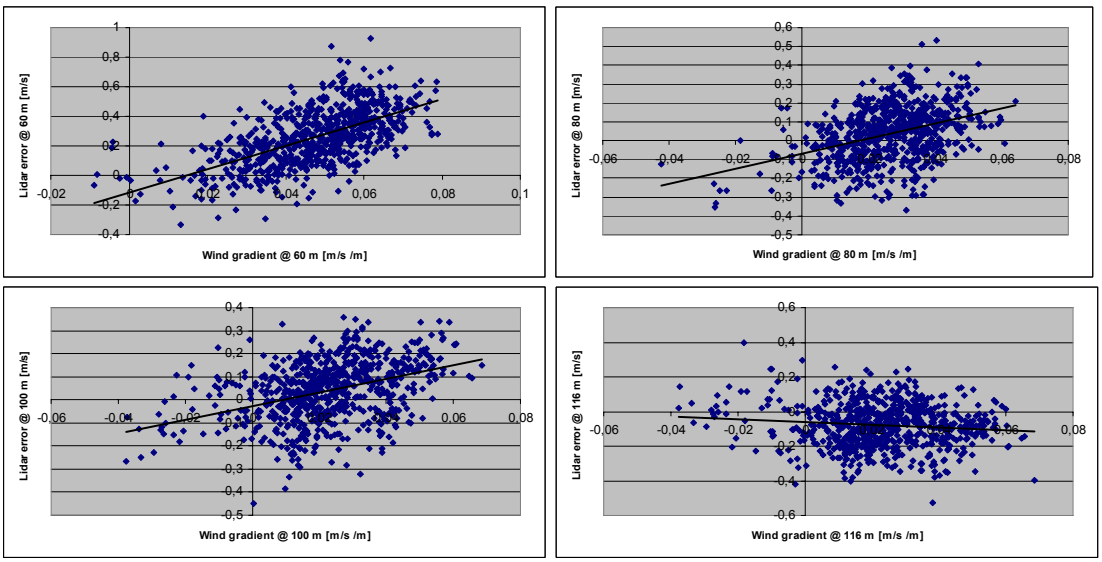

Period 1.

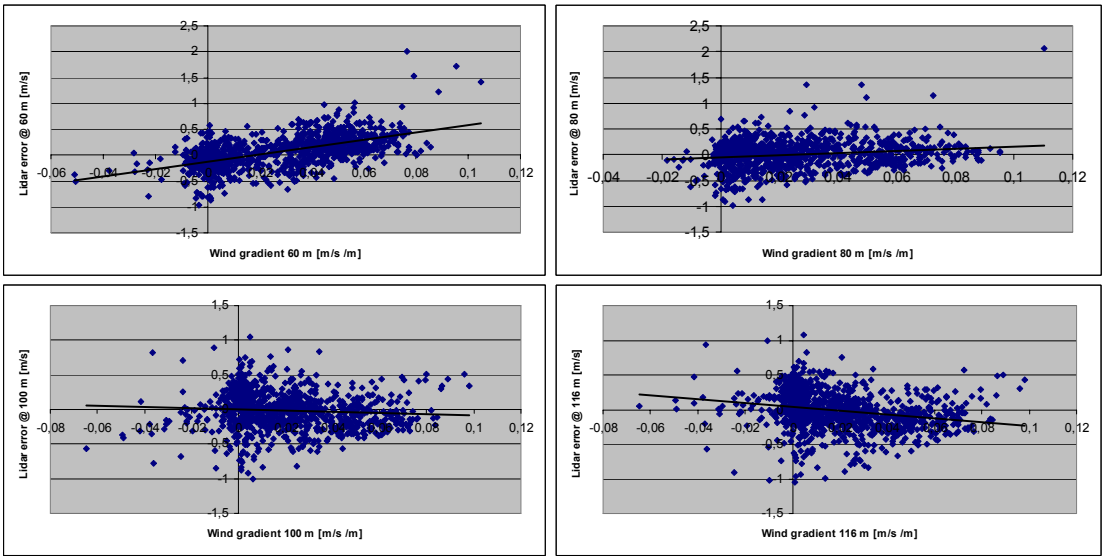

Period 2.

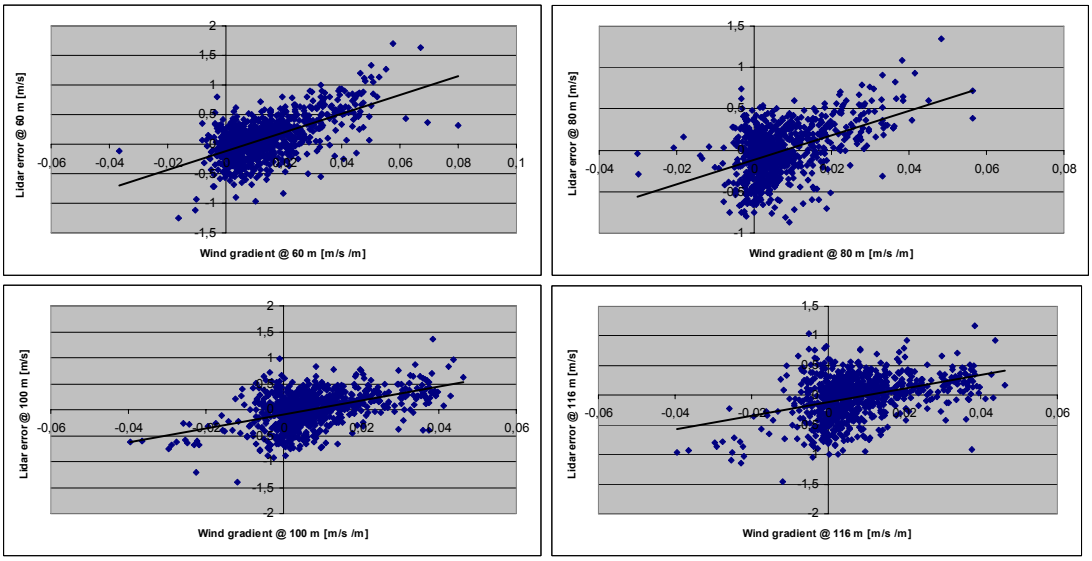

Period 3.

Figure 94 : Lidar deviation from cup anemometer measurements as a function of the wind gradient at altitudes 60, 80, 100 and 116 m clockwise from top left.

Period 1	**k = Estimated altitude error [m]**	**m = Estimated average bias [m/s]**
Range gate centre 60 m	7.9	-0.12
80 m	4.0	-0.07
100 m	3.0	-0.03
116 m	-0.8	-0.06
Period 2	**k**	**m**
Range gate centre 60 m	7.2	-0.14
80 m	2.1	-0.05
100 m	-0.9	-0.00
116 m	-2.8	0.03
Period 3	**k**	**m**
Range gate centre 60 m	16.0	-0.12
80 m	14.8	-0.11
100 m	13.4	-0.10
116 m	11.6	-0.12

Table 16 : Parameters obtained from a least square fit to the lidar error vs wind gradient plots.

The correlation between the lidar error and the wind gradient is stronger than the correlation between the lidar error and the wind velocity, exemplified in Figure 95 on the measurement at 100 m during period 1. For example, the R^2 is in the range of 0.1-0.4 in the lidar error vs wind gradient fit during the second period but less than 0.1 for the lidar error vs wind velocity.

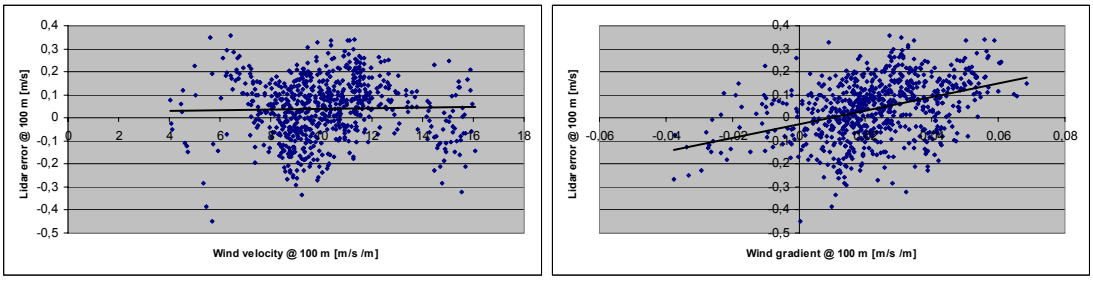

Figure 95 : Lidar error vs horizontal wind velocity (left) and vs wind gradient (right) at 100 m altitude during period 1.

The results indicate an error in the intended sensing altitude with an amount which depends on altitude. This behavior can be explained by a shift of the effective range gate center due to the range dependent collection efficiency of the focused telescope. A fixed offset in effective range gate center, e.g. due to a trigger error or an asymmetric pulse, would give a k value which is independent of altitude.

An effective range gate center above the intended altitude, and thus above the reference cup anemometer, would give an overestimation of the wind velocity when the wind profile had a normal positive gradient while an effective range gate center below the intended altitude would give an underestimation. The effective range gate center would be moved towards the focus distance in a range gated system focused at a fixed altitude. The pivot altitude, i.e. the altitude where the k value changes from positive to negative, would give the focus distance if the lidar error is exclusively due to range gate center displacement by focusing. If the lidar also has a constant offset in altitude due to other factors the focus distance should be corrected accordingly.

For the first period it is known that the range gate center is 1 m below the cup anemometer at 116 m. The focusing effect would thus only be responsible for moving the effective range gate center 0.2 m upwards. The known altitude errors, 0.4, 0.5, 0.7 and 0.8 m in the 30 º configuration, due to cone angle error should also be accounted for. However, the accuracy in the deduction of the altitude offset from linear regression is hardly that precise. The focus distance can be roughly estimated to lie at about 115, 95 and 160 m altitude for the respective periods with intra and extrapolation and disregarding other unknown altitude errors.

The focus point is not expected to change between period 1 and period 2, while the lidar error vs wind gradient study indicates that the focus was slightly closer for period 2. The pivot altitude is at a higher altitude for period three which correlates to efforts made to increase the focus distance. It is likely that the assumption of linear wind gradient between cup and actual range gate center is less accurate when the altitude offset is large, as in the third period.

The dependence is strongest for the 15 ° configuration during the third period. This is expected since an error in distance would be more strongly transferred to altitude when the cone angle is lower.

6.4. The Windcube for wind turbine site evaluation

The relatively weak significance of the lidar error can be exemplified by comparing the simplified estimation of the wind potential in Høvsøre given by the lidar and the cup anemometers. The wind potential is here simplified as the time integral of the cube of the ten minute winds speeds averaged at the four altitudes, i.e.

$$W_{potential} = \sum_{period} \left(\frac{w_i(60) + w_i(80) + w_i(100) + w_i(116)}{4} \right)^3$$

The wind potential measured with the lidar would underestimate the actual wind potential measured with cup anemometers according to Table 17.

Period 1: overestimation with 2.0 %
Period 2: overestimation with 0.2 %
Period 3: overestimation with 3.1 %

Table 17 : Wind potential overestimation of the Windcube for the three periods.

6.5. Modeled range gate distortion in a focused lidar

The actual range gate shape can be calculated by combining the WPP measurement from the hard target with the collection efficiency model as explained in chapter 2.5.6. The resulting WPP model for the four range gates of the Windcube during period 2 are plotted in Figure 96. The collection efficiency function has been modeled to correspond to a system with an effective lens radius of 1.5 cm focused at 110 m distance corresponding to 95 m altitude with a 30 º cone angle. The collection efficiency function, in dashed green, and the hard target WPP, in red, are plotted for comparison.

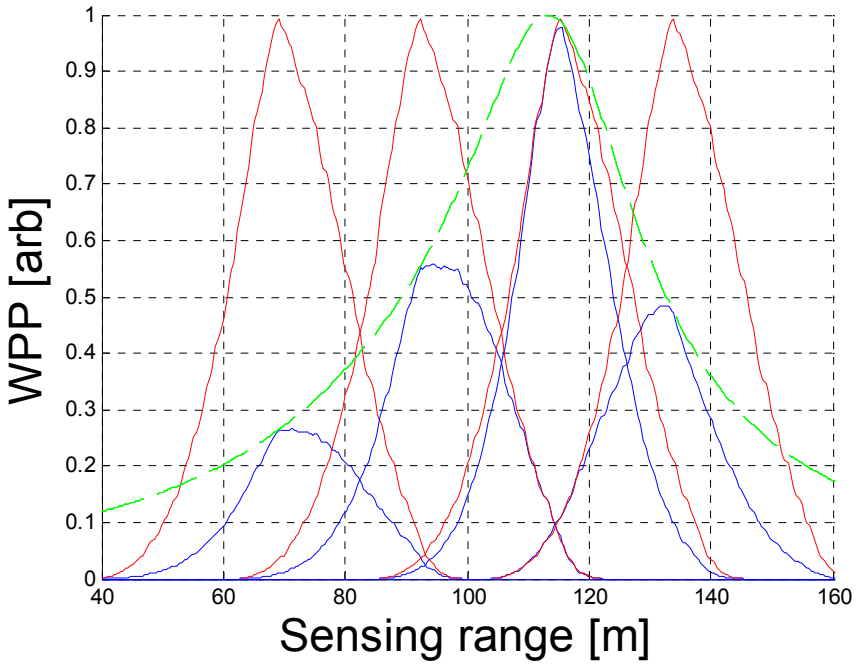

Figure 96 : Modeled WPPs for the four range gates of the Windcube (blue), measured WPP from a hard target (red) not including the range dependent collection efficiency function (dashed green).

From these WPPs it is possible to estimate deviations of the effective altitude, i.e. the range gate centers. The experimentally estimated and the modeled altitude error are compared in Table 18. The center of the range gate has been defined as the centroid of the WPP and the collection efficiency functions were modeled with a focus at 115, 95 and 160 m altitude for each period respectively.

Altitude	Period 1: Estimated altitude error	Period 1: Modeled altitude error	Period 2: Estimated altitude error	Period 2: Modeled altitude error	Period 3: Estimated altitude error	Period 3: Modeled altitude error
60	7.9	2.4	7.2	3.4	16.0	2.4
80	4.0	2.5	2.1	3.5	14.8	2.4
100	3.0	2.4	-0.9	0.3	13.4	2.3
116	-0.8	1.3	-2.8	-2.2	11.6	2.2

Table 18 : Table of the experimentally estimated altitude errors and the modeled altitude errors.

An error in the sensing altitude of up to 4 m, depending on focus and range gate distance, is predicted by the modeled WPP. The error will saturate as the focus distance diverges from the range gate position. Such altitude errors would give a limited, but important, error in wind velocity of about 0.2 m/s for a typical wind gradient of 0.05 m/s /m.

The altitude errors deducted experimentally are much larger but follow the trend of the modeled errors. The error in intended altitude can reach up to 16 m and wind velocity errors of 0.5 m/s were regularly registered. Several reasons can be given as sources to the deviation of the modeled and the experimentally obtained values. The altitude offset estimated of the linear regression plots is dependent on several assumptions, notably errors independent from wind velocity and linearity of wind profile. Another issue is how well the modeled collection efficiency describes the Windcube. The actual focus distance is unknown and could not be determined from the CNR vs height profiles. Furthermore, there is a possibility for fixed offsets due to other errors, e.g. offset triggering, in the intended sensing altitude.

Nevertheless, if the optic system can be satisfactorily modeled and the focus distance can be maintained at a set value, or be continually determined, it is possible to adjust the range gate positions such that the range gate profile is maximized at the sought altitude.

6.6. Conclusions on lidar measurement deviation proportional to wind shear

A likely error source in remote wind sensing is an error in the intended range gate center altitude. Offsets in intended altitude can be revealed by studying the lidar error as a function of wind gradient. The lidar accuracy has classically[11, 13, 22] been experimentally verified by studying the linearity in the lidar vs cup regression plots. However, errors proportional to the wind velocity, e.g. cone angle errors, might be hidden or confused with errors in intended altitude.

The results from the Høvsøre campaign indicate a lidar error dependence on wind profile gradient which changes with altitude. A likely explanation for this dependence is a shift of the effective range gate center due to the range dependent collection efficiency of the focused telescope. The offset in altitude will be towards the focus, i.e. range gate centers below the focus distance will be shifted upwards while range gate centers above focus will be shifted downwards. The lidar might also suffer from a constant offset in altitude due to other factors. An unadjusted system will make limited, but important, errors since the wind velocity typically increases slowly with height.

Estimation of the effective range gate center altitude from models predict altitude errors of up to 4 m, giving wind velocity errors of 0.2 m/s during typical wind profiles. However, larger errors are registered experimentally.

When debugging or verifying wind sensing lidars by comparing it with cup anemometers on a met mast it is important to study both the wind velocity proportional deviations as well as the wind gradient proportional deviations in a two parametric regression analysis.

7. Conclusions on fiber based coherent lidars for remote wind sensing

The knowledge of wind flow is important within several fields. For many of them the only viable solution is to sense the wind remotely. Fiber based coherent lidars are fully frequency resolving, cost effective and robust, and can operate without safety restrictions; they are thus an ideal choice for non-scientific applications.

A few lidar models are commercially available and have been verified to provide sensing with high availability over flat terrain and in typical atmospheres. Typical standard deviations in the 10 minute average horizontal wind lie in the order of 0.1-0.2 m/s. However, the systems ability to sense accurately over complex terrain, at high temporal resolution and for atmospheres including low clouds remains to be investigated.

Signal modeling of coherent lidars is important for predicting the lidar performance and for optimizing the signal processing. The standard signal model has been expanded upon by considering range dependent correlated contribution durations in a range gate which significantly affects the narrowband signal to noise description and the weighting of the sample volume.

The range dependent collection efficiency obtained by focused fiber based lidars has been modeled by considering the effects of a small aperture size and co-propagation of received scatter and local oscillator. The result of a first verification of the collection efficiency function shows that the developed model is purposeful.

The standard deviation of a wind measurement is improved by accumulating a large number of speckle takes which can be acquired at high rate by using frequency modulation techniques.

Frequency stepped pulse train modulation is a novel method appropriate for range resolved coherent lidar sensing of wind. The technique is based on equidistantly frequency stepped pulse trains and a frequency pursuing local oscillator. FSPT modulation provides unique mapping of the Doppler shifted backscatter from a set of ranges. It operates at high pulse repetition but will despite this avoid the customary disadvantages; range ambiguity and a limitation of the sensing range. This novel concept could provide more accurate systems while avoiding the use of high peak powers.

A lightwave synthesized frequency sweeper, appropriate for FSPT modulation, has been constructed and evaluated. It can provide appropriate equidistantly stepped FSPTs. However, side modes, likely to originate from seed or loop leakage, could limit the train length and deteriorate the accuracy in the wind sensing.

A continuous wave lidar has successfully been modified into a FSPT modulated prototype. Velocity measurements were well replicated when compared to the corresponding measurement using the lidar in cw mode. Almost twice the signal strength was obtained in FPST mode which is promising when regarding the pump power conversion efficiency of FSPT stimulated amplifiers. However, significant

amounts of noise were observed which need further investigation. Methods to mitigate or correct for this noise will be necessary before wind measurements can be performed.

An investigation of wind data collected with the Windcube lidar has revealed that the weighting of the sample volume of a focused range gated system will be significantly influenced by the range dependent collection efficiency function. This effect imposes an altitude dependent error in the intended range gate center which manifests itself as a horizontal wind velocity deviation dependent on the wind shear. It is important to study both the wind velocity proportional deviations as well as the wind gradient proportional deviations in a two parametric regression analysis when debugging or experimentally verifying wind sensing lidars.

An applied investigations of wind data collected with the Zephir system has revealed that the weighting of the wind distribution spectrum, obtained by focused continuous wave systems, is influenced by single particles with atypically long correlated scatter durations. Reducing the sample duration so it matches the average atmospheric correlation time will reduce the influence of this scatter.

The main achievements accomplished in this thesis are listed below.

- Invented and patented Frequency Stepped Pulse Train modulation of coherent lidars. Constructed and investigated an appropriate frequency sweeper and performed a proof of principle.

- Established the range dependent correlated contribution duration of range gated systems influence on the narrowband signal to noise ratio. Proposed a definition for the weighting function of the sample volume and refined figure of merits, taking in to account the narrowband signal, and not simply the collected energy, and thus being more appropriate for comparison of cw and range gated systems.

- Established a new model for the range dependent collection efficiency function of fiber based focused coherent lidars. Performed a first verification study of the collection efficiency function of both the new and an older model.

- Established a computer model for simulations of the wind distribution spectra obtained from a Frequency Stepped Pulse Train modulated lidar sensing atmospheres with inhomogeneous Doppler shifts and backscatter coefficients.

- Investigated experimental data from a comparative study of lidar and cup anemometer measurements. Revealed and estimated the impact on the accuracy in the wind measurement from unadjusted distortions of the range gates due to the range dependent collection efficiency of the focused commercial Windcube. Suggested possible solutions and showed on the importance of simultaneous study of both wind velocity and wind gradient dependent lidar errors.

- Revealed and estimated implications of scatter from single large particles with atypically long correlation durations on the wind sensed with a commercial variable focus cw Zephir.

Several unexpected phenomena, which need further investigation, were observed, e.g. the sporadic appearance of signals in the frequency slot centers and the indication of phase correlation in the beat signal generated by the FSPT modulated lidar. Procedures to mitigate the leakage in the LSFS or post-correct noise in the wind distribution spectra should be explored.

Furthermore, the pump power conversion efficiency of fiber amplifiers stimulated by close laying frequencies and the optimal number of accumulated spectra and thus the best trade off between PRF and pulse energy should be determined.

APPENDIX A Laser coherence

Although a well defined wavelength is one of the specific characteristics of lasers they are never truly monochromatic. A laser will have a certain spectral width caused by several phenomena. Laser coherence describes the purity of the light frequency which is often given as the FWHM linewidth of the generally Lorentzian spectrum. The spectrum can be roughly measured with a prism and a detector array, but for detailed studies homodyne spectra have to be constructed with a setup as illustrated in Figure 97. The laser output is split into two beams, of which one is made to propagate for a certain delay distance. The light in this path will constitute a delayed copy of the other. The homodyne spectrum is generated by mixing the two beams on a square law detector and detecting the homodyne current with an ESA. One path can also include an AOM which offsets the frequency so that the spectrum is relocated away from the zero frequency and low frequency noise.

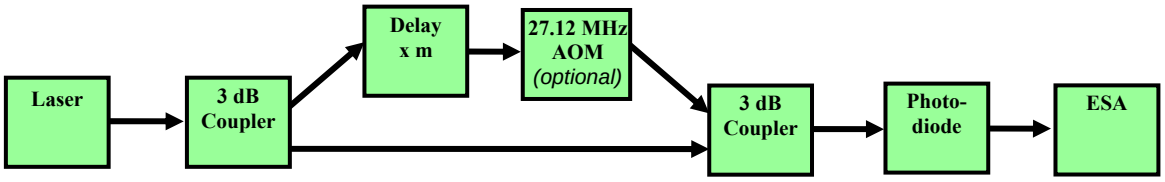

Figure 97 : Set up for the generation of the homodyne spectrum of a laser.

The so called instantaneous spectrum is generated if the propagation path difference is zero. In this case, the spectral width is due to, for example, thermal motion in the lasing media and a spectral spread in the reflectivity of the cavity mirrors.

The homodyne spectrum will broaden further as the propagation difference increases. This broadening is due to instabilities in the emitted frequency, i.e. jitter or frequency drift, typically due to cavity vibrations.

The relevant linewidth for a coherent lidar is the linewidth of the spectrum generated with a propagation path difference equivalent to two times the target range. This linewidth should preferably be smaller than the spectral spread originating from turbulence and the limited correlated scatter duration, in order to optimize the narrowband CNR. Lidar systems measuring frequency with high accuracy have to use highly coherent lasers. The velocity is obtained from the Doppler shift, using $v_{LOS} = \frac{\lambda \cdot f_{Doppler}}{2}$. The laser linewidth should not drift more than 130 kHz during the propagation time difference between the LO and the back and forth propagation of the pulse if the velocity accuracy of a 1.5 μm lidar shall be better than ± 0.1 m/s.

Regular semiconductor lasers for fiber optic communications have linewidths in the region of 10-100 MHz, which is insufficient for most wind sensing applications. The coherence of distributed feedback fiber lasers is extremely good due to the extended cavity mirrors. Fiber and YAG lasers can reach linewidths below 1 kHz.
Distributed feedback fiber lasers of the mark Basik and Adjustik produced by Koheras were used in this thesis. The homodyne spectrum of these lasers for two different delays, with and without frequency shift and amplification, can be seen in Figure 98. The spectra for the different cases have been normalized for easy comparison. The

ESA was calibrated by deducting the spectrum generated without incoming light. The FWHM linewidths were measured to 1.6 kHz and 70 kHz with propagation differences corresponding to 200 m and 39 km respectively in free space. Frequency broadening during amplification in a HighWave EDFA or frequency shifting in an N26027 AOM from NEOS is unnoticeable. Broadening of typical wind spectra due to laser coherence is insignificant when sensing up to 20-30 km with these fiber lasers as seeders.

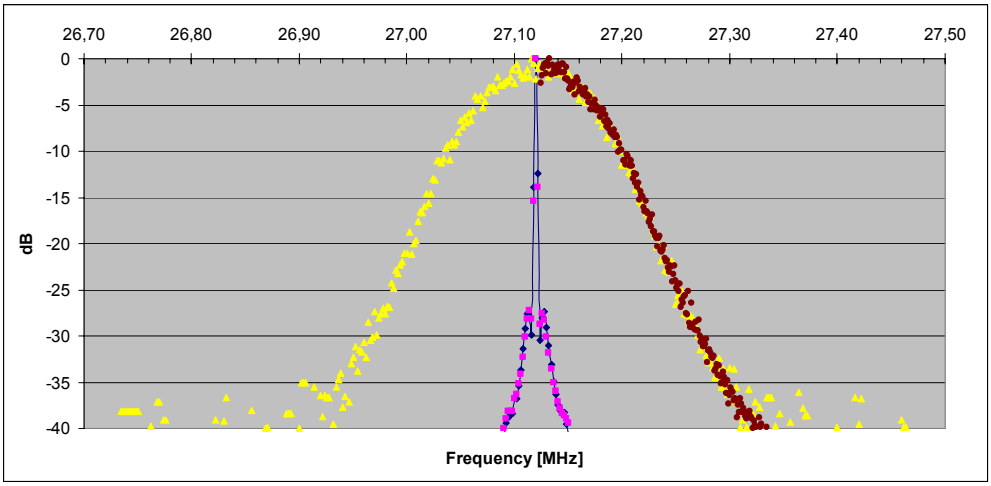

Figure 98 : Homodyne spectra of the distributed feedback fiber lasers used in this thesis. Homodyne spectrum with 39 km delay (●), spectrum moved to 27.12 MHz for comparisons. Same spectrum but with an AOM of 27.12 MHZ and 39 km delay propagation (▲), AOM and 200 m delay (♦) and AOM, EDFA and 200 m delay (■). FWHM linewidths of 1.6 kHz and 70 kHz for propagation differences corresponding to 200 m and 39 km respectively.

Another often used measure of laser coherence is the coherence length. The coherence length, $L_{coherence}$, is a measure of a lasers ability to form interference patterns. It is defined as the path length difference of a self interfering laser beam which corresponds to 60.7% ($1/e^{1/2}$) fringe visibility. The fringe visibility, V, is defined as

$$V = \frac{I_{\max} - I_{\min}}{I_{\max} + I_{\min}}$$

where I is the fringe intensity of the time average static pattern[36].

However, this definition does not imply that the sensed volume has to be within the coherence length to perform wind sensing.

A mathematical approximation between coherence length and linewidth is given by

$$L_{coherence} \approx \frac{c}{\Delta f} = \frac{\lambda^2}{\Delta \lambda}.$$

APPENDIX B Atmospheric correlation duration

A frequency component in a wind spectrum is built up from back reflections from numerous individual aerosols suspended in the atmosphere. These aerosols will quickly redistribute relatively to each other and the frequency component will only be correlated, i.e. have an essentially constant phase, for a limited duration. The correlation duration of the signal from dispersed targets is drastically shorter than for hard targets. A wind spectrum will never be narrower than one over the correlated return duration.

The duration of correlated backscatter from the atmosphere depends on several factors. It is fundamentally limited by the uninterrupted sample duration. However, if the aerosols will reconfigure considerably during one sample duration, due to turbulence or due to scanning, the effective redistribution time will set the limit of the duration of correlation. Relative redistribution is difficult to quantify but several influencing factors can be listed:

- *Turbulence.* If the small scale turbulence is strong within the contributing volume the aerosols will redistribute faster and the correlation duration will be shorter.
- *Wavelength*. The time it takes to make a relative distribution is proportional to the time it takes for aerosols to move one wavelength. The duration of correlation is thus proportional to the wavelength of the laser.
- *Volume.* In a big volume there are more particles involved in generating a frequency component. The correlation duration will fall with the sample volume. In addition the turbulence is stronger over a large volume.
- *Scanning*. As the beam sweeps the atmosphere new aerosol generates the frequency component with a new phase uncorrelated return.

It is expected that focused systems will receive backscatter with shorter correlation durations as the sensing distance increases since the sensed volume increases at the same time as the beam focus is scanned faster.

Pulsed systems typically have a correlated scatter duration which is limited by the pulse duration rather than atmospheric correlation. The atmosphere can generally be considered as frozen during short pulses but redistributed till the next. However, aerosols in the center of a range gate will contribute to the range gated wind spectrum throughout the full pulse duration while aerosols at the edges of the range gate will contribute for a shorter duration, as illustrated in Figure 39. The temporal speckle of the signal will increase and the effective correlation duration might be even shorter than postulated by the short sampling duration.

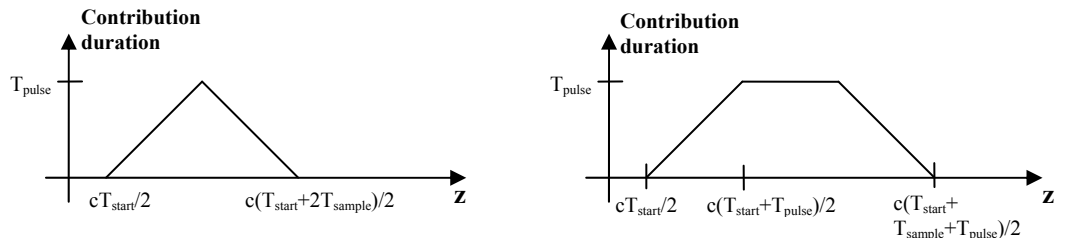

Figure 99 : Contribution duration of scatter to a range gated wind spectrum as a function of distance. For the typical case when $T_{pulse} = T_{sample}$ (right) and for $T_{sample} > T_{pulse}$ (left).

For cw systems the longest correlation duration might not be set by the, typically long, uninterrupted sample duration. It is important to know typical atmospheric correlated scatter durations since it can be advantageous to accumulate DFTs of sample durations which correspond to the correlation duration in order to suppress effects from inhomogeneous correlation durations, typically due to dominant particles.

Experiments and theoretical predictions on a pulsed[62] and a cw[35] CO_2 based system with λ = 10.6 μm and relatively long probe lengths, during moderate turbulence showed on correlation durations of less than 2.5 μs. If this estimation is extrapolated to a system with λ = 1.5 μm the correlation duration decreases to 360 ns. Still, the beam will be better defined for shorter wavelengths and the correlation duration could increase.

However, extrapolation between different systems is uncertain. In this thesis a new method has been used to estimate the correlation duration of the atmosphere. The change in the spectral width of the wind spectra obtained with a cw lidar is studied with varying sample durations. The data amount is very limited and the conclusions should be treated accordingly.

B.1. Estimation of the atmospheric correlation duration by studying the return from a cw lidar.

It is possible to make an estimation of the correlation duration of the atmosphere by studying how the wind spectra change with sample duration. The signal received from a cw coherent lidar has been Fourier transformed for different sample durations and the spectral changes were studied.

The width of a DFT spectrum is inversely proportional to the correlation duration, τ, unless it is dominantly spread by turbulence. The peak height of an FFT spectrum is proportional to the square of the sample duration if the signal is phase correlated. The accumulated spectra grow linearly with the number of accumulations. Thus, if the scatter is correlated during the full sample duration a halving of the sample duration should reveal itself as a halving of the peak height over the noise floor in the accumulated spectrum. For example, the peak height of the accumulated spectrum for sample duration T is $H(T)=N\cdot T^2$, where N is the number of accumulated samples. Halving the sample duration and thus doubling the number of accumulated samples would give a peak height $H(T/2) = 2N\cdot(T/2)^2 = (N\cdot T^2)/2=H/2$.

Nevertheless, it is difficult to determine the average scatter duration in most of these wind spectra since they include some signals with atypically high correlation durations. It is possible to look at the width of the signal but it could be widened by turbulence.

B.2. Data set

The data set is made up of heterodyne currents sampled at 50 MHz for 2.62 ms at five altitudes. The values are taken by an early cw Zephir prototype focused at 60, 100, 120, 140 and 200 m. The lidar was directed upwards with a 30 ° tilt and made a 360 ° scanning sweep in one second. The current has been low pass filtered to remove most of the low frequency RIN while still allowing low wind velocity signals to pass. The signal from 140 and 200 m is very weak and it is difficult to draw conclusions for those altitudes.

B.3. Method

Fourier transforms were made over different sample vector lengths. The frequency resolution of the Fourier transform drops considerably for short sample vectors giving rise to extensive spectral leakage. The study was for that reason also performed with zero padded sample vectors so that the sample vectors had a constant length giving a constant frequency resolution of the wind spectrum.

The energy of the smoothened accumulated spectrum was constant since the same amount of sample points were transformed independently of the sample vector size, i.e. the spectrum generated from shorter sample vectors is built up from more accumulations. The combinations of sample vectors and number of accumulated spectra in table 19 were used.

Sample duration for each spectra [μs]	Number of points in DFT	Frequency resolution of DFT [kHz]	Number of accumulated spectra	Color in plots
20.48	1024	49	128	Yellow
10.24	512	98	256	Red
5.12	256	195	512	Green
2.56	128	391	1024	Magenta
1.28	64	781	2048	Black
0.5	25	2000	5242	Blue
0.2	10	5000	13107	Cyan

Table 19 : Color allocation for the combinations of sample vector length and number of accumulated spectra used in this study.

The 10.24 μs sample represents the original setting of the Zephir prototype. Note that each simulation of an accumulated spectrum uses practically the same number of sample points (131072).

When the samples were zero padded to reduce spectral leakage the sample vectors were filled out with zeros so that every DFTs contained 1024 points. In the cases where zero padding was used the frequency resolution of the spectrum is 49 kHz independent of the sample duration.

B.4. Data processing

Accumulation of this data will take the same amount of time for a system with 100% duty cycle. However, the accumulation time will be longer for a range gated system. Accumulation of 131072 sample points will take 660 ms for a system with a PRF of 20 kHz and not 2.62 ms as for the Zephir prototype independent of sample vector length.

Processing and saving of data will also be different. The number of operations needed for a DFT follows nlog(n), where n is the size of the sample vector. 256 DFT processes of size 512 will need $256 \cdot 512 \cdot \log(512) = 355110$ operations while 2048 DFT processes of size 64 will take $2048 \cdot 64 \cdot \log(64) = 236740$ operations, i.e. one third less. Reducing the sampling duration will thus reduce the number of operations even if the total number of sample points is kept constant. If the sample vectors have to be zero padded the number of operations will increase. Since the vectors have a constant

length a decrease in sample duration will give an increase in the number of operations with the same factor.

An alternative to zero padding is to do phase uncorrelated concatenation of the return. This will not increase the correlation duration of the signal and thus not make the peaks narrower, but the frequency resolution will be improved in the same way as when using zero padding and the number of operations will not increase.

B.5. Results

Figure 100 shows the LOS wind spectrum generated from accumulations of DFTs of sample vectors with different lengths. The system was focused at 60 m.

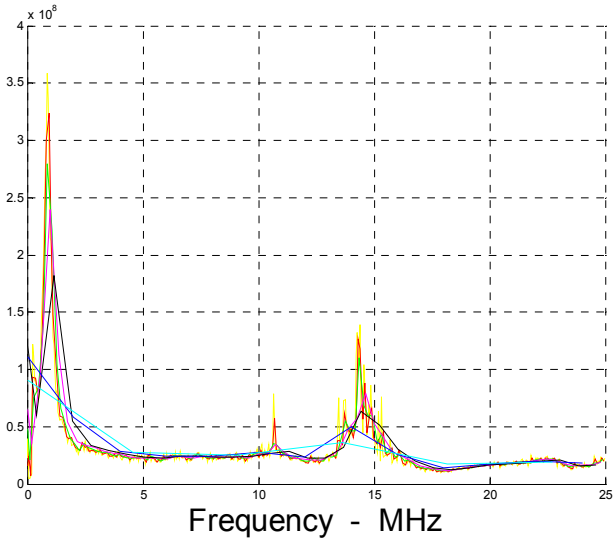

Figure 100 : Wind spectra at 60 m generated from accumulated DFTs according to the color allocation in Table 19.

The wind signal is spread over about 3 MHz around 14 MHz corresponding to a LOS wind speed of about 10.5 m/s.

The strong well confined signal at 2 MHz is the residue of the RIN after low pass filtering. The RIN can be taken into account by using a balanced receiver or by reducing the spectrum with a previously recorded noise spectrum. This has not been done for this data.

The spectral leakage for these non-zero padded samples is severe for sample durations of 1.28 μs and shorter. The spectral leakage would cause an average wind estimator to make an incorrect decision and spread the RIN up to 4 MHz which would make it difficult to deduct low wind velocities.

Figure 101 shows the wind spectrum obtained when the sample vectors have been zero padded so that all sample durations have the same frequency resolution.

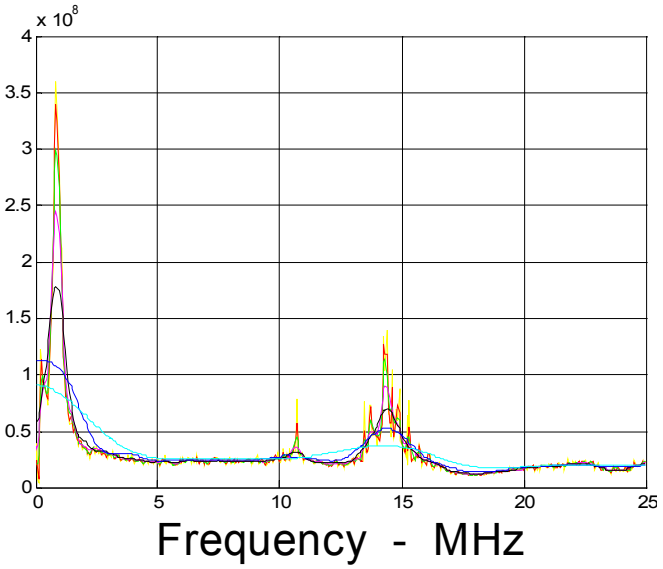

Figure 101 : Wind spectra generated from accumulated DFTs of zero padded sample vectors according to the color allocation in Table 19.

The RIN spread is less severe but still strong for the 0.2 µs sample duration. The RIN spread repeats for all altitudes and is not shown for the other focus ranges.

The signal at 11 MHz, noticeable for sample durations longer than 10.24 µs, is probably originating from a bigger particle in the beam path. The frequency component seems to have a correlation duration of more than 20.48 µs since the peak height seems to halve when the sample duration decreases from 20.48 to 10.24 µs. In this case it seems as if this particle moves with a LOS velocity of about 8 m/s. This indicates that the particle is situated at a lower altitude than the focus area since the wind typically increases with height. Although the signal at 11 MHz is well separated in this case it illustrates the potential problem with inhomogeneous correlation durations when sample durations are longer than the average atmospheric correlation duration. A single particle can give a dominant signal although it is positioned outside the effective sample volume predicted by theory for a homogenous atmosphere.

An estimation of how well the wind spectra, generated using different sample durations, represent the weighted wind distribution in the sample volume can be performed in Figure 102 and Figure 103.

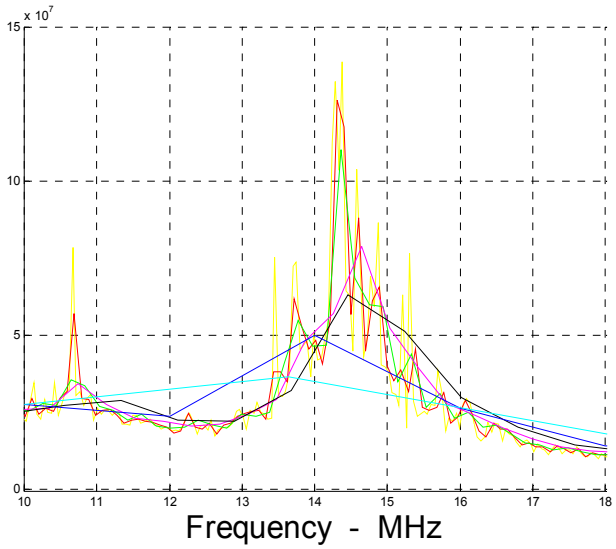

Figure 102 : Zoom of the wind spectra generated from accumulated DFTs according to the color allocation in Table 19.

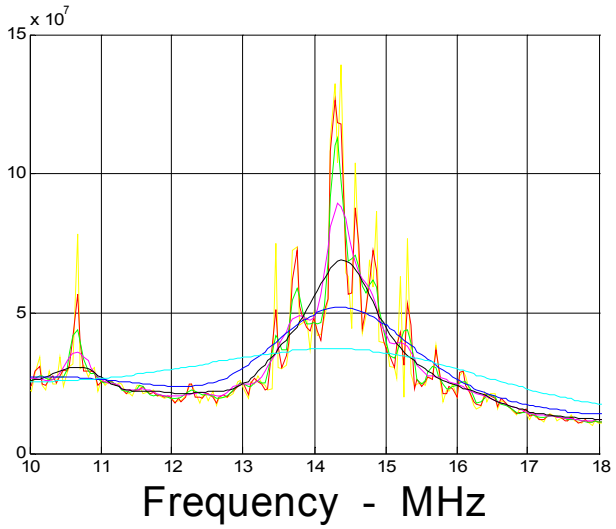

Figure 103 : Zoom on wind spectra generated from accumulated DFTs of zero padded sample vectors according to the color allocation in Table 19.

For the non-zero padded samples the frequency leakage is strong and only 5.12 µs (green) are representative of what is seen for the longer sample durations. The spectrum includes a lot of well confined energy assumingly from particles with longer correlation durations, up to 20.48 µs. For the zero padded samples the 1.28 µs and possibly also the 0.5 µs samples might even give a better representation of the spatially averaged wind spectrum in the sample volume since they are less influenced by long correlation components, which would give a significant signal even if they were not scattered from distances close to the focus. The spectrum generated with the 0.2 µs sample duration has a significantly lower narrowband CNR. The correlation duration seems to be shorter than 5 µs since the spectra do not change much for sample durations longer than this. A rough estimation of the average atmospheric correlation duration is between 0.5 and 2.5 µs since the signal bandwidth seems to be similar for these sample durations.

Figure 104 shows the LOS wind spectrum from 100 m and illustrates the problem with RIN spread due to spectral leakage for sample vectors shorter than 64 points. The spectra appear to be reasonably well described even for sample durations of 2.56 µs. However, it is possible to find an average velocity from the spectrum also for the 0.5 µs samples when zero padding is used to increase the frequency resolution. The atmospheric correlation duration is in this case judged to be 0.5 to 1.5 µs.

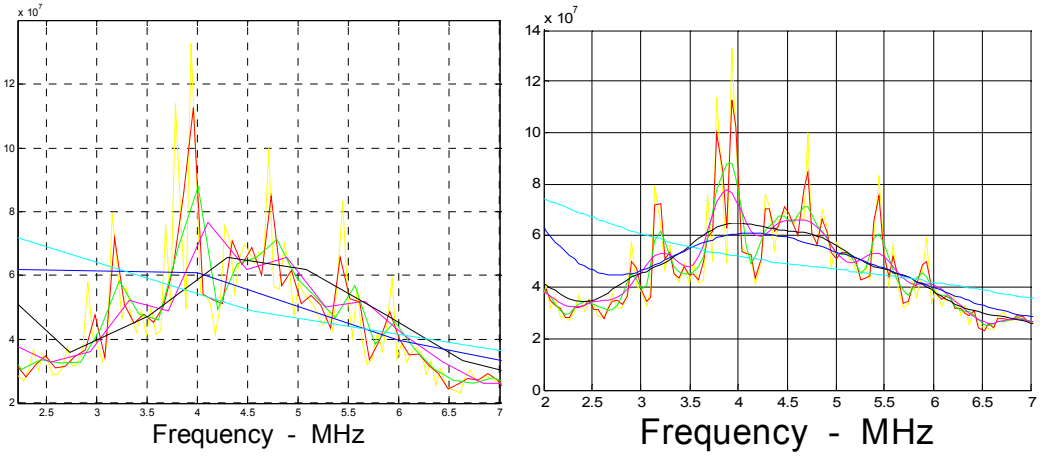

Figure 104 : Zoom on wind spectra from 100 m generated from accumulated DFTs, the spectra generated with zero padded sample vectors on the right. Color allocation according to Table 19.

Similar conclusions can be drawn for the data from 120 and 200 m in Figure 105.

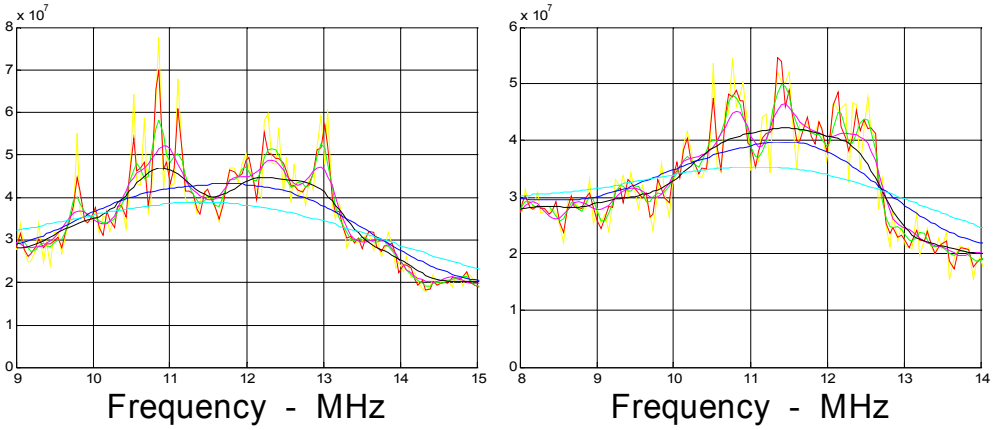

Figure 105 : Zoom on wind spectra from 120 m (left) and 200 m (right) generated from accumulated DFTs of zero padded sample vectors. Color allocation according to Table 19.

B.6. Conclusions on the atmospheric correlation duration

The weighting of the wind distribution spectrum is influenced by single particles with atypically long correlated scatter durations when sensed by focused continuous wave systems. Doppler spectra generated with sample durations longer than the average atmospheric correlation duration could be skewed if larger particles are present in the beam but outside the effective sample volume of a cw system. Reducing the sample duration will reduce the influence of scatter with uncharacteristically long correlation durations, most likely scattered off larger particles.

Shorter sampling durations will diminish the accuracy of the velocity sensing since the frequency resolution in the wind distribution spectrum decreases. Zero padding can make up for this, though to the cost of heavier calculation.

The correlation duration of the signal from aerosols in the atmosphere sensed with a 1.5 μm cw lidar can be roughly estimated to be 0.5-2.5 μs for this study. Uncharacteristically long correlation durations, longer than 20 μs, assumed to come from larger particles have been registered.

The RIN becomes severely more spread with a decrease in the sampling duration to less than < 1 μs, even when zero padding was used. Low wind speed measurements might become hidden in this noise.

Using zero padded sample vectors from sampling durations of 0.5-1 μs seems to give results which have sufficient frequency resolution to give representative wind velocity imaging and at the same time reduce possible skewing effects due to larger particles.

Acronyms

LOS	Line Of Sight
DWL	Doppler Wind Lidar
DIAL	Differential Absorption Lidar
CNR	Carrier-to-Noise Ratio
MOPA	Master Oscillator Power Amplifier
AOM	Acousto-Optic Modulator
RIN	Relative Intensity Noise
LO	Local Oscillator
PRF	Pulse Repetition Frequency
EDFA	Erbium Doped Fiber Amplifier
cw	Continuous Wave
OSA	Optical Spectrum Analyzer
DFT	Discrete Fourier Transform
SBS	Stimulated Brillouin Scattering
SPM	Self-Phase Modulation
ASE	Amplified Spontaneous Emission
LNA	Low Noise Amplifier
FWHM	Full Width Half Maximum
RBP	Received Backscatter Profile
WPP	Wind Peak Profile
FOM	Figure Of Merit
FSPT	Frequency Stepped Pulse Train
SRS	Stimulated Raman Scattering
OCT	Optical Coherence Tomography
FBG	Fiber Bragg Grating
EOM	Electro-Optic Modulator
LSFS	Lightwave Synthesized Frequency Sweeper
MZ	Mach-Zehnder
ESA	Electrical Spectrum Analyzer
LP	Low Pass
HP	High Pass

Bibliography

[1] John E. Koroshetz, "Fiber Lasers for Lidar", Optical Fiber Communication Conference, 2005. Technical Digest. OFC/NFOEC, vol. 6, pp. 2200 (2005)
[2] C. Karlsson, F. Olsson, D. Letalick, M. Harris, "All-fiber multifunction continuous-wave coherent laser radar at 1.55 μm for range, speed, vibration and wind measurements", Appl. Opt. vol. 39, No. 21, pp. 3716-3726 (2000)
[3] M. Bennet, "Doppler lidar for boundary-layer measurements: must it be expensive", Proc. of SPIE vol. 5226, pp 249-259 (2003)
[4] H. Nielsen and P. Lindelöw, "Frequency stepped pulse train modulated coherent lidar system, method and use", Patent Application PA 2006 01409/P/ADJ (2006)
[5] C. M. Sonnenschein and F. A. Horrigan "Signal-to-Noise Relationship for Coaxial Systems that Heterodyne Backscatter from the Atmosphere" in Applied Optics, vol. 10, No 7, pp. 1600-1604 (1971)
[6] R. Hunter et al., "Wind speed measurement and use of cup anemometry" in "Recommended practices for wind turbine testing and evaluation", Chapter 11, (2003)
[7] Zak, J. A., "Atmospheric Boundary Layer Sensors for Application in Wake Vortex Advisory System." NASA/CR-2003-212175. April 2003.
[8] N. Douglas, "Practical experience with remote sensing – A consultancy perspective" 51st IEA topical expert meeting pp. 31- 40 (2007)
[9] I. Antoniou and H. Jørgensen, "Wind measurement in flat terrain and offshore using sodars" 51st IEA topical expert meeting pp. 47- 54 (2007)
[10] Crescenti, G. H. "A Look Back on Two Decades of Doppler SODAR Comparison studies.", Bull. Amer. Meteorol. Soc.; Vol. 78, 1997; pp. 651-673
[11] D. Smith, M. Harris, A. Coffey, T. Mikkelsen, H. Jørgensen, J. Mann, R. Danielian, "Wind Lidar evaluation at the Danish wind test site in Høvsøre" Wind Energy, vol. 9, No. 1, pp. 87-93 (2006)
[12] J.P. Cariou, R. Parmentier, M. Valla, L. Sauvage, I. Antiniou and M. Courtney, "An Innovative and autonomous 1.5 μm coherent lidar for PBL wind profiling", Proceedings of 14th Coherent Laser Rasar Conference (2007)
[13] A. Albers, "Evaluation of Zephir", Internal report, VC05050, PWG 06005, Deutsche WindGuard (2006)
[14] A. Jelalian, in "Laser Radar Systems", Artech House (1992)
[15] N. Takeuchi, "Elastic Lidar Measurement of the Troposphere" in Laser Remote Sensing chap. 3 (Taylor & Francis 2005)
[16] S. Henderson, P. Gatt, D. Rees and M. Huffaker, "Background", Chapter 7.2.1 in Laser Remote Sensing edited by T. Fujii and T. Fukuchi, Taylor and Francis, pp. 475-479 (2005)
[17] V. Kovalev and W. Eichinger, "Differential Absorption Lidar Technique" in *Elastic Lidar* chap. 10 (Wiley-Interscience 2004)
[18] M. Harris, G. Constant and C. Ward, "Continuous-wave bistatic laser Doppler wind sensor", Appl. Opt. vol. 40, No. 9, pp. 1501-1516 (2001)
[19] M. J. Kavaya and P. J. M. Sume, "Continuous wave coherent laser radar: calculation of measurement location and volume", Appl. Opt. vol. 30, pp. 2634-2642 (1991)
[20] T. Okoshi, K. Kikuchi, A. Nakamura, "Novel method for high resolution measurement of laser output spectrum", Electron. Lett. 16, pp. 630-631 (1980)
[21] C. L. Korb, B. M. Gentry and C.Y. Weng, "Edge technique: theory and application to the lidar measurement of atmospheric wind", Appl. Opt. vol. 31, No. 21, pp. 4202-4209 (1991)
[22] D. Foussekis, F. Mouzakis, P. Papadopoulos and P. Vionis, "Wind Profile Measurements using a LIDAR and a 100m Mast", Conference proceedings of EWEC 2007 (2007)
[23] J. Mann, F. Bingöl, M. Courtney, I. Antiniou, G. Larsen, T. Mikkelsen, E. Dellwik and H. Jørgensen, "Lidars in Wind Energy", Proceedings of 14th Coherent Laser Rasar Conference (2007)
[24] M. Harris, M. Hand, A. Wright, "Lidar for Turbine Control", Technical report NREL/TP-500-39154,(2006)
[25] P. Ingmann, "The Science Aspects of the ADM-Aeolus Mission, ADM-Aeolus Workshop" ESA-ESTEC, (2006)
[26] M. Harris, D. Smith and A. Coffey, "Laser radar device and method", Patent Application WO 2005/ 114253 A1 (2005)
[27] S. Hammond, S. Vetorino, J. Pelk, "Next Generation Doppler Lidar Sensors at 1.6 μm", 14th Coherent Laser Radar Conference (2007).
[28] R. Calhoun, A. Wieser, M. Princevac and C. Kottmeier, "Comparison of lidar data with tower, profiler, radiosonde and thethersonde data", presented at 85th AMS Annual Meeting (2005)

[29] S. Kameyama, T. Ando, K. Asaka, Y. Hirano and S. Wadaka, "Compact all-fiber pulsed coherent Doppler lidar system for wind sensing", Appl. Opt. Vol. 46, No. 11 pp. 1953-1962 (2007)
[30] G. Pearson and J. Eacock, "A fibre-based coherent pulsed Doppler lidar for atmospheric monitoring", Proceedings of SPIE, Vol. 4484, pp. 51-57 (2002)
[31] G. Pearson, P. Roberts, J. Eacock and M. Harris "Analysis of the performance of a coherent pulsed fiber lidar for aerosol backscatter applications", Appl. Opt. Vol. 41, No. 30 pp. 6442-6450 (2002)
[32] V. Philippov, C. Codemard, Y. Jeong, C. Alegria, J. Sahu, J. Nilsson and G. Pearson, "High-energy in-fiber pulse amplification for coherent lidar applications", Opt. Lett. Vol. 29, No. 22, pp. 2590-2592 (2004)
[33] G. Pearson and C. Collier, "A pulsed CO_2 lidar for boundary layer meteorology", Q. J. R. Meteorol. Soc. vol. 125, No. 559, pp. 2703-2721 (1999)
[34] F. Gibert, L. Joly, I. Xueref-Remy, M. Schmidt, M. Ramonet, P. Flamant, D. Bruneau and D. Edouart, "2-μm Heterodyne Differential Absorption Lidar for both atmospheric CO_2 and wind measurements: validation and geophysical application", Proceedings of 14th Coherent Laser Rasar Conference (2007)
[35] R. M. Hardesty, R. J. Keeler, M. J. Post and R. A. Richter, "Characteristics of coherent lidar returns from calibration targets and aerosols," Appl. Opt. Vol. 21, pp 3763-3769 (1981).
[36] M.Harris, G. Pearson and M. Vaughan, "The role of laser coherence length in cw coherent laser radar", Journal of modern optics, Vol. 45, No. 8, pp. 1567-1581 (1998)
[37] T. Ando, S. Kameyama, T. Sakimura, K. Asaka and Y. Hirano, "Long range all-fiber Coherent Doppler LIDAR (CDL) system for wind sensing" Proceedings of 14th Coherent Laser Rasar Conference (2007)
[38] M. Valla, "Etude d'un lidar Doppler impusionnel à laser Erbium fibré pour des measures de champ de vent dans la couche limite de l'atmosphere", Doctoral thesis, Ecole Doctorale d'informatique, télécommunications et électronique de Paris (2005)
[39] A. Dabas, P. Drobinski and P. Flamant, "Adaptive filters for frequency estimate of heterodyne Doppler lidar returns: Recursice implementation and quality control", Jour. of Atmospheric and Oceanic Tech. Vol. 16 pp. 361-372 (1999)
[40] R.Frehlich and M. Yadlowsky, "Performance of Mean-Frequency Estimators for Doppler Radar and Lidar", J. Atmos. Oceanic Technol., Vol 11, pp 1217-1230 (1994)
[41] H. Jørgensen, T. Mikkelsen, J. Mann, D. Bryce, A. Coffey, M. Harris, D. Smith, "Site wind field determination using a cw Doppler lidar - comparison with cup anemometers at Risø" Proceedings. Special topic conference: The science of making torque from wind, Delft (NL), p. 261-266 (2004)
[42] V. Banakh and C. Werner, "Computer simulation of coherent Doppler lidar measurement of wind velocity and retrieval of turbulent wind statistics", Optical Engineering, vol. 44(7), pp 1-19 (2005)
[43] B. Rye and M. Hardesty, "Discrete spectral peak estimation in incoherent backscatter heterodyne lidar. I: Spectral accumulation and the Cramer-Rao lower bound", IEEE trans. Geoscience and remote sensing, vol. 31, No 1, pp 16-27 (1995)
[44] B. Rye and M. Hardesty, "Discrete spectral peak estimation in incoherent backscatter heterodyne lidar. II: Correlogram accumulation", IEEE trans. Geoscience and remote sensing, vol. 31, No 1, pp 28-35 (1993)
[45] C. Werner, F. Köpp and R. L. Schwiesow, "Influence of clouds and fog on LDA wind measurements", Appl. Opt., vol. 23 No. 15, pp. 2482-2484 (1984)
[46] M. I. Skolnik, "Frequency-Modulated CW Radar" in "Introduction to Radar Systems" chap. 3.3, pp. 81-84 (McGraw-Hill International Editions, Second edition 1988)
[47] A. Dorrington, R. Künnemeyer and P. Danehy, "Reference-beam storage for long-range low-coherence pulsed Doppler lidar", Appl. Opt., vol. 40 No. 18, pp. 3076-3081 (2001)
[48] V. A. Banakh, I. N. Smalikho, F. Köpp and C. Werner, "Representativeness of wind measurements with a CW Doppler lidar in the atmospheric boundary layer", Appl. Opt., vol. 34 No. 12, pp. 2055–2067 (1995)
[49] M. W. Phillips, P. J. M. Suni, J.A. L. Thomson, "Fiber-based LADAR Transceiver for range/Doppler imaging with frequency comb generator", United States Patent 5,835,199 (1998)
[50] E.T.Wetjen, D.M.Sonnenfroh, M.G.Allen and T.F.Morse, "Demonstration of a rapidly tuned Er3+-doped fiber laser for sensitive gas detection", Appl. Opt., vol. 38, pp. 3370-3375 (1998)
[51] Koheras' Product Information Sheet - "Koheras ADJUSTIK™ Fiber laser system", July (2005)
[52] Dynamic-structures Product Information Sheet – "2LD, Two-Level Piezo Driver" (2005)
[53] F. D. Nielsen, L. Thrane, J. Black, A. Bjarklev, P. Andersen, "Broad bandwidth light-wave frequency synthesizer in the 1-1.1 μm range", Proceedings of the SPIE. Vol. 5709, pp. 222-230 (2005)

[54] K. Iizuka, Y. Imai, A. P. Freundorfer, R. James, R. Wong, S. Fuji, “Optical step frequency reflectometer”, J. Appl. Phys. Vol. 68 No. 3, pp. 932 -936 (1990)
[55] K. Shimizu, T. Horiguchi and Y. Koyamada, “Frequency translation of light waves by propagation around an optical ring circuit containing a frequency shifter: 1. Experiment.”, Appl. Opt., vol. 32 No. 33, pp. 6718-6726 (1993)
[56] P. Coppin and T. G. Hodgkinson, “Novel optical frequency comb synthesis using optical feedback”, Electron. Lett., vol. 26 No. 1, pp. 28-30, 1990
[57] Koheras’ Product Information Sheet - "Koheras BASIK™ Fiber laser system", (July 2005)
[58] JDS Uniphase’s Product Information Sheet - "Dual Parallel Mach-Zenhder Modulator", (November 2006)
[59] IntraAction Corp.’s Product Information Sheet - "Model FCM series Fiber pigtailed Acousto-Optic Modulator"
[60] IPG photonics’ Product Information Sheet - "EAR SF-LP Series: 1-100W C & L Band Single Frequency Linearly Polarized Erbium Fiber Amplifier"
[61] H. Takesue and T. Horiguchi, ”Broad-Band Lightwave Synthesized Frequency Sweeper Using Synchronous Filtering”, J. Lightwave Tech. vol 22. 775-762 (2004)
[62] G. Ancellet, R. Menzies, “Atmospheric correlation-time measurements and effects on coherent Doppler lidar”, J. Opt. Soc. Am. A/Vol. 4, No.2 (1987)

Appended papers and patent application

This thesis includes the following papers. The contents of the papers are also provided in the main text.

Paper A : P. Lindelöw and J. Mohr "Coherent lidar modulated with frequency stepped pulse trains for unambiguous high duty cycle range and velocity sensing in the atmosphere", in proceedings of the IEEE-2007 International Geoscience and Remote Sensing Symposium (2007)

Paper B : P. Lindelöw "Velocity sensing FSPT-modulated coherent lidar", in proceedings of the 14th Coherent Laser Radar conference (2007)

Extract of patent application : H. Nielsen and P. Lindelöw, "Frequency stepped pulse train modulated coherent lidar system, method and use", Patent Application PA 2006 01409/P/ADJ (2006)

Coherent lidar modulated with frequency stepped pulse trains for unambiguous high duty cycle range and velocity sensing in the atmosphere

Petter Lindelöw and Johan Jacob Mohr
Ørsted•DTU, COM•DTU
Technical University of Denmark
Kongens Lyngby, Denmark
pli@oersted.dtu.dk

***Abstract*— Range unambiguous high duty cycle coherent lidars can be constructed based on frequency stepped pulse train modulation, even continuously emitting systems could be envisioned. Such systems are suitable for velocity sensing of dispersed targets, like the atmosphere, at fast acquisition rates. The lightwave synthesized frequency sweeper is a suitable generator yielding fast pulse repetition rates and stable equidistant frequency steps. Theoretical range resolution profiles of modulated lidars are presented.**

Keywords: coherent lidar; frequency modulation; frequency step; frequency sweeper; LSFS; high PRF; range unambiguity

I. INTRODUCTION

Coherent lidar is a technology suited for remote wind velocity sensing [1]. Range resolved wind velocity is typically found from the Doppler shift and the time of flight of scatter generated by a coherent laser pulse reflecting off aerosols. The resulting range gated Doppler power spectra from typically thousands of pulses are accumulated to improve the accuracy since the received scatter from clear atmospheres are weak and speckled. The three dimensional wind velocity vector is constructed by probing in several directions. The pulse repetition frequency (PRF) is principally limited by range ambiguities. Focused cw systems and frequency modulation techniques have been used to increase duty cycles [2, 3]. However, focused systems are limited in range and rely on atmospheric homogeneity [4]. Saw tooth chirping is unsuitable for range resolved velocity sensing of the atmosphere since it introduces irresolvable range-Doppler ambiguities.

This paper proposes and describes a FM technique based on Frequency Stepped Pulse Trains (FSPT) suitable for high duty cycle range resolved coherent lidar sensing of primarily dispersed moving targets. FSPT modulation provides a unique range-cell to frequency-slot mapping, thus avoiding range and range-Doppler ambiguities. FSPT modulated continuously emitting lidars could potentially reach the resolution of low duty cycle systems based on short high peak power pulses.

Multi-frequency carrier wave systems based on range gating of pulses containing several frequencies simultaneously have previously been proposed [5]. The advantage being that the resulting spectra contained a comb of Doppler peaks related to the wind velocity. However, such solutions do not permit for a faster PRF without compromising the range ambiguity.

Recently several commercial initiatives, most notably Qinetiq's Zephir and Leosphere's Windcube, have been launched targeting the wind power industries need for remote wind velocity sensing in the first 200 m. Initial applications are site evaluation and power curve verification but also as a diagnostic tool. Future commercial applications might include airport wind surveillance and active wind turbine control. Existing cw lidar designs can be modified to use FSPT modulation with minimum changes to the transmitter side using a Lightwave Synthesized Frequency Sweeper (LSFS). Such systems will be insensitive to cloud induced range ambiguities and the range resolution at long distances will be improved. FSPT can also be employed to provide faster acquisition rates than in current low PRF systems.

II. METHOD

A single frequency coherent lidar emitting a frequency f_{trans} generates Doppler shifted scatter from a moving target with frequency $f_{rec} = f_{trans} + f_D$ where $f_D = 2v_{LOS}/\lambda$ and v_{LOS} is the target's line-of-sight velocity. The received backscatter beats with a reference local oscillator (LO) in a square law detector to form a heterodyne signal current. The LO has a frequency f_{LO}, possibly offset from the transmitted frequency by a known f_{offset}, i.e $f_{LO} = f_{trans} - f_{offset}$. The generated heterodyne signal will have an intermediate frequency $f_i = f_{rec} - f_{LO} = f_D + f_{offset}$, typically of some MHz, from which the

Doppler shift can be deducted. When sensing a dispersed moving target, like the atmosphere, the heterodyne signal will contain a spectrum of frequencies, here referred to as a peak. The peak represents a speckle take of the wind distribution in the volume contributing with scatter during the sampling duration.

An FSPT modulated lidar emits a train of pulses. The carrier wave frequency is stepped between consecutive pulses by an equidistant step, Δf. The FSPT is further more described by the duration of fixed frequency, T_{pulse}, and the duration without emission, T_{inter}, according to Fig. 1.a. In a preferred embodiment the pulses are emitted without intervals, i.e. $T_{inter} = 0$ s. The train is thus emitting continuously and is only pulsed in the sense that the emitted frequency steps every T_{pulse}. An FSPT modulated lidar will concurrently receive Doppler shifted and frequency stepped light scattered from several range sets of the atmosphere as illustrated in Fig. 1.b. Mixing this scatter with an LO and Fourier transforming the beat signal will give a heterodyne spectrum with a set of separate peaks each representing speckle takes of the wind velocities in the respective range set. If the frequency step is larger than the plausible variations in Doppler shift, the detected peaks will be uniquely allocated in a specific closed range of frequencies. Such frequency ranges will be referred to as frequency slots, shown in Fig. 1.c.

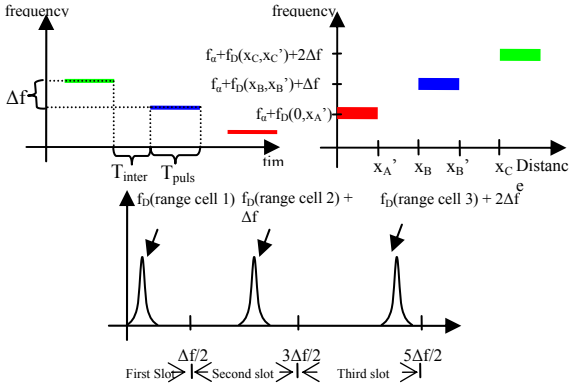

Figure 1 a) An FSPT with pulse duration, T_{pulse}, interpulse duration, T_{inter}, and pulse-to-pulse frequency step, Δf. b) Frequency as a function of scattered distance received by the lidar at time t_α when a full pulse has just been emitted. Note that the ranges contributing at t_α are $x_A' = (c/2)(T_{pulse})$, $x_B = (c/2)(T_{pulse} + T_{inter})$ and $x_B' = (c/2)(2T_{pulse} + T_{inter})$ etc. c) The scatter from the first three range cells mapped into their allocated frequency slots, $f_{offset} = 0$ MHz in this case.

The LO of an FSPT modulated lidar is a copy of the emitted train, possibly delayed with T_{delay}. Triggered sampling for one spectrum is done during a full LO pulse of duration T_{pulse}. The range set contributing to the peak in a specific frequency slot during a full sampling period will be referred to as a range cell. Each range-cell is continuously and uniquely mapped into its allocated frequency slot since the scattered frequency keeps its relation with the LO over consecutive pulses if the train parameters are effectively constant, as in Fig. 2.

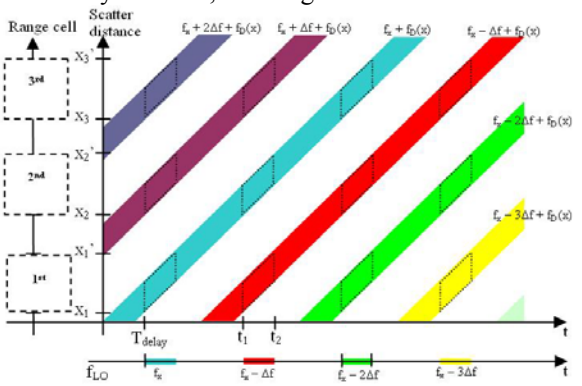

Figure 2: Time-space representation of scatter detected by an FSPT modulated lidar with a delayed LO and a considerable inter pulse duration for clarity.

E.g. The scatter received from the second range cell, x_2 to x_2', at time T_{delay} to $T_{delay} + T_{pulse}$, illustrated by the first purple parallelogram from the left, will generate a peak at $(f_x + \Delta f + f_D(x_2..x_2')) - f_x = \Delta f + f_D(x_2..x_2')$ when mixed with the LO pulse of frequency f_x. The scatter received from the same range cell at $t_1 = T_{delay} + T_{pulse} + T_{inter}$ to $t_2 = T_{delay} + 2T_{pulse} + T_{inter}$, the second light blue parallelogram from the left, mixed with the LO pulse of frequency $f_x - \Delta f$, will generate a second speckle take of the wind distribution in the second range cell, likewise allocated into the second frequency slot. Range cell i extends from x_i to x_i' described from

$$x_i = \left(T_{delay} + (i-2)T_{pulse} + (i-1)T_{inter}\right)\cdot\frac{c}{2} \qquad (1)$$

$$x_i' = \left(T_{delay} + i\cdot T_{pulse} + (i-1)T_{inter}\right)\cdot\frac{c}{2} \qquad (2)$$

Note that the first range cell will be cropped if $T_{delay} < T_{pulse}$ and that neighboring cells will overlap partly if $T_{pulse} > T_{inter}$.

Range cell i will generate a Doppler peak in frequency slot i extending from f_i to f_i' according to

$$f_i = f_{offset} + \left(i - \frac{3}{2}\right)\cdot\Delta f \qquad (3)$$

$$f_i' = f_{offset} + \left(i - \frac{1}{2}\right)\cdot\Delta f \cdot \qquad (4)$$

Note that the first frequency slot will include velocity ambiguities if $f_{offset} < \Delta f/2$, this ambiguity will reduce to an incapability to tell the sign of the wind velocity in the first range cell if $f_{offset} = 0$.

The line-of-sight wind distribution in range cell i is found from

$$v_{LOS} = \frac{\lambda}{2}\left(f_{peak} - (i-1)\Delta f\right) \cdot \quad (5)$$

The train length will be limited in any embodiment. However, the FSPT can be restarted at the initial frequency if the train repetition frequency is low enough to ensure that the return from previously emitted trains can be disregarded. Note that during the first n LO pulses of a train only n+1–i returns will arrive from range cell i. Trains will typically contain more than hundred frequency stepped pulses in suitable embodiments. Inter-train ambiguities will therefore be unlikely and initial return losses will be insignificant.

III. RANGE RESOLUTION

All scatter distances within a range cell will not contribute with the same amount of energy to the allocated frequency slot. Aerosols in the beginning and the end of a range cell will contribute to the peak for a much shorter time than the aerosols in the middle of the range cell. The duration that aerosols at distance x backscatter a frequency allocated to frequency slot i, during the LO triggered sample duration T_{pulse}, is denoted $\tau_i(x)$ and given as

$$\tau_i(x) = T_{pulse}\left(1 - \left|\frac{x - c_i}{c_i}\right|\right) \cdot \frac{c}{2} \text{ for } x_i < x < x_i' \quad (6)$$

where $c_i = (T_{delay} + (i-1)\cdot T_{pulse} + (i-1)\cdot T_{inter}) \cdot c/2$ is the center of range cell i.

Note that aerosols at the edges of a range cell will contribute to two frequency slots for high duty cycle trains with partly overlapping neighboring range cells, i.e. $T_{pulse} > T_{inter}$.

The FWHM range resolution of collimated systems will be $cT_{pulse}/2$ in accordance with single frequency pulsed range gated systems. The discrete Fourier transform will spread the contribution of the energy contributed by aerosols at the edges over a wider bandwidth, since the contribution to frequency slot i from aerosols at the edges will have a shorter duration than those in the center of range cell i. The power in the discrete frequency bin corresponding to the wind velocity in the center of the range cell will thus be additionally significant and the effective range resolution improved.

FSPT can with advantage be used in monostatic focused systems. A focused system drastically improves the received optic power and can improve the range resolution without deteriorating the frequency resolution. The range resolution of range cell i can be calculated from the received energy profile $W_i(x) = \tau_i(x)\cdot W_{focus}(x)$ where $\tau_i(x)$ is the normalized weight function for rectangular pulses due to the varying contribution time and $W_{focus}(x)$ is the normalized weighting due to the focused telescope [6].

IV. FREQUENCY STEPPED PULSE TRAIN GENERATOR

A suitable embodiment of an FSPT generator for coherent lidars is the lightwave synthesized frequency sweeper [7] (LSFS) shown in Fig. 3. The loop is seeded with a pulse of duration T_{pulse} from an amplitude modulated coherent laser, e.g. using a Mach-Zehnder (MZ) modulator to generate a pulse from a highly coherent fiber laser with incorporated fiber grating. The seed pulse is amplified by an erbium doped fiber amplifier (EDFA). Most of the amplified light is coupled to the telescope while a fraction reenters the loop to be shifted in frequency by Δf in an acousto-optic modulator (AOM). This new input pulse becomes the base for the following frequency stepped pulse of duration T_{pulse}. A filter suppresses the build up of ASE noise and a fiber optic loop delay ensures the separation of consecutive pulses. The LSFS can be restarted in less than a microsecond by closing the AOM and letting the MZ generate a new seed pulse. The AOM gives a stable frequency step, the MZ can from practically rectangular pulses with good extinction ratio and the emission can be made continuous by adjusting the loop length to fit with the seed pulse duration. LSFS configurations can provide pulse trains suitable for wind velocity sensing with T_{pulse} down to 200 ns, a standard Δf = 27.12 MHz and trains including several hundred pulses. All opto-electronic components are commercially available at 1.55 μm with fiber pigtails.

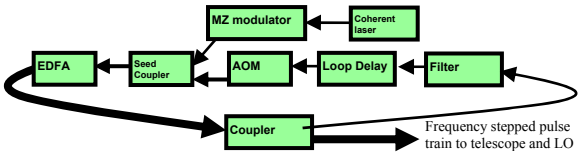

Figure 3: LSFS concept for generating FSPTs.

V. SYSTEM EXAMPLE

The layout of an FSPT modulated coherent lidar can be seen in Fig. 4. To keep power levels low in the LSFS the signal leaving the FSPT generator can be amplified by an external high power EDFA. A LO line can be branched out and possibly delayed in a fiber length and offset in frequency by an AOM. An undelayed, non-offset LO can alternatively be formed from a reflection after the circulator. Such reflections must be avoided for solutions with a separate LO path. The generated beat signal is band pass filtered in accordance with the frequency slots of interest. Sampling of the beat signal is triggered by the LO pulses. The sampled signal is Fourier transformed, some thousand spectra are accumulated and the wind velocity in each range cell is deducted. It might be useful to split the signal and filter out each slot separately, noise will be minimized and it will be

possible to undersample each slot at a sampling frequency Δf.

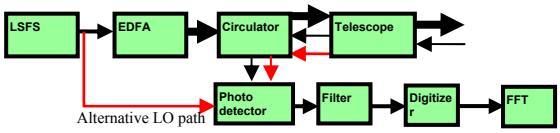

Figure 4 : Layout of an FSPT modulated coherent monostatic lidar. LO in red.

A focused cw system based on a fiber laser and a high power EDFA with an average output power of 1 W and a lens diameter of 7 cm has proven to give reliable wind measurements up to 116 m also for very clear atmospheres [2]. Similar performance is expected of an FSPT modulated lidar with the same average power and optic dimensions. The FSPT lidar would be insensitive to cloud reflections and have improved range resolution for longer ranges. Velocity sensing with an FSPT modified cw system based on the commercial Zephir system is under preparation.

Normalized received energy profiles for the three first range cells of an undelayed collimated FSPT modulated lidar continuously emitting rectangular pulses with T_{pulse} = 200 ns can be seen in Fig. 5.

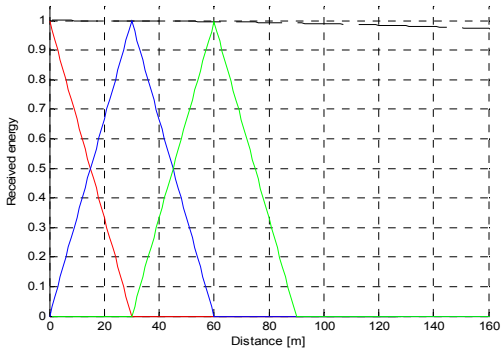

Figure 5: Normalized received energy profiles of the three first range cells of an undelayed collimated FSPT modulated lidar. Range cell one in red, two in blue and three in green. The dashed black line outlines $W_{collimated}(x)$.

The profiles of a cw system and the range cells of an undelayed FSPT-modulated lidar continuously emitting rectangular pulses with T_{pulse} = 500 ns are compared in Fig. 6. The monostatic systems have a telescope radius of 2.12 cm a following Sonnenschein's definition[6]. The focus is set so that the maximum energy is received from 150 m.

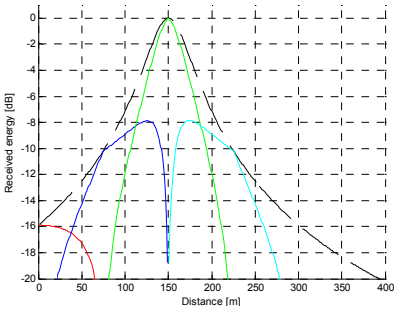

Figure 6: Comparison of the profiles of a cw system (black dashed) and an FSPT modulated lidar continuously emitting rectangular pulses with duration T_{pulse} = 500 ns. Range cell one in red, two in blue, three in green and four in cyan. Note that the y-axis is plotted in dB.

VI. CONCLUSIONS

Frequency stepped pulse train modulated lidars have attractive features for range resolved velocity sensing, e.g. of wind velocity. FSPT modulated lidars offer unambiguous range resolved velocity sensing of a dispersed target at high repetition rates. The sensing is unambiguous since scatter from range cells are uniquely mapped into frequency slots. In comparison with focused cw lidars will FSPT-modulated systems be isolated from cloud reflections and have improved range resolution when sensing at longer distances. Possible near term applications are sensing of wind in airports or for evaluation of wind power sites.

The lightwave synthesized frequency sweeper is a suitable FSPT generator. It can in principle emit continuously with stable equidistant frequency steps at fixed intervals. The LSFS can give several hundreds of sub-microsecond pulses before amplified spontaneous emission noise builds up. A 1.55 µm LSFS can be assembled from commercially available fiber pigtailed components.

References

[1] G. Pearson and C. Collier, "A pulsed CO_2 lidar for boundary layer meteorology", Q. J. R. Meteorol. Soc. vol. 125, No. 559, pp. 2703-2721 (1999)

[2] D. Smith et al., "Wind Lidar evaluation at the Danish wind test site in Høvsøre", Wind Energy, vol. 9, No. 1, pp. 87-93 (2006)

[3] C. Karlsson, F. Olsson, D. Letalick, M. Harris, "All-fiber multifunction continuous-wave coherent laser radar at 1.55 µm for range, speed, vibration and wind measurements", Appl. Opt. vol. 39, No. 21, pp. 3716-3726 (2000)

[4] C. Werner, F. Köpp, R. L. Schwiesow, "Influence of clouds and fog on LDA wind measurements", Appl. Opt. vol. 23, No. 15, pp. 2482-2484 (1984)

[5] M. W. Phillips, P. J. M. Suni, J.A. L. Thomson, "Fiber-based LADAR Transceiver for range/Doppler imaging with frequency comb generator", US Patent 5,835,199 (1998)

[6] C. M. Sonnenschein, F. A. Horrigan "Signal-to-Noise Relationship for Coaxial Systems that Heterodyne Backscatter from the Atmosphere" in Applied Optics, vol. 10, No 7, pp. 1600-1604 (1971)

[7] K. Shimizu, T. Horiguchi, Y. Koyamada, "Frequency translation of light waves by propagation around an optical ring circuit containing a frequency shifter: 1. Experiment.", Appl. Opt. vol. 32, No. 33, pp. 6718-6726 (1993)

Velocity sensing FSPT-modulated coherent lidar

Petter Lindelöw
Ørsted-DTU, COM•DTU, Technical University of Denmark
Ørsteds plads 1, building 348, 2800 Kongens Lyngby
Denmark
pli@oersted.dtu.dk

INTRODUCTION

This paper proposes and describes a FM technique based on Frequency Stepped Pulse Trains (FSPT) suitable for high duty cycle range resolved coherent lidar sensing of primarily dispersed moving targets. FSPT modulation provides a unique range cell to frequency slot mapping, thus avoiding range ambiguities and range-Doppler ambiguities, while providing a high duty cycle. FSPT modulated continuously emitting lidars could potentially reach the resolution of low duty cycle systems based on short high peak power pulses. Initial results from a suitable FSPT generator and from a FSPT modulated lidar prototype are presented.

Focused cw systems[1] and frequency modulation techniques[2] are used to increase duty cycles. However, focused systems are limited in range and rely on homogeneity of the atmosphere. Saw tooth chirping modulation is unsuitable for range resolved velocity sensing of dispersed moving targets like the atmosphere since it introduces irresolvable range-Doppler ambiguities.

Multi-frequency carrier wave systems have previously been proposed[3]. However, such systems have been based on range gating of pulses containing several frequencies simultaneously, the advantage being that the resulting spectra contains a comb of Doppler peaks related to the wind velocity. However, such solutions do not permit for a faster PRF without compromising the range ambiguity.

METHOD

A FSPT modulated lidar emits a train of pulses each stepped in frequency by an equidistant step Δf between consecutive pulse. The FSPT is further more described by the duration of fixed frequency, T_{pulse}, and the duration without emission, T_{inter}, according to Figure 1.a. In a preferred embodiment the pulses are emitted without intervals, i.e. T_{inter}= 0 s. The train is thus emitting continuously and is only pulsed in the sense that the emitted frequency steps every T_{pulse}. An FSPT modulated lidar will concurrently receive Doppler shifted and n·Δf-stepped light scattered from several range sets of the atmosphere as illustrated in Figure 1.b. Mixing this scatter with a LO, with the same frequency as the most previously emitted pulse, and Fourier transforming the beat signal will give a heterodyne spectrum with a set of separate peaks each representing a speckle take of the wind velocities in the respective range set. If the frequency step is larger than the plausible variations in Doppler shift, the detected peaks will be uniquely allocated in a specific closed range of frequencies. Such frequency ranges will be referred to as frequency slots, shown in Figure 1.c.

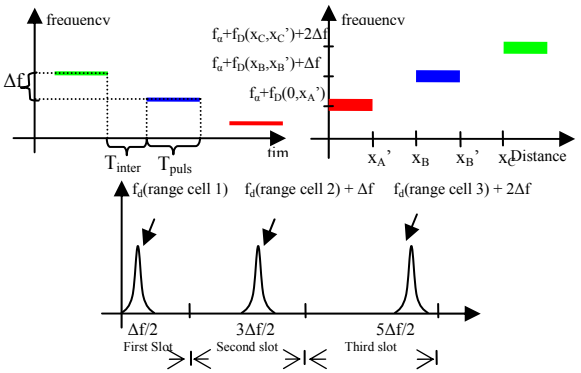

Figure 1 a) An FSPT with pulse duration, T_{pulse}, interpulse duration, T_{inter}, and pulse-to-pulse frequency step, Δf. b) Frequency as a function of scattered distance received by the lidar at time t_α when a complete pulse has just been emitted. Note that the ranges contributing at t_α are $x_A' = (c/2)(T_{pulse})$, $x_B = (c/2)(T_{pulse} + T_{inter})$ and $x_B' = (c/2)(2T_{pulse} + T_{inter})$ etc. c) The scatter from the first three range cells mapped into their allocated frequency slots. The LO offset is in this case 0 MHz.

The LO of an FSPT modulated lidar is a copy of the emitted FSPT, possibly delayed with T_{delay}. Triggered sampling for one spectrum is done during a full LO pulse of duration T_{pulse}. The range set contributing to the peak in a specific frequency slot during a full sampling period will be referred to as a range cell. The range cells and frequency slots will self assemble if the frequency step, pulse and possible inter pulse durations are constant, i.e. for every sample the

peaks will be mapped into their allocated frequency slots continuously and uniquely, as seen in Figure 2.

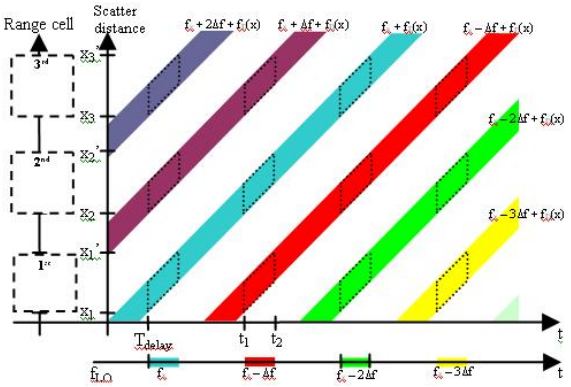

Figure 2: Time-space representation of scatter detected by an FSPT modulated lidar with a delayed LO and a considerable inter pulse duration for clarity. Each range-cell is continuously mapped into its allocated frequency slot since the scattered frequency keeps its relation with the LO over consecutive pulses. E.g. The scatter received from the second range cell, x_2 to x_2', at time T_{delay} to $T_{delay} + T_{pulse}$, here described by the first purple parallelogram to the left, will generate a peak at ($f_x + \Delta f + f_D(x_2..x_2')$) – $f_x = \Delta f + f_D(x_2..x_2')$ when mixed with the LO pulse of frequency f_x. The scatter received from the same range cell at $t_1 = T_{delay}+T_{pulse}+T_{inter}$ to $t_2 = T_{delay}+2T_{pulse}+T_{inter}$, second light blue parallelogram to the left, mixed with the LO pulse of frequency $f_x – \Delta f$, will generate a second speckle take of the wind distribution in the second range cell, likewise allocated into the second frequency slot.

Range cell i will extend from x_i to x_i' described from

$$x_i = \left(T_{delay} + (i-2)T_{pulse} + (i-1)T_{inter}\right)\cdot\frac{c}{2} \qquad (1)$$

$$x_i' = \left(T_{delay} + i\cdot T_{pulse} + (i-1)T_{inter}\right)\cdot\frac{c}{2} \qquad (2)$$

Note that the first range cell will be cropped if $T_{delay} < T_{pulse}$. Also note that the range cells will overlap for a continuously emitting train, i.e. with $T_{inter} = 0$.

Range cell i will generate a Doppler peak in frequency slot i covering f_i to f_i' according to

$$f_i = f_{offset} + \left(i - \frac{3}{2}\right)\cdot\Delta f \qquad (3)$$

$$f_i = f_{offset} + \left(i - \frac{1}{2}\right)\cdot\Delta f \qquad (4)$$

Note that it will not be possible to correctly tell the sign of the wind velocity in the first range cell if $f_{offset} < \Delta f/2$. The LOS wind distribution is in range cell i is found from

$$V_{LOS} = \frac{\lambda}{2}\left(f_{peak} - (i-1)\Delta f\right) \qquad (5)$$

The train length will be limited in any embodiment. However, the FSPT can be restarted at the initial frequency if the train repetition frequency is low enough to ensure that the return from previously emitted trains can be disregarded. Note that for the first n LO pulses there will only be n+1–i returns from range cell i. In a suitable embodiment there will typically be more than a hundred frequency stepped pulses in a train and inter-train ambiguities will be low.

The duration that aerosols at distance x backscatter a frequency allocated to frequency slot i, during the LO triggered sample duration T_{pulse}, is nominated by $\tau_i(x)$ and given as

$$\tau_i(x) = T_{pulse}\left(1 - \left|\frac{x - c_i}{c_i}\right|\right)\cdot\frac{c}{2} \quad \text{for } x_i<x<x_i' \qquad (6)$$

where $c_i = (T_{delay}+(i–1)T_{pulse}+(i–1)T_{inter})c/2$ is the center of range cell i. Note that aerosols at the edges of a range cell can contribute to two frequency slots for high duty cycle trains with $T_{pulse}>T_{inter}$.

The FWHM length of the sample volume of collimated systems will be $cT_{pulse}/2$ in accordance with single frequency pulse range gated systems. The discrete Fourier transform will spread the contribution of the energy contributed by aerosols at the edges over a wider bandwidth, since the contribution to frequency slot i from aerosols at the edges will have a shorter duration than those in the center of range cell i. The power in the discrete frequency bin corresponding to the wind velocity in the center of the range cell will thus be additionally significant. In a focused system the most significant volume of range cell i can be calculated from the power profile $W_i(x) = \tau_i(x)\cdot W_{focus}(x)$ where $\tau_i(x)$ is the normalized weight function due to contribution time and $W_{focus}(x)$ is the normalized weighting due to the focused telescope[4].

FSPT MODULATED LIDAR SET UP

To generate FSPTs the Lightwave Synthesized Frequency Sweeper (LSFS)[5], as set out in Figure 3, was used. The loop was seeded by a 3 mW fiber laser with an incorporated fiber grating at 1545 nm. One seed pulse was formed by

using two acousto-optic modulators (AOM) each giving a -27.12 MHz shift to the carrier frequency. The seed pulse entered the loop via a 3dB coupler and then passed through 90 meters of fiber before it was amplified by an erbium doped fiber amplifier (EDFA). The pulse then passed through a 2 nm optical bandpass filter centered around the fiber laser wavelength. A 10th of the pulse was fractioned out of the loop by a 10:1 dB coupler and before re-entering the loop the pulse was frequency shifted with - 27.12 MHz by the loop AOM. After 17 revolutions the loop was purged by closing the loop AOM. After a few µs a new seed pulse entered the loop. All electro-optic components are commercially available with fiber pigtails.

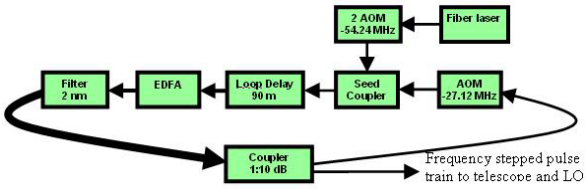

Figure 3: Layout of the LSFS used for generating the FSPTs.

This LSFS was coupled to the coherent lidar setup seen in Figure 4. The FSPT output was amplified with a strong EDFA to 0.8 W. The emission passes through a circulator to a focused telescope with a 7 cm lens diameter. A LO is formed by the reflection from the surfaces after the circulator. The undelayed, non offset LO and the received backscatter are mixed in a pin-diode and the beat signal is directly sampled at 200 MHz triggered by the LO pulse. 400 ns sections of the sampled signal with peak power were zero padded and individually 512 point Fourier transformed. The Doppler shift was deducted from the spectra by subtracting the appropriate multiples of 27.12 MHz. The set up could easily be transferred from FSPT operation to cw operation by coupling the seeding fiber laser directly to the high power EDFA; in this way comparative studies could be made.

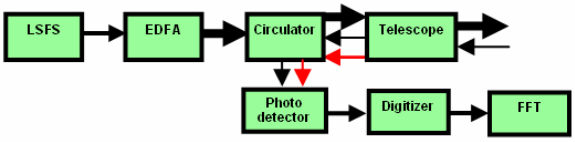

Figure 4 : Layout of FSPT modulated coherent monostatic lidar. LO in red.

MEASUREMENT RESULTS

In the first phase the LSFS was studied by an optical oscilloscope, see Figure. The AOM are relatively slow amplitude modulators and the rise and fall times were about 120 ns. The pulse period was measured as 700 ns. The peak power was limited to 200 µW since the experimental set up has high loss and the EDFA was set so the train had a steady power level. About 500 loops could be done before ASE build up could be detected.

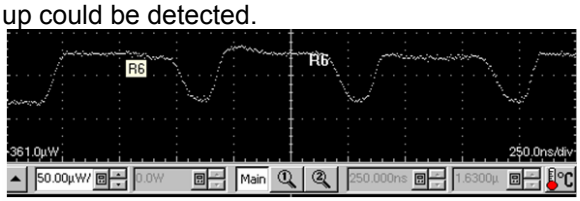

Figure 5: 700 ns pulses from the LSFS.

The LSFS output was mixed with a cw LO branched from the seeding fiber laser. The heterodyne signal from a 1 GHz 3dB bandwidth photodetector was studied in an electrical spectrum analyzer, see Figure 6.

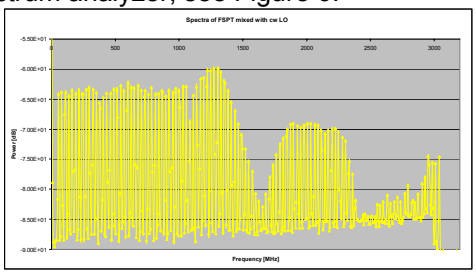

Figure 6: Heterodyne spectrum from mixing the output of the LSFS with a cw LO. It is possible to identify frequencies of multiples of 27.12 MHz in the train all the way up to 3 GHz.

To verify the frequency purity in the pulses the LSFS output was split into two paths by a 3 dB coupler. One path was delayed with $2*T_{pulse}$ in a fiber length. The two trains were mixed to give the spectrum in Figure 7. A weak impurity can be seen at 27.12 MHz. This impurity can come from loop or seed leakage or a slightly unsynchronized pulse overlap.

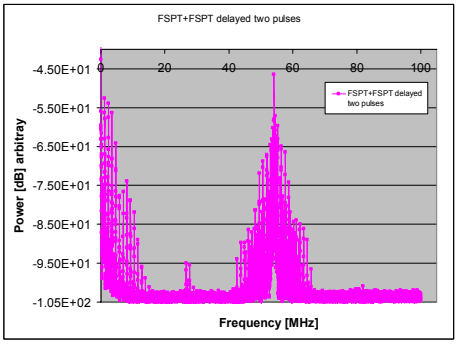

Figure 7: Heterodyne spectrum from mixing the LSFS with a two pulse delayed copy of it self.

In the second phase the FSPT-modulated lidar targeted a fan at 105 m. The average output

power from the FSPT modulated lidar was about 0.75 W. The peak power was slightly higher than for the cw case. The shape of the LSFS output in Figure was copied when amplified. High dynamics of the LO pulse train made it difficult for the receiver to follow. A noise term at 54.24 MHz, which grew with the number of revolutions, also made it difficult to study the Doppler shift in pulses after about $4T_{pulse}$. However, it was possible to measure a good relation between the peak of the cw case and the peak in the spectrum of the FSPT modulated lidar. Figure.a shows the 512-point FFT spectrum generated from a 300 ns zero padded sample using the lidar in cw operation. The Doppler shift from the fan was measured as 10.2 MHz. Figure 8.b shows the 512-point FFT spectrum generated from the 300 ns zero padded sample, sampled during the third LO pulse using the lidar in FSPT operation. The peak is measured as 37.6 MHz. The Doppler shift from the fan was 37.6 – 27.12 = 10.5 MHz since the fan is in the second range cell.

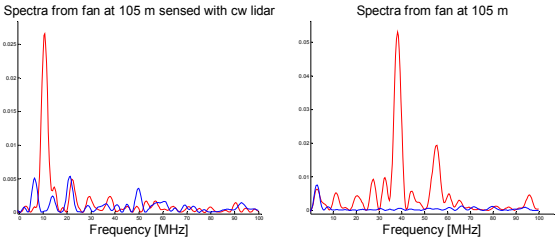

Figure 8: a) Doppler spectrum from a fan at 105 m sensed with the lidar in cw mode. b) Doppler spectrum from a fan at 105 m sensed with the lidar in FSPT mode.

CONCLUSION

FSPT modulated lidars have attractive features for range resolved velocity sensing, particularly for dispersed targets like the atmosphere. An FSPT modulated lidar can emit continuously and still avoid range ambiguities. Applications could be avoiding cloud reflections when sensing wind in airports or at wind turbine sites with focused, continuously emitting coherent lidars or to improve the resolution for sensing at medium distances, e.g. in front of airplanes. A suitable FSPT generator was constructed and characterized and a lidar prototype was modified with FSPT modulation. Proof-of-concept measurements were performed with a modified lidar prototype.

REFERENCES

[1] D. Smith, M. Harris, A. Coffey, T. Mikkelsen, H. Jørgensen, J. Mann, R. Danielian, “Wind Lidar evaluation at the Danish wind test site in Høvsøre”, Wind Energy, vol. 9, No. 1, pp. 87-93 (2006)

[2] C. Karlsson, F. Olsson, D. Letalick, M. Harris, “All-fiber multifunction continuous-wave coherent laser radar at 1.55 μm for range, speed, vibration and wind measurements”, Appl. Opt. vol. 39, No. 21, pp. 3716-3726 (2000)

[3] M. W. Phillips, P. J. M. Suni, J.A. L. Thomson, “Fiber-based LADAR Transceiver for range/Doppler imaging with frequency comb generator”, United States Patent 5,835,199 (1998)

[4] C. M. Sonnenschein, F. A. Horrigan “Signal-to-Noise Relationship for Coaxial Systems that Heterodyne Backscatter from the Atmosphere” in Applied Optics, vol. 10, No 7, pp. 1600-1604 (1971)

[5] K. Shimizu, T. Horiguchi, Y. Koyamada, “Frequency translation of light waves by propagation around an optical ring circuit containing a frequency shifter: 1. Experiment.”, Appl. Opt. vol. 32, No. 33, pp. 6718-6726 (1993)

FREQUENCY STEPPED PULSE TRAIN MODULATED COHERENT LIDAR SYSTEM, METHOD AND USE

ABSTRACT

The invention relates to a coherent LIDAR system. The invention further relates to a method of sensing specifically dispersed and/or moving objects and to the use of a coherent LIDAR system. The object of the present invention is to provide an alternative method of remote sensing of stationary or moving objects using coherent laser light. It is a further object to provide a scheme for minimizing range ambiguities in a coherent LIDAR system. The problem is solved in that a coherent LIDAR system is provided comprising a transmitter for transmitting an optical signal along a predetermined path, the optical signal comprising laser light, and a receiver for receiving and processing a reference (LO) signal and backscattered light from one or more objects along said path wherein said transmitter is adapted to provide that said laser light comprises a train of frequency stepped pulses. An advantage of the present invention is that the spatial range exposed to a frequency stepped pulse train (FSPT), e.g. an atmosphere, or any other dispersed target, can be partitioned into several range cells each uniquely mapped to a distinct frequency window, when sensed by a coherent LIDAR. The invention may e.g. be used for environmental sensing (e.g. aerosol sensing), wind measurements, etc.

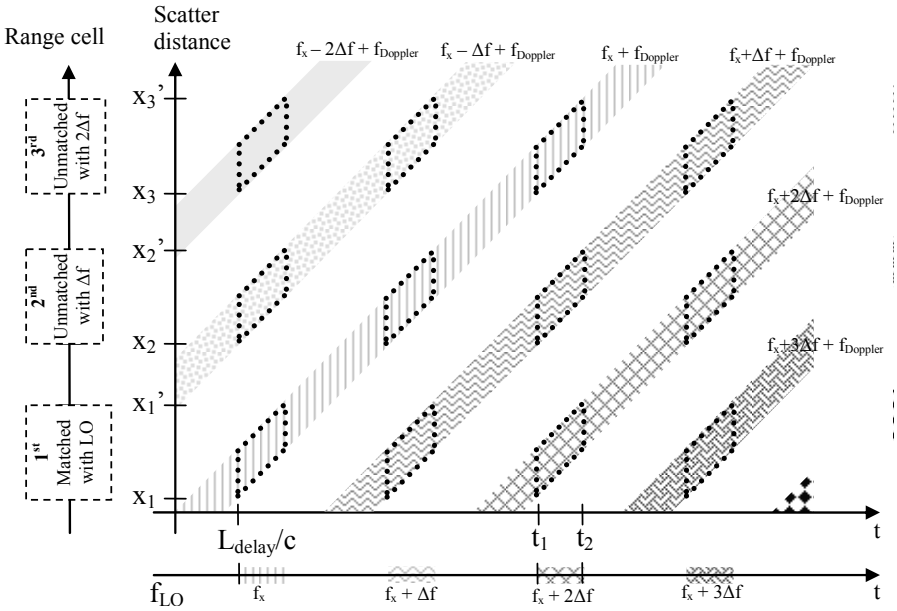

www.oersted.dtu.dk

Ørsted·DTU
ElectroScience
Technical University of Denmark
Ørsteds Plads
Building 348
DK-2800 Kgs. Lyngby
Denmark
Tel: (+45) 45 25 38 00
Fax: (+45) 45 93 16 34
E-mail: info@oersted.dtu.dk

ISBN 978-87-911-8482-6